New Physics Searches in High Mass Dimuons at the Collider Detector at Fermilab

Tracey Pratt

St. Edmund Hall

University of Oxford

Thesis submitted in partial fulfilment

of the requirements for the degree of

Doctor of Philosophy

Michaelmas Term 2002

This thesis is dedicated to my grandfather, William Pratt, whom I will always remember and love.

Acknowledgments

I would like to thank my mum, dad and Neil for their endless support and encouragement and for all the emails when I was in the USA. Also, thanks to mum for her apple crumbles! Thanks too to Michelle for all those twinny moments, and in particular for ensuring that my life is never uneventful!

I would also like to thank my work colleagues. Thanks, of course, to my supervisor, Todd Huffman, especially for showing me the highlights of Iowa and Nebraska and for introducing me to some true American cuisine; velveta 'cheese', root-beer and wine-coolers - a memorable experience! I would like to thank profusely Kaori Maeshima, without whom I would not have a DPhil analysis. I would like to thank both Kaori and Koji Ikado for all the meetings at Fermilab and for the numerous phone conferences when I was in Oxford, for which I am much indebted. In addition, I would like to thank Kaori for introducing me to running, my new sport! Thanks also to the muon group, in particular to Ken Bloom, for his help and inspiration, and to Michael Schmitt. Thanks to Farrukh for adding fish to his amazing lamb-shank cooking repertoire. I would also like to thank Pete Renton for proof reading my thesis. Finally, thanks to both Aidan Robson and Giulia Manca for being great office-mates.

I also acknowledge the Particle Physics and Astronomy Research Council for providing my studentship.

Contents

List of Figures

List of Tables

Acronyms

A list of commonly used acronyms are listed below in alphabetical order.

ADD	Arkani-Hamed, Dimopoulos and Dvali
BMU	Barrel muon chamber
CAL	Calorimeter
CDF	Collider detector at Fermilab
CES	Central electromagnetic preshower
CL	Confidence level
CLC	Cherenkov luminosity counter
CHA	Central hadronic calorimeter
CMU	Central muon
CMP	Central muon upgrade
CMX	Central muon extension
CP	Charge parity
COT	Central open tracker
CR	Cosmic ray
CSP	Central scintillator upgrade
CSX	Central scintillator extension
GUT	Grand unified theory
DY	Drell-Yan
EM	Electromagnetic
HAD	Hadronic
HAD TDC	Hadron time-to-digital converters
ID	Identification

IMU	Intermediate muon detector
ISL	Intermediate silicon layers
KK	Kaluza Klein
L00	Layer 00, part of silicon detector
LC	Linear collider
LEP	Linear electron positron collider
LHC	Large hadron collider
PDF	Parton distribution function
QED	Quantum electrodynamics
QCD	Quantum chromodynamics
RS	Randall Sundrum
SLC	Stanford linear collider
SM	Standard model
SSM	Sequential standard model
SVT	Silicon vertex tracker
SVX	Silicon vertex detector
TDC	Time-to-digital converter
ToF	Time-of-flight
WLS	Wavelength Shifter
XFT	Extremely fast tracker
XTRP	Extremely fast extrapolator
Zee	Z boson dielectron dataset
Zmm	Z boson dimuon dataset

Chapter 1: Introduction

The Standard Model, which is summarised in Section 1.1, is the present model used to describe fundamental particles and their interactions. There are, however, reasons to believe that this is not a complete theory, and that there exists physics beyond-the-Standard Model. In this thesis two extensions are considered: the existence of new neutral gauge bosons and of extra dimensions. An introduction to these concepts is presented in Section 1.2 and Section 1.3 respectively. A search for their predicted phenomena was performed using dilepton data collected at the Collider Detector Facility (CDF) at the Fermilab Tevatron, which are described in Chapter 2. An overview of how the search was conducted is presented in Chapter 3.

1.1 Standard Model of elementary particles

In Standard Model theoretical framework, the fundamental constituents of matter are spin-1/2 fermions, shown in Table 1.1 [1]. These consist of quarks, which have fractional charges ($+\frac{2}{3}$e and $-\frac{1}{3}$e, where e is the positron charge) and leptons, which have integral electric charges. There are six quark flavours, distinguished by the assignment of quantum numbers, which are labeled u, d, s, c, b and t. Both the quarks and leptons are grouped into three generations of SU(2) doublets, which correspond to doublets of left-handed and singlets of right-handed quarks and leptons, of increasing mass. These constituents can interact by exchange of fundamental bosons (shown in Table 1.2), which are carriers or quanta of four distinct types of fundamental interaction or field.

Fundamental Fermions							
Quarks			Q ($\|e\|$)	Leptons			Q($\|e\|$)
u	c	t	+2/3	ν_e	ν_μ	ν_τ	0
d	s	b	-1/3	e	μ	τ	-1
The quarks and leptons also have antiparticle counterparts							

Table 1.1: The fundamental fermions of the Standard Model grouped by generation

The four fundamental forces in Nature are:

- electromagnetic
- weak
- strong
- gravitational.

These forces have varying strength and range, summarised in Table 1.2.

Interaction	Gravity	Electromagnetic	Weak	Strong
Field quantum/ Intermediate bosons	Graviton (G)	Photon (γ)	$W^{\pm}$, Z^0	8 gluons (g)
Spin-parity	2^+	1^-	1^-,1^+	1^-
Mass (GeV/c^2)	0	0	80.4, 91.2	0
Range (m)	∞	∞	10^{-18}	$\leq 10^{-15}$

Table 1.2: Fundamental interactions in the Standard Model.

The charged leptons have electromagnetic and weak interactions, while the neutrinos are distinguished by only having weak interactions with other particles. Quarks, in addition to the weak and electroweak interactions, are subject to strong interactions. All particles interact through the gravitational interaction. So far gravity has not been incorporated into the SM, and so shall not be considered in the remainder of this introduction to the SM; however, some beyond-the-Standard Model theories, such as studied in Section 1.3, do include gravity. The gauge theories which describe the electromagnetic, weak and strong interactions within the SM and are outlined in the following sections.

Quantum Electrodynamics (QED): $\mathbf{U(1)}_Q$

The electromagnetic interactions are described by quantum electrodynamics (QED) to impressive precision. This is a relativistic gauge field theory which combines the ideas of relativity and quantum mechanics. Originally the theory was proposed to describe the electromagnetic

interactions of electrons and photons. It was subsequently extended to include quarks as well as leptons.

An important property of the QED theory is that it is renormalisable. A single electron can emit and reabsorb virtual photons, and such "self-energy" terms contribute to the electron's physically measurable quantities. These closed loops of virtual particles result in divergent integrals, which cause the theoretically calculated quantities, such as the "bare" mass m_0 or charge e_0, to become infinite. However, it is possible to absorb all the divergences into m_0 or e_0, and then redefine the mass and charge, replacing them by their physical values, e, m (which are determined by experiment). This process is called renormalisation. Calculations within the SM are performed using perturbative expansions in terms of the strengths of the couplings. The result, after renormalisation, is that the QED calculations, if expressed in terms of the physical quantities (e and m), always give finite values, because of the cancellations of divergent terms, order by order in the coupling constant α.

A second vital property of the electromagnetic interaction is that of gauge invariance. The Lagrangian for a free Dirac field (ψ) with spin $\frac{1}{2}$, mass m and electric charge eQ is given by Equation 1.1,

$$\mathcal{L}_{QED}^{free} = \bar{\psi}(x)(i\gamma_\mu \delta^\mu - m)\psi(x) \tag{1.1}$$

This Lagrangian is invariant under both global phase U(1) transformations and local gauge transformations. The global invariance can be demonstrated by considering a global phase U(1) transformation of Qθ, where θ is the continuous parameter, which transforms the fields as follows:

$$\psi \rightarrow e^{iQ\theta}\psi; \quad \bar{\psi} \rightarrow \bar{\psi}e^{iQ\theta}; \quad \delta_\mu\psi \rightarrow e^{iQ\theta}\delta_\mu\psi. \tag{1.2}$$

On substitution for these transformed fields into the Lagrangian, Equation 1.1, the phase ($e^{iQ\theta}$) cancels and the Lagrangian reduces to its original form, *i.e* it remains invariant under such a transformation. In the case of a local transformation, in which θ depends on the space-time point,

the Lagrangian remains invariant if a massless vector field, A_μ, with which the particle interacts is introduced. A_μ is identified as the field for the propagator of the electromagnetic force, the photon. The local phase transformations on the particle wavefunction must be accompanied by local gauge transformations on the field A_μ, and this specifies the particle-field interaction. Under local gauge transformations A_μ transforms as;

$$A_\mu \rightarrow A_\mu - \frac{1}{e}\delta_\mu \theta(x). \tag{1.3}$$

The derivative δ_μ in the QED Lagrangian can be rewritten in terms of the covariant derivative, D_μ:

$$D_\mu \psi \equiv (\delta_\mu - ieQA_\mu)\psi. \tag{1.4}$$

Under simultaneous phase transformation on $\delta_\mu \phi(\mathrm{x})$ and gauge transformation on A_μ then $\phi(\mathrm{x})^* D_\mu \ \phi(\mathrm{x})$ is invariant. The fact that D_μ rather than δ_μ must be used specifies the form of the interaction ($\mathrm{e}A_\mu$) of the charged particle with the field.

The total QED Lagrangian is obtained by adding a term to account for the propagation of the vector field, which is also gauge invariant. This kinetic term is given in terms of the field strength tensor:

$$F_{\mu\nu} = \delta_\mu A_\nu - \delta_\nu A_\mu. \tag{1.5}$$

Thus the QED Lagrangian is:

$$\mathcal{L}_{QED} = \bar{\psi}(x)(i\gamma_\mu D_\mu - m)\psi(x) - \frac{1}{4}F_{\mu\nu}(x)F^{\mu\nu}(x). \tag{1.6}$$

In order to keep the QED Lagrangian invariant under a local gauge transformation then the addition of a mass term $\frac{1}{2}m^2 A_\mu A^\mu$ is not permitted. Consequently, the gauge field, the photon, is massless. This is consistent with experimental observation and ensuring that the electromagnetic force has infinite range.

The success of QED, allowing exact calculations of electromagnetic processes to all orders of the coupling constant α, resulted in the general belief that all theories of fundamental fields should be renormalisable gauge theories.

Weak interactions

The first attempt at constructing a theory of weak interactions was made by Fermi (1934), in which he assumed the existence of the neutrino and formulated a theory of β-decays. In contrast to the exchanged boson of QED to mediate the force, Fermi's theory postulated that the weak interaction was an interaction of four spin-1/2 fermions at the same point. This theory was successful and the leading-order predictions were correct, however, the next-to-leading order calculations were divergent and the theory was found to be non-renormalisable. In order to solve this problem, a locally gauge invariant theory was required. Consequently a gauge theory of weak interactions based on the $SU(2)_L$ group was developed.

Electroweak interactions: $SU(2)_L \times U(1)_Y$

In 1961, Glashow unified the electromagnetic and weak interaction. This model is based on the non-Abelian gauge group $SU(2)_L \times U(1)_Y$. $SU(2)_L$ is the weak-isospin group which acts only on the left-handed fermions and $U(1)_Y$ is the weak hypercharge group.

The desired interactions are "generated" by the requirement of invariance under local phase transformations for the $SU(2)_L$ and $U(1)_Y$ groups:

$$U = exp\{-i[\frac{g}{2}\sigma_i\theta_i(x) + \frac{g'}{2}Y\theta'(x)]\} \tag{1.7}$$

where the first term is the local phase transformation for the SU(2) group weak isospin and the second for the U(1) group weak hypercharge. σ_i are the Pauli spin matrices and here Y is the diagonal matrix of the weak hypercharges of the particles being transformed. Such transformations are different for left- and right-handed particles.

In the same way as for electromagnetism a gauge-invariant description can be obtained, in this case by introducing four vector fields which describe the interactions between the particles. Three of these fields are identified with the $SU(2)_L$ triplet (W_μ^1, W_μ^2, W_μ^3), and one field with the $U(1)_Y$ transformations, B_μ. The electroweak Lagrangian is as follows:

$$\mathcal{L}_{EW} = i\bar{\psi}\gamma_\mu\delta^\mu\psi - \bar{\psi}_L\gamma_\mu(\frac{g}{2}\sigma\cdot\mathbf{W}^\mu + \frac{g'}{2}Y_L\mathbf{I}B^\mu)\psi_L - \bar{\psi}_R\gamma_\mu\frac{g'}{2}Y_RB^\mu\psi_R - \frac{1}{4}\hat{\mathbf{W}}^{\mu\nu}\hat{\mathbf{W}}_{\mu\nu} - \frac{1}{4}B^{\mu\nu}B_{\mu\nu} \quad (1.8)$$

The triplet of gauge fields W_μ^a couple to weak isospin with coupling g, whereas the U(1) gauge field, B_μ, couples to weak hypercharge with coupling g'.

The massless fields in the above Lagrangian can be combined to form the four physical fields of the electroweak theory; the photon, $W^\pm$ and Z^0. The charged W bosons couple to left-handed chirality states and are composed of components of $\mathbf{W}^\mu$;

$$W_\mu^\pm = \frac{1}{\sqrt{2}}(W_\mu^1 \mp W_\mu^2). \quad (1.9)$$

The Z^0 and photon couple to both left- and right-handed fermions and are formed from orthogonal linear combinations of the $\mathbf{W}$ and B fields;

$$Z_\mu = cos\theta_W W_\mu^3 - sin\theta_W B_\mu \quad (1.10)$$

$$A_\mu = sin\theta_W W_\mu^3 + cos\theta_W B_\mu \quad (1.11)$$

where θ_W is the Weinberg or weak mixing angle, which relates the couplings of the electromagnetic and weak interactions according to

$$gsin\theta_W = g'cos\theta_W = e. \quad (1.12)$$

The neutral current component of the SM electroweak Lagrangian is thus;

$$-\mathcal{L}_{NC,SM} = \bar{\psi}_i \gamma^\mu \{t_{3i} g W_{3\mu} + Y_i \frac{g'}{2} B_\mu\} \psi_i \tag{1.13}$$

where t_3 and Y are the standard isospin and hypercharge charges, shown in Table 1.3.

	t_{3i}	$\sqrt{\frac{5}{3}} Y_i$
$\begin{pmatrix} u \\ d \end{pmatrix}_L$	$\frac{1}{2}$ $-\frac{1}{2}$	$\frac{1}{6}$
$\begin{pmatrix} \nu \\ e \end{pmatrix}_L$	$\frac{1}{2}$ $-\frac{1}{2}$	$-\frac{1}{2}$

Table 1.3: Isospin t_{3i} and hypercharge Y_i for the fermions, where u and d represent the up-type and down-type quarks respectively.

The SM neutral current Lagrangian, Equation 1.13, can be written in terms of the physical fields, Z_μ and A_μ, by substitution for W^3_μ and B_μ using the relationships in Equation 1.10 and Equation 1.11. In this basis the SM neutral current Lagrangian has the form:

$$\mathcal{L}_{NC,SM} = e \sum_i q_i \bar{\psi}_i \gamma^\mu \psi_i A_\mu + \frac{g}{cos\theta_W} \sum_{i=L,R} \bar{\psi}_i \gamma^\mu (t_3 - Q sin^2\theta_W) Z_\mu \psi_i. \tag{1.14}$$

The coupling of the Z^0 boson to the fermions can be rewritten in terms of two coupling constants v^i and a^i, which are defined by Equations 1.15 and displayed in Table 1.4.

$$v^i = t_{3i} - 2 q_i sin^2\theta_W \qquad a^i = t_{3i} \tag{1.15}$$

In this case, the SM neutral current Lagrangian can be expressed in the form;

$$\mathcal{L}_{NC,SM} = e \sum_i q_i \bar{\psi}_i \gamma^\mu \psi_i A_\mu + \frac{g}{cos\theta_W} \sum_{i=L,R} \bar{\psi}_i \gamma^\mu (v^i - a^i \gamma_5) Z_\mu \psi_i. \tag{1.16}$$

	q_i	v^i	a^i
q (u-type)	$\frac{2}{3}$	$\frac{1}{2}$ - $\frac{4}{3}$ $sin^2\theta_W$	$\frac{1}{2}$
q (d-type)	-$\frac{1}{3}$	-$\frac{1}{2}$ + $\frac{2}{3}$ $sin^2\theta_W$	-$\frac{1}{2}$
ν	0	$\frac{1}{2}$	$\frac{1}{2}$
e	-1	-$\frac{1}{2}$ + 2 $sin^2\theta_W$	-$\frac{1}{2}$

Table 1.4: Electric charge, $q_i = t_{3i} + \sqrt{\frac{5}{3}}Y_i$, and vector and axial couplings for Z_μ: $v^i = t_{3i}$ - $2q_i sin^2\theta_W$, $a^i = t_{3i}$; for the fermions in Table 1.3.

Electroweak theory predicts the existence of four gauge bosons, γ, $W^\pm$ and Z, however, the addition of a mass term into electroweak Lagrangian (Equation 1.8) of the form $\frac{1}{2}m_W^2 W_\mu W^\mu$ for the bosonic field would break gauge invariance, because such terms are not invariant under gauge transformations of $SU(1)\times U(1)$. In analogy to the photon, which must be massless because a mass would spoil the invariance of QED; the principle of gauge invariance requires that the electroweak gauge bosons are also massless. This makes the theory inconsistent with experimental observation which requires massive electroweak W and Z^0 bosons, because of the short range of the weak interaction. The solution was found to be spontaneous symmetry breaking, in which masses can be generated without violating gauge invariance. This is achieved via the Higgs mechanism.

Electroweak symmetry breaking: the Higgs mechanism

To accommodate massive vector bosons ($W^\pm$, Z^0) spontaneous symmetry breaking (SSB) of the electroweak $SU(2)_L\times U(1)_Y$ symmetry was proposed by the introduction of a complex Higgs scalar doublet, as outlined in Appendix A.1. This causes the decoupling of the weak and electromagnetic forces and leads to the $W^\pm$ and Z^0 gauge bosons and all the fermions acquiring masses and while keeping one vector boson, the photon, massless. This is achieved while preserving the local gauge invariance of the whole electroweak theory and the theory remains renormalisable. A consequence of SSB is the prediction of there being a massive scalar (spin-0) particle known

as the Higgs boson, which is yet experimentally undiscovered and is the focus of many searches[1].

Quantum Chromodynamics: QCD

A gauge theory, known as quantum chromodynamics, which also has the property of local gauge invariance, was introduced to describe the strong interactions. This is based on an $SU(3)_C$ gauge group, where C stands for colour. Eight massless vector bosons, known as gluons, mediate the quark-quark interactions[2]. The gluons carry colour charge. There are six types of colour charge; three colour (R,G,B) and their anti-colours. Because the gluons themselves carry colour they have strong self-interactions, so QCD is a non-Abelian theory, in contrast to QED, which is Abelian. This results in the effective force between quarks increasing with distance which leads to "confinement" of quarks within hadrons and means that a single quark can not exist more than about 1 fermi from another.

The QCD Lagrangian is written in terms of the quarks and their covariant derivatives and contains a kinetic term for the gluon fields;

$$\mathcal{L}_{QCD} = \sum_q \bar{q}(x)(i\gamma_\mu D^\mu - m_q)q(x) - \frac{1}{4}F^\alpha_{\mu\nu}(x)F^{\mu\nu}_\alpha(x). \tag{1.17}$$

Limitations of the Standard Model

The SM $SU(3)_C \times SU(2)_L \times SU(1)_Y$ theory, of the electroweak interaction and of QCD, was developed over a period of years from both theoretical and empirical discoveries. The predictions of the SM of particle physics have been confirmed by high energy experiments with no significant deviations from theory. Despite the agreements with all existing data, many puzzles remain:

- Fermion masses: The SM does not address the origin of flavour, number of generations of leptons and quarks, fermion mass pattern or mixing.

[1] The mass of the Higgs (M_H) has been experimentally determined to be greater than 114.3 GeV/c^2 at the 95 % confidence level [2].

[2] The number of gauge bosons is equal to the number of generators, n, for the group, *i.e.* for the group SU(N), n= N^2 - 1.

- Hierarchy problem: The hierarchy problem is the large disparity between the electroweak scale ($\sim 10^3$ GeV), where electroweak symmetry breaking occurs, and the apparent fundamental scale of gravity, defined by the Planck scale (M_{Pl}~10^{19} GeV). In the SM the Higgs particles receive self-energy corrections (from one-loop diagrams) which grow quadratically with the cutoff energy, assumed to be the order M_{Pl}. Thus these particles "naturally" have masses at the Planck scale rather than the electroweak scale. However, from theorectical grounds M_H must be less than 1 TeV. In order to maintain the Higgs mass (M_H) at the electroweak scale the bare Higgs mass and its coupling must be fine-tuned to the order of sixteen decimal places. Such fine-tuning is considered extremely unnatural.

- A dark matter candidate: There is no dark matter candidate in the SM, however, one is needed. Most beyond-the-SM theories provide one.

- Lack of Grand Unification: Although the SM has been very successful, it only unifies two of the four interactions. From a theoretical point of view it is desirable to have a single theory which describes all of the fundamental interactions in nature. The aim of such a theory is to find a gauge group G, with a single coupling constant, which describes all interactions and thus has $SU(3) \times SU(2) \times U(1)$ as a subgroup. This implies that a scale must exist some high "unification" energy where the $SU(3)$, $SU(2)$ and $U(1)$ couplings become equal, as implied in Figure 1.1. If the three couplings in the $SU(3) \times SU(2) \times U(1)$ model are extrapolated to large scales then they do not meet at one point.

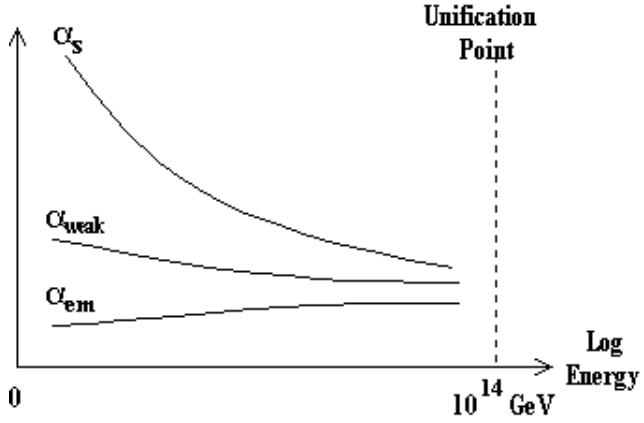

Figure 1.1: Unification of the strong (α_S), weak (α_{weak}) and electromagnetic (α_{em}) coupling constants.

In addition, the SM requires 19 empirically determined parameters. These are:

- three gauge coupling strengths; α_s, g and g' for the strong, electromagnetic and weak interaction,
- nine parameters for the charged fermion masses,
- four mixing angles in the 3×3 unitary Cabbibo-Kobayashi-Maskawa matrix, which parameterise the level of quark mixing,
- M_H the mass of the Higgs boson and v the vacuum expectation value of the Higgs potential and
- the QCD θ parameter, which parameterises CP violation in strong interactions.

Consequently, the SM is considered to have too many arbitrary parameters and leaves open too many unresolved questions to be considered complete. It is thought that the SM is just an effective theory, a low-energy approximation of a more complete one. Such a theory would be expected to explain the phenomena described in the SM, but also have associated new phenomena. It is predicted that new physics would appear, at a scale (Λ) comparable to the mass of the Higgs boson, *i.e.* $\Lambda \leq 1$ TeV.

Numerous beyond-the-SM theories have been proposed in attempts to explain these phenomena, many of which involve the introduction of new symmetries, particles or interactions. In this thesis two major extensions are considered; that of new gauge bosons which appear when tackling the challenge of unification of the interactions and the existence of extra dimensions, which proposes a solution to the hierarchy problem. An introduction to the theory of these concepts is given in Section 1.2 and Section 1.3 respectively.

1.2 Z' boson

The existence of heavy neutral gauge vector bosons (Z') is a feature of many extensions to the SM. New gauge bosons will arise if the SM is enhanced by additional gauge symmetries or embedded into a larger gauge group. For example; Z' arise in grand unified theories (GUTS) [3], superstring theories [4], Left-Right symmetric models and models of composite gauge bosons [5].

Traditionally, the most studied such extensions were motivated by GUTs, which were introduced in an attempt to unify the strong and electroweak interaction. GUTs extend the SM gauge group to a group of higher rank, predicting the presence of at least one extra neutral gauge boson Z'. The minimum unification group of the strong (SU(3) colour) and electroweak interactions (SU(2)×U(1)) is SU(5). In this theory the electron and the d-quark are placed into the same representation of SU(5) (leptoquarks), consequently quarks can be transformed into anti-quarks, and quarks into leptons, which means that the proton is no longer stable. SU(5) GUT has many desirable features, for example, it accommodates the fact that the charge on the electron is three times the charge on the down quark and that the difference between the u and d quarks charges is one. However, it is ruled out by several experiments. LEP I measured the weak mixing angle $\sin^2\theta(M_Z)$ to be 0.23159(21) and fits to all present data yield 0.23113(15) [6], whereas SU(5) predicts this angle to be 0.21. Also proton decay, which is predicted by SU(5) at the rate of $\tau(p \to e^+\pi^0)$ 10^{28} - 10^{30} years, has not been observed at the rate expected; SuperKamioKande constrains the rate to be greater than 5.0×10^{33} years [7] [8]. Therefore the SU(5) GUT cannot be correct, unless it is a subgroup of a larger gauge group. Other unified theories involving groups larger than SU(5) can accommodate the present bounds on the nucleon lifetime [3] [4]. The next extension of the unification group is $SO(10)$, which is consistent with experimental data. Another example of a larger group which includes SU(5) is E_6. This model corresponds to enlarging the electroweak SM gauge group by including one extra U$'$(1) factor and results in adding one extra neutral gauge boson, Z'. Certain compactifications of string theory lead naturally to the E_6 gauge group, or one of its sub-groups.

Also more recently, a new motivation for Z' searches comes from the development of extra dimensional models, which are extensions of those considered in this thesis, in Section 1.3. Z' bosons can arise in certain classes of theories with extra dimensions, in which the gauge bosons of the SM can propagate in the extra dimensions, see page 43. The bosons from extra dimensional models are searched for in the same way as Z' bosons from extended gauge groups.

1.2.1 Production of Gauge Bosons

The interacting neutral current Lagrangian ($\mathcal{L}_{NC}$) for the SM with an additional U(1), denoted by U(1)$'$ ($SU(2)_L \times U(1)_Y \times$ U$'$(1)), using same notation as the Aguila [9], is;

$$-\mathcal{L}_{NC} = \bar{\psi}_i \gamma^\mu \{t_{3i} g W'_{3\mu} + Y_i g'_{11} B'_\mu + Y_i g'_{12} Z'_{2\mu} + Q'_i g'_{21} B'_\mu + Q'_i g'_{22} Z'_{2\mu}\} \psi_i. \tag{1.18}$$

This is similar to the SM neutral current Lagrangian, shown in Equation 1.13. Here B'_μ, $W'_{3\mu}$ are the field strength tensors for $U(1)_Y$, $SU(2)_L$, previously introduced as B_μ and $W_{3\mu}$. There are also extra terms which involve the the field strength tensors for $U(1)'$, $Z'_{2\mu}$ and Q$'$ is the extra U$'$(1) charge, shown in Table 1.5.

	Q$'$
$\begin{pmatrix} u \\ d \end{pmatrix}_L$	q'_{qL}
$\begin{pmatrix} \nu \\ e \end{pmatrix}_L$	q'_{lL}

Table 1.5: Extra $U(1)'$ charge, Q$'$, assignments for ordinary fermions.

The physical implications of the introduction of a new gauge boson can be obtained by considering the Lagrangian in the physical (or mass) eigenbase of the Z-Z' system. This is analogous to the transition in the SM, from representing the neutral current Lagrangian in terms of

the $SU(2)_L$ and $U(1)_Y$ massless gauge fields (W^3_μ and B_μ respectively), shown in Equation 1.13, to representing it in terms of the physical fields, Z_μ and A_μ, shown in Equation 1.14. The parameters and fields in the original, mixed basis are expressed as primed, and those in the physical basis without primes.

In terms of the physical fields, the neutral current Lagrangian is expressed as [9]:

$$-\mathcal{L}_{NC} = \bar{\psi_k}\gamma^\mu\{t_{3k}gW_{3\mu} + Y_k g_{11}B_\mu + Y_k g_{12}Z_{2\mu} + {Q'}_k g_{22}Z_{2\mu}\}\psi_k, \tag{1.19}$$

where

$$B_\mu = c'B'_\mu - s'Z_{2\mu}, \tag{1.20}$$

$$Z'_{2\mu} = s'B_\mu + c'Z_{2\mu}. \tag{1.21}$$

c' and s' are the cosines and sines of the angle corresponding to the rotation between the two bases and they relate the couplings and field strength tensors in the two bases. c' and s' fulfil the constraints that:

$$g_{21} = g'_{21}c' + g'_{22}s' = 0. \tag{1.22}$$

The measurable couplings (which are those in the physical eigenbasis, Equation 1.19) satisfy the relations:

$$g_{11} = g'_{11}c' + g'_{12}s', \quad g_{12} = -g'_{11}s' + g'_{12}c' \quad and \quad g_{22} = -g'_{21}s' + g'_{22}c'. \tag{1.23}$$

As in the SM case, the photon is defined to be a combination of $W_{3\mu}$ and B_μ, as shown in Equation 1.11, and the positron charge (e) expressed in terms of the couplings is $\frac{\sqrt{3/5}gg_{11}}{\sqrt{g^2+\frac{3}{5}g^2_{11}}}$.

Comparing the form of the extended neutral current Lagrangian, Equation 1.19, to that of the SM, Equation 1.13, indicates that any extra neutral gauge interaction can be written in the current eigenstate gauge boson basis adding an extra term for the new gauge boson (Z_2 term),

similar to the SM, but allowing for the linear combination of the extra charge Q' and the SM hypercharge (Y): $g_{22}Q' + g_{12}Y$. This combination originates from the process of rotating to the physical eigenbasis, which introduces new interactions among the gauge bosons and the matter fields.

In analogy with rewriting the SM neutral current Lagrangian, Equation 1.14, in terms of the Z vector and axial couplings, resulting in Equation 1.16, the extended neutral current Lagrangian, Equation 1.19, can be expressed in terms of Z' vector and axial couplings; v^i and a^i for $Z_{1\mu}$, and v'^i and a'^i for $Z_{2\mu}$. This results in Equation 1.24 [9].

$$-\mathcal{L}_{NC} = e\sum_i q_i\bar{\psi}_i\gamma^\mu\psi_i A_\mu + \frac{g}{2c_w}\sum_i \bar{\psi}_i\gamma^\mu(v^i - a^i\gamma_5)\psi_i Z_{1\mu} + \frac{g}{2c_w}\sum_i \bar{\psi}_i\gamma^\mu(v'^i - a'^i\gamma_5)\psi_i Z_{2\mu}. \tag{1.24}$$

The v'^i and a'^i couplings are functions of g_{22}, $\frac{g_{12}}{g_{22}}$, t_3 and Y and are related by Equation 1.25 and Equation 1.26 respectively [9]. (Y and t_3 are shown in Table 1.3 and v^i, a^i in Table 1.4.) The values of both v'^i and a'^i can be determined, once the charge of the extra U$'$(1), Q' is specified (because from Q' both g_{22} and $\frac{g_{12}}{g_{22}}$ can be obtained). The neutral current Lagrangian for $SU(2)_L\times U(1)_Y\times$U$'$(1) therefore depends on only four independent measurable parameters: e, s_W, g_{22} and $\frac{g_{12}}{g_{22}}$.

$$\frac{g}{cos\theta_W}v'^i = g_{22}[(q'_{iL} + q'_{iR}) + \frac{g_{12}}{g_2}\sqrt{\frac{3}{5}}(-t_3 + 2q_i)], \tag{1.25}$$

$$\frac{g}{cos\theta_W}a'^i = g_{22}[(q'_{iL} - q'_{iR}) + \frac{g_{12}}{g_2}\sqrt{\frac{3}{5}}(-t_3)], \tag{1.26}$$

By comparing the SM neutral current Lagrangian, Equation 1.16, to the extended one, Equation 1.24, it can be deduced that there is one massless eigenstate (the photon, A_μ), and two massive eigenstates (denoted $Z_{1,2}$).

In the extended electroweak model the $Z_{1\mu}$ and $Z_{2\mu}$ fields in Equation 1.24 can mix with

a mixing angle θ_3. The two resulting observed states, the Z_μ and the Z'_μ, are related to these fields by Equation 1.27 and Equation 1.28.

$$Z_{1\mu} = c_3 Z_\mu + s_3 Z'_\mu \tag{1.27}$$

$$Z_{2\mu} = -s_3 Z_\mu + c_3 Z'_\mu \tag{1.28}$$

The $Z_1 Z'$ mixing depends on the mixing angle, where s_3 (c_3) $\equiv \sin\theta_3(\cos\theta_3)$. If there is no mixing *i.e.* s_3=0 and c_3=1, then Equation 1.27 and Equation 1.28 reduce to Z_1=Z and Z_2=Z' respectively. In this case Z_1 is identified as the electroweak eigenstate Z^0 boson and Z_2 is the new gauge boson (Z'). If, however, there is mixing, then the observed bosons are a mixture of the $Z_{1\mu}$ and $Z_{2\mu}$ fields and the Z resonance is not the electroweak eigenstate (Z^0) of $SU(2)_L$ $\times$ $U(1)_Y$. Instead, the observed Z boson must be identified as one of the mass eigenstates of the $Z'Z^0$ system while the mass of the second eigenstate ($M_{Z'}$) is not constrained. The experimentally observable effects of the new gauge boson depend on its mass ($M_{Z'}$) and the energy at which the effects are being probed; these are discussed in Section 1.2.3.

1.2.2 Z' models

There are several different Z' models. The model searched for in this analysis is the "Sequential Standard Model" (SSM). This consists of a Z' which couples to SM fermions identically to the usual Z, is more massive than the Z and has a width that is proportional to the mass of the Z' (see Equation 1.33). Although this model can not occur in extended gauge theories, it can occur in composite models and it is similar to the Z' boson produced in extra dimensional models in which gauge bosons propagate in the extra dimensions. It also provides a useful reference for comparing the sensitivity of experimental signals. The analysis was conducted in a model independent way, and so the results found could be applied to other Z' models, which for completeness are mentioned below, and their Z' mass limits could be obtained. This was not

done, because of the small data sample and low event efficiency. Improvements and extensions to the analysis are discussed in Chapter 15.

Popular extended electroweak models are particular cases of Equation 1.24, whose vector (v^i) and axial (a^i) couplings are determined by their corresponding charges, given in Table 1.6 [9]. In all of these models $g_{22} = \sqrt{\frac{5}{3}}\,\frac{e}{c_w}$ and $g_{12} = 0$.

- Model χ occurs when SO(10) breaks down to SU(5) $\times\, U(1)_\chi$ ($E_6(\chi)$).
- Model ψ occurs when E_6 breaks down to SO(10) $\times\, U(1)_\psi$ ($E_6(\psi)$).
- Model η occurs in superstring-inspired models in which E_6 breaks directly to rank 5 group ($E_6(\eta)$).

Q′	$2\sqrt{10}Q_\chi$	$2\sqrt{6}Q_\psi$	$2\sqrt{15}Q_\eta$
q'_{qL}	-1	1	-2
$q'_{u^c_L}$	-1	1	-2
$q'_{d^c_L}$	3	1	1
q'_{lL}	3	1	1
$q'_{e^c_L}$	-1	1	-2

Table 1.6: Charges of popular Z' models.

1.2.3 Experimental searches for Z' bosons

It is possible to search for evidence of new gauge bosons using a variety of different experiments and techniques. This section summarises briefly the methods employed and the present constraints are given in Section 1.2.5.

Constraints on the existence of a Z' gauge boson arise from four main types of experimental searches [10];

- precision measurements of neutral-current processes at low energies,
- Z-pole constraints on ZZ' mixing,

- indirect constraints from precision electroweak measurements off the Z-pole and
- direct search constraints from production at very high energies.

Low energy neutral current experiments, such as lepton-quark, lepton-lepton scattering experiments and atomic parity violation measurements constrain the direct exchange of the Z' boson [11]. If a Z' boson existed, then interference effects, either constructive or destructive, between the Z' boson and the Z contribution would be expected.

Evidence for the existence of the Z' boson can also be searched for by observing the properties of the Z boson. Deviations of results from those expected if the Z was the $SU(2)_L \times U(1)_Y$ electroweak eigenstate (*i.e* Z^0) could imply mixing and indicate the presence of an additional gauge boson, as indicated in Equation 1.27. This type of deviation at the Z resonance was searched for at LEP-I by measuring direct shifts in the Z-pole observables and via measuring shifts in forward backward and left and right asymmetries. [12]. No indication for new effects beyond the SM were found. The constraints on the mixing angle depend on Z' model. The LEP-I results from DELPHI were: $0.0070 \leq \theta_3 \leq 0.0078$ for $E_6(\chi)$, $0.0075 \leq \theta_3 \leq 0.0095$ for $E_6(\psi)$ and $0.0029 \leq \theta_3 \leq 0.0029$ for $E_6(\eta)$ [13]. The LEP-I data from the combined experiments showed that the mixing is consistent with zero [14]. In addition, Z-Z' mixing would also cause a shift in the usual oblique parameters (S,T,U) (as described by Holdom [15]). Current bounds on S and T translate into stringent constraints on the mixing angle, requiring that it is much less than 1.

- Electroweak measurements made sitting on the Z resonance are generally sensitive to Z' physics only through the mixing with the Z, unless the Z and Z' are very nearly degenerate. However, at large lepton colliders it is possible to search for indirect constraints on new Z' physics, at centre of mass energy $\sqrt{s} < M_{Z'}$, but off the Z pole, from measuring deviation of asymmetries and leptonic and hadronic cross sections from their SM predictions. In this case, processes are still sensitive to Z-Z' mixing, but the main effects of a new gauge boson, far off-shell, result from its direct Z' exchange, primarily through interference with the photon (γ-Z')

and the Z boson (Z-Z'). Recent studies at LEP, in which they studied data collected above the Z peak, rely on this approach [14]. Limits are obtained by comparing differences between measured values and SM predictions in terms of Z' parameters.

• For heavy Z' bosons ($M_{Z'} >> M_Z$), some of the highest mass limits have been obtained from $p\bar{p}$ machines via Drell-Yan production and subsequent decay to charged leptons ($p\bar{p} \rightarrow$ Z/γ $\rightarrow l^+l^-$), as indicated on the left of Figure 1.2. High-energy colliders search for on-shell Z' production and decay. The component of the Lagrangian ($L_{NC,Z'}$) for the Z'_μ can be obtained from substitution for $Z_{1\mu}$, from Equation 1.27, and for $Z_{2\mu}$, from Equation 1.28, into Equation 1.24:

$$-L_{NC,Z'} = \frac{g}{2cos\theta_w} \sum_i \bar{\psi}_i \gamma^\mu [(v'^i c_3 + v^i s_3) - (a'^i c_3 + a^i s_3)\gamma_5)]\psi_i. \tag{1.29}$$

The precision available at large colliders and the experimental limit on the $Z_1 Z$ mixing (s_3) permits the γ, Z contributions and the $Z_1 Z$ mixing to be neglected (*i.e.* s_3 can be set to zero). Therefore Z_1 can be identified as the Z^0 boson and Z_2 the new gauge boson of the extra U(1), Z'. In this case, the Lagrangian for Z'_μ, Equation 1.29, reduces to the last term in Equation 1.24; the $Z_{2\mu}$ term:

$$\frac{g}{2cos\theta_w} \sum_i \bar{\psi}_i \gamma^\mu (v'^i - a'^i \gamma_5)\psi_i. \tag{1.30}$$

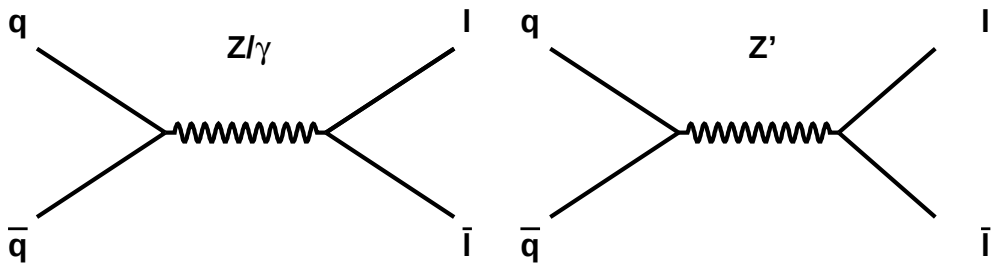

Figure 1.2: Feynman diagrams for the virtual Z/γ and Z' exchange processes, where the initial ($q\bar{q}$) initial states are predominantly u and d quarks.

The main detectable production channels at hadron colliders are decay to leptons ($p\bar{p} \rightarrow$

$Z' \to \bar{l}l$ ($l = e,\ \mu$)), illustrated in Figure 1.2. The leptonic decay channels can be more easily distinguished, than the dijet or quark decay channels, from the large hadronic background, which is produced in proton anti-proton collisions. It is also possible to search for Z' bosons which decay to WW and ZH and to detect the W, Z and H decay products [16]. Other possible decay modes include rare decays such as $Z' \to f_1\ \bar{f}_2\ V$, where V is an ordinary gauge boson (Z, W) emitted by bremsstrahlung from one of the fermionic ($f_{1,2}$) legs, or decays to new/exotic fermions, or supersymmetric particles. However, many of these decays have large SM backgrounds [17]. In addition, Z' could be produced in association with photons (or jets, but this too suffers from a large background) and measurements of the ratios of such production to that of the conventional Z' could be used to probe the Z' boson couplings [18]. These additional channels could be important in determining the Z' couplings, however, the cleanest signature for the Z' is from its decay to two leptons and it is in this channel that discovery is most likely.

1.2.4 Two fermion final states $p\bar{p} \to Z' \to \bar{l}lX$

The cross section for Z' production of on-shell Z's can be derived from neutral current Lagrangian, Equation 1.29, and is shown in Equation 1.31 [19].

$$\frac{d\sigma_{ll}(p\bar{p} \to f\bar{f})}{dy} = \frac{x_A x_B \pi^2 \alpha^2 (g_{Z'}/g_{Z^0})^4}{9 M_{Z'} \Gamma_{Z'}} (C_L^{f\,2} + C_R^{f\,2}) \sum_q (C_L^{q\,2} + C_R^{q\,2}) G_q^+(x_A, x_B Q^2) \qquad (1.31)$$

where

$$G_q^+(x_A, x_B Q^2) = \sum_q [f_{q/A}(x_A) f_{\bar{q}/B}(x_B) \pm f_{\bar{q}/A}(x_A) f_{q/B}(x_B)], \qquad (1.32)$$

$C_{L,R} = \frac{1}{2}(v'^i \pm a'^i)$ and $(g_{Z'}/g_{Z^0})$ $(= \frac{g_{22}}{g_{12}})$ is the ratio of the U(1)$'$ coupling strength to the U(1)$_Y$ coupling strength. The quark and lepton masses have been neglected in this equation and A and B represent the two colliding hadrons at the centre of mass energy $\sqrt{s}$. The quantities $f_{q\bar{q}}^{A,B}$ are the relevant parton distribution functions for the proton for the momentum fractions of the colliding partons, x_a and x_b, which give the probability that a parton with the appropriate

momentum fraction is formed from the proton.

The cross section for Z' production and decay into a give fermion pair at high energy colliders is inversely proportional to the Z' width, as is shown in Equation 1.31. If exotic decay modes are kinematically allowed then the Z' width becomes larger and therefore the branching ratio to conventional fermions becomes smaller. A larger resonance width would be more difficult to detect above the background. In this analysis it was assumed that the Z' bosons decay to only SM particles. In this scenario the partial widths are given (at tree level) by:

$$\Gamma_{Z' \to f\bar{f}} = M_{Z'} g_{Z'}^2 (C_L^{f\,2} + C_R^{f\,2})/24\pi. \tag{1.33}$$

The width for Z' to decay to dimuons depends on the number of decay channels available and is therefore a function of the Z' mass, as can be seen from Equation 1.33. In the Sequential Standard Model the branching ratio to dielectrons or dimuons is the same as that of the Z^0, which is measured to be 0.033.

1.2.5 Present constraints on the Z' boson mass

Searches for Z' boson decaying into dileptons were performed at the CDF (described in Chapter 2) using data collected between 1992 and 1996, corresponding to an integrated luminosity of 110 pb^{-1}. From these searches a limit on the production cross section times branching ratio of a Z' boson decaying into dileptons (electrons and muons) ($\sigma(p\,\bar{p} \to Z'\mathrm{X})\cdot\mathrm{B}(Z' \to l^+l^-)$) of 40 fb for a Z' mass of greater than 600 GeV/c^2 was obtained [20]. Lower mass limits were ascertained from this cross section limit for various Z' models. At the time, these results set the world's highest Z' limits. Recently, for certain Z' models, the CDF limits have been surpassed by LEP II results. The present limits from electroweak fits at LEP and from direct searches performed at CDF are displayed in Table 1.7, where no mixing is assumed. CDF has maintained the highest limit for the $E_6(\psi)$ and $E_6(\eta)$ models of 590 GeV/c^2 and 620 GeV/c^2 respectively.

Model	LEP GeV/c^2	CDF GeV/c^2
$E_6(\chi)$	673	595
$E_6(\psi)$	481	590
$E_6(\eta)$	434	620
Sequential SM	1787	690

Table 1.7: Comparison of the 95 % confidence level lower limits on $M_{Z'}$ (GeV/c^2) from LEP one parameter electroweak fits [14] and direct searches (CDF Run I) [20] for no mixing.

Direct searches at e^+e^- colliders have ruled out any light Z' ($M_{Z'} < M_{Z^0}$) unless it has extremely weak coupling to leptons [10]. If the Z' has suppressed, or no, couplings to leptons (*i.e.* it is leptophobic) then experimental sensitivities are much weaker. For example, a search for a Z' boson via hadronic decay was performed at D0 and ruled out a Z' with quark couplings identical to those of the Z only in the mass range 365 GeV $< M_{Z'} <$ 615 GeV [21].

1.3 Extra Dimensions

1.3.1 Beyond-the-SM solutions to the hierarchy problem

In order to stabilize the hierarchy between the electroweak and Planck energy scale several beyond-the-SM theories have been developed. Traditionally these introduced new symmetries, particles, or interactions at the electroweak scale. Two main classes of beyond-the-SM models have evolved; one introduces a fundamental Higgs scalar (EWSB) and the other a composite Higgs (new strong interactions).

The first requires the introduction of supersymmetric theories. In these models there is an extended Poincare group symmetry between bosons and fermions, and every particle has a new mirror particle, or sparticle. The SM quadratic divergences (described on page 10) are cancelled by contributions from new particles, thus cancelling out the requirement of fine-tuning for the bare Higgs mass and thereby stabilizing the hierarchy. Unfortunately, Supersymmetry introduces a large number of new parameters (105 in minimal SUSY SM).

The second class of model proposes a composite Higgs. Technicolor and topcolor are examples of this type. In such strong coupling theories a new scale for gauge interactions is envisioned with a new set of fermions operating at the 1-10 TeV scale. For example, the "technicolour" model predicts analogue "technicolour" particles like the ordinary π, ρ, ω and new massive Z gauge bosons are typical.

Many of these models, particularly supersymmetric models, predict a rich low-energy phenomenology, but all of them banish quantum gravitational effects to the experimentally inaccessible Planck scale. A very different approach to solving the hierarchy problem, which does not necessitate the introduction of many new particles, is that there may be extra spatial dimensions. In such extra dimensional scenarios, the gravitational field lines spread throughout the full higher dimensional space and modify the behaviour of gravity. It is therefore the geometry of these extra spatial dimensions which may be responsible for the hierarchy.

There are two primary extra dimensional models, the ADD [22] and the RS model [23]. In the first such model (ADD) the hierarchy is eliminated by taking the compact space to be very large. This contrasts with the RS model, which was introduced later, in which the hierarchy between the electroweak and Planck scale is generated by the curvature of the extra dimensions, rather than its size. In both cases the existence of extra dimensions can be tested at high energy colliders. One method is to look for evidence of graviton exchange in the dilepton decay channel. A brief introduction to both models is given in Section 1.3.2 and Section 1.3.3 respectively. In the following chapters a search for the latter model is described, which was conducted as outlined in Chapter 3. The resulting graviton mass limits obtained are summarised in Section 15.1.

1.3.2 ADD model

Arkani-Hamed, Dimopoulos, Dvali (1998) [22] proposed that the electroweak scale (M_{EW}) is the only fundamental distance, at which the gravitational and the gauge interactions become united, and the Planck scale is not a fundamental scale, its large magnitude is simply a consequence of the large size of the new (n) dimensions. ADD proposed that the fundamental 4+n dimensional Planck scale, $M_{Pl(4+n)}$, is related to our effective 4-dimensional value through the volume of the compactified dimensions (V_n), by the relation (derived in Appendix A.2):

$$M_{Pl}^2 = V_n M_{Pl(4+n)}^{2+n}. \tag{1.34}$$

Typically, the extra spatial n dimensions are compactified on a n-dimensional torus with radius R each way (as described on page 26), in which case if the compactified dimensions are flat and of equal size then $V_n = 2\pi {R_c}^n$. In order to remove the hierarchy, $M_{Pl(4+n)}$ is chosen to be $\sim$ 1 TeV, which requires that $R_c \sim 10^{\frac{30}{n}-19}$ m. Consequently, the fundamental Planck scale can be brought down to the TeV range by requiring that the extra dimensions are very large. A result of this is that gravitational interactions become strong near the weak scale. This can be

explained in terms of the geometry; gravity can propagate in the higher dimensional volume, therefore, the gravitational field spreads throughout the full 4 + n space-time volume, known as the bulk. Consequently gravitational interactions take place mainly in the n new large spatial dimensions and the apparent weakness of gravity in our 4-dimensional world results from the geometrical suppression of the gravitational flux lines by a factor proportional to the volume of the compact dimensions, as shown in Equation 1.34.

The lack of observation of experimental evidence for the extra dimensions[3], implies that, unlike the graviton, the SM particles do not propagate freely in the extra n dimensions, because they do not appear to feel the effects of additional dimensions of this size. Instead, the SM particles and gauge forces are confined to a 4-dimensional subspace within the (4+n) dimensional space-time. This is depicted in Figure 1.3. This framework can be embedded into string theories, where the effective Planck scale can be identified with the string scale M_S and a string inspired braneworld hypothesis is used [25]. In this case the gravitons are represented by closed strings and the SM particles by open strings which end on the 3-dimensional sub-space, called a 3-brane, on which SM particles are confined. From this view point, gravity only appears to be weak in ordinary 4-dimensional space-time because SM particles only experience its projection onto the brane.

Figure 1.3: Cartoon to illustrate the Standard Model fields confined to a 4-dimensional space-time sub-space (brane), compared to gravity, which can propagate in the full 4+n dimensions (bulk).

[3]The electroweak and strong forces are known to a great precision down to distances of the order of 10^{-15} mm, which corresponds to $\sim$ (100 GeV)$^{-1}$ [24].

ADD Theory

Compactification

It would be expected, from conventional wisdom, that if the additional dimensions were too large, this would result in observable deviations from the Newtonian gravity (see Appendix A.2). The large extra dimensional space must therefore be *compactified*, *i.e.* made finite. (However, in some alternative theories, like the RS model [23], considered in Section 1.3.3, the extra dimensions can be infinite and the gravitational deviations are suppressed by other means.) Compactification on to a torus and the resulting Kaluza-Klein states is a simple and elegant way to hide the extra dimensions [26]. It is simple because it relies on an elementary observation, and elegant, because the quantum numbers and interactions of the elementary particles can be accounted for by the topological and geometrical properties of the internal space.

At each point of our four-dimensional space, the extra-dimensions can be considered to form a D-dimensional torus of volume $(2\pi)^D\ R_1\ R_2 .... \ R_D$. The $(4+\delta)$-dimensional Poincare invariance is replaced by the direct product of a four-dimensional one and the symmetry group of the δ-dimensional space which contains translations along the δ extra dimensions. The $(4+\delta)$-dimensional momentum satisfies the following mass-shell condition

$$P^2{}_{(4+D)} = p^2{}_0 - p^2{}_1 - p^2{}_2 - p^2{}_3 - \sum_i p^2{}_i = m^2{}_0 \tag{1.35}$$

and looks from the four dimensional point of view as a mass squared of

$$M_{KK}{}^2 = p^2{}_0 - p^2{}_1 - p^2{}_2 - p^2{}_3 = m^2{}_0 + \sum_i p^2{}_i. \tag{1.36}$$

Assuming periodicity of the wave functions along each compact direction, one has $p_i = n_i/R_i$ which leads to:

$$M_{KK}{}^2 \equiv M_{\vec{n}}{}^2 = m_0{}^2 + \frac{n_1{}^2}{R_1{}^2} + \frac{n_2{}^2}{R_2^2} + ... \frac{n_\delta{}^2}{R_\delta{}^2} \tag{1.37}$$

with ${m_0}^2$ the higher-dimensional mass and n_i non-negative integers. The states with $\sum_i n_i \neq 0$ are called the Kaluza-Klein (KK) states and collectively the Kaluza-Klein excitations are referred to as the "gravitons", independent of their mass. The picture of a massless graviton propagating in δ dimensions is equivalent to the picture of massive KK gravitons propagating in 4-dimensions and the Kaluza-Klein gravitons can be considered to correspond to multiple winding modes of the graviton field around the compactified dimensions where the Kaluza-Klein excitations recur once every $1/R_c$ per extra dimension n, as shown in Equation 1.37. In order to be aware of the i^{th} extra-dimension requires experiments which can probe at least an energy of the order of $1/R_i$, with sizable couplings of the KK states to four-dimensional matter.

ADD graviton interactions

The existence of extra dimensions is revealed through the interactions between gravitons and the SM particles on the brane. The interactions of the graviton fields are described by the action [27];

$$S_{int} = -\frac{1}{{M_D}^{\delta/2+1}} \int d^4x d^n y_i h_{AB}(x_\mu, y_i) T_{AB}(x_\mu, y_i), \tag{1.38}$$

where the upper case indices extend over the full (4+δ) D-dimensional spacetime, μ over the 3+1 dimensions on the wall, and i over the δ bulk dimensions. The bulk graviton is represented by h_{AB}, and T_{AB} is the symmetric, conserved stress-energy tensor in the bulk. Upon compactification, the graviton field-strength tensor, h_{AB}, decomposes into the various 4-dimensional spin states and Fourier expands into Kaluza-Klein towers of spin-0, 1 and 2 states[4] which have equally spaced masses of $M_{\vec{n}} = \sqrt{\vec{n}^2/{R_c}^2}$, where $\vec{n} = (n_1, n_2, \ldots\ n_\delta)$ labels the excitation level.

[4] In performing the decomposition of Equation 1.38 into the 4-dimensional states, it is found that for spin-1 states $T_{\mu i} = 0$ and hence the spin-1 KK states do not interact with the (wall) fields on the 3-brane. The spin-0 state (scalar, or dilaton) couples proportionally to the trace of the stress-energy tensor. For interactions with fermions, this trace is linear in the fermion mass (and therefore vanishes for massless particles), while for gauge bosons it is quadratic in the boson mass. Hence, the dilaton does not contribute to the processes under consideration here. Their phenomenology is described by Giudice *et. al* [28]. Consequently, only the interactions of the KK spin-2 gravitons with the SM fields need be considered [29].

The mass of each KK mode corresponds to the modulus of its momentum in the direction transverse to the brane (as shown on page 26). The interactions of the graviton KK states with the SM fields ($G_{\mu\nu}$) can be derived from the KK expansion for the spin-2 tower by integrating the action, Equation 1.38, over the extra dimensional coordinates y_i. The complete Feynman rules are derived in detail in [27] and the corresponding Feynman rules are catalogued [30]. The interacting Lagrangian for the KK states is given in Equation 1.39.

$$\mathcal{L} = -\frac{1}{\bar{M}_{Pl}} G_{\mu\nu}{}^{j} T^{\mu\nu} \tag{1.39}$$

Here, j labels the Kaluza-Klein mode, $\bar{M}_{Pl} = M_{Pl}/\sqrt{8\pi}$ and $T^{\mu\nu}$ is the energy-momentum tensor. It can be seen from Equation 1.39 that gravitons couple to the energy-momentum tensor and they can therefore be produced in any SM process. Also, the effective Lagrangian (Equation 1.39) shows that all the gravitons in the KK tower, including the $\vec{n} = 0$ massless state, couple in an identical manner with universal strength which has the suppression factor of $\bar{M_{Pl}}^{-1} (\sim {M_{Pl}}^{-1})$.

Because the coupling of each KK excitation is M_{Pl} suppressed, it may seem that the effects at colliders would be too suppressed to be detectable. However, the overall coupling is obtained by summing over all (the whole tower of) the KK states which can be exchanged or emitted in a physical process. The mode spacing is determined by the compactification scale ($\mu_c = 1/R_c$). In the ADD model, because the extra dimensions are large, the mode spacing is very small compared to typical collider energies. Consequently, individual resonances associated with the graviton are not observable, instead, graviton tower emission is important. The effect of the summation is to reduce the suppression of $1/M_{Pl}$ to $1/M_S$, which is the order of $\sim TeV^{-1}$ (M_{EW}^{-1}), as demonstrated in Appendix A.3. Therefore, the effective gravitational interaction is of strength comparable to that of the electroweak interaction, and thus can give rise to many consequences that can be tested in both accelerator and non-accelerator experiments. The present constraints on the ADD model graviton are summarised on page 32.

There are two classes of collider signatures for large extra dimensions;

- emission of real gravitons into extra dimensions, resulting in missing energy signals, and
- exchanges of virtual gravitons which frequently lead to an enhancement or deviations from the SM predictions.

The latter is described in more detail in the following section.

Virtual graviton exchange

In the virtual exchange process, KK towers of gravitons can be exchanged in the s channel together with the photon (γ) and the Z, and because gravitons couple to all forms of stress-energy, there is also a new contribution to the lepton pair production from the gluon-gluon initiated process (gg) in addition to the usual quark-quark ($q\bar{q}$) initial state, as illustrated in Figure 1.4.

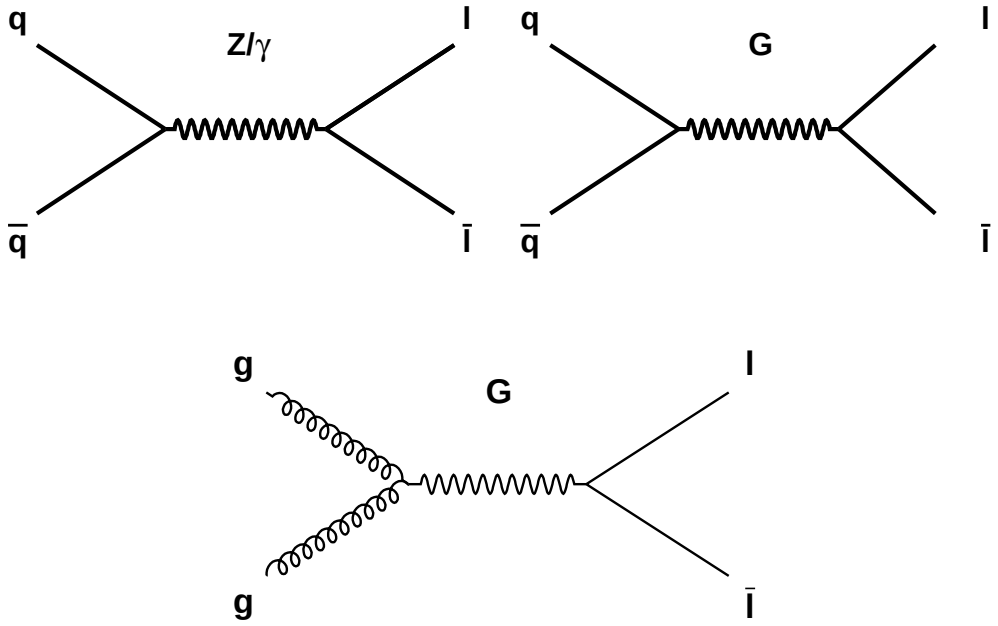

Figure 1.4: Feynman diagrams for virtual graviton exchange. In the virtual exchange process KK towers of gravitons can be exchanged in the s channel together with the photon and the Z. There is also a new contribution to the lepton pair production from the gluon gluon initiated process (gg) in addition to the usual quark-quark ($q\bar{q}$) initial state.

The cross section for virtual graviton exchange can be obtained from the scattering amplitude for the process. Although this amplitude is suppressed by M_{Pl} (as indicated by Equation 1.39), it is also proportional to the sum over the propagator for the graviton tower. This summation may be converted to an integral over the density of KK states in the virtual Kaluza-Klein graviton exchange process, because the spacing of the KK tower states is so small. However, in the case where there is no specific cut-off associated with the kinematic process, the integral is divergent for the number of extra dimensions n > 1, therefore, in order to keep the sum over the KK states finite, it is necessary to introduce an explicit upper cut-off, of order of M_S. A naive argument for the existence of the cut-off is that the effective theory breaks down above M_S, where detailed understanding of string dynamics is required. In order to regulate this integral several approaches have been proposed as summarised by Cheung and Landsberg [31]. The tree-level cross section for lepton pair production is shown in Equation 1.40, where the couplings used were described by Guidice *et. al.* [30] and Han *et. al.* [27].

$$\begin{aligned}
\frac{d^3\sigma}{dM_{ll}dydz} = \quad & K \quad \sum_q \frac{{M_{ll}}^3}{192\pi\hat{s}} f_q(x_1) f_{\bar{q}}(x_2)[(1+z)^2(|M_{LL}|^2+|M_{RR}|^2)+(1-z)^2(|M_{LR}|^2+|M_{RL}|^2) \\
& + \quad \pi^2 \left(\frac{\lambda}{{M_S}^4}\right)^2 {M_{ll}}^4(1-3z^2+4z^4) - 8\pi e^2 Q_l Q_q \left(\frac{\lambda}{{M_S}^4}\right) z^3 \\
& + \quad \frac{8\pi e^2}{\sin^2(\theta_W)\cos^2(\theta_W)} \left(\frac{\lambda}{{M_S}^4}\right) \frac{{M_{ll}}^2}{{M_{ll}}^2-{M_z}^2}(a^l a^q \frac{1-3z^2}{2} - v^l v^q z^3)] \\
& + \quad K\frac{\pi {M_{ll}}^7}{128\hat{s}} f_g(x_1) f_g(x_2) \left(\frac{\lambda}{{M_S}^4}\right)^2 (1-z^4),
\end{aligned}$$

where

$$M_{LR} = \frac{e^2 Q_l Q_q}{\hat{s}} + \frac{e^2}{\sin^2\theta_W \cos^2\theta_W} \frac{{C_L}^l {C_R}^q}{\hat{s}-{M_Z}^2} \tag{1.40}$$

Here, the centre of mass energy of the colliding partons is represented by $\sqrt{\hat{s}} = M_{ll}$ and $z = \cos\theta^*$ is the cosine of the scattering angle in the parton centre of mass frame. The parton

distribution functions ($f_{q,g}(\mathrm{x})$) are expressed in terms of $x_{1,2} = \frac{M_{ll}}{\sqrt{s}}e^{\pm y}$, where y is the rapidity of the final-state dilepton pair and the K-factor accounts for the next-to-leading order QCD corrections [32].

The graviton induced cross sections involve two new parameters: M_S and λ.

- M_S ($\equiv {M_{Pl}}^{(4+d)}$) is the effective string scale at which gravity becomes strong, corresponding to the fundamental Planck scale in the bulk. M_S is approximately independent of number of extra dimensions.

- λ, which is the effective coupling at M_S, which arises when all possible KK modes of the graviton are summed over. Because M_S and λ always appear in the combination $\lambda/{M_S}^4$, the magnitude of λ is absorbed into M_S. Therefore λ is a dimensionless parameter ($\lambda = \pm 1$) and its sign is not known *a priori*, its value depends on whether the graviton exchanges constructively or destructively with the SM interactions.

The production cross section, Equation 1.40, has three terms: the SM term (involving Z and γ), an interference term proportional to $\lambda/{M_S}^4$ and a term from direct gravity effects proportional to $(\lambda/{M_S}^4)^2$. If the dependence on the parton distribution functions (pdfs) is integrated out, the differential cross section can be written in the form:

$$\frac{d^2\sigma}{dM_{ll}dz} = \left.\frac{d\sigma}{M_{ll}dz}\right|_{SM} + \left(\frac{\lambda}{{M_S}^4}\right)\left.\frac{d\sigma}{M_{ll}dz}\right|_{int} + \left(\frac{\lambda}{{M_S}^4}\right)^2\left.\frac{d\sigma}{M_{ll}dz}\right|_{KK}. \tag{1.41}$$

Crucially, the shapes σ_{int} and σ_K are independent of λ and M_S; they are determined completely by the pdfs and the general structure of the Lagrangian. Therefore in searches for ADD model virtual graviton exchange, one can generate templates for the interference and direct shapes and determine $\lambda/{M_S}^4$ by fitting the distributions of $cos\theta^*$ vs M_{ll} in the data, as advocated by Cheung and Landsberg [33].

The dilepton cross section including the effects of the ADD model graviton are shown in Figure 1.5 [34]. The data points show the dilepton invariant mass distribution recorded at the

CDF using data collected between 1992-1996, corresponding to an integrated luminosity of 110 pb^{-1}. The dashed lines indicate the expected cross section for this quantity of data if the ADD model graviton existed, where the labels correspond to different values of M_S.

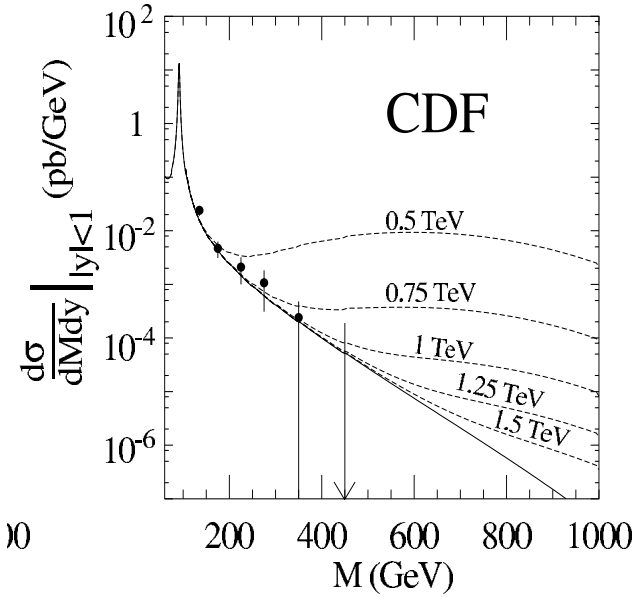

Figure 1.5: The data points show the dilepton invariant mass distribution recorded at the CDF using data collected between 1992-1996, corresponding to an integrated luminosity of 110 pb^{-1}. The dashed lines indicate the predicted cross sections if the ADD model graviton existed in the scenario where M_S has the values indicated, from 0.5 to 1.5 TeV. [34].

Constraints on the ADD model

The are some existing constraints on the size and therefore number of extra dimensions ($R_c \sim 10^{\frac{30}{n}-19}$ m) for the ADD model from astrophysics and short-range gravity experiments (a review of these is given in Reference [35] and [24]). For example, n=1 theories are automatically excluded because R_c would be so large ($R_c \sim 10^{11}$ m which is the size of the solar system!) that it would cause deviations from Einstein gravity at solar system scales. Since these have not been observed, n is constrained to be greater than one. Effects of non-Newtonian gravity have been tested at Cavendish-type experiments and attempts have been made to observe the transition from $1/r^2 \rightarrow 1/r^4$ (for derivation see Appendix A.2). For n=2 current data results imply that $R_c < 190$ μm [24]. For n > 2, R_c is too small for the effects of extra dimensions to be detected

in mechanical experiments. Constraints also come from supernova cooling and distortion of γ ray flux and the limit is $M_S \geq$ 50 - 110 TeV for n=2 [36]. For n varying from between 3 and 6, the radius R_c of the extra dimensions ranges from a fraction of a millimeter to $\sim$ 10 fermi, hence there is no conflict with known facts. Therefore ${M_{Pl}}^{4+n}$ (M_S) can be arranged to be a TeV for any value n $>$ 1.

Additional constraints on the ADD model arise from high-energy collider experiments [30] [37] [27] [38]. The virtual graviton exchange processes, such as $p\bar{p} \rightarrow \mu^+\mu^-$, e^+e^-, $\gamma\gamma$, provide bounds up to several TeV, on the string scale, which are essentially independent of the number of extra dimensions. The highest energy constraints from these processes are from the Tevatron, where the combined dilepton and diphoton data collected (at a centre of mass energy ($\sqrt{s}$) of 1.8 TeV) between 1992 to 1996, which corresponded to an integrated luminosity of 110 pb^{-1}, was used to constrain M_S to be greater than 1.0-1.4 TeV. The range corresponds to the number of extra dimensions n=7-2 [24] [39]. (This reach is expected to be improved to 1.3-2.5 TeV with an integrated luminosity of 2 fb^{-1} for the Tevatron operating at the higher centre of mass energy of 1.96 TeV [40].)

In addition, n is required to be less than 7, since this is the largest number allowed if the string theory is derivable from M-theory, which is believed to be the fundamental theory of all interactions.

1.3.3 RS model

An alternative higher dimensional scenario, for solving the hierarchy problem, was proposed by Randall and Sundrum [23]. In this theory, the hierarchy between the Planck and electroweak scale is generated by a large curvature of the extra dimension, rather than its size.

The curvature is created by having a non-factorisable geometry, *i.e.* dependent on co-ordinates in the extra dimensions, in contrast to the ADD model. In the RS model it was proposed that the four-dimensional metric is multiplied by an exponential function of the compactification radius, called a "warp" factor, which is a rapidly changing function of a single additional dimension. The curved background can support a "bound state" of the higher-dimensional graviton, which is localised in the extra dimension. Having the non-factorizable metric allows for a large mass hierarchy to be generated from one additional extra dimension, which is not compactified, rather than from compact large extra dimensions.

The simplest framework is comprised of just one additional spatial dimension of finite size, in which gravity propagates. The geometry is that of a 5-dimensional Anti-de-Sitter space (AdS_5). Every slice of the 5^{th} dimension corresponds to a 4-d Minkowski metric. RS first considered a finite volume by introducing two branes (with equal and opposite tension, later models consider other brane tension combinations). The branes were separated by a distance πR_c and were positioned at the boundaries of a finite fifth dimension, taken to be $\phi = 0$, π, where ϕ is the angular co-ordinate parameterising the extra dimensions [41]. In this particular model, the 3-brane located at the boundary ϕ=π is considered to contain the SM fields and is referred to as the TeV-brane and gravitational wavefunction is localised at ϕ=0 on the Planck brane, as illustrated in Figure 1.6.

In the RS model, the effect of the higher-dimensional curvature is to reduce the effective 4-dimensional planck scale, $\bar{M}_{Pl}$ (where $M_{Pl}/\sqrt{8\pi} = 2.4 \times 10^{18}$ GeV). $\bar{M}_{Pl}$ can be derived from the 5-dimensional action in the 4-dimensional effective theory [23], and is related to the

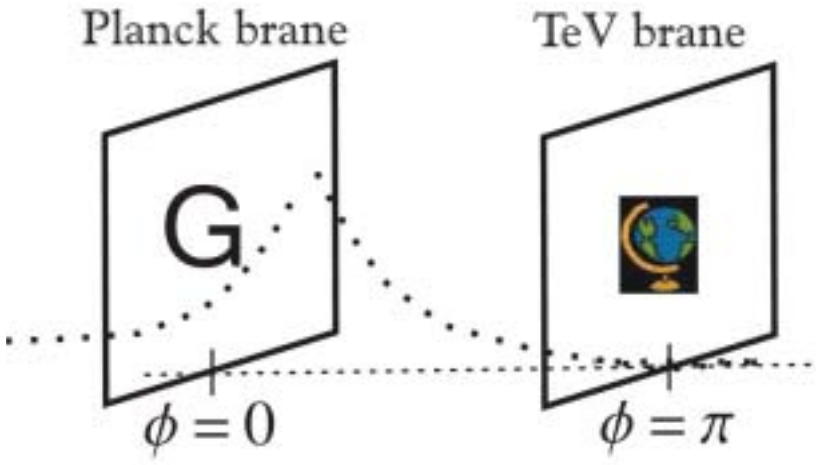

Figure 1.6: In the RS model, the SM fields are confined to a 3-brane, known as the TeV brane, which is located at ϕ=π in the 5-dimensional space. The gravitational wavefunction is localised on a 3-brane at ϕ=0, called the Planck brane. The weakness of gravity arises because of the small overlap of the graviton wave function with the TeV brane.

5-dimensional fundamental scale, $\bar{M}_5$, by Equation 1.42.

$$\bar{M}_{Pl}^2 = \frac{\bar{M}_5{}^3}{k}[1 - e^{-2kR_c\pi}] \tag{1.42}$$

The parameter k governs the degree of curvature of the (AdS_5) space and it is assumed to the of order the Planck scale (10^{18} GeV). The (reduced) 5-dimensional fundamental scale $\bar{M}_5$ is also of the order of $\bar{M}_{Pl}$. It is interesting to note that there is a well-defined value for $\bar{M}_{Pl}$, even in the infinite radius limit ($R_c \to \infty$). In this case the usual Newtonian force law is obtained. This is in sharp contrast to the product-space expectation that $\bar{M}_{Pl}{}^2 = \bar{M}_5^3\ R_c\ \pi$, which would result in an infinite limit.

In this scenario, the scale of physical phenomena, on the TeV-brane is specified by the exponential warp factor, $\Lambda_\pi \equiv \bar{M}_{Pl}\ e^{-kR_c\pi}$. TeV scales ($\Lambda_\pi \sim$ TeV), on this 3-brane at $\phi = \pi$, can therefore be generated from fundamental scales of order M_{Pl} (via the geometrical exponential factor) if $kR_c \simeq$ 11-12. The hierarchy is thus naturally established by the warp factor. It has been demonstrated that this value of kR_c can be stabilised within this configuration without the fine tuning of parameters [42]. In addition, because $kR_c \simeq$ 11-12 and it is assumed that k $\sim 10^{18}$

GeV, TeV scales can be produced without requiring the extra dimension to be large. Similarly to the ADD model, in the RS model, one can regard the TeV scale as fundamental, and the Planck scale of 10^{19} GeV as the derived scale. This is the viewpoint that a four-dimensional observer residing on the TeV brane would naturally take: the Planck scale (and therefore the weakness of gravity) arises because of the small overlap of the graviton wave function (due to the warp factor) in the fifth dimension with TeV-brane.

The graviton spectrum is quite different in this scenario than in the case with factorisable geometry, resulting in distinctive phenomenology, which is described on page 37. As in the case of large extra dimensional models, the Feynman rules are obtained by a linear expansion of the metric ($G_{\mu\nu}$),

$$G_{\mu\nu} = e^{-2ky}(\eta_{\mu\nu} + 2h_{\mu\nu}/{M_5}^{3/2}), \tag{1.43}$$

where $h_{\mu\nu}$ (μ, ν=0,1,2,3) are the tensor fluctuations and the metric tensor is defined as $\eta_{\mu\nu}$ = diag(1,-1,-1,-1) (the definitions used are those by Davoudiasl *et. al.*, [41]). In this scenario, the usual linear expansion is multiplied by the warp factor. After compactification, the resulting KK tower states are the coefficients of a Bessel expansion. The Bessel functions replace the Fourier series of a flat geometry because of the strongly curved space and the presence of the exponential warp factor.

The mass spectrum of the graviton KK modes in the effective the 4-dimensional theory on the 3-brane at $\phi = \pi$ is $m_n = x_n$ k $e^{-kR_c\pi} = x_n\Lambda_\pi \mathrm{k}/\bar{M}_{Pl}$ where x_n are the roots of the first-order Bessel function, *i.e.*, $J_1(x_n) = 0$ [41]. Therefore it can be seen that a field on this brane, with the fundamental mass parameter m_0, will appear to have the physical mass m $= e^{-kr_c\pi}m_0$. If k$R_c \sim 11$, then the first excitation is naturally of the order of a TeV, which implies that these KK states can be separately produced on resonance with observable rates at colliders up to the kinematic limit. (This is not possible in the ADD model because the spacing is so small ($1/R_c$.)) In addition, the KK states are not evenly spaced; instead the spacing is dependent on

successive roots of J_1. This result gives a distinctively identifiable signature for the RS model, which originates from the non-factorisable geometry of the model.

The interactions of the graviton tower with the SM fields on the TeV-brane are described by Equation 1.44 [41].

$$\mathcal{L} = \frac{-1}{\bar{M}_{Pl}} T^{\mu\nu}(x) h^0{}_{\mu\nu}(x) - \frac{1}{\Lambda_\pi} T^{\mu\nu}(x) \sum_{n=1}^{\infty} h^n{}_{\mu\nu}(x) \tag{1.44}$$

$T^{\mu\nu}(x)$ is the symmetric conserved Minkowski space energy-momentum tensor of the matter fields and $h^n_{\mu\nu}$ are the interactions with the matter fields on the 3-brane. The first term, in Equation 1.44, represents a single normalisable mode, which is the massless graviton of the effective 4-dimensional theory and the second term the other massive eigenstates, which are continuum modes. From Equation 1.44 it can be deduced that the zero mode decouples from the sum and couples with the usual 4-dimensional strength, $\bar{M}_{Pl}^{-1}$, however, all the massive KK states are only suppressed by Λ_π^{-1}, where $\Lambda_\pi = e^{-kr_c\pi}\bar{M}_{Pl}$, which is of the order of the weak scale. This is in contrast to the ADD model which couples with gravitational strength to the SM particles.

RS model phenomenology

In this scenario, the principal collider signature is the direct resonant production of the spin-2 states in the graviton KK tower. The cleanest signal for graviton resonance production will be either an excess of dilepton events ($q\bar{q}$, gg $\rightarrow G^{(1)} \rightarrow l^+l^-$) or in the dijet channel ($q\bar{q}$, gg $\rightarrow G^{(1)} \rightarrow q\bar{q}$, gg). However, at high centre of mass energy, the dijet channel is expected to have a large QCD background.

The shape and distribution of the resonances observed depends on the two parameters which govern the 4-d effective theory of this scenario; Λ_π and the ratio k/$\bar{M}_{Pl}$. (Note that the approximate values of these parameters are known due to the relation of this model to the hierarchy problem.) The effect of changing these variables is discussed below, followed by a description

of how the model parameters can be determined from the observation of the first graviton KK state.

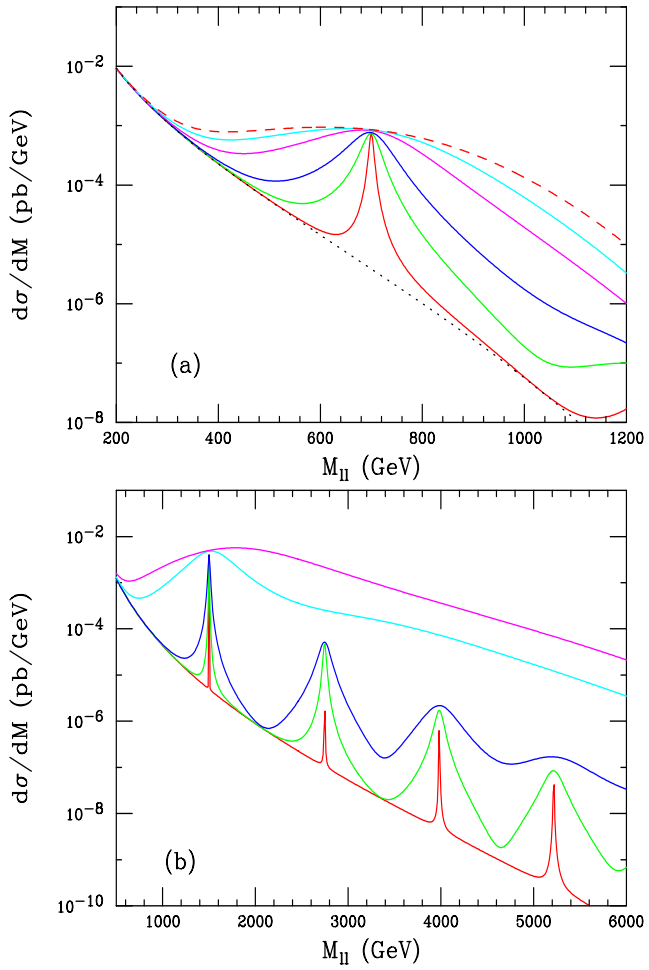

Figure 1.7: Drell-Yan production of a (a) 700 GeV KK graviton at the Tevatron with k/ $\bar{M}_{Pl}$ = 1,0.7,0.5,0.3,0.2 and 0.1, respectively, from top to bottom; (b) 1500 GeV KK graviton and its subsequent tower states at the LHC. From top to bottom, the curves are for k/$\bar{M}_{Pl}$ = 1,0.5,0.1,0.05 and 0.01 respectively [43].

For small values of k/$\bar{M}_{Pl}$ the gravitons appear as ever widening peaks and are almost regularly spaced, with width and spacing both being dependent on successive roots of J_1. This is demonstrated in Figure 1.7, which illustrates the cross section of the graviton resonances and the Drell-Yan contribution as a function of the invariant mass of the lepton pair at the Tevatron, with m_1=700 GeV, and at the LHC, with m_1=1000 GeV, for various values of k/$\bar{M}_{Pl}$ [43]. As k/$\bar{M}_{Pl}$ is increased the width of the resonances increases (because their width is proportional to $(k/\bar{M}_{Pl})^2$). The peak of the cross section for the first resonance is independent of the value

$k/\bar{M}_{Pl}$, as can be seen in Figure 1.7. This is in contrast to the higher mass resonances, whose height reduces as the higher KK excitations prefer to decay to the lighter graviton states, once it is kinematically allowed. As $k/\bar{M}_{Pl}$ increases further[5], such that $k/\bar{M}_{Pl} \geq 0.5$, the combination of the peaks becomes wider and the interference from the higher excitations means that the peaks can not be identified as true resonances. Consequently, the classic KK signature of successive peaks becomes lost. Instead it would appear experimentally that there is an overall large enhancement of the cross section, similar to what might be expected from a contact interaction and the ADD model [41], as illustrated in Figure 1.5. In this case, the 4-fermion matrix element can be computed from the Lagrangian, Equation 1.44, and is similar to that derived for the scenario of ADD with large extra factorizable dimensions [38], Equation 1.40, with the replacement

$$\frac{\lambda}{M_s^4} \rightarrow \frac{i^2}{8\Lambda_\pi^2} \sum_{n=1}^{\infty} \frac{1}{s - {m_n}^2}. \tag{1.45}$$

The advantage in this scenario (RS) over the factorizable case (ADD) is that there are no divergences associated with performing the sum since there is only one new dimension, and hence uncertainties with the introduction of a cut-off do not appear. In the limit of ${m_n}^2 >> s$, the sum over the KK graviton propagators rapidly converges.

In the circumstances that gravitons are too massive to be directly produced at colliders, their contribution to fermion pair production may still be felt via virtual exchange. For smaller values of $k/\bar{M}_{Pl}$, this would be similar to observing the effects of the SM Z boson before the resonance turns on; or for larger values, to searching for contact interactions, as mentioned above.

In the case where no direct production is observed, bounds on the parameter space in the contact interaction limit can be computed.

[5] If the theorectical assumption that $k/\bar{M}_{Pl} < 0.1$ is evaded (see page 41).

Determination of RS model parameters

From the observation of the width (Γ_1) and the location (m_1) of the first graviton KK state resonance all of the model parameters can be uniquely determined. The parameters Λ_π and k/$\bar{M}_{Pl}$ can be obtained from the relations $\Lambda_\pi = m_1\bar{M}_{Pl}/kx_1$ and $\Gamma_1 = \rho m_1 {x_1}^2\ (k/\bar{M}_{Pl})^2$ respectively. In these equations x_1 is the first non-zero root of the J_1 Bessel function and ρ is a constant which depends on the number of open decay channels. If it is assumed that the graviton decays only to SM fields, then ρ is fixed. The compactification radius (R_c) and k can also be calculated from the following relations: R_c= - $log[m_1/kx_1]/k\pi$ with k= $\bar{M}_{Pl}[\Gamma_1/m_1\rho x_1^2]^{1/2}$.

Graviton angular distribution

Virtual graviton exchange leads to deviations not only in the cross sections, but also in the asymmetries of SM processes, such as $q\bar{q} \to f\bar{f}$, because gravitons are spin-2 and conserve C and P separately. Table 1.8 displays and Figure 1.8 illustrates the angular distribution for the decay of particles of various spins into fermions, in the dilepton centre of mass frame where θ^* is the angle between the decay lepton and the beam direction. Spin-0 resonances have a flat angular distribution and spin-1 correspond to a parabolic shape, which contrasts strongly with the quartic distribution from spin-2 particles. However, the ability of a collider to distinguish between these scenarios depends on the amount of available statistics. Figure 1.8 shows the fermion angular distribution from spin-0, -1 and -2 decays for a sample of 1000 events, including statistical errors, which corresponds to a value of $m_1^{grav} < 4200$ TeV with k/$\bar{M}_{Pl} = 0.1$ at the LHC with 100 fb^{-1}. At this level the spin-2 nature of a KK graviton can be determined [43].

Process	Angular Distribution
$gg \to G \to l^+l^-$	1- $cos^4\theta^*$
$q\bar{q} \to G \to l^+l^-$	1- $3cos^2\theta^* + 4cos^4\theta^*$
$q\bar{q}$, $gg \to V \to l^+l^-$	1+ $\alpha cos^2\theta^*$
$q\bar{q}$,$gg \to S \to l^+l^-$	1

Table 1.8: Angular distributions in graviton (G), vector (V) and scalar (S) boson production and decay. $\alpha = 1$ in Standard Model processes.

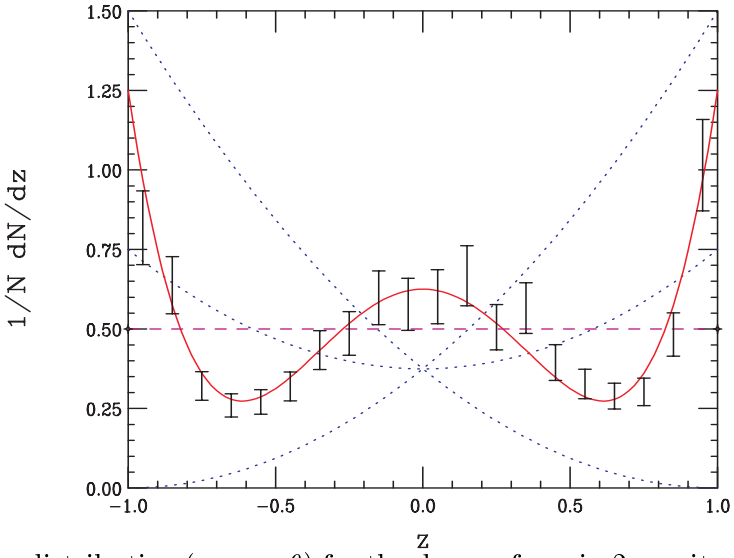

Figure 1.8: Angular distribution ($z = \cos\theta$) for the decay of a spin-2 graviton into fermions (the w-shaped curve) in comparison to similar decays by either the spin-0 (dashed) or spin-1 (dotted with minima at $z = \pm 1$) maximally parity violating particles or spin-1 (dotted with minima at $z = 0$) parity conserving particles. The data errors show the result from a typical sample of 1000 events, which corresponds to a value of $m_1^{grav} < 4200$ TeV with $k/\bar{M}_{Pl} = 0.1$ at the LHC with 100 fb^{-1} [43].

RS constraints

Constraints on this model come from three main sources; theoretical limitations, precision of electroweak (EW) observables and from graviton resonance searches in Drell-Yan and dijet data. These are summarised in Figure 1.9 [43]. The theoretical assumptions made are;

- $\Lambda_\pi \leq 10$ TeV. The scale of physics on the TeV-brane is desired to be not far above the electroweak scale so that an additional hierarchy is not generated and the hierarchy problem is solved, and
- $k/\bar{M}_{Pl} \leq 0.1$, from bounds on the curvature of the ADS_5 space [44].

Experimental constraints on the existence of gravitons can be provided by probing deviations in electroweak data. For example, shifts in the oblique parameters S, T, U would indicate new physics [43]. In the case of graviton KK towers, loops involving such particles would contribute to the transverse components of the SM gauge boson self-energies, which would then reveal themselves as deviations in S, T and U. It is found that smaller values of $k/\bar{M}_{Pl}$ are inconsistent

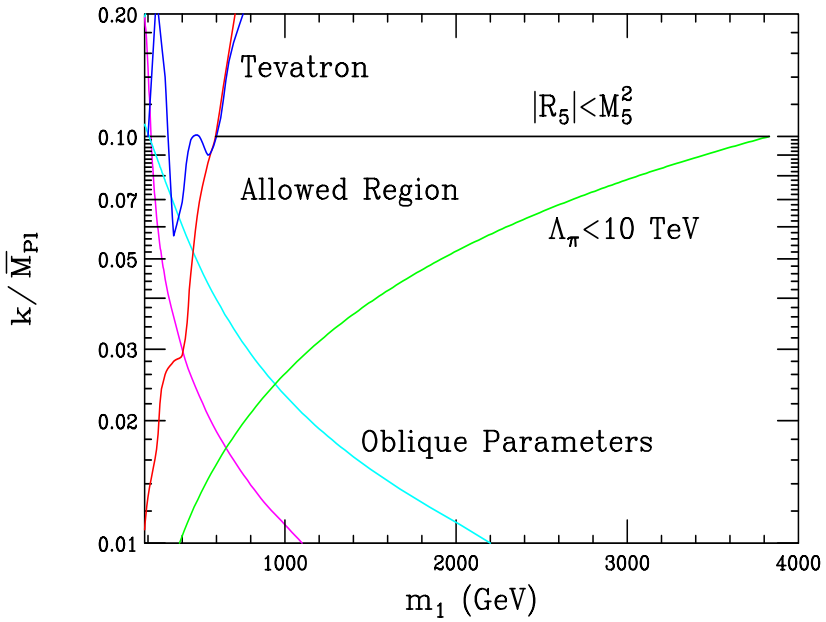

Figure 1.9: Summary of present experimental and theorectical constraints on the RS model, in the $k/\bar{M}_{Pl}$ and m_1^{grav} plane. The allowed region lies in the centre, as indicated [43]. The limits obtained from the Tevatron for the data collecting from 1992-1996, which corresponds to an integrated luminosity of 110 pb^{-1}, is shown by the two solid curves on the left; the higher bumpier blue one is from dijet production and the straighter red curve is from dilepton data. The oblique parameter constraints originate from global fits to the parameters T and S, and are shown on the left and right respectively. Theorectical constraints from the curvature of the space yield $k/\bar{M}_{Pl} < 0.1$, and to solve the hierarchy problem; $\Lambda_\pi < 10$ TeV.

with precision electroweak data, as illustrated by the oblique parameter exclusion region in Figure 1.9 [43].

Limits were obtained from dijet and dilepton data at the Tevatron (which was then operating at a centre of mass energy of 1.8 TeV) for the data collecting from 1992-1996, called Run I, which corresponded to an integrated luminosity of 110 pb^{-1}. The exclusion region is shown in Figure 1.9 by the two solid curves on the left; the higher bumpier blue one is from dijet production and the straighter red curve is from dilepton data [43]. These dilepton limits were obtained from data obtained from both detectors; CDF and D0. In the analysis for this thesis, the first CDF dimuon limits using $p\bar{p}$ collision data at a higher centre of mass energy of 1.96 TeV were obtained and also Run I mass limits were obtained for the Randall-Sundrum model graviton using dilepton data from CDF alone.

Extension to the RS model

The RS model has been extended in number of different ways. Randall and Sundrum initially extended this scenario by taking the second brane to infinity ($R_c \rightarrow \infty$), thereby removing it from the physical set-up, resulting in one additional spatial dimension of infinite size, where the higher dimensional space is non-compact [45]. In this model the SM fields are confined to the brane at ϕ=0 where gravity is localized. The possibility of having the SM fields (gauge and fermion) propagate in the RS bulk was investigated by Davoudiasl *et. al.* [43]. An alternative extension to the model was considered by Dienes *et. al.* [46] and Pomarol *et. al.* [47], in which the SM gauge bosons, but not the fermions, were allowed to propagate in extra dimensions. Collider signatures for this model are due to the existence of the Kaluza-Klein (KK) states of γ, W and Z bosons. The observation of a KK boson would be similar to that of a SSM Z$'$ boson, however, the coupling of these bosons is highly model-dependent. In the simplest case, in which all the SM fields all live on the same 3-brane, then the couplings of the KK bosons are identical to those of the usual gauge fields, but enhanced by a factor of $\sqrt{2}$. In this scenario, the bounds on the SSM Z$'$ (described in Section 1.2), are almost precisely the bounds on the first KK mode of the Z^0 with a factor of $\sqrt{2}$ to account for the enhancement of the coupling strength. An approximate bound on the Sequential SM Z$'$ of 820 GeV/c^2 was inferred from the data collected between 1992 and 1996 at the CDF (110 pb^{-1}) [20] [48]. Other models also predict ordinary fermions living on a different, parallel branes in the extra dimensions. Such models were introduced because they naturally suppress proton decay [49]. In these models, different fermions have very different coupling strengths for the KK states; the effective coupling varies fermion by fermion, and also mode by mode.

Chapter 2: Experimental apparatus

The detector used in the analysis is the Collider Detector at Facility (CDF), at Fermilab, Illinois, USA. The CDF is one of two detectors, the other is D0, which are located on the Tevatron ring at Fermilab, shown in Figure 2.1. This chapter contains a description of both the Tevatron and of the CDF detector followed by a brief history of the CDF. The CDF detector is described from the inner to the outer detectors, concentrating on the parts of the detector relevant to the analysis.

Figure 2.1: Aerial view of Fermilab, Illinois, USA. The larger ring is the Tevatron (1 km radius) and the smaller the Main Injector.

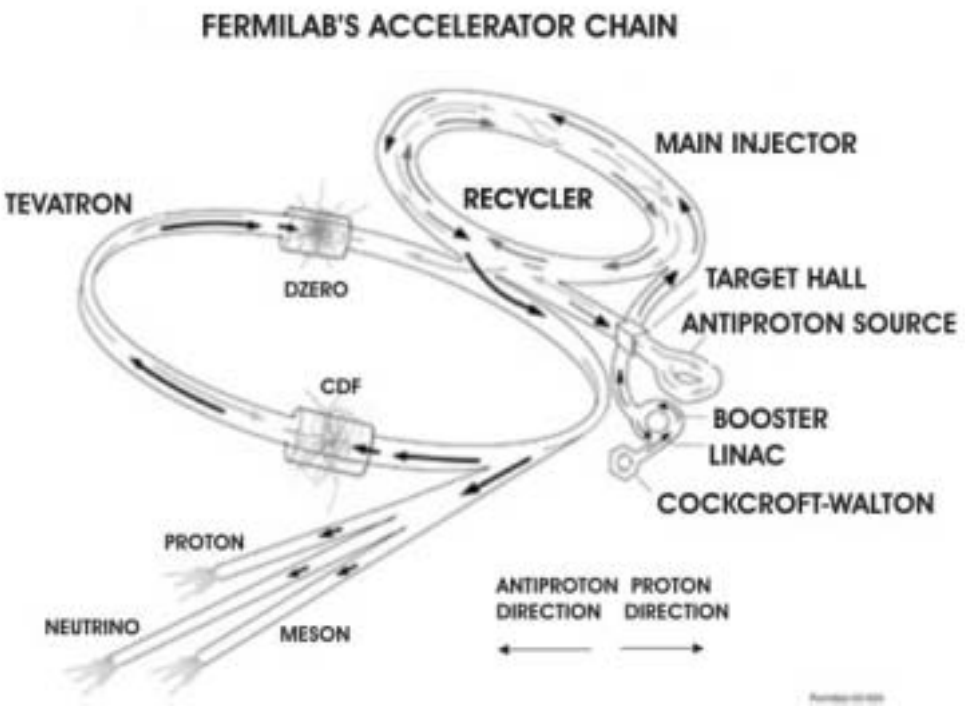

Figure 2.2: Schematic diagram of the accelerator chain at Fermilab.

2.1 The Tevatron overview

The Tevatron is a proton-anti-proton collider which operates at the centre of mass energy of 1.96 TeV. It is, therefore, the highest energy particle collider operational in the world and will remain so until the LHC is commissioned. Producing, accelerating and storing the protons and, in particular, anti-protons in sufficient numbers is challenging. To achieve such high energies, a series of accelerators is required. The accelerator chain, shown in Figure 2.2, and proton and anti-proton production are described in the subsequent sections [50].

2.1.1 Proton production and boosting

The first stage of the accelerator chain is the Cockcroft-Walton pre-accelerator where the protons are created. Inside this device hydrogen gas is ionized to create 25 keV negative ions. The ions are accelerated by a positive voltage in an electrostatic accelerating column to reach an energy of 750 keV. They then enter a 150 m linear accelerator, abbreviated to Linac, in which an

oscillating electric field accelerates the negative hydrogen ions to 400 MeV. Finally, the ions are stripped of electrons by passing them through a carbon foil, which leaves only the positively charged protons.

The protons are accelerated to 8 GeV by the Booster, a Proton Synchrotron, which has a diameter of about 150 m and is located about 6 m below ground. Together, the Linac and Booster are able to provide pulses of 5×10^{12} protons for anti-proton production every 1.5 s.

2.1.2 Main Injector

Protons are injected from the Booster machine to the Main Injector at 8 GeV. The Main Injector is a rapid cycling proton synchrotron, with a 3 km circumference (half that of the Tevatron, shown in Figure 2.1). It is in a tunnel separate from that of the Tevatron. The Main Injector essentially accelerates particles and transfers beams and has four functions, which are to

- accelerate protons from 8 GeV to 150 GeV,
- produce 120 GeV protons, which are extracted for anti-proton production or to an external experiment,
- receive anti-protons from the Anti-Proton Source and accelerate them to 150 GeV and
- inject protons and anti-protons into the Tevatron.

2.1.3 Anti-proton production

The anti-protons are produced by firing pulses of 5×10^{12}, 120 GeV protons from the Main Injector on to a nickel target. The collisions produce a wide range of secondary particles, including anti-protons. The anti-protons are focused with a lithium lens and collected in a debuncher ring at 8 GeV. Here they are transformed into a continuous beam and stochastically cooled. From the debuncher they are transferred to the Accumulator ring, where they are further cooled. When a sufficient number of anti-protons (up to 10^{12}) is available, the anti-protons are

further cooled and then transferred to the anti-proton Recycler ring.

2.1.4 Recycler

The Recycler is an 8 GeV permanent magnet storage ring equipped which lies in the the Main Injector tunnel. The Recycler not only collects and stores the anti-protons ready to be sent to the Main Injector for acceleration and injection into the Tevatron (where they reach the full energy), but also permits reuse of the anti-protons which remain in the Tevatron at the end of a store. These remaining anti-protons are slowed down by the Tevatron and Main Injector, back to an energy of 8 GeV. They may then be stored in the Recycler Ring, subject to electron cooling and reused in the following run. This is very important, because anti-proton production is one of the limiting factors in the efficiency of Fermilab's colliders. The collider luminosity is controlled by the total number of anti-protons available to accelerate and store. Most of the luminosity degradation results from beam dilution rather than anti-proton loss. At the end of a store, which typically lasts approximately 15 hours, 75 % of the anti-protons are expected to remain circulating in the Tevatron. By recycling two-thirds of these anti-protons, the average luminosity can be increased by a factor of two. Therefore, recycling effectively doubles the available anti-protons for collisions.

2.1.5 Tevatron

The final acceleration is done in the Tevatron, a 6 km circular accelerator. The Tevatron receives the injections of 150 GeV protons and anti-protons, called a shot, from the Main Injector and accelerates them in opposite directions to 0.98 TeV. This becomes a store when 36 bunches of protons and 36 bunches of anti-protons are circulating and ready to be brought into collision. The proton and anti-proton beams intersect at four points along the circumference of the ring. Only two of these are collision points, which are located at the centres of the 5000 ton CDF and D0 detectors inside the Tevatron tunnel, where the resulting interactions are observed.

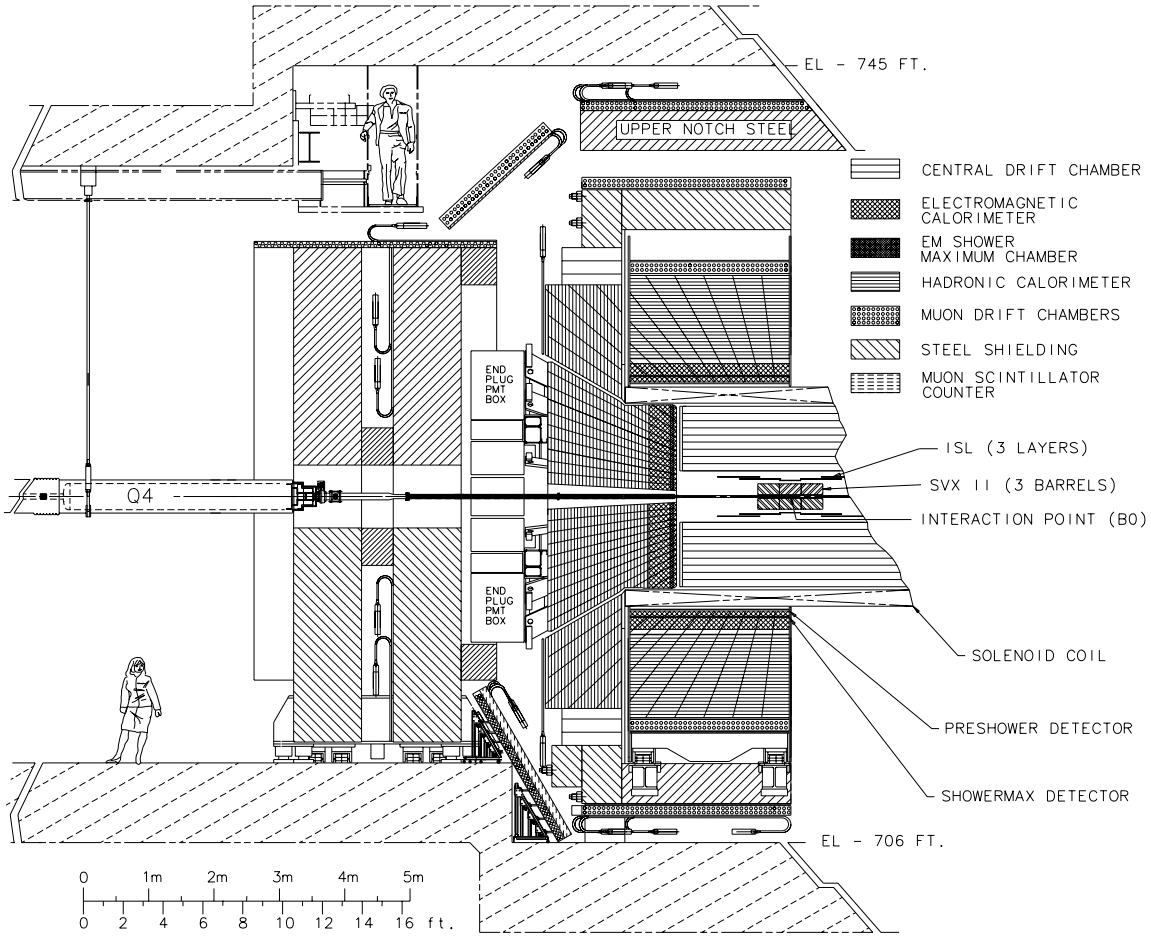

Figure 2.3: Elevation view of one half of the CDF II detector. At the centre of the detector is the tracking detector system, which consists of silicon vertex detectors and a drift chamber. Surrounding these detectors is the magnet, followed by the calorimeters; electromagnetic, then hadronic. Encompassing the calorimeters are muon drift chambers, scintillators and their steel shielding.

Quadrupole magnets are used to focus the beams at the collision points. At the other two points the beams are prevented from colliding by using electrostatic magnets.

2.2 The CDF detector overview

The detector consists of a 1.4 Tesla superconducting solenoid surrounded by projective tower geometry calorimeters and outer muon chambers, enclosing a tracking detector system, as shown Figure 2.3. A detailed description of the detector is published in the CDF Technical Design Report [51].

2.2.1 Geometry

In general the CDF detector is described in cylindrical co-ordinates, using the principal axes r, ϕ and z. CDF standard geometry defines the z axis to be oriented along the beam line, in the direction of the proton bunches and the origin is at the centre of the detector. Other co-ordinates also used are the x axis which points horizontally away from the centre of the Tevatron and the y axis which points vertically upwards. ϕ is measured in an anticlockwise direction from the x axis viewed in the proton direction. Convenient variables used are the polar angle, θ, which is measured upwards from the positive z axis, and is related to r and z by Equation 2.1, and the pseudorapidity (η) which is defined by Equation 2.2.

$$z = r \times cot\theta \tag{2.1}$$

$$\eta = -log(tan(\frac{\theta}{2})) \tag{2.2}$$

2.2.2 Tracking system

The tracking system consists of three silicon vertex detectors encompassed by a drift chamber, the central outer tracker (COT).

Silicon vertex detector

At the very heart of the detector CDF are three concentric silicon detectors; Layer 00 (L00), the silicon vertex detector (SVX) and the intermediate silicon layers (ISL). Information from neither L00 nor the ISL were used in this analysis, because these detectors were being commissioned.

Layer 00 is a single-sided, radiation-hard silicon layer, placed immediately outside the beam pipe, at approximately 1.5 cm.

SVX consists of three 29 cm long barrels, shown in Figure 2.4, which extend 45 cm, in the z direction, on either side of the interaction point. SVX provides track information to $|\eta| <$

2. The barrels are segmented into 12 wedges in ϕ, each with five layers of double-sided silicon wafers located at radial distances of 2.5 to 10 cm from the proton and anti-proton beams, shown schematically in Figure 2.5. Of the five layers, three have 0°-90° stereo alignment of the wafers, while two have 1.2° small-angle stereo. One side of each wafer provides measurements in the transverse (r-z) plane (axial strips) and the other side's strips deliver three-dimensional hit position information. The three dimensional hit information from the five layers is combined to form a track.

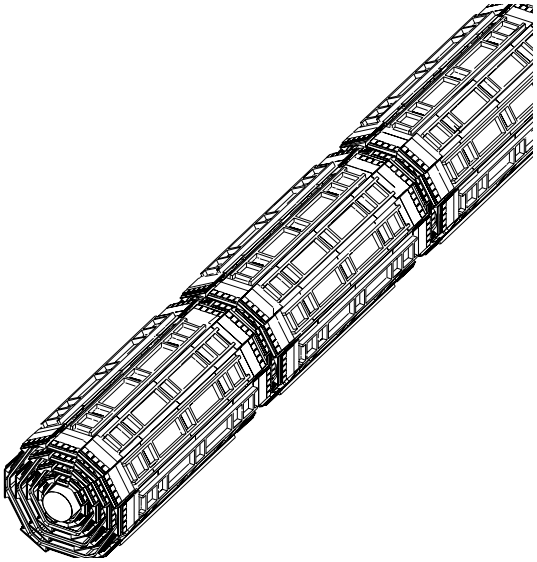

Figure 2.4: View of three barrels of the silicon detector.

Outside SVX are three additional layers of double-sided silicon detectors, similar to those in SVX, positioned at 20, 22 and 28 cm from the collision point. Together these form the ISL detector. The layer positioned at 22 cm is in the central η region, and the other two are more forward, from $1 < |\eta| < 2$, as illustrated in Figure 2.6.

Together with the SVX, the ISL make it possible to reconstruct three-dimensional tracks in the forward pseudorapidity region, which lies beyond the acceptance region of the central outer tracker ($|\eta| < 1$). This will be essential for matching muon stubs to tracks in the forward region and determining the forward muons' momenta. However, in this analysis, only central muons,

up to $|\eta| < 1$, were used. The silicon tracker can be operated in stand-alone mode, in which tracks are formed without input from the COT. This mode is useful to determine the COT tracking efficiency.

The COT+SVX track resolutions in the r-ϕ and z direction are parameterised by the resolution of the intersection of a track with the beamline relative to the nominal centre of the detector (0,0,0) in the r-z plane (z_0) and of the impact parameter corrected for the beam position (d_0^{corr}). The impact parameter corrected for the beam position is defined to be the minimum perpendicular distance, in two-dimensions, between the beam interaction point and the track[1]. The respective resolutions are $\sigma_{z_0} < 2.04 \pm 0.08$ mm and $\sigma_{d_0^{corr}} < 47.7 \pm 0.8$ μm, which includes the beam-spot resolution of 27-35 μm [52]. The high resolution can be used to determine the position of secondary vertices as well as to measure the $p\bar{p}$ collision point and to determine the track impact parameter more precisely than is possible with only the central tracking chamber. The latter is particularly important for dimuon searches, because impact parameter cuts provide an effective method of rejection of cosmic ray background, as described in Chapter 6. In high energy dimuon searches this is the dominant background. The high resolution of the SVX tracks allows finer impact parameter cuts to be placed than would be possible with only COT tracks, and therefore enables better background rejection.

[1]The relationship between the uncorrected impact parameter, which assumes the track originated from the centre of the detector, and the impact parameter corrected to account for the beam interaction not occurring at the origin is derived in Appendix B.

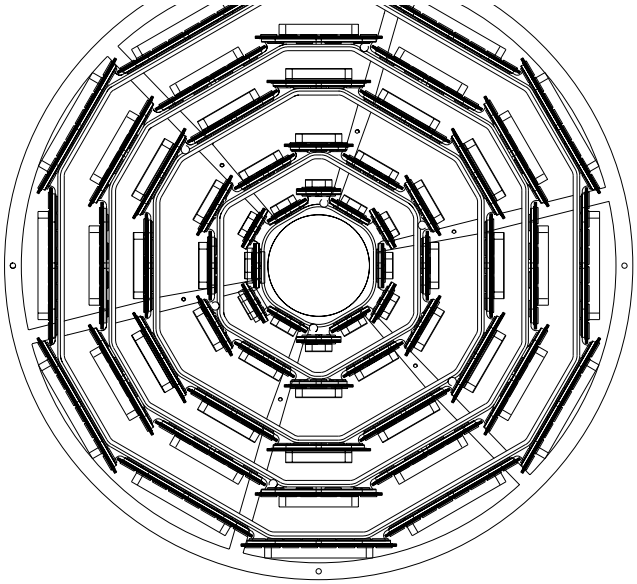

Figure 2.5: End view showing the five layer and twelve wedge segmentation in ϕ design of the CDF SVX detector.

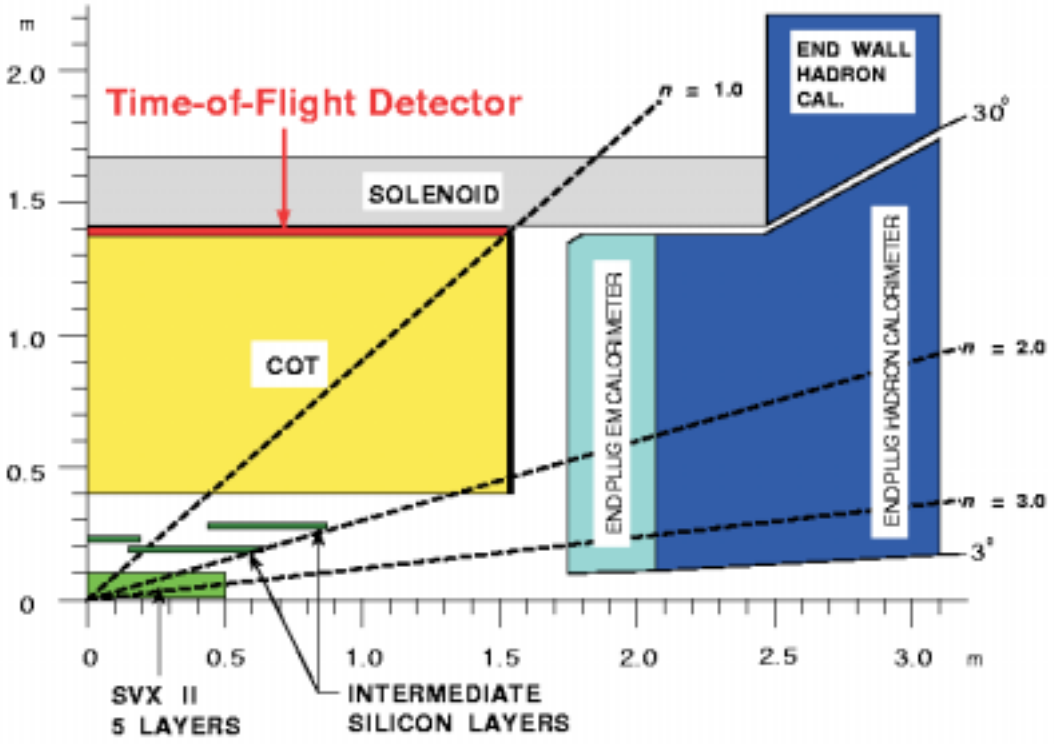

Figure 2.6: Quarter of the CDF detector showing the tracking region.

Central Outer Tracker

Additional tracking information, up to an $|\eta| < 1$, is provided by the central outer tracker (COT). This is a drift chamber composed of eight superlayers of cells, each of which consists of twelve layers of sense wires alternating with field-shaping (potential) wires in a plane. The superlayers are located at radial distances of 40 to 137 cm from the beamline, as shown in Figure 2.7. A single cell layout is illustrated in Figure 2.8 and a summary of the COT design is shown in Table 2.1. Four of the superlayers are axial, between each is a stereo layer, thus the COT provides 48 axial and 48 stereo measurements for each charge particle track. High energy particles produce ionisation in the gas within the COT and this charge is collected on the sense wires. The drift time yields the r-ϕ position of the hits (where the charged ions originated). The COT was designed to operate with a maximum drift time of 100 ns, to ensure that the maximum drift time was less than the 132 ns bunch spacing (which is intended to be used later in the present data operating period (Run II)), in order to avoid event pile-up. To achieve a maximum drift distance of ~ 1 cm, a gas mixture of Argon and Ethane is used, which has a drift velocity ~ 100 μm/ns. The stereo wires, together with the axial wires are used in determining the z position of the hits. A three-dimensional sequence of hits is fitted to form a track. From the curvature of the track in the magnetic field (of strength B) the transverse momentum of the particle (p_T) can be obtained and from its direction of curvature the sign of the charge of the particle (q) can be determined. These are related by Equation 2.3.

$$p_T = Bqr \tag{2.3}$$

The fractional error on the transverse momentum caused by detector resolution ($\frac{\sigma_{p_T}}{p_T}$) is proportional to the transverse momentum (p_T) of the track; consequently the resolution decreases

for high momentum particles, as shown in Equation 2.4.

$$\left(\frac{\sigma_{p_T}}{p_T}\right) = c \times p_T \tag{2.4}$$

In COT simulation c was measured to be 0.003 [52]. The implications of the momentum-dependent resolution for high energy dimuon searches were considered and are described in Section 10.1. The COT track d_0^{corr} resolution ($\sigma_{d_0^{corr}}$) is 380 $\pm$ 30 μm and the z_0 resolution (σ_{z_0}) is 4.1 $\pm$ 0.07 mm for tracks with $p_T > 20$ GeV/c. This is better than the resolution for low momentum tracks (for $p_T > 1.5$ GeV/c, $\sigma_{d_0^{corr}} = 554 \pm 19$ μm and $\sigma_{z_0} = 6.00 \pm 0.09$ mm), because higher p_T tracks experience less multiple scattering in both the SVX and COT [52].

The tracking detectors are essential in identifying muons, because possible muon candidates are composed of isolated high momentum tracks which are matched to muon stubs. In this analysis the central drift chamber (COT) was used to measure the momenta of the muon tracks.

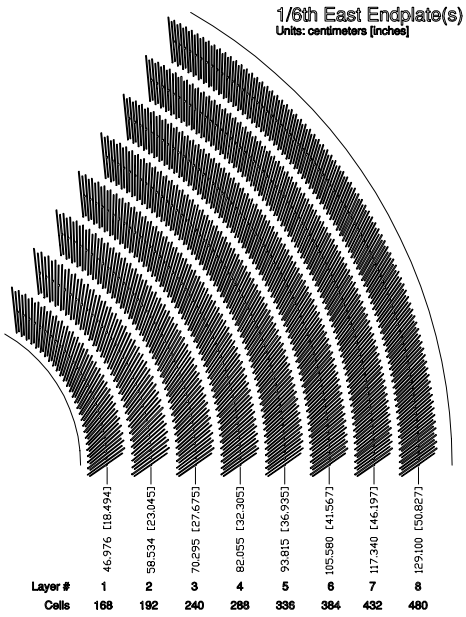

Figure 2.7: East endplate slots. The sense and field planes are at the clock-wise edge of each slot.

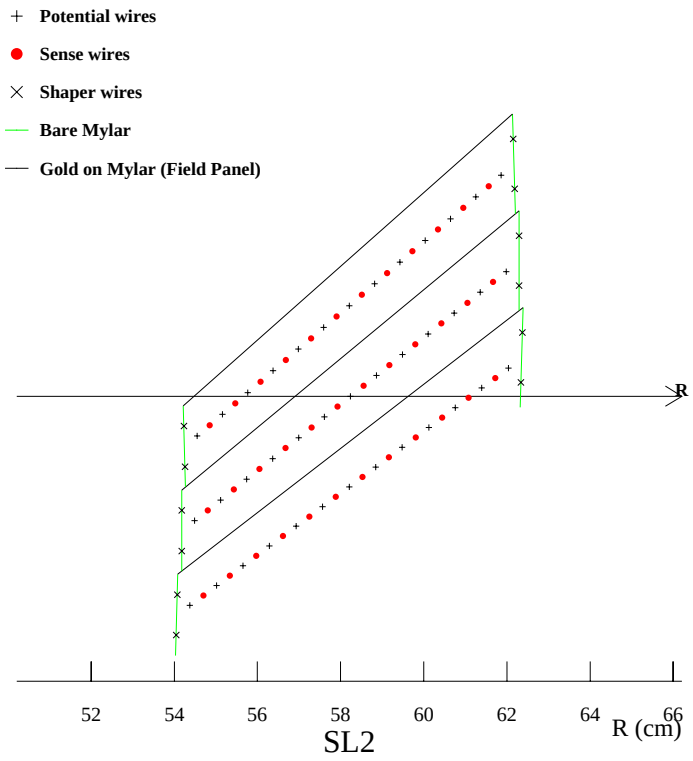

Figure 2.8: Nominal cell layout for superlayer two (SL2) in the CDF central tracking chamber (COT) detector.

Gas	Ar:Et
Maximum drift distance	0.88 cm
Maximum drift time	100 ns
Lorentz angle	35°
Drift field	2.5 kV/cm
Radiation lengths	1.6 %
Total layers	96
Layers/SL	12-12-12-12-12-12-12-12
Stereo angle	$\pm\ 3^0$
Number of superlayers	8
Stereo angle	$+3\ 0\ -3\ 0\ +3\ 0\ -3\ 0^0$
Cells/layer	168 192 240 288 336 384 432 480
Sense wires/cell	12 12 12 12 12 12 12 12
Sense wire spacing	7.62 mm in plane of wires
Wire diameter	1.6 mil gold plated Tungsten
Tilt angle	35°
Length of active region	310 cm
Total sense wires	30,240
Total wires	63,000

Table 2.1: Summary of the components of the CDF central tracking chamber (COT) detector.

2.2.3 Time-of-Flight

The Time-of-Flight (ToF) detector consists of an array of 216 scintillator bars, about three metres long, matching the COT active volume. These are placed at the outer edge of the COT, at a radial co-ordinate of 140 cm, as indicated in Figure 2.6. Photomultiplier tubes, attached to both ends of each bar, provide time and pulse height measurements. By comparing the two pairs of results, the detector determines the instant in which a particle crossed the scintillator and the z co-ordinate of the intersection. The latter measurement is compared to the results of 3D track reconstruction in the inner tracking volume in order to associate a time-of-flight to each track. The ToF timing resolution is 110 ps [53].

The timing resolution of the ToF detector allows particle identification, which is essential in B physics studies. Also the time difference between two muons, as recorded by the ToF detector, provides a very effective method to distinguish cosmic ray muons from interaction muons; as described in Chapter 6. This is demonstrated in Figure 2.9 in which the left plot shows the time difference between two muons, one recorded in the upper and the other recorded in the lower half of the ToF detector, of a Z $\rightarrow \mu\mu$ data sample, which peaks around zero. In contrast, the right plot shows the same distribution for a cosmic ray sample, where the time difference peaks around -9 ns. The ToF detector is used in this analysis to reject cosmic rays.

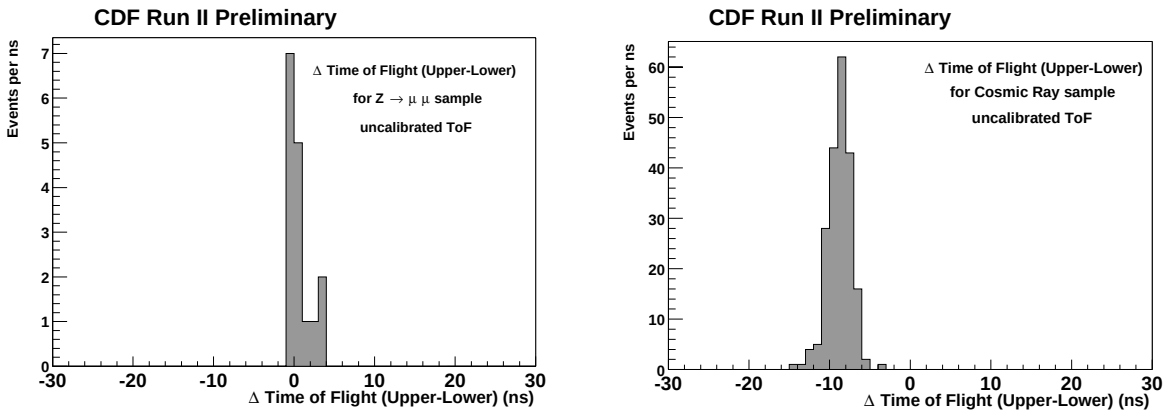

Figure 2.9: Comparision of the time difference between two muons, one recorded in the upper and the other recorded in the lower half of the ToF detector, of a Z $\rightarrow \mu\mu$ data sample to a cosmic ray data sample. The contrasting peak positions, around 0 and -9 ns for the respective dimuons samples, can be used to distinguish cosmic ray events from interaction events.

2.2.4 Magnet

The CDF tracking systems are enclosed by a superconducting solenoid, which provides a uniform magnetic field of 1.4 T along the detector axis over a cylindrical fiducial volume 3.5 m long and 2.8 m in diameter. The solenoid is built of an Al-stabilized NbTi superconductor and operates at liquid helium temperature. The magnetic field strength is determined by the current flowing in the superconducting coil. The magnet enables the tracking chambers to measure the momentum of charged particles from the curvature of their path in the magnetic field.

2.2.5 Calorimeter overview

After traversing the tracking chambers, the particles encounter the sampling calorimeters, which measure the energy of photons, electrons and jets and detect the missing transverse energy associated with neutrinos and neutral exotic particles. The calorimeters not only provide energy information used to identify muon candidates, by the characteristically small fraction of their energy which they deposit, unlike electrons, photons and jets. In addition, the hadron calorimeter provides timing information, which is used in muon triggers (see page 62, Section 2.2.6) and can be used to reject cosmic ray background.

Central and plug calorimeters

CDF has two calorimeters; a central and a plug. The central calorimeter (including the endwall, whose position is shown in Figure 2.6) covers a pseudorapidity region $|\eta| < 1.1$. The plug calorimeter extends the pseudorapidity coverage from 1.1 to 3.64. The calorimeters provide complete coverage in ϕ. Both the central and plug calorimeters have two separate projective tower calorimeters; the electromagnetic (EM) and the hadronic (HAD), shown in Figure 2.3. The positions of the plug calorimeters are labelled in Figure 2.6. The central calorimeter is constructed as 24, 15°, "wedges" in ϕ and each tower covers about 0.1 in pseudorapidity (η). The plug detective elements follow the same η and ϕ segmentation where possible. Each tower

consists of alternating layers of scintillator tile and passive material, which is lead for the electromagnetic sections and iron for the hadronic sections. The signal is read via wavelength shifters (WLS) embedded in the scintillator. Light from the WLS is then carried to photo-multiplier tubes.

Table 2.2 summarises the thickness in terms of radiation length (X_0) and hadronic interaction length (λ), the material dimensions, light yield and resolutions of each calorimeter sector. The energy resolution of the electromagnetic calorimeter sections is approximately 16 %/$\sqrt{E}$ and the hadronic sections is approximately 80 %/$\sqrt{E}$.

	Central and End-wall	Plug
Electromagnetic		
Thickness	19 X_0, 1 λ	21 X_0, 1 λ
-per sample (Pb)	0.6 X_0	0.8 X_0
-per sample (scint.)	5 mm	4.5 mm
Light Yield	160 p.e./GeV	300 p.e./GeV
Resolution	14 % / $\sqrt{E}$	16 % / $\sqrt{E}$
Hadronic		
Thickness	4.5 λ	7 λ
-per sample (Fe)	1 in (central) 2 in (end-wall)	2 in
-per sample (scint.)	6 mm	6 mm
Light Yield	40 p.e./GeV	39 p.e./GeV
Resolution	75 % / $\sqrt{E} \oplus$ 3 %	80 % / $\sqrt{E} \oplus$ 5%

Table 2.2: Characteristics of the CDF Run II calorimeter. X_0 is the radiation length and λ the hadronic interaction length.

Central hadron calorimeter timing

In addition to providing energy information, the central hadron calorimeter provides pulse timing information from time-to-digital converters (TDCs). These TDCs measure the time elapsed for particles to traverse the detector and reach the scintillators in the calorimeter with respect to the beam-beam crossing time. The timing resolution ($\sigma_{TDCtime}$) depends on the energy of the particle, for particles with energies below 4 GeV, as displayed in Equation 2.5. For energies above 4 GeV, which applies to the muons studied in the analysis, the resolution distribution is

flat at approximately 2 ns [54]. Similarly to the ToF timing, the hadron TDC timing information can be used to distinguish interaction muons from cosmic ray events. Timing information from the hadron TDCs was utilised for this purpose in the analysis, and played a vital role in the rejection of cosmic rays; as demonstrated in Chapter 6.

$$\sigma_{TDCtime} = \frac{2.3}{\sqrt{E(GeV)}} \oplus 2.0 \ \ ns \tag{2.5}$$

Pre-shower and shower maximum detectors

Embedded into the electromagnetic calorimeters are two two-dimensional strip wire chambers; one of which acts as a pre-shower detector (labelled CES for the central calorimeter) and the other a maximum shower position detector. Their location is shown in Figure 2.3. The pre-shower detectors are located immediately in front of the electromagnetic calorimeters. These detectors provide information which can be used to distinguish photons from uncharged pions, which is useful in rejection of electron background and to decrease the electron trigger fake rate.

2.2.6 Muon detectors

Outside the hadron calorimeter are the scintillators, drift chambers and steel absorbers used for the detecting muons. There are four muon detectors: the central muon detector (CMU), the central muon upgrade detector (CMP), the central muon extension detector (CMX) and the barrel muon detector (BMU). Their positions in the CDF detector are labelled in Figure 2.10 and Figure 2.11. All four detectors are composed of layers of single wire drift chambers, of which alternating layers are staggered, in order to eliminate hit position ambiguities, as explained in Section 2.2.7. The physical shape of the chambers is different because of the geometry of each detector and is summarised in Table 2.3. A brief physical description of each muon detector is given in the following sections. The process of forming a muon stub from hits in the drift chambers and matching the stub to a track to create a muon candidate is described in Section 2.2.7.

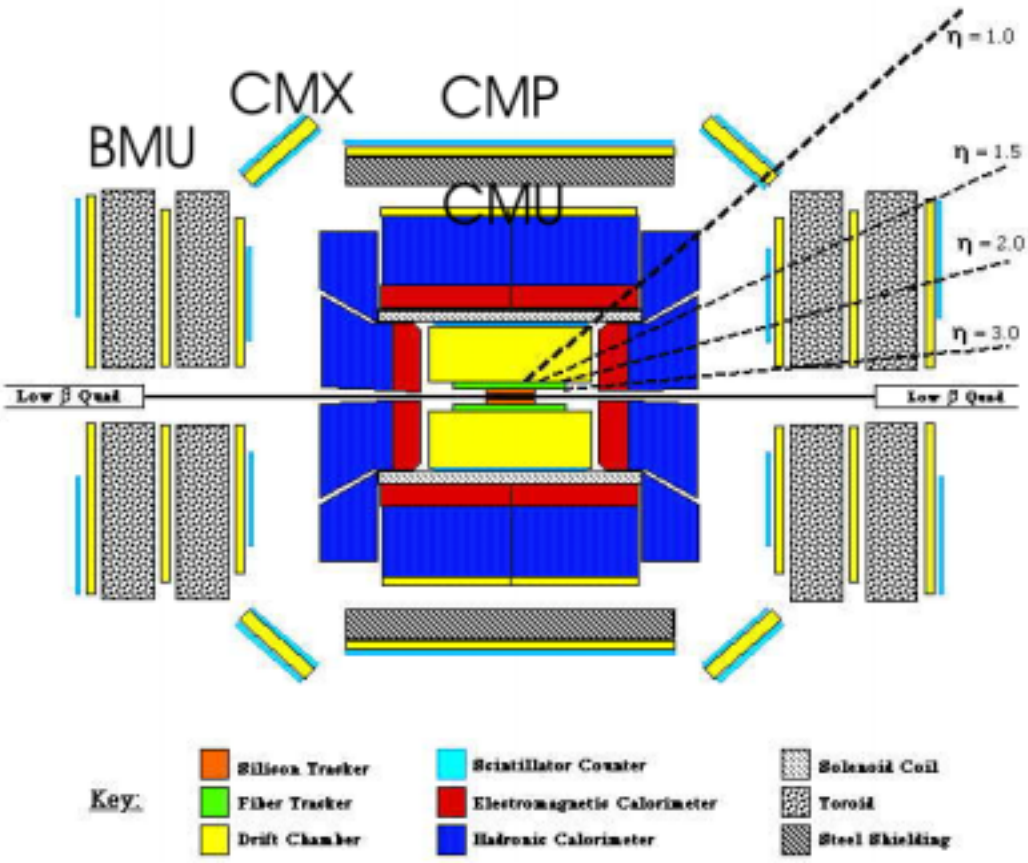

Figure 2.10: Schematic diagram of the CDF detector, with labels indicating the positions of the four muon detectors, which are composed of drift chambers and scintillators.

	CMU	CMP/CSP	CMX/CSX	BMU
η coverage	0-0.6	0-0.6	0.6-1.0	1.0-1.5
Drift tubes:				
Thickness	2.68 cm	2.5 cm	2.5 cm	2.5 cm
Width	6.35 cm	15 cm	15 cm	8.4 cm
Length	226 cm	640 cm	180 cm	363 cm
Maximum drift time	0.8 μs	1.4 μs	1.4 μs	0.8 μs
Number tubes	2304	1074	2208	1728
Scintillators:				
Thickness	N/A	2.5 cm	1.5 cm	2.5 cm
Width	N/A	30 cm	30-40 cm	17 cm
Length	N/A	320 cm	180 cm	180 cm
Number tubes	N/A	269	324	864
π^0 interaction lengths	5.5	7.8	6.2	6.2-20
Minimum P_t (GeV/c)	1.4	2.2	1.4	1.4-2.0

Table 2.3: Parameters of muon detection at CDF. Pion interaction length and the limit on resolution due to multiple scattering are computed at $\theta = 90°$ in the central detectors CMU,CMP,CSP; at $\theta = 55°$ in CMX and CSX; and on the entire θ coverage for the BMU [51].

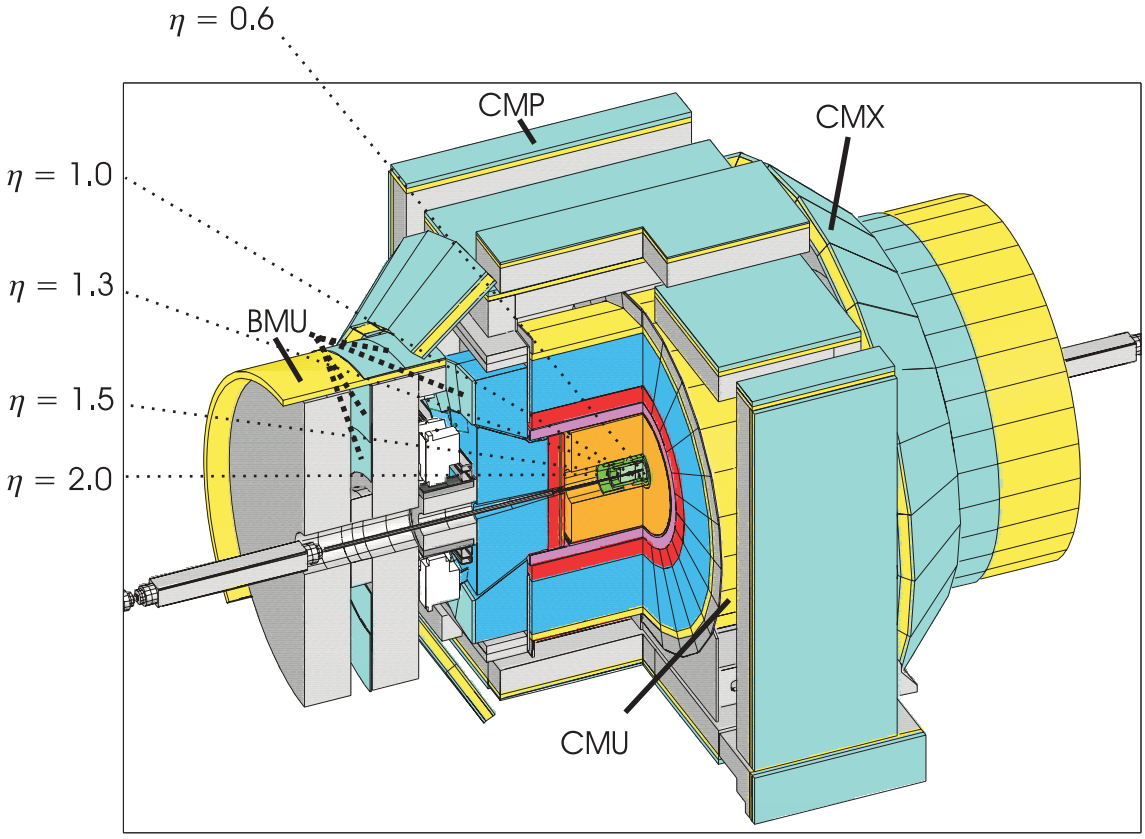

Figure 2.11: Three dimensional view of the CDF Run II detector. The positions of the muon chambers are indicated by the solid lines and the location of the BMU scintillators are shown by thicker dotted lines. The muon scintillators are darkly shaded (in blue) and muon chambers are lightly shaded (in yellow).

Central muon detector

The central muon detector (CMU) is a barrel-shaped detector which surrounds the central calorimeters and covers a solid angle region up to $|\eta| \leq 0.6$. The ϕ and η coverage is shown in Figure 2.12. The CMU is located behind ~ 5.5 absorption lengths of material, as illustrated in Figure 2.13. It consists of 144 modules, each has 16 rectangular cells per module. Each cell is $6.35 \times 2.68 \times 226$ cm and has a 50 μm stainless steel wire in the centre. The CMU chambers operate in proportional mode to survive the high luminosity and event rates. The transverse co-ordinate ϕ is measured by converting the drift time to a drift distance from the wire using readout by a TDC. The z co-ordinate is measured using charge division and is determined by time-over-threshold (rather than charge-to-voltage conversion).

Since the maximum drift time of the CMU chambers is of the order of 800 ns and the bunch crossing separation is 396 ns, there is an ambiguity as to which of the two bunches the muon belongs. This is resolved by associating a muon track with both bunches for the Level-1 trigger decision (the trigger system is described in Section 2.2.8). The correct bunch is determined by associating the muon stub with a track extrapolated from the tracking chambers and obtaining its appropriate hadron calorimeter TDC time, which is capable of resolving a single bunch crossing ($\sigma_{TDCtime} \sim 2$ ns for particles with an energy greater than 4 GeV).

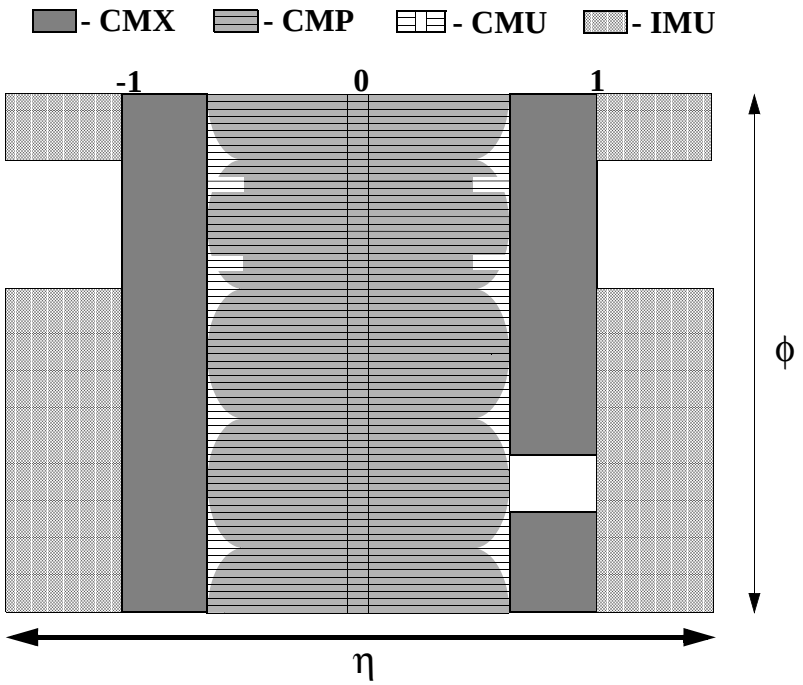

Figure 2.12: Location of the central muon chamber components in azimuth (ϕ) and pseudorapidity (η) for the CDF detector.

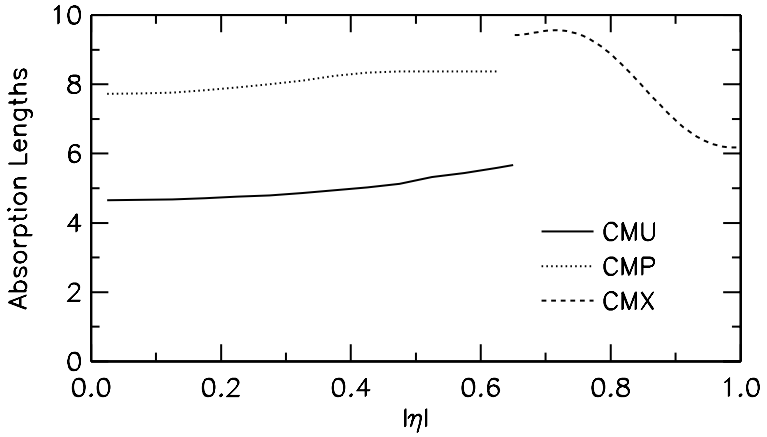

Figure 2.13: Number of absorption lengths as a function of pseudorapidity averaged over azimuthal acceptance of the CMU, CMP and CMX systems.

Central muon upgrade detector

A second set of muon chambers, the central muon upgrade (CMP), forms a box around the CMU, as shown in Figure 2.11, and is shielded by an additional layer of 60 cm of steel. It covers a region of $|\eta| < 0.6$ and, due to the detector geometry, this coverage varies with aximuth as shown in Figure 2.12. The CMP drift tubes have a cross-section of 2.5 cm $\times$ 15 cm and are 640 cm long (except where there are obstructions). The CMP chambers are also operated in proportional mode and have a maximum drift time of approximately 1.4 μs.

On the outer surface of the CMP lies the central scintillator upgrade (CSP), which is a layer of rectangular scintillator tiles. Each of the tiles covers two upgrade chambers in width and half in length. In total there are 216 scintillation counters, each readout by single phototubes. The CSP scintillator counters provide timing information which is used to associate the CMP muon stubs with the appropriate event (because the drift time is longer than the event separation time). Also muon triggers, which require CMP confirmation as were used in this analysis, utilise this CSP information in conjunction with the trigger information from the CMU chambers. More details of the trigger systems and muon triggers are given in Section 2.2.8 and Section 4.1.1

Central muon extension detector

The muon coverage is extended beyond a polar angle of 55° of the CMU and CMP to 42°, which corresponds to a pseudorapidity region $0.6 < |\eta| < 1.0$, by the central muon extension (CMX) and associated central scintillator extension (CSX). The CMX consists of a conical array of 180 cm long drift tubes. These lie in a truncated cone with scintillators on both sides. The positions of the CMX detectors are indicated in Figure 2.10, and their cone shape geometry can be seen in Figure 2.11. The drift tubes partially overlap each other in order to form a conical surface with rectangular cells. The overlap is therefore greatest overlap at the inner edge of the detector. This gives a stereo angle of 3.6 mrad between adjacent cells, allowing the measurement of the polar angle of the track. There are twelve drift tubes for each 15° sector. Mounted on

both the outside and the inside of each 15° sector of the CMX is a layer of four CSX scintillation counters. The counters are trapezoidal in shape with the same length as the drift tubes and a width of 30 cm at the smaller end and 40 cm at the larger end.

There is a 30° ϕ gap at the top of the detector for the Tevatron Main Ring and the solenoid cryogenic system. There is also a 90° (6 wedges of ϕ) azimuthal gap at the bottom of the detector where the conical sections are interrupted by the floor of the collision hall. To cover this region a 90° fan-shaped CMX/CSX, called the miniskirt, was installed. Because the chambers penetrate the nominal floor of the collision hall, they require a different geometrical configuration than that of the upper 270°. There are six counters per 15° wedge as opposed to four as in the rest of the detector. During the data-taking for this analysis the CMX miniskirt was turned off due to noise problems.

Barrel muon chamber detectors

The barrel muon chamber muon detector (BMU), as the name suggests, consists of a horizontal cylindrical "barrel" of CMP-like chambers and CSP-like scintillator counters, shown in Figure 2.11. The BMU chambers cover a pseudorapidity region from 1.0 to 1.5. These are shielded by and mounted on the outer radius of the toroids. Also, there is a vertical pinwheel of scintillation counters on the endwall (η = 1.0 to 1.3) and two pinwheels (one above the other at η = 1.3 to 1.5 and η = 1.5 to 2.0) between the toroids for triggering. The position of the chambers and the three scintillator sections; barrel, toroid and endwall, are labelled in Figure 2.11. The scintillators are darkly shaded (in blue) and chambers lightly shaded (in yellow).

Together with the ISL, the BMU will make it possible to trigger on forward muons, up to a pseudorapidity of 1.5, and to identify muons up to a pseudorapidity of 2. The BMU detector was not used in this analysis, because when the data sample was collected there were no triggers implemented for the BMU, there were noise problems in the chambers and, in addition, its off-line reconstruction software was being developed.

2.2.7 Formation of a muon candidate

All of the muon detectors consist of four layers of drift chambers. A muon passing through one of the muon detectors will leave hits in the layers of drift chambers. These hits are then associated together to form a muon stub in a process called "stub-finding". A muon candidate is formed by linking a track to a muon stub. These two processes are described in below.

Hit position ambiguity

When a muon passes through one of the drift chambers, it ionises the gas and charged ions are formed. The drift chamber determines the position where the ions were formed ("hit" positions) and hence where the muon track passed, by the time taken for the ions to drift to the central wire. Assuming an equal drift velocity in all directions of the chamber, there is an ambiguity in determining the direction from which the ions originated, because ions originating an equidistance from the wire take an identical time to reach the wire.

If a two dimensional drift chamber is considered, when a muon passes through the chamber two "hit" positions are reconstructed equi-distant, but either side of the wire. One represents the position where the muon passed and the other is a mirror hit. If four such chambers are stacked on top of each other, then a muon passing through the chambers would produce eight hits. Four of these would line up and indicate where the muon passed, and the other four would form a mirror image of this. It would not be possible to distinguish which was the real path of the muon and which the mirror image. For this reason successive layers of muon chambers are offset. In this case, each layer of the chamber still has two hits which can not be distinguished, and the four real hits in the four chambers will form a line indicating the muon path. The mirror hits will not line up, so the real and mirror path can be identified. This is illustrated in Figure 2.14 which shows a muon stub formed by data in the CMP detector. In this case the wires, which are not shown in the diagram, run horizontally into the page. The wire position in each layer can be deduced from the position of left/right ambiguity and they are located mid-way between

these two hits. The four hits which indicate the muon path are clearly aligned. The mirror hits in successive layers are offset and hence the ambiguity is resolved.

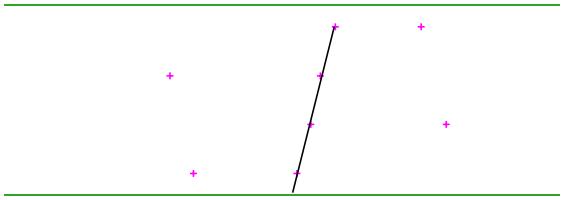

Figure 2.14: Stub in the central muon upgrade chamber. There are two hits in each of the four horizontal drift chambers because of the ambiguity in drift direction. Successive drift chamber layers are offset to resolve this ambiguity. The line shows the stub track chosen which minimises the combinations of residuals for the four layers and indicates where the muon passed through the detector.

Stub Finding

The stub finding algorithm performs the following procedure; it takes all of the reasonable pairs of hits in layers 0 and 2 (repeats this for layers 1 and 3), forms a line between these two points, and looks for hits in the other two layers that fall in a reasonable road around that line. If both of the other layers have at least one hit, then a 4-hit stub is formed. If only one of the other layers has a hit, then a 3-hit stub is created. All possible combinations of hits that lie in the road are considered.

In the next step of the process, for each stub, the residual for each chamber layer is calculated. The residual is the perpendicular distance, along the mid-plane of the chamber which contains the wire and is parallel with the chamber boundary, from the reconstructed hit position to the line drawn connecting the hits in the chambers. For example, if the four hits are perfectly aligned, then the line drawn connecting any two of the hits (in different layers) will also contain the other two hits. In this case the residuals in all the layers would be zero. If one of the mirror hits is included then the residual for this layer would not be zero. The residuals for each layer are combined to give a χ^2 for the residuals of each stub.

A fit is then made to all of the stubs in order to rank the stubs by their number of hits and

χ^2 of the residuals. Of all the hits/stub combinations, the favoured stub is the one with the most hits whose combination of residuals for the four layers is the minimum.

Track-stub linking

The final stage in forming a muon candidate is to associate a track to the muon stub. Loose quality cuts are applied to the track, summarised in Table 2.4. The track is required to have a transverse momentum (p_T) greater than 1.3 GeV/c (which a muon must have in order to be able to reach the muon detectors, see Table 2.3), more than 10 axial hits (N_{ax}), an impact parameter (d_0) of less than 6 cm and the track intercept with the detector axis (z_0) must be less than 60 cm (so that the muon is within the physical volume of the detector). Note that no minimum ionising selection criteria are imposed to form a muon candidate, which is important for very high energy muons, which may deposit more than the typical "minimum ionising" energy deposited by muons in the calorimeters, as discussed in Chapter 5. The tracks are extrapolated from the tracking chambers to the relevant muon detector. If the extrapolated muon track matches the position of the muon stub within pre-determined matching criterion, then the track and stub are linked to form a muon candidate. The matching criteria are shown in Table 2.4 for CMU, CMP and CMX muons. The track and stub are required to match in $r-\phi$ plane ($\Delta X = r \times \phi$) and very loosely in the z direction. A muon candidate can have several stubs; *e.g.* both a CMU stub and a CMP stub, if the track matches a stub in both the CMU and the CMP chamber.

Detector	CMU	CMP	CMX
Track-stub matching variable	Criteria		
ΔX (cm)	< 30.0	< 60.0	< 50.0
z (cm)	$20.0 <$ z < 250.0	z < 330.0	$325.0 <$ z < 550.0
Track requirements			
p_T (GeV)	> 1.3		
N_{ax} (hits)	> 10		
d_0 (cm)	< 6		
z_0 (cm)	< 200		

Table 2.4: Track-stub matching criteria for the central muon (CMU), central muon upgrade (CMP) and central muon extension (CMX) detector.

2.2.8 Triggers

In hadron collider experiments the trigger plays an important role, because the collision rate, which is effectively equal to the crossing rate of 7.6 MHz, exceeds the rate at which data can be written to and stored on tape. At CDF the data storage rate is limited to less than 50 Hz. The aim of the trigger is therefore to reduce the rate at which data is collected by efficiently extracting the most interesting physics events from the large number of minimum bias events.

The CDF trigger system was designed to accommodate an accelerator bunch spacing of 132 ns. During this analysis the accelerator was operating with a bunch spacing of 396 ns.

The trigger system is composed of a three-level pipelined and buffered trigger system, schematicised in Figure 2.15. Each level provides a sufficient rate reduction to permit processing of the next level with minimal deadtime. A summary of the three trigger levels is given below and the three levels are described in more detail in the following sections.

- The Level-1 trigger finds physics objects, using hardware, based on a subset of detector information and makes a decision based on simple counting of these objects (e.g. one 1.5 GeV muon or two 12 GeV electrons).
- The Level-2 trigger is capable of combining event information and does a limited event reconstruction, using hardware, which can be processed in programmable processors.
- The Level-3 trigger is more sophisticated and is able to fully reconstruct events using the full detector resolutions, this is done on a processor farm.

Level-1 trigger

Level-1 reduces the rate of data passing to Level-2 to less than 50 kHz, from the 7.6 MHz crossing rate, a reduction factor of about 150. In order to allow the 5.5 μs that Level-1 requires for transmission, processing of the trigger signals to make a trigger decision, a pipeline is required to buffer the data for the 28 beam crossings (at 396 ns separation) which occur during the latency

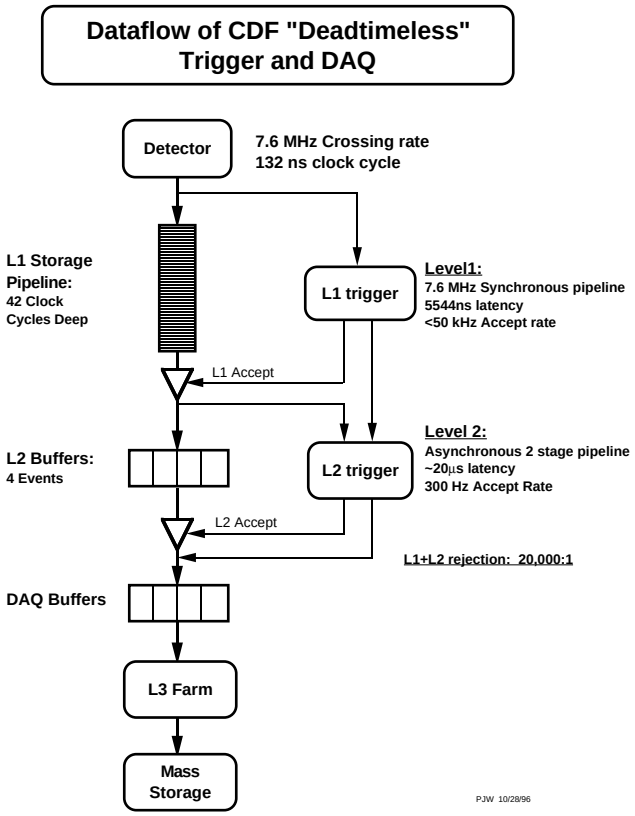

Figure 2.15: The CDF Run II readout functional block diagram, which shows the three level pipelined and buffered trigger system. Each level provides a sufficient rate reduction to permit processing of the next level with minimal deadtime.

period. Consequently, the front-end electronics of all detectors are fitted with synchronous pipelines, in which the entire data regarding each event are stored for the 5.5 μs while they are being examined and simultaneously other data are being collected. The Level-1 trigger will take a decision within 4 μs, while the event's data are still in the pipeline. The first trigger level truly is therefore deadtimeless.

The Level-1 trigger has three, synchronous, parallel hardware processors which feed inputs of the single Global Level-1 decision unit (as illustrated in Figure 2.16). The input to Level-1 hardware comes from the calorimeters (labelled CAL and CES in Figure 2.16), tracking chambers (COT and SVX) and muon detectors (MUON). The three triggers find the following objects:

- **Track trigger (L1 TRACK)** finds tracks in the central tracking chamber, using the extremely fast tracker (XFT). An extrapolation unit (XTRP) then propagates these tracks

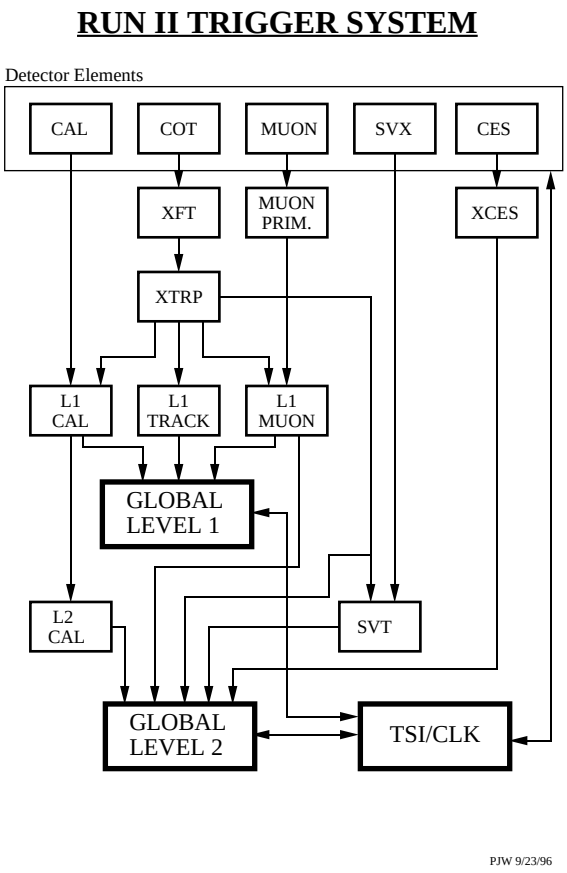

Figure 2.16: The CDF Run II trigger-system block diagram.

from the tracking chambers to the calorimeter and muon chambers, because the muons and electron triggers require the presence of a track pointing to the corresponding outer detector element. The track information is therefore sent to the calorimeter and muon stream, as well as the track stream.

- **Calorimeter trigger (L1 CAL)** finds calorimeter-based objects, for example, electron and photon candidates, jets, total transverse energy and missing transverse energy.

- **Muon trigger (L1 MUON)** matches XTRP tracks to stubs in the muon chambers.

The Global Level-1 decision unit combines the object information from these three streams using simple ANDs and ORs. The decision to reject or to retain an event for further processing is based on the number and energies of the electron, muon and jet candidates, as well as the missing E_T in the event. For example, one Level-1 trigger could require a combination of two

muon candidates both with transverse momentum (p_T) greater than 12 GeV/c. A Level-1 accept can also be generated on the kinematic properties of observed track pairs. Up to 64 different triggers can be formed and each can be prescaled independently of the others.

All elements of the Level-1 trigger are synchronised to the same 132 ns clock (labelled by CLK or TSI (trigger supervisor interface) in Figure 2.16) with a decision made every 132 ns by Global Level-1. Because the accelerator was operating with a bunch spacing of 396 ns for the analysis, in this mode the trigger was clocked every 132 ns with two intermediate clock cycles rejected automatically.

If an event is accepted by the Level-1 trigger, the front-end electronics move the data to one of four Level-2 buffers.

Level-2 trigger

Events matching the requirements of Level-1 are downloaded into one of four asynchronous event buffers analysed by a second set of hardware processors. When the data was collected for this research, Level-2 was set to auto-accept, which meant that Level-2 automatically passed all Level-1 events. This was because the Level-2 hardware was incomplete. The Level-2 trigger is described here as it was designed to operate.

Trigger Level-2 is asynchronous; events remain in a buffer until they are accepted or rejected depending on the Level-2 decision and meanwhile this buffer can not be used for additional Level-1 accepts. Consequently, if four buffers are full, there is a dead time incurred by the experiment. In order to limit the dead time to less than 10 %, with a Level-1 rate of 50 kHz, Level-2 is split in two pipelined stages of approximately 10 μs each. Initially the Level-2 trigger assimilates data from various sources, as shown schematically in Figure 2.16:

- Level-2 takes data originally from the Level-1 trigger systems, which is stored in the Level-2 buffer. All of the information used in the Level-1 decision is available to the Level-2 system, but with higher precision.

- Level-2 receives data from the hardware cluster finder (L2CAL) which processes the calorimeter data to provide measurements of the total jet energy in events. Because a jet usually deposits energy in more than one calorimetric tower, clustering algorithms are used to sum the energies collected by single towers surrounding a tower above a certain "seed" threshold energy. The seed finding, clustering and summing is also pipelined.

- In addition, Level-2 data uses information from the central calorimeter shower maximum detector. This requires that a cluster is above a certain threshold, which reduces the rate of fake electrons and photons and removes the background from single-phototube discharge. Also, the improved spatial resolution of the calorimeter shower maximum detector compared to the size of the calorimeter wedge enables better matching of XFT tracks to their calorimetric clusters.

- Level-2 accepts data from the SVX via the silicon vertex tracker (SVT). The SVT combines the silicon vertex detector data with the Level-1 tracking information and computes track parameters with resolution and efficiency comparable to full off-line analysis. The SVT provides jet reconstruction and impact parameter information. Triggering on the impact parameter has the potential to be extremely useful in reducing the very high rate of the high transverse momentum (p_T) inclusive muon trigger, which is caused by cosmic rays (see Chapter 6). Also, the SVT could be used to reduce the accidental rate by demanding that an SVX track points towards the primary vertex.

In the second stage of Level-2, the event data accumulated in the first stage is compared with the Level-2 selection criteria. The examination of one event can occur simultaneously as the data for the next event is loaded into the memory. Level-2 is expected to test each event for about one hundred different triggers. Requirements can range from "a single energetic lepton" to "two tracks from a secondary vertex, within a given invariant mass window". The acceptance rate is expected to be dominated by single lepton triggers. The data acquisition system is designed

to allow the Level-2 trigger to accept up to 300 events per second, and it is anticipated that the rejection rate will be about 150. The accepted events are transferred to the Level-3 trigger processor farm.

Level-3 trigger

After being accepted by the Level-2 trigger, the entire event data is read out and loaded into a Linux PC (personal computer) farm, where the event is fully reconstructed and filtered in software. After an event is reconstructed, it is sent to an event counter and, if the event passes the Level-3 cuts, it is also permanently stored to tape. An average event size is approximately 250 kB. Less than 50 Hz is written to permanent storage. The Level-3 reconstruction program is almost fully written in the C++ programing language, using object-oriented techniques.

Trigger Path

Each trigger path is composed of a specific Level-1, Level-2 and Level-3 trigger. For an event to pass a specific trigger path all of the requirements at each level must be satisfied. Each trigger path feeds one of eight data streams, labelled alphabetically from A to H.

The trigger paths used to collect the analysis data samples and the efficiency data samples are described in Chapter 4.

2.3 A brief history of CDF

The CDF detector first detected events in 1985. Since then there have been several data collecting periods, called Runs, which are summarised in Table 2.5. Analyses of experimental Run I data (1992-1996) resulted in the publication of more than 170 papers, ranging over the entire spectrum of hadron collider physics. For example, data collected from CDF provided the first experimental evidence for the top quark [55]; was used to perform precision electroweak measurements, such as the mass of the W boson [56]; determine average lifetimes for several b hadrons [57]; and to search for new particles in a variety of decay different channels (*e.g.* dijets [58] and dielectrons [59]).

Run	Year	Integrated luminosity (pb^{-1})
	1987	0.025
Run 0	1988-1989	4.5
Run 1a	1992-1993	19
Run 1b	1994-1996	90

Table 2.5: Integrated luminosity collected for runs before Run II at the CDF.

After Run I, in 1996, the Tevatron was shutdown in order for it to be upgraded. The improvements included construction of the Fermilab Main Injector, a new anti-proton accumulator ring and the addition of a Recycler (these components are described in Section 2.1.2, 2.1.3 and 2.1.4 respectively). These resulted in an increase in the centre of mass energy from the Run I value of 1.8 to 1.96 TeV, an increase in the achievable luminosity and an increase in the collision rate. This higher rate was due to the increase in the number of bunches in each beam, which was increased by a factor of six with respect to Run I, thereby reducing the time between two successive interactions from 2.4 μs, in Run I, to 396 ns. In order to accommodate the higher collision rate and to maximise the physics potential of the enhancements made to the Tevatron, several components of the CDF detector were totally rebuilt in the upgrade, while some parts were extended or modified and others remained unchanged.

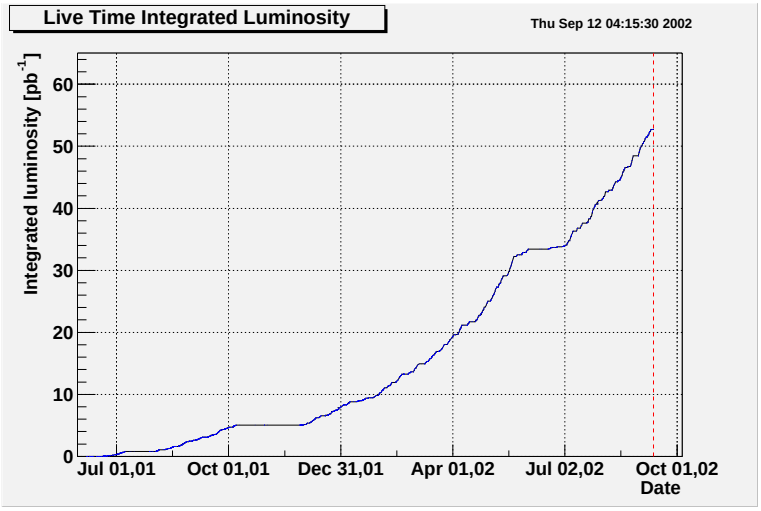

Figure 2.17: Tevatron integrated luminosity vs store number, shown for the period from 1^{st} July 2002 until 12^{th} September 2002. The data used in the analysis was collected between February 9^{th} 2002 and June 3^{rd} 2002.

Many of the upgrades to CDF significantly improved the dilepton search sensitivity. In particular, the muon and electron acceptance were increased in the upgrade, by extending the muon detector geometrical coverage and installing a new plug calorimeter, described in Section 2.2.5. In addition, a Time-of-Flight detector was introduced (outlined in Section 2.2.3) which enabled better rejection of cosmic ray background, which is the dominant background in high energy dimuon searches (see Chapter 6). CDF also has an improved triggering system and tracking system. High efficiencies for both triggering on events and identifying their final state are essential in new physics searches.

Commissioning of the CDF detector began in March 2001, and CDF recorded its first "physics quality" data in July 2001. At the time of this research the initial luminosity of the Tevatron was $\sim 2 \times 10^{30}$ cm^{2}s^{-1}. This was increased to $\sim 20 \times 10^{30}$ cm^{2}s^{-1} by April 2002, as shown in Figure 2.17. The peak luminosity achieved by the Tevatron pre-October 2002, was 30.2×10^{30} cm^{2}s^{-1} (on September 24, 2002), which exceeded the Run I record of 25.0×10^{30} cm^{2}s^{-1} set in 1995. The maximum weekly integrated luminosity attained was 4.8 inverse picobarns (pb^{-1}) (in September 2002), close to the Run I record of 4.9 pb^{-1} [60].

Chapter 3: Analysis overview

In this analysis a search for new physics was performed, using an integrated luminosity of 16.5 pb^{-1} high mass dimuon data produced in $p\bar{p}$ collisions at a centre of mass energy of 1.96 TeV and collected at the CDF. No significant deviations from the expected background were observed. Using the dimuon data, 95 % confidence level upper limits were determined on the production cross section times branching fraction of Z' bosons and Randall-Sundrum gravitons decaying to dimuons ($\sigma \cdot \mathrm{Br}(Z'/\mathrm{G} \rightarrow \mu^+ \mu^-)$). From these, lower mass limits were obtained for the Z' boson and the Randall-Sundrum graviton. Lower mass limits were also obtained for Randall-Sundrum graviton using the previously published Run I upper cross section limits for Z' decay to dileptons, which was obtained using an integrated luminosity of 110 pb^{-1} produced in $p\bar{p}$ collisions at the lower centre of mass energy of 1.8 TeV [20]. The analysis outline is summarised below.

In the Run II search, three data samples were used: a dimuon analysis sample, a Z dimuon sample and a Z dielectron sample. The selection of these data samples is described in Chapter 4. In particular, the Z samples were selected to have an invariant mass range around the Z mass and the leptons were required to have charges of the opposite sign. These two samples were used to determine the selection criteria to apply to the dimuon analysis sample and to obtain efficiencies. Monte Carlo was used to study properties of the signal events.

The selection criteria used to create the dimuon analysis sample are summarised in Table 4.3, Section 4.1.2. Because the search was for very high momentum muons, which can deposit more than the minimum ionisation amount of energy in the calorimeters, momentum-dependent cuts for the energy deposited in the calorimeters and the calorimeter isolation were investigated, as explained in Chapter 5.

Cosmic rays were the dominant background in the dimuon data sample. The characteristic properties of cosmic rays were studied, as outlined in Chapter 6. Several selection criteria were

imposed specifically to reject cosmic ray events. These cuts were composed of track cuts applied to the two muons and timing cuts, which were applied to both the Time-of-Flight time and hadron TDC time of the muons. In particular, the timing from the Time-of-Flight detector was found to be a very effective and efficient method to discriminate between cosmic rays and muons from a beam interaction.

The effect of the application of the selection criteria on the analysis dimuon data sample was investigated and is summarised in Chapter 7. The data was compared to the expected Standard Model backgrounds, as shown in Figure 11.4.

The efficiency of selecting a dimuon analysis event was determined using various samples (summarised in Chapter 8), predominantly a Z dimuon sample and a Z dielectron sample. Since the data samples were very small, the efficiency of each component of the dimuon event efficiency was obtained using two independent samples. The results were then compared for consistency. The acceptance was studied using Monte Carlo (described in Chapter 9). In order to check that the efficiency and acceptance obtained were of a reasonable order, the cross section at the Z mass was determined and compared with both the theoretical prediction and the published Run I result.

To determine the upper cross section limits, a signal region was chosen, as described in Chapter 10, the expected background in this region was estimated (as explained in Chapter 11) and the number of dimuon events observed in the same region were counted. The uncertainties were calculated as shown in Chapter 12. Upper limits, at the 95 % confidence level, on the production cross section times branching fraction of Z' bosons and Randall-Sundrum gravitons decaying to dimuons were obtained for the Run II data (16.5 pb^{-1}), both with and without uncertainties (in Chapter 13). The limits are shown in Figure 13.1 and 13.2 on page 191 for the Z' boson, and in Figure 13.3, on page 192, and Figure 13.4, on page 193, for the Randall-Sundrum graviton, exluding and including uncertainties respectively.

Run I mass limits on the Randall-Sundrum graviton were also determined by comparing the

acceptance of Z' boson decays to dileptons (electrons and muons) to that of Randall-Sundrum graviton decays and by using the upper cross section limit ascertained in the Run I Z' decaying to dileptons search (110 pb^{-1}), as described in Chapter 14. The limits are displayed in Figure 14.4, page 202.

Finally, methods to extend and improve the analysis were considered and are discussed in Chapter 15. This chapter begins with a summary of the results obtained (Section 15.1), and concludes with the predicted Z' boson and the Randall-Sundrum model graviton mass limits expected in Run II with an integrated luminosity of 2 fb^{-1}.

Chapter 4: Data Sample

4.1 Dimuon data samples

4.1.1 Trigger for inclusive high-p_T muon data sample

The data used in the analysis was collected between February 9^{th} 2002 and June 3^{rd} 2002, which corresponded to run numbers 138819 to 145669. From this sample, 249 "good runs" were selected[1], as defined by the muon group [61]. The integrated luminosity [2] ($\mathcal{L}$) of these good runs was 16.5 pb^{-1} and the uncertainty in the luminosity was of the order of 6 % [62]. The dominant sources of systematic uncertainty in the luminosity are discussed in Section 12.2. This data was extracted from the stream B inclusive high transverse momentum (p_T) muon data sample which was fed by two trigger paths [63], a CMUP path and a CMX path.

The three levels of the CMUP trigger path were;

- Level-1: L1_CMUP6_PT4, which required a CMU and CMP stub, the presence of CMP scintillator confirmation (CSP) and an extrapolated track (XFT) with $p_T > 4$ GeV/c,
- Level-2: L2_AUTO_L1_CMUP6_PT4, which passed Level-1 accepts automatically and
- Level-3: L3_Muon_CMUP18, which required $p_T > 18$ GeV/c. A loose track-stub match in the r-ϕ plane ($|\Delta X|$) was required to be less than 10 cm.

The CMX trigger path consisted of:

- Level-1: L1_CMX6_PT8 which required a CMX stub, the presence of CMX scintillator confirmation (CSX) and an XFT track with a transverse momentum (p_T) > 8 GeV.

[1] In order to select a good run; on-line log books were read and trigger tables checked to eliminate periods when the chambers were not operating properly or the trigger was used for tests. Also a good run was required to have the ANA bit set in the control room, the run type to be "physics" and data type to be "beam". Runs which were not on the COT good run list [64] were eliminated. Several distributions pertaining to muon reconstruction were examined. The good runs were required to have an integrated luminosity ($\mathcal{L}$) of greater than 10 nb^{-1}.

[2] This was calculated by the W analysis muon group [65] based on the method described by the luminosity group [66].

- Level-2: L2_AUTO_L1_CMX, which passed Level-1 accepts automatically.

- Level-3: L3_Muon_CMX12 or L3_Muon_CMX18, which required the $p_T > 12$ GeV/c or $>$ 18 GeV/c respectively and the track-stub match in the r-ϕ plane ($|\Delta X|$) was required to be less than 20 cm.

It is interesting to note that no electromagnetic or hadronic energy cuts were placed at the trigger level. This has particular relevance for very high momentum muons, which may deposit more than the minimum ionising amount of energy in the electromagnetic or hadronic calorimeter (see Chapter 5). Typically, as in Run I, cuts placed at the trigger level required the muons to be minimum ionising and consequently high momentum muons were removed from the data sample. The exclusion of fixed energy requirements at the trigger level constitutes a significant improvement for Run II high energy muon searches. The increased efficiency of implementing sliding energy cuts was investigated and is described in Chapter 5.

The events which passed the trigger requirements were reconstructed using production offline version 4.5.2 and written to the stream B bhmu03 data set.

The inclusive high-p_T muon bhmu03 data sample was further reduced by two sets of selection criteria. Initially a sub-sample was formed, called the "inclusive high-p_T muon data set", and from this a dimuon data set was created. The first reduction was made by the StripHighPtMuon module [67], which accepted an event if it contained at least one muon which passed the relatively loose selection criteria summarised in Table 4.1. To form the "inclusive high-p_T muon data set" the muon transverse momentum (p_T) was required to be greater than 18 GeV/c, the presence of at least one muon stub was required and loose sliding electromagnetic (E_{EM}) and hadronic (E_{HAD}) energy cuts had to be satisfied. Requirements were placed also on the track-stub matching in the azithumal plane between the track in the central tracking chamber (COT) and the stub ($\Delta X = r \times \Delta\phi$) for all three muon detectors; the central muon (CMU), central upgrade (CMP) and central extension (CMX).

Track based transverse momentum (p_T) > 18 GeV/c
Electromagnetic calorimeter energy deposition (E_{EM}) E_{EM} < 0.5×6.0 GeV if muon p_T < 100 GeV/c or E_{EM} < 0.5×(6.0 +0.0280×(p_T-100 GeV/c)) GeV if muon $p_T \geq$ 100 GeV/c
Hadron calorimeter energy deposition (E_{HAD}) E_{HAD} < 1.5×6.0 GeV if muon p_T < 100 GeV/c or E_{HAD} < 1.5×(6.0 +0.0280×(p_T-100 GeV/c)) GeV if muon $p_T \geq$ 100 GeV/c
Presence of at least one muon stub with the matching parameters CMU stub $\lvert\Delta X_{CMU}\rvert$ < 5 cm CMP stub $\lvert\Delta X_{CMP}\rvert$ < 10 cm CMX stub $\lvert\Delta X_{CMX}\rvert$ < 20 cm

Table 4.1: Selection criteria used to select events from the inclusive high-p_T muon bhmu03 data sample to form the "inclusive high-p_T muon data set".

The sliding energy cuts which were applied were designed to be loose enough not to remove high energy muons from the data sample. Calorimeter cuts were applied in order to reduce background from hadronic punch-through events, such as pions. Punch-through events are events in which hadrons do not deposit all of their energy in the calorimeters and penetrate through to the CMU chamber, where they cause a muon stub to be formed. In most cases the hadrons do not have sufficient energy then to penetrate through the extra steel between the CMU and CMP chambers, and so no CMP stub is formed (see Table 2.3 for number of pion interaction lengths to reach each muon chamber and Figure 2.13 for the absorption lengths as a function of pseudorapidity for each muon chamber). Because the hadrons have formed a muon stub, they mimic a muon; however, they often deposit more than the minimum ionising energy (which is by definition the amount a muon would deposit) in the calorimeters. Consequently, calorimeter selection criteria are used to remove such events.

4.1.2 Dimuon data sample

A dimuon data set was extracted [68] from the "inclusive high-p_T muon data set" by requiring the presence of one muon which satisfied the criteria required to pass the "inclusive high-p_T muon" cuts (shown in Table 4.1) and another muon stub in the event was also required. A prerequisite of the associated track of the second muon was that it had a transverse momentum

greater than 10 GeV/c. The additional cuts applied are summarised in Table 4.2. 35.2 % of the "inclusive high-p_T muon data set" and 18.9 % of the original events remained in the final dimuon data sample. Note that the muons were not required to have charges of the opposite sign.

Requirements placed on the second muon in the event
Presence of at least one muon stub with track based $p_T > 10$ GeV/c

Table 4.2: Additional selection criteria used to select events from the original "inclusive high-p_T muon data set" to form the dimuon data sample.

The analysis dimuon data sample, the data samples used to measure efficiencies, and those used to determine the position of the cosmic ray timing selection criteria were subsets of this dimuon data sample.

4.1.3 CMUP-CMUP dimuon analysis data sample

A sub-sample of the dimuon data sample was used in the analysis. Selection criteria were imposed to distinguish high-p_T dimuon events originating from real $p\bar{p}$ collisions from cosmic ray, QCD and other background events. The selection criteria applied to the dimuon sample and the purpose for which each was applied are summarised in Table 4.3 and explained in the following text. The definitions of each variable are as listed below. Identical requirements were placed on both muons in the event and for the analysis sample no opposite sign charge requirement was imposed.

The selection criteria were divided into three classes: initial cuts, muon identification cuts (ID) and cosmic ray (CR) cuts. The initial cuts were the trigger, the kinematic (p_T) and fiducial (CMUP) cut. A comparison of Monte Carlo muon identification variables to data is given in Section 4.1.4. The cosmic ray cuts are described in detail in Chapter 6.

Class	Purpose	Variable	Restriction on both muons
Trigger	enforce online trigger	demand Level-1, -2 and -3 trigger bits	
Kinematic	high trigger efficiency	$p_T{}^{\mu}$ (bc)	> 20 GeV
Fiducial	high-p_T muon		CMUP
Fiducial	calorimeter projectivity	$\lvert z_0{}^{\mu}\rvert$	< 60 cm
ID	good quality tracking	$N_{ax}{}^{COT}$	> 24
ID	good quality tracking	$N_{st}{}^{COT}$	> 24
ID	good track-CMU match	$\lvert\Delta X_{CMU}\rvert$	< 3 cm
ID	good track-CMP match	$\lvert\Delta X_{CMP}\rvert$	< 6 cm
ID	minimum ionization	E_{EM} p < 100 GeV	< 2 GeV
ID	minimum ionization	E_{EM} for p >100	$< 2{+}0.0115{\times}$(p-100)
ID	minimum ionization	E_{HAD} for p < 100	< 6 GeV
ID	minimum ionization	E_{HAD} for p >100	$< 6{+}0.0280{\times}$(p-100)
ID	QCD rejection	$I_{0.4}$ for $M_{\mu\mu}$ <110	< 4 GeV
ID	QCD rejection	$I_{0.4}$ for $M_{\mu\mu}$ >110	$< 0.1{\times}p_T$ GeV
CR	CR rejection	$\lvert d_0{}^{corr}\rvert$ for SVX, COT	< 0.02 cm, < 0.15 cm
CR	CR rejection	vertex reconstructed within 10 cm of muon	
CR	CR rejection	$z_0{}^{\mu\mu}$ - $z_{vtx'}$	< 3 cm
CR	CR rejection	$\lvert z_0^{\mu 1} - z_0^{\mu 2}\rvert$	< 4 cm
CR	CR rejection	Time-of-Flight time cuts	
CR	CR rejection	Hadron TDC time cuts	

Table 4.3: Summary of the three classes of analysis selection cuts used to select the analysis dimuon sample; initial cuts (trigger, kinematic and fiducial), the muon identification cuts (ID) and the cosmic ray (CR) cuts. Two muons are required, both passing the same selection criteria.

Kinematic selection

- **$p_T{}^{\mu}$ (bc)** is the beam-constrained (bc) transverse momentum of the muon track, as measured in the central tracking chamber (COT). If the track is beam-constrained then the helix of the track is constrained to have originated from the beam interaction point, rather than the nominal centre of the detector. The curvature of the track in the magnetic field can then be more accurately determined and the beam-constrained transverse momentum gives a more precise measurement of the transverse momentum of the muon track.

Fiducial selection

- A **CMUP** muon is defined to be a muon with a stub in both the CMU and CMP chambers, whereas one with only a CMU stub is a CMU muon and one with only a CMP stub is called a CMP muon. The presence of a stub implies that the muon is within the fiducial region of the muon detectors. In the dimuon analysis sample both muons were required to

have a stub in the CMU muon chamber and CMP chamber, which lies behind the CMU chamber and is shielded by extra steel. Requiring a CMP chamber muon stub in addition to a CMU stub reduces mis-identification of hadronic punch-through as muons[3].

- $\mathbf{z_0}$ is the intersection of muon track with beamline relative to the nominal center of the detector (0,0,0) in the r-z plane. The z_0 cut distance was determined by the physical size of the detector.

Muon identification selection criteria

- Track quality cuts were applied. Such cuts indirectly reject cosmic rays, because often cosmic ray tracks have few hits associated with them, since they pass through the detector out-of-time with an interaction event. Also one of the cosmic ray muon legs travels from the outside in, rather than from the inside of the detector out. Consequently, they can have poor quality tracks.
  - $\mathbf{N}_{ax}{}^{COT}$ is the number of axial hits of the muon track, as measured in the COT.
  - $\mathbf{N}_{st}{}^{COT}$ is the number of stereo hits of the muon track, as measured in the COT.
- $\Delta\mathbf{X}_{CMU}$ is the track-stub matching in the azithumal (r-ϕ) plane between the track in the central tracking chamber (COT) and the stub ($\Delta X = \mathrm{r} \times \Delta\phi$) for the central muon detector (CMU) and similarly ΔX_{CMP} for the central upgrade muon detector (CMP). Such matching reduces the background caused by noise in the muon chambers.
- Minimum ionising cuts were required because muons deposit a minimum amount of energy in the calorimeters compared with other particles, such as hadrons and electrons, which deposit a significant fraction of their energy in the detector (as discussed for punch-through events on page 81). The improved efficiency of sliding minimum ionising cuts rather than non-sliding for very high momentum muons is demonstrated in Chapter 5.

[3]However, some muons are lost due to this requirement, because there are regions covered by the CMU which are not also covered by the CMP detector (as shown in Figure 2.12), in such places only a CMU stub is possible.

- $\mathbf{E}_{EM}$ is the energy deposited in the electromagnetic calorimeter (EM) associated with the muon. A muon usually deposits very little energy in the calorimeters and this energy is typically deposited in only one tower. If, however, the muon passes between towers, then energy is shared between these towers. In this case a electromagnetic cluster is formed. This consists of a "seed" EM tower, which is one above a certain threshold energy, and its surrounding towers. The energy in these towers is then combined using a clustering algorithm. Clustering is more important for electrons then muons, which deposit a larger fraction of their energy in the calorimeters.
- $\mathbf{E}_{HAD}$ is the energy deposited in the hadronic calorimeter associated with the muon.
- Calorimeter isolation ($\mathbf{I}_{0.4}$) is defined as the sum of the transverse calorimeter energy in a cone around the muon, excluding the muon's transverse energy. The transverse electromagnetic energy (E_T) is calculated as EM cluster energy $\times$ sin θ, where θ is measured by the COT track associated with the muon. The cone is defined in pseudorapidity (η) and azimuthal angle (ϕ) space, such that it has a radius (R = $\sqrt{(\Delta\eta)^2 + (\Delta\phi)^2}$) of 0.4 centred around the muon cluster and R is defined between the muon cluster centroid and the centre of a candidate tower. This selection cut was used in order to reject background, for example from jets. Often a muon is contained within a jet. The particles associated with the jet accompanying the muon deposit energy in the calorimeter's tiles surrounding the muon. This is in contrast with muons from the signal (Z′ or graviton decay) which are typically isolated and therefore deposit little energy in the neighbouring calorimeter towers.

- **Rejection of cosmic rays** was achieved using a variety of techniques, for which more details are given in Chapter 6, and by placing restrictions on a number of different variables:
  - $\mathbf{d}_0{}^{corr}$, the two-dimensional impact parameter corrected for the beam position,
  - $\mathbf{z}_0{}^{\mu\mu}$ - $\mathbf{z}_{vtx'}$, a cosmic ray track cut which is explained in Section 6.1,

- $\mathbf{z}_0^{\mu 1}$ - $\mathbf{z}_0^{\mu 2}$, a cut to require that the two muons ($\mu 1$ and $\mu 2$) originate from the same vertex, where z_0^{μ} is the z intercept of the muon track with the beam line, and
- **timing cuts**, which are summarised in Table 6.3 and Table 6.7. The order of their application is described in Section 6.2.3 and the selection of the cut positions is explained in detail in Section 6.2.

4.1.4 Comparison of Z$\rightarrow \mu^+\mu^-$ Monte Carlo muon identification variables to those of Z$\rightarrow \mu^+\mu^-$ data

A comparison of Z$\rightarrow \mu^+\mu^-$ Monte Carlo to Z $\rightarrow \mu^+\mu^-$ data was made in order to give an appreciation of the effect of the muon identification cuts imposed. In addition, the effect of removing one of the selection criteria, from the dimuon analysis sample, after all of them had been applied was investigated and the results are presented in Chapter 7.

The data was compared with a 5000 event Monte Carlo Z $\rightarrow \mu^+\mu^-$ sample, which was generated as described in Section 4.3. The data sample used was essentially a Z region subset of the analysis data sample, outlined in Section 4.1.3, with the exception that muon identification cuts were applied only to one of the two muons. The second muon in each event was required to pass the kinematic (beam constrained $p_T > 20$ GeV/c) and fiducial (CMUP) cuts. For both the Monte Carlo and the data sample, a Z$\rightarrow \mu^+\mu^-$ sample was selected by limiting the dimuon invariant mass to be within the range of 66 to 116 GeV/c^2 and requiring the muons to have charges of the opposite sign. In order to compare the two samples, the Monte Carlo sample was scaled such that it contained the same number of dimuon entries within the specified invariant mass window as the data sample. The muon identification variables (displayed in Table 4.3) for the second muon, to which no identification cuts were applied, were plotted and are shown in Figure 4.1. In the case where both muons passed the muon identification criteria, then the muon with the highest transverse momentum was plotted. Data is denoted by the crosses and the shaded histogram illustrates the Monte Carlo simulation. The arrows in Figure 4.1 indicate the

positions where the selection cuts were placed. In the cases where sliding selection criteria were applied, the positions of the arrows are indicative of the low energy non-sliding cut positions.

All of the muon identification cuts removed either no events, or only a very small fraction of the events. The Monte Carlo and data agreed within the errors for the electromagnetic energy, whereas the hadronic energy was not well simulated in the peak region and the energy deposited by the data peaked slightly lower than that of the Monte Carlo. However, the hadronic energy cut at 6 GeV was loose enough that this discrepancy did not cause signal events to be rejected and consequently, for both data and simulation, the efficiency for the cut was high. Similarly, the number of COT and of SVX hits were poorly simulated, as can be seen in Figure 4.1, since in Monte Carlo the tracking efficiency was almost perfect, therefore, there were more hits in the simulation sample than in the data. This was to be expected because the track finding is much simpler in the Monte Carlo. Nevertheless, the cuts were loose enough, requiring that the number of hits was greater than 25, that none of the $Z \rightarrow \mu^+\mu^-$ data events were removed. The simulated isolation energy was slightly lower than the data; however, again the cut imposed was loose enough that this discrepancy was not significant. The fairly good agreement, particularly for ΔX_{CMU} and for ΔX_{CMP}, indicated that the muon systems were well aligned and that the multiple scattering, which dominates the width, was well simulated. The detector simulation and reconstruction were still being improved and tuned during this analysis, hence, where possible, efficiencies were calculated using data samples rather than Monte Carlo.

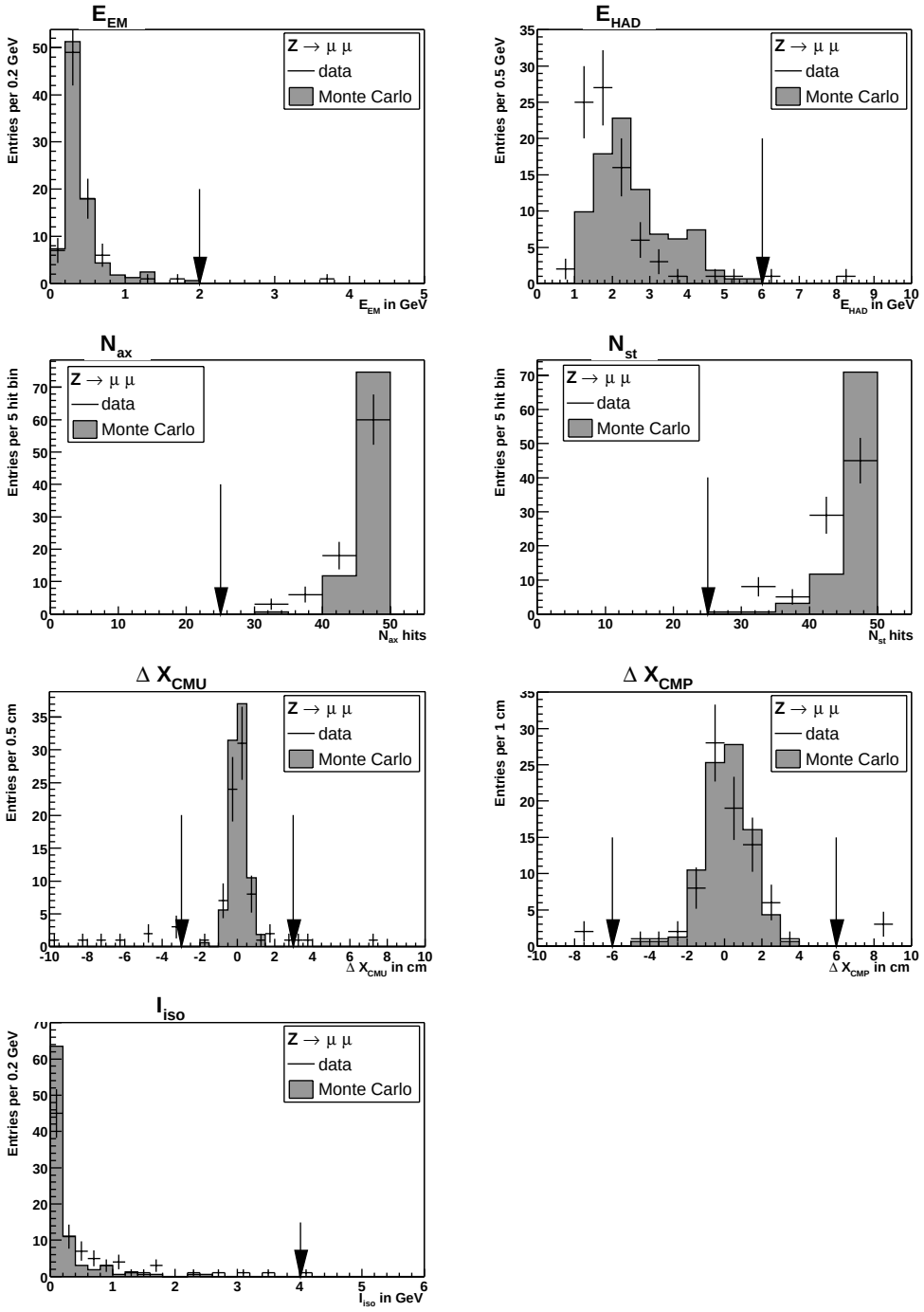

Figure 4.1: Comparison of Z $\rightarrow \mu^+\mu^-$ Monte Carlo to data (16.5 pb^{-1}) for muon identification variables; electromagnetic energy (E_{EM}), hadronic energy (E_{HAD}), number of axial COT hits (N_{ax}), number of stereo COT hits (N_{st}), the CMU track-stub matching (ΔX_{CMU}), the CMP track-stub matching (ΔX_{CMP}), calorimeter isolation (I_{iso}). The arrows indicate the position of the selection criteria imposed.

4.1.5 Z dimuon CMU/CMP/CMX data sample

A Z dimuon (Zmm) data sample was used to determine the positions of the cosmic ray timing cuts. The dimuon data sample was a sub-set of the dimuon data sample. The muon identification selection criteria in Table 4.3 were applied, with the exception that looser stub requirements were imposed. Rather than requiring CMUP-CMUP dimuon stub combinations, as in the dimuon analysis sample, the muon stubs were specified to be of type CMU, CMP or CMX. The track-stub matching criteria for the respective stubs were $|\Delta X_{CMU}| < 3$ cm, $|\Delta X_{CMP}| < 6$ cm and $|\Delta X_{CMX}| < 10$ cm. No timing cuts were placed on the muons. In order to create a Z sample, the dimuons' invariant mass was restricted to be within the range from 80 to 100 GeV/c^2 and the muons were required to have charges of the opposite sign.

4.2 Z dielectron data sample

A Z dielectron (Zee) data set was used for efficiency studies and to determine the cosmic ray background rejection cut positions. This data sample was a sub-sample of the inclusive high transverse momentum (p_T) electron data sample. The trigger for the inclusive high-p_T electron data sample is explained in Section 4.2.1 and the selection criteria used to create the Zee data sample are described in Section 4.2.2.

4.2.1 Trigger for inclusive high-p_T electron data sample

The data was collected between March 23, 2002 and June 2, 2002, which corresponded to run 141544 to 145654 and an integrated luminosity of 10.4 pb^{-1}, which had a systematic uncertainty of $\sim$ 6 %. This data originated from the stream B inclusive high-p$_T$ central electron sample which was initiated by the "Electron_Central_18" trigger [63]. The trigger had the following path:

- Level-1: L1_CEM8_PT8, which required at least one seed central EM tower with $E_T > 8$

GeV and an extrapolated track (XFT) pointing to the seed tower with $p_T > 8$ GeV/c.

- Level-2: L2_AUTO_L1_CEM8_PT8, which passed Level-1 accepts automatically.
- Level-3: L3_Electron_Central_18, which required at least one central electron candidate with $E_T > 18$ GeV, $p_T(bc)$ >9 GeV and $E_{had}/E_{EM} < 0.125$.

The electron variables, used at the trigger level, are defined below.

- Electromagnetic (EM) cluster and E_T

  As defined on page 85, Section 4.1.3 for muons.

- $p_T(bc)$

  The electron track is defined as the COT track with the highest beam-constrained transverse momentum ($p_T(bc)$) pointing to the electron cluster.

- E_{HAD}/E_{EM}

  E_{HAD}/E_{EM} is ratio of the total hadron calorimeter to the total electromagnetic energy (E_{HAD}/E_{EM}) for the towers included in the EM cluster.

Events passing this path were processed with the off-line Production version of 4.5.3.

4.2.2 Z dielectron data set

From the inclusive high-p_T data set a Z dielectron (Zee) data set was stripped using the selection criteria shown in Table 4.4.

Both electrons were required to be central, rather than plug electrons, because the purpose of the dielectron sample was to study electron track and timing quantities which would be comparable with that of the dimuon analysis sample. Since the central muon coverage extends up to a pseudorapidity of 0.6 and the central calorimeter covers a larger pseudorapidity region of up to 1, it was unnecessary to further increase the pseudorapidity coverage by including the plug calorimeter electrons. The electrons were both required to have a transverse energy (E_t)

greater than 20 GeV, an E_{HAD}/E_{EM} ratio less than 0.05 and have a calorimeter isolation of less than 0.1 GeV. In addition, one electron had to satisfy tighter cuts and this was called the tight electron, while the other was called the loose electron. The loose electron was required to have a transverse momentum greater (p_T) than 10 GeV/c. The tight electron had to have a track momentum such that its ratio of energy over momentum (E/P) was between 0.5 and 2.0, an L_{shr} of less than 0.2, ΔX $<$ 3.0 cm, ΔZ $<$ 3.0 cm and $\chi^2_{strip} < 10$, where these quantities are defined below. In order to get a clean Zee sample, the electrons were also required to have an invariant mass between 80 and 100 GeV/c^2 and be have charges of the opposite sign.

Variable	Central tight electron	Central loose electron
E_t	$>$ 20 GeV	$>$ 20 GeV
E_{HAD}/E_{EM}	$<$ 0.05	$<$ 0.05
Isolation ($I_{0.4}$)	$<$ 0.1 GeV	$<$ 0.1 GeV
Track momentum	0.5 $<$ E/P $<$ 2.0	$P_t >$ 10.0 GeV/c
L_{shr}	$<$ 0.2	
ΔX	$<$ 3.0 cm	
ΔZ	$<$ 3.0 cm	
χ^2_{strip}	$<$ 10	
Sign of charge	Opposite	
M_{ee}	80 $< M_{ee} <$ 100 GeV/c^2	

Table 4.4: Selection criteria used to select events from the original inclusive high-p_t electron data set to form the Zee data set.

Additional electron variable definitions used to select the Zee data sample:

- **I**$_{0.4}$ (Isolation E_T within a cone of R = 0.4)

  As defined on page 85, Section 4.1.3 for muons.

- E/P

  E/P is the ratio of the electromagnetic energy, E, of the electrons cluster measured in the calorimeter to the electron momentum, P, measured in the COT.

- **L**$_{shr}$ (transverse profile)

  The transverse profile, L_{shr}, of an electron allows a comparison of the lateral sharing of energy in the calorimeter towers with electron shower shapes from test-beam data. The

variable L_{shr} is defined by Equation 4.1.

$$L_{shr} = 0.14\Sigma_i \frac{E_i^{adj} - E_i^{expected}}{\sqrt{\left(0.14\sqrt{E}\right)^2 + \left(\Delta E_i^{expected}\right)^2}}. \quad (4.1)$$

Where E_i^{adj} is the measured energy (in GeV) in a tower adjacent to the seed tower, $E_i^{expected}$ is the expected energy (in GeV) in the adjacent tower calculated using a parameterisation from test beam data, $0.14\sqrt{E}$ (E in GeV) is the error on the energy measurement and $\Delta E_i^{expected}$ is the error on the energy estimate.

- **ΔX and ΔZ**

  The COT track associated with the electron was extrapolated to the central electromagnetic shower detector (CES), and the extrapolated position was compared with the shower position as measured in the CES. The variable ΔX is the separation in the r-ϕ view between the extrapolated track position and the CES cluster position. The variable ΔZ is the corresponding separation in the z view.

- χ^2_{strip}

  The pulse height shape in the CES was compared with test beam data using a χ^2 test. The variable χ^2_{strip} is the χ^2 of the fit of the energy deposited on each of the 11 strips in z in the CES shower compared to the test beam shape.

The sample consisted of 79 dielectrons and their invariant mass distribution is shown in Figure 4.2.

4.3 Monte Carlo data samples

Various Monte Carlo samples were used in the analysis. Several samples were generated with the FakeEvent generator [69], however, unless otherwise specified the Monte Carlo samples were generated with PYTHIA 6.203 [70], using parton distribution function CTEQ 5L [71].

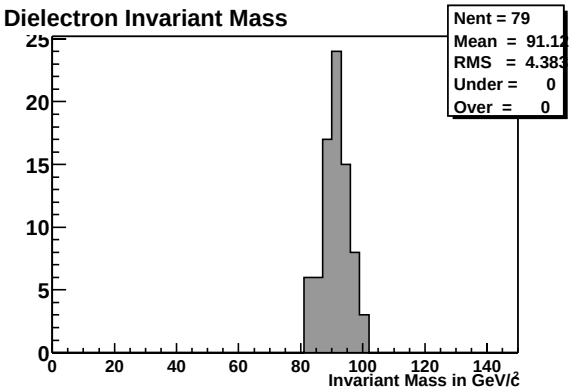

Figure 4.2: Invariant mass distribution for the Z dielectron data sample (10.4 pb^{-1}). To select Z events, a cut was placed to restrict the invariant mass to be between 80 and 100 GeV/c^2.

These samples were simulated with cdfSim [72] and reconstructed with ProductionExe [73] using version 4.5.3 of the CDF off-line code [74]. When generating Z′ and graviton signal samples, in general, no restrictions were placed on the transverse momentum of the final state leptons or on their pseudorapidity. Initial and final state electromagnetic radiation were turned on, and so were multiple interactions and fragmentation and decay. In order to generate Monte Carlo which modelled the data, the beam energy used was set to 980 GeV/c^2 and the vertex parameters were adjusted to better match the data [65]. The vertex parameter mean was set to 3 cm and the gaussian spread to 25 cm. To enable comparisons of Monte Carlo with data collected, sections of the CMP and the CMX which were not operating in the detector were turned off in the simulation.

Chapter 5: Momentum dependent selection criteria

Very high momentum searches introduce new challenges for lepton identification. Typical muon identification selection criteria were established for muons from Z decays or of lower energy, such as those from B decays. These are not always the most efficient selection criteria to use for high momentum muon searches. In this analysis momentum-dependent (sliding) cuts were applied to the electromagnetic energy, hadronic energy and calorimeter isolation variable, as described in Section 5.1 and Section 5.2.

5.1 Momentum dependent energy cuts

Muons by definition deposit a minimum ionising signal in the calorimeters. Typically, in Run I analyses non-sliding calorimeter isolation cuts were imposed. The standard Run I cuts were:

- electromagnetic energy (E_{EM}) < 2 GeV and
- hadronic energy (E_{HAD}) < 6 GeV.

However, the mean energy deposition in the electromagnetic and hadronic calorimeters increases linearly with momentum and, consequently as the muon momenta increase, these standard cuts become less efficient. The mean energy deposition in the hadron calorimeter, for a muon with momentum (P) greater than 20 GeV, is given approximately by Equation 5.1, in which P is measured in GeV/c [75].

$$E_{HAD} = 2 + 4 \times P/500 \tag{5.1}$$

The increase originates from large high energy tails from muon interactions such as e^+e^- pair production and bremsstrahlung processes. So although the standard Run I cuts are suitable for muons from Z decays, which deposit a mean energy of 0.4 GeV in the electromagnetic calorimeter (E_{EM}) and 2.0 GeV in the hadron calorimeter (E_{HAD}), they become inefficient for very high momentum muons [75]. For example, a 200 GeV/c muon deposits a mean energy in the hadron calorimeter of 3.6 GeV; however, a muon with momentum greater than 500 GeV/c will deposit more than 6 GeV/c and will consequently exceed the Run 1 minimum ionising cut.

The increase in energy deposited by higher momenta muons was investigated using Monte Carlo GEANT simulation[1]. Figure 5.1 illustrates the energy deposited, in both the electromagnetic and hadronic calorimeters, by muons with momenta of 50 GeV/c which can be compared with that of muons with momenta of 400 GeV/c. The Monte Carlo samples were generated with the FakeEvent program and consisted of 1000 events. The muons were specified to have $|\eta| < 0.7$. The simulation and reconstruction were performed as outlined in Section 4.3. It was found that a muons with momenta of 400 GeV/c deposit on average more energy in the detector than 50 GeV/c muons, which is illustrated in Figure 5.1. The mean hadron (electromagnetic) energy deposited was 3.3 (0.69) GeV for the 400 GeV/c muon sample compared with 2.5 (0.45) GeV for the 50 GeV/c muons. These results confirmed the expected increase in energy deposited for higher momentum muons. From Equation 5.1 muons with a momenta of 50 GeV would be expected to deposit a hadronic energy of 5.2 GeV, compared with 2.5 GeV for muons with a momentum of 400 GeV/c. From these results, it can be implied that non-sliding cuts would become more inefficient for higher momentum muons.

In order to maintain good efficiency for high energy muons, energy-dependent cuts were proposed in Run I in CDF note 4092 [76]. The following minimum ionisation cuts were suggested:

[1] An extensive study of the energy deposition of muons in an iron-scintillator calorimeter was performed by the CCFR collaboration. Both the CDF and the CCFR calorimeters are constructed of alternating layers of steel plates and scintillator counters. The data from the CDF GEANT Run I simulation was compared to that obtained using CCFR data and agreement between them was found. This supported the use of a GEANT simulation to model the hadron calorimeter [75].

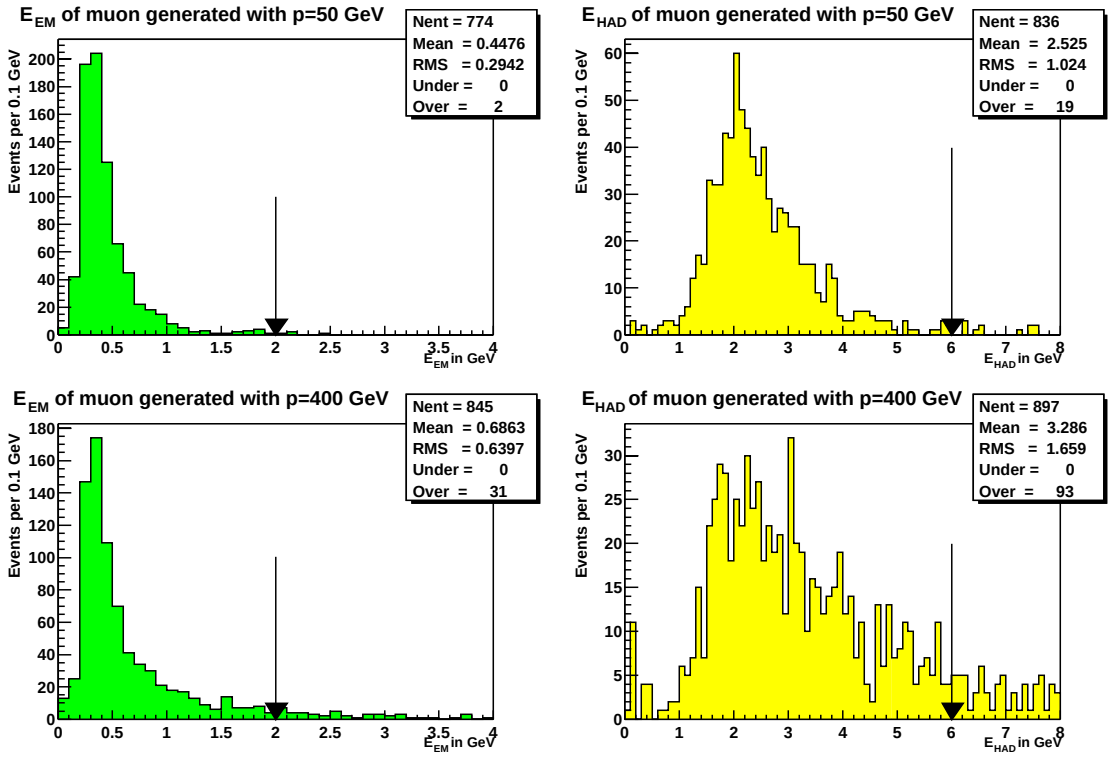

Figure 5.1: Comparison of the electromagnetic (left) and hadronic (right) energy distributions of single Monte Carlo muons generated with a momentum 50 GeV/c (upper) to those generated with a momentum of 400 GeV/c (lower).

- for $E_\mu < 100$ GeV: $E_{EM} < 2$ GeV and $E_{HAD} < 6$ GeV.
- for $E_\mu \geq 100$ GeV energy dependent cuts were proposed:

  $E_{EM} < 2 + C_1 \times (E_\mu$ - 100) GeV and

  $E_{HAD} < 6 + C_2 \times (E_\mu$ - 100) GeV

where C_1 and C_2 were determined to maintain a electromagnetic (EM) and hadronic (HAD) energy cut at a certain efficiency.

In this analysis similar sliding energy cuts were used. C_1 and C_2 were chosen to have the values selected in the Run I measurement of the Z^0 and Drell-Yan production cross section using dimuons [76]. These values were originally selected to maintain the electromagnetic energy cut to be 98% efficient (C_1=0.0115) and the hadronic energy cut 97% efficient (C_2=0.028). The energy dependence of these cuts is illustrated schemetically in Figure 5.2. In future, with more

data available, it would be possible to tune the coefficients to Run II data. Nevertheless the Run II central electromagnetic and hadronic calorimeters are those used in Run I, so these numbers were expected to be valid. The efficiency of the energy-dependent cuts was investigated and the results are demonstrated in the following sections for both single muons (Section 5.1.1) and Z' Monte Carlo samples (Section 5.1.2). It would have been interesting to have also studied the efficiency of the sliding cuts for a jet background sample, however, the limited size of the jet data samples available made this unfeasible.

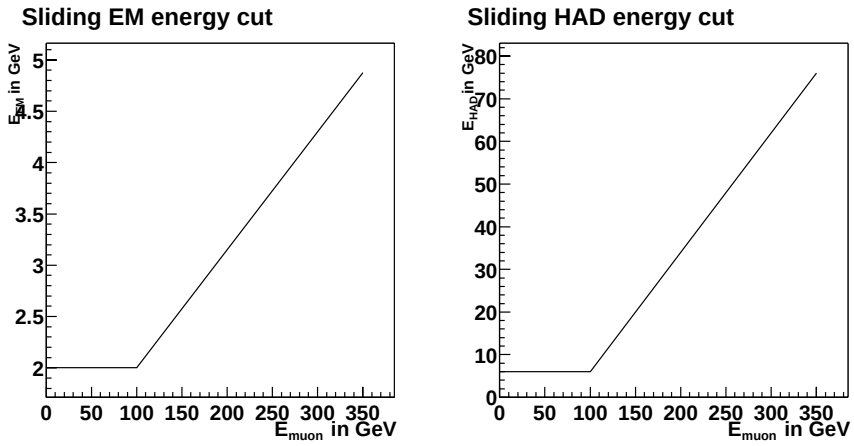

Figure 5.2: Energy dependence of the sliding EM (left) and sliding HAD (right) energy selection criteria.

5.1.1 Efficiency of sliding energy selection criteria for single muons

In this section, the increased efficiency of the sliding cuts compared to non-sliding cut is illustrated for single Monte Carlo muons.

The Monte Carlo sample consisted of 5000 muons generated using FakeEvent with a uniformly distributed spread in momentum from 15 to 500 GeV/c and $|\eta|<0.7$. The events were simulated and reconstructed as described in Section 4.3. The muons were required to pass the transverse momentum cut ($p_T > 20$ GeV/c) and have CMUP stubs. The electromagnetic and hadronic energy deposited by the muons as a function of their momenta are shown in Figure 5.3. In these plots the horizontal lines indicate the position of the non-sliding cuts and the diagonal lines the position of the sliding cuts, where the cuts are defined in Table 5.1[2] and were illus-

[2]The use of momentum (p) rather than energy (E) for the sliding cut dependence is arbitrary for muons at

trated in Figure 5.2. The numbers above the lines correspond to the number of muons removed by the specific cut. From these figures it can be seen that the non-sliding cuts removed more muons than the sliding cuts and muons with a larger momentum tended to deposit more energy in the calorimeters than those with smaller momentum. From this it can be inferred that the implementation of non-sliding cuts would have resulted in a momentum-dependent efficiency for the energy selection criteria.

Non-sliding energy selection criteria
EM $<$ 2.0 GeV
HAD $<$ 6.0 GeV
Sliding energy selection criteria
EM $<$ 2.0 GeV if muon p $<$ 100 GeV/c or
EM $<$ (2.0 +0.01150$\times$(p-100 GeV/c)) GeV if muon p $\geq$ 100 GeV/c
HAD $<$ 6.0 GeV if muon p $<$ 100 GeV/c or
HAD $<$ (6.0 +0.0280$\times$(p-100 GeV/c)) GeV if muon p $\geq$ 100 GeV/c

Table 5.1: Momentum dependence of electromagnetic (EM) and hadronic (HAD) energy selection criteria.

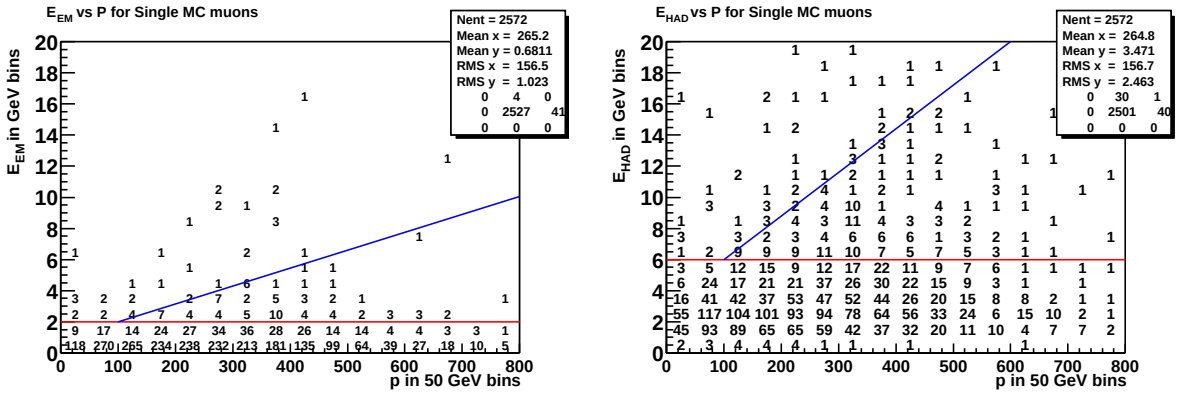

Figure 5.3: Momentum dependence of the electromagnetic (left) and hadronic (right) energy deposited in the calorimeter for the Monte Carlo sample of single muons.

The efficiency of the non-sliding and sliding cuts was compared as a function of muon momentum for a similar Monte Carlo sample of muons. This sample consisted of 15000 events and the efficiency is shown in Figure 5.4. The stars ($*$) indicate the efficiencies of the non-sliding cut and the crosses ($\times$) the efficiencies of the sliding cut. The non-sliding cuts were more inefficient

energies of the order of 50 GeV/c^2, because energy and momentum are related by the equation; $E^2 = p^2 + m^2$, and m is 0.105 GeV/c^2, so the quantity m^2 can effectively be neglected in comparison to E^2. Therefore $E \sim p$. In the detector, it is the muon transverse momentum and not the energy which is measured, so the cuts were chosen as a function of momentum rather than energy.

than the sliding cuts.

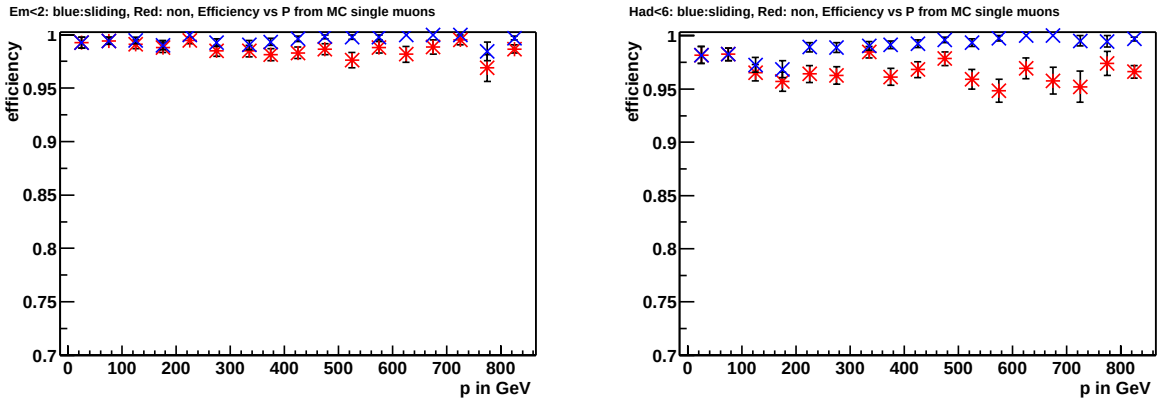

Figure 5.4: Comparison of the efficiency of the non-sliding ($*$) with sliding (crosses, $\times$) cuts as a function of muon momentum for a Monte Carlo sample of single muons.

5.1.2 Efficiency of sliding energy selection criteria for Z' signal

The efficiency of each individual cut, as defined in Table 5.1, (EM and HAD, sliding and non-sliding) and combination of cuts (EM and HAD, both sliding or both non-sliding) was investigated using Z' Monte Carlo data, and the results are described below.

2000 Z $\rightarrow \mu^+\mu^-$ events and 2000 $Z' \rightarrow \mu^+\mu^-$ with Z' mass of 200, 400, 600 and 800 GeV/c^2 were generated using PYTHIA version 6.203, simulated by cdfSim and reconstructed with version 4.6.0 of the offline code. The events were generated to have $|\eta| < 1.0$ and $p_T > 20$ GeV/c. The following initial selection criteria were applied to both muons: $|d_0^{corr}| < 0.2$ cm , $|z_0| < 60$ cm, $N_{ax} > 24$, $I_{iso} < 2$ GeV and both CMU and CMP stubs were required, with $|\Delta X(CMU)| <$ 3 cm. Note that no initial restrictions were placed on either the electromagnetic or hadronic energy deposited by the muon.

The efficiencies of applying electromagnetic and hadronic, sliding and non-sliding energy cuts, were plotted as a function of Z and Z' boson mass. The efficiency of the electromagnetic non-sliding energy cut was compared to that of the sliding energy cut and is shown on the left in Figure 5.5. In this case the non-sliding hadronic energy cut was first applied to the data sample and the efficiency of the cut (sliding/non-sliding) was defined to be the number of dimuon events

for which both muons passed the electromagnetic energy cut (for the sliding/non-sliding case) divided by the total number of dimuon events which passed the initial selection criteria and also the hadronic non-sliding cut. Similarly, the efficiency of the hadronic energy non-sliding cut was compared to that of the sliding energy cut and is shown on the right in Figure 5.5. In this case the electromagnetic non-sliding energy cut was first applied and the efficiency was defined in a similar manner to the electromagnetic cut above. The efficiency of applying both electromagnetic and hadronic energy cuts simultaneously was compared for sliding and non-sliding cuts and is shown in Figure 5.6. Here, the efficiency (sliding/non-sliding) was defined as the number of dimuon events for which both muons passed the electromagnetic and hadronic energy cut (sliding/non-sliding) divided by the total number of dimuon events which passed the initial selection criteria.

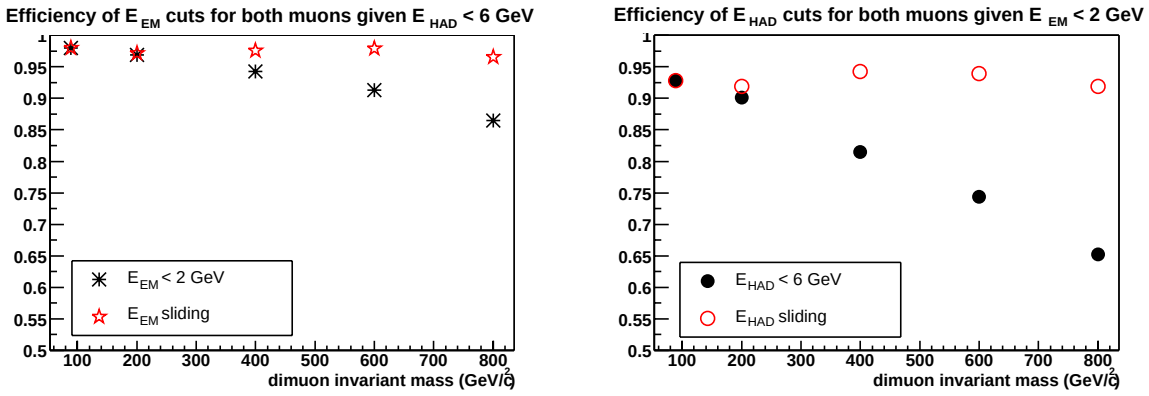

Figure 5.5: Comparison of efficiency of sliding to non-sliding cut for electromagnetic (left) and hadronic energy (right) as a function of Z and Z' boson mass, for Monte Carlo data samples.

The non-sliding electromagnetic and the hadronic energy cuts became increasing inefficient as the dimuon invariant mass increased, as is indicated in Figure 5.5 by the falling eight-pointed star markers ($\ast$) and filled circle markers ($\bullet$) with increasing dimuon invariant mass respectively. The sliding cuts were more efficient for both the electromagnetic and the hadronic energy, also illustrated in Figure 5.5, on the left and right respectively. In addition, the non-sliding hadronic energy cut was more inefficient at higher dimuon masses than the electromagnetic cut (as can be seen by comparing the left and right plots in Figure 5.5). The efficiency for both electromagnetic

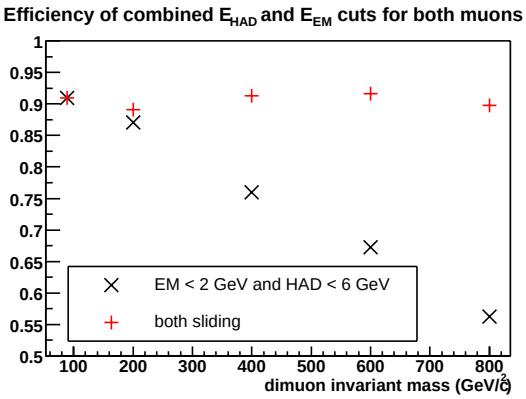

Figure 5.6: Comparison of efficiency of sliding to non-sliding cut for both the electromagnetic and hadronic energy cuts applied simultaneously, as a function of Z and Z' boson mass, for Monte Carlo data samples.

and hadronic sliding cuts (+) compared to both non-sliding cuts (×) is shown in Figure 5.6. From this it can be concluded that the combined sliding cuts were more efficient than the combined non-sliding cuts, particularly for large dimuon invariant masses. The combined sliding cut remained over 89 % efficient for a dimuon invariant mass of up to 800 GeV/c^2, whereas the non-sliding cut efficiency dropped to 56 % at this invariant mass. The sliding energy cuts not only had an increased efficiency, but they had an efficiency which was energy-independent (by choice of the form of the cuts), therefore, sliding energy cuts were used in the analysis.

5.2 Momentum dependent calorimeter isolation

Muons from Z' bosons and from graviton decays are expected to be isolated. This property can be used to remove background from other physics processes which produce jets and leptons from heavy flavours (b/c quarks) (QCD background). In such processes the associated muons have other particles nearby. An isolation cut was used which limited the amount of transverse energy in a cone of calorimeter towers surrounding the muon tower, and is defined on page 85. However, final state quantum electrodynamic radiation increases as a function of the lepton energy in the dilepton centre of momentum frame, therefore at high dimuon invariant mass a non-sliding isolation cut would become less efficient. Consequently, a sliding isolation cut was

used [77]. For a dimuon invariant mass less than 110 GeV/c^2 the isolation variable was required to be less than 4 GeV, and above a dimuon invariant mass of 110 GeV/c^2 a sliding isolation cut, $I_{0.4} < 0.1 \times p_T$, was used. Identical cuts were used in the Run 1 measurement of the Z^0 and Drell-Yan dimuon cross-section [76].

To compare the dependence of the calorimeter isolation on the transverse momentum, two Monte Carlo samples each consisting of 1000 events were generated with the FakeEvent program, one with a momentum of 50 GeV/c and the other 400 GeV/c. The muons were specified to have $|\eta| < 0.7$. The simulation and reconstruction were performed as outlined in Section 4.3. Figure 5.7 shows the calorimeter isolation for the two samples. The mean calorimeter energy deposited by the muons with momenta of 400 GeV/c was 0.27 ± 0.35, compared with 0.14 ± 0.07 GeV for the 50 GeV/c momenta muon sample. The Monte Carlo samples therefore confirmed that higher momentum muons, on average, deposit more energy in the calorimeters than lower energy muons.

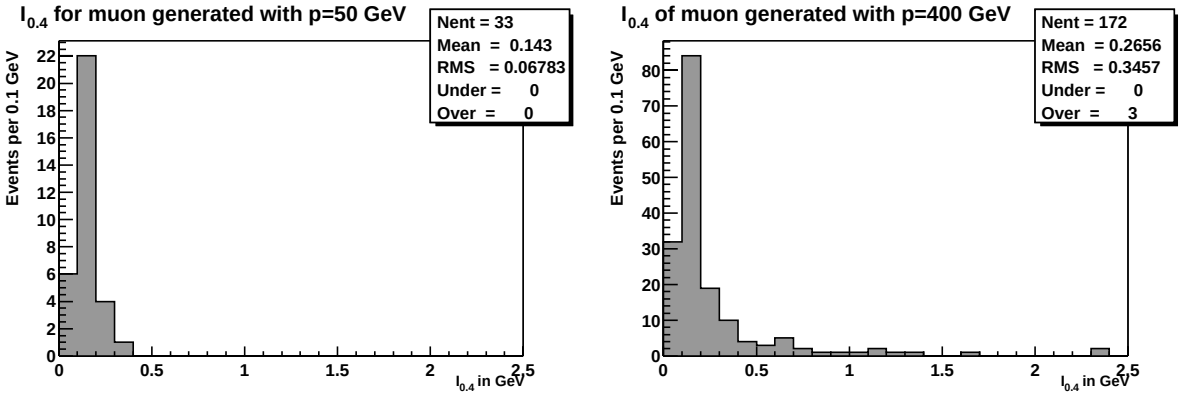

Figure 5.7: Histograms showing the calorimeter isolation for Monte Carlo muons generated with momenta of 50 GeV (left) and 400 GeV (right).

Chapter 6: Cosmic ray rejection

Cosmic rays are the dominant source of background in high energy dimuon searches. Before the application of cosmic ray cuts the dimuon data sample was dominated by cosmic rays (as can be seen by comparing the invariant mass distribution with and without the cosmic ray cuts, shown in Figure 7.1 and Figure 7.3 respectively, in Chapter 7). Cosmic rays have distinctive properties, which can be identified and exploited to remove them. Section 6.1, outlines the cosmic ray cuts placed in the analysis and Section 6.2 describes how the positions of the timing selection criteria were chosen.

6.1 Cosmic ray characteristic properties

The characteristic properties which can be used to identify cosmic rays in dimuon events and the cuts imposed in the analysis are summarised below.

1 A cosmic ray passes from the upper half of the detector to the lower, whereas a dimuon from a $p\bar{p}$ collision originates from the interaction point. Therefore, the time difference between the muon recorded in the upper and the muon in the lower half of the detector (T_{upper} - T_{lower}) can be used to distinguish these scenarios. If L_1 and L_2 are the distances traversed by the cosmic ray in the upper and the lower half of the detector, then $L_1 \approx L_2$. The time difference for the cosmic ray is:

$$\begin{aligned} \Delta_T &= T_{upper} - T_{lower} \\ &= (L_1 + L_2)/c \\ &\approx 2L_1/c \approx 2L_2/c. \end{aligned}$$

This can be compared to the time difference of two muons originating from the centre of the detector which is approximately zero (this is exactly zero if the interaction point

occurs at the origin of the detector and the timing detectors are exactly aligned, because in this case $L_1 \equiv L_2$):

$$\begin{aligned} \Delta_T &= T_{upper} - T_{lower} \\ &= (L_1 - L_2)/c \\ &\approx 0. \end{aligned}$$

The muon times can be measured by the Time-of-Flight (ToF) detector or by the hadron TDCs. The selection of the timing cuts imposed and the specific cuts which were applied are described in Section 6.2.1 for the ToF and in Section 6.2.2 for the hadron TDCs.

2 In addition, cosmic rays do not necessarily pass through the interaction point, or near the beam line. Therefore, they can be rejected by requiring the muons to have passed close to the interaction point, by placing a cut on the two-dimensional impact parameter of the muon corrected for the measured position of the beam ($|d_0^{corr}|$). The cut imposed depended on whether the muon track had silicon hits in addition to COT hits. If the track had silicon hits then the cut $|d_0^{corr}(SVX)| < 0.02$ cm was applied. If the track had no silicon hits then a cut of $|d_0^{corr}(COT)| < 0.15$ cm was imposed. A narrower cut was placed on the track if it had silicon information, because the silicon vertex detector has a better resolution than the central drift chamber (47.7 ± 0.8 μm compared to 380 ± 30 μm).

3 In some cosmic ray events, one side of the track is not reconstructed, because the cosmic ray passes through the detector out-of-time with the beam crossing events. Consequently, the cosmic ray appears as a single track. In such cases, these cosmic ray tracks are usually displaced in the z-direction from the tracks produced by the $p\bar{p}$ interactions. Therefore, if there is also an interaction muon in the event, a restriction on the quantity $|z_0^{\mu 1} - z_0^{\mu 2}|$, where $z_0^{\mu 1}$ and $z_0^{\mu 2}$ are the z intercepts of the muons' tracks with the detector axis, reduces backgrounds from cosmic rays and from fake tracks. This cut ensures that the muons came from the same vertex, as they should if they come from the decay of a single particle. If

both legs of a cosmic ray are reconstructed then this cut does not reject the event, since in this case the two muon tracks also have the same z intersection with the detector axis. In the analysis a cut of $|z_0^{\mu 1} - z_0^{\mu 2}| < 4$ cm was applied[1].

4 Typically there are very few other tracks in a cosmic ray event. Also cosmic rays are in general displaced from the vertex of the tracks from the $p\bar{p}$ collision. Therefore the displacement of the two muons in the z direction from the z position of the vertex constructed from all the other nearby tracks, excluding the dimuon tracks, can be used to identify cosmic rays. This cut was applied in imposed in two stages. First a seed z position (${z_0}^{\mu\mu}$) was calculated, which was the average of the two muons' intersection with the detector z axis: $\frac{1}{2}({z_0}^{\mu 1} + {z_0}^{\mu 2})$. Then a seeded vertex algorithm was used in which a window of $\pm$ 10 cm was opened around the seed z position and the weighted average of z_0 of all other tracks inside this window was computed. If there were no tracks in this window, then no vertex was reconstructed and the event was rejected as a cosmic ray. Secondly, if there was at least one track found in the 10 cm window around the seed z position, then the separation, in the z direction, of the dimuon from the mean vertex ($|\Delta z| = |{z_0}^{\mu\mu} - z_{vtx'}|$) was required to be less than 3 cm, otherwise the event was rejected as a cosmic ray event [78].

5 Cosmic rays muon tracks are spatially back-to-back in both η and ϕ, since they come from a single track, so a cut which rejects dimuons which are back-to-back can be used to exclude these events. However, the muons produced in the decay of very high mass Z' bosons and gravitons are also back-to-back. Therefore, a back-to-back cut would remove signal in addition to background dimuons. Consequently, in this analysis, a back-to-back cut was not applied. (The efficiency of the back-to-back cut used in the Run I Z' dimuon search [75] was investigated as a function of the Z' mass and the results are summarised in Appendix C.1.)

[1] The z_0 resolution of the COT ($\sigma_{z_0}^{COT}$) is 4.1 $\pm$ 0.07 mm for tracks with $p_T > 20$ GeV/c and the resolution of the SVX ($\sigma_{z_0}^{SVX}$) is 2.04 $\pm$ 0.08 mm.

The cosmic ray selection criteria used in the analysis were grouped into two sets; track cuts and timing cuts. The former was composed of the cuts 2, 3 and 4 listed above. The timing cuts and their selection are described in Section 6.2.

6.2 Selection of cosmic ray timing cut positions

In dimuon events the difference in timing between the upper and lower muon ($\Delta_T = T_{upper}$ - T_{lower}) can be used to distinguish cosmic ray events from interaction dimuon events, as described in Section 6.1. Both the Time-of-Flight (ToF) detector and the hadron time-to-digital-converters (TDCs) provide timing information for muons. Unfortunately they were not 100 % efficient, and therefore not every muon had timing information associated with it. Consequently, in some events only one or neither of the muons had time information. In this case the time difference of the muons could not be used to identify cosmic ray events. However, the individual muon timing can also be used to discriminate between muons which are from cosmic rays and those from interaction events. Muons from interactions originate from the centre of the detector at the time of the interaction, therefore the time recorded by the timing detectors is the time taken for the muon to travel out to the timing detector. This time is determined by the speed of the muon and the radius of the timing detector. Cosmic rays, however, are not associated with the interaction, therefore they often pass through the detector out-of-time with a beam crossing, and they do not originate from the centre of the detector. Therefore the spread in times recorded for cosmic ray muons is typically much larger than that from interaction muons. Also the timing distributions for the upper and lower interaction muons are expected to be similar, since a muon from the centre of the detector travels an equal distance to both the upper and lower half of the timing detectors. In contrast, cosmic ray muons pass through the detector and so the upper time recorded is expected to be less than the lower time. Therefore, in this case, the upper and lower time distributions are expected to be different. Consequently, the upper and lower time distributions, as well as the time difference, can be used to distinguish cosmic ray from

interaction dimuon events.

To determine the position of the time cuts to be imposed in order to reject cosmic rays, but keep interaction muons, first, the characteristic cosmic ray and interaction muon times as recorded by the Time-of-Flight detector (ToF) and by the hadron TDCs were ascertained. Cosmic ray and Z data samples were used to compare their timing distributions.

The position of the timing cuts for the ToF and the hadron TDC timing cuts were chosen by studying the distribution of the quantity signal^2/background against signal efficiency for various cuts, where "signal" was the number of signal events within the selected cut range and by analogy "background" was the number of background events within this range. The efficiency for a specific cut was defined to be number of signal events within the cut range divided by the total number of signal events. The ratio of these quantities, signal^2/background (s^2/b), was chosen as the measure of significance of each chosen cut, because statistically the number of signal events increases linearly with the size of the data set, whereas the background increases as the square root of this number. Signal and background samples were chosen, several cut ranges selected and s^2/b vs efficiency plotted for each cut range.

To chose the cut, the cut which had the maximum s^2/b ratio was identified. Widening this cut range increased the signal efficiency of the cut (except when all the signal events were contained, in which case the efficiency remained 100 %), but decreased the ratio of s^2/b, since the background also increased (more rapidly than the signal^2). Because the signal samples were small the statistical errors on the s^2/b ratios[2] were very large. The cut which had the maximum s^2/b ratio often had a low signal efficiency and therefore would have removed a large fraction of the signal events had it been applied. Consequently, when selecting the cut, a balance between the maximum s^2/b ratio and the efficiency of the cut was reviewed.

In the cases where there was a cut which was 100 % efficient with a large enough s^2/b ratio that it lay within the statistical error of the cut with the maximum s^2/b ratio, then this 100 %

[2]The error on the s^2/b ratio is derived in Appendix C.2.

efficient cut was chosen. In the alternative scenario, where the 100 % efficient cut had a s^2/b ratio that lay below the statistical error of the cut with the maximum s^2/b ratio, then the cut chosen was the one which optimised both s^2/b and efficiency simultaneously, and had a s^2/b ratio that lay within the statistical error of the cut with the maximum s^2/b ratio (see the upper hadron TDC cut selection, page 118 in Section 6.2.2).

6.2.1 Selection of the position of the Time-of-Flight cuts

To determine Time-of-Flight (ToF) signal properties a Zee dielectron data sample was used and a cosmic dimuon ray sample to obtain the background characteristic times. The Zee sample was cosmic free, and so represented a pure signal sample. Since the Zee sample was very small, the result was confirmed using a Zmm dimuon data sample (CMU/CMP/CMX combinations).

The Zee signal sample analysed is defined in Section 4.2 and the Zmm (CMU/ CMP/CMX combinations) selection used is described in Section 4.1.5. The cosmic ray data set originated from the dimuon data set. The selection criteria imposed were the same as those applied to the CMUP-CMUP dimuon analysis data sample, outlined in Section 4.1.3; however, rather than rejecting events which failed the cosmic ray cuts, instead, these events were retained. In this case the cosmic ray cuts consisted of the cosmic ray track cuts OR'ed with a hadron TDC time difference cut of less than -12 ns. Consequently, to be included in the cosmic ray sample then either the time difference of the two muons was less than -12 ns or the event failed one of the cosmic ray track cuts (*i.e.* the difference ($z_0^{\mu 1}$ - $z_0^{\mu 2}$) or the impact parameter (d_0^{corr}) was large, or there were no other tracks near the dimuon tracks). In order to study the ToF timing distributions no ToF timing cuts were applied.

The ToF timing distributions are shown as follows: upper and lower are shown on the left and right of Figure 6.1 for the Zee sample, Figure 6.2 for the Zmm and Figure 6.3 for the cosmic ray sample. The time difference distributions ($\Delta\ ToFtime_{Upper-Lower}$) are shown in Figure 6.4 for the Zee, Figure 6.5 for the Zmm and Figure 6.6 for the cosmic ray sample. Of the 79 dielectron

events, 38 had timing information for the upper leg, 42 for the lower and 18 events had ToF timing information for both electrons. The Zmm dimuon sample contained 69 events of which 30 events had timing information for both muons, 48 for the upper and 42 for the lower muon.

Selection of the ToF upper and lower timing cuts

The ToF upper and lower cuts were two-sided, with a minimum and maximum. The minimum of the cut was set to be 0.0 to 5.0 ns and incremented in 0.5 ns steps and the maximum cut ranged from 5.5 to 11.0 ns, also incremented in 0.5 ns steps for each minimum cut position. The number of signal events, number of background events, the ratio of s^2/b, the signal efficiency and the errors for each cut range were calculated and are displayed in Appendix C.3. Signal^2/background vs cut efficiency was plotted for each cut. The ToF upper, lower and time difference cuts were selected using the criteria described on page 107. The chosen cuts are summarised in Table 6.3. More details of the selection of the upper, lower and time difference ToF cut follow.

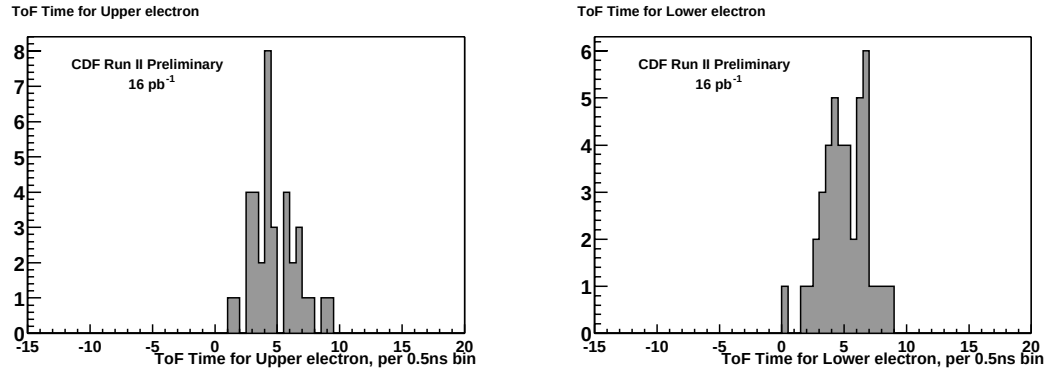

Figure 6.1: Time-of-Flight time distribution for upper and lower electrons from the Zee dielectron data sample (10.4 pb^{-1}), shown on the left and right respectively. The times lie within the range from 0 to 10 ns.

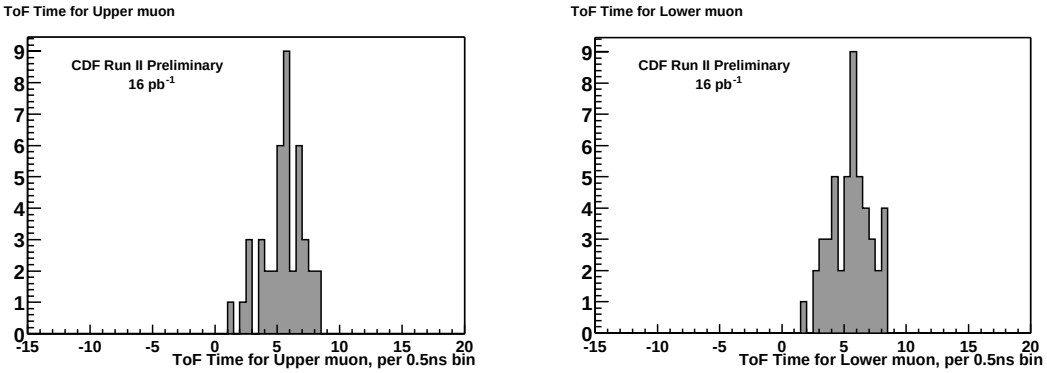

Figure 6.2: Time-of-Flight time distribution for upper and lower muons for the Zmm dimuon data sample (16.5 pb^{-1}), shown on the left and right respectively. The times lie within the range from 0 to 10 ns.

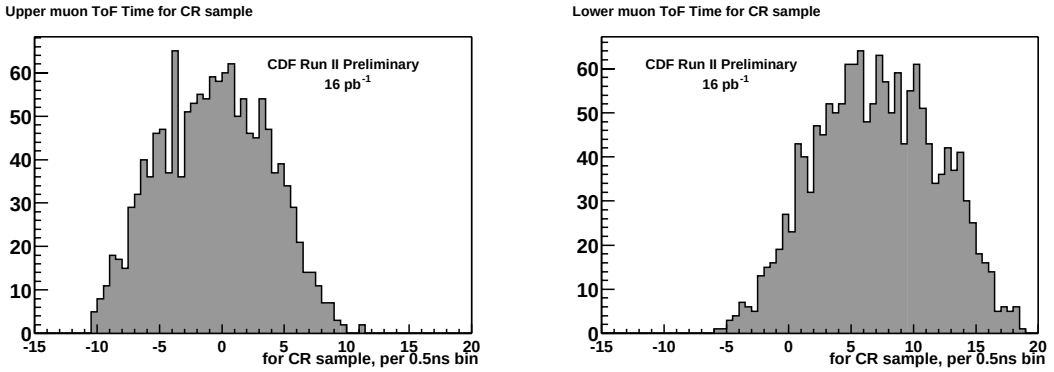

Figure 6.3: Time-of-Flight time distribution for upper and lower muons for a cosmic ray data sample (16.5 pb^{-1}), shown on the left and right respectively. The cosmic ray upper and lower timing distributions are asymmetric and have a much wider range than that of the Zmm muons and Zee dielectrons, which was from 0 to 10 ns. The Time-of-Flight difference can therefore be used to discriminate between interaction muons and cosmic rays.

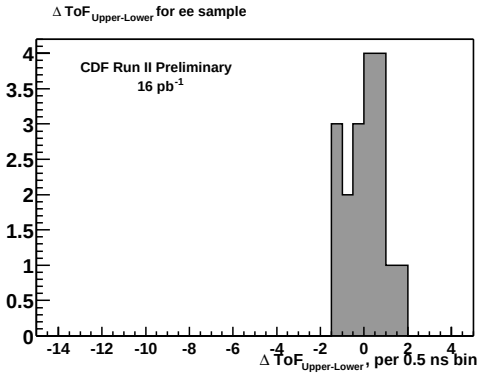

Figure 6.4: Time-of-Flight time difference (upper-lower) distribution for the Zee dielectron data sample (10.4 pb^{-1}). The time differences peak around zero and all lie above -2 ns.

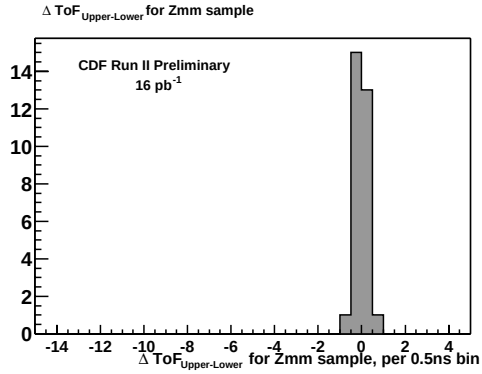

Figure 6.5: Time-of-Flight time difference (upper-lower) distribution for Zmm dimuon data sample (16.5 pb^{-1}). The time differences peak around zero and all lie above -2 ns.

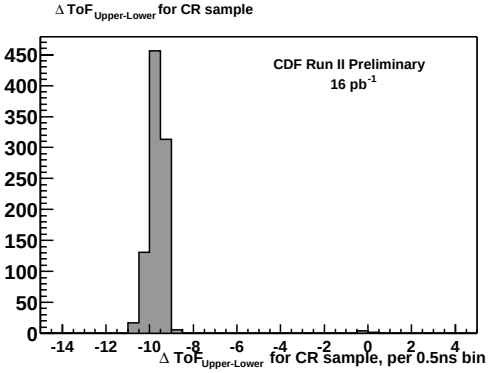

Figure 6.6: Time-of-Flight time difference (upper-lower) distribution for the cosmic ray data sample (16.5 pb^{-1}). The time differences peak around -9.5 ns, which is in contrast to the peak around zero for both the Zee and Zmm sample. Consequently the Time-of-Flight time difference can provide excellent discrimination between interaction muons and cosmic rays. A few events are clustered around zero; these indicate an impurity in the cosmic ray sample.

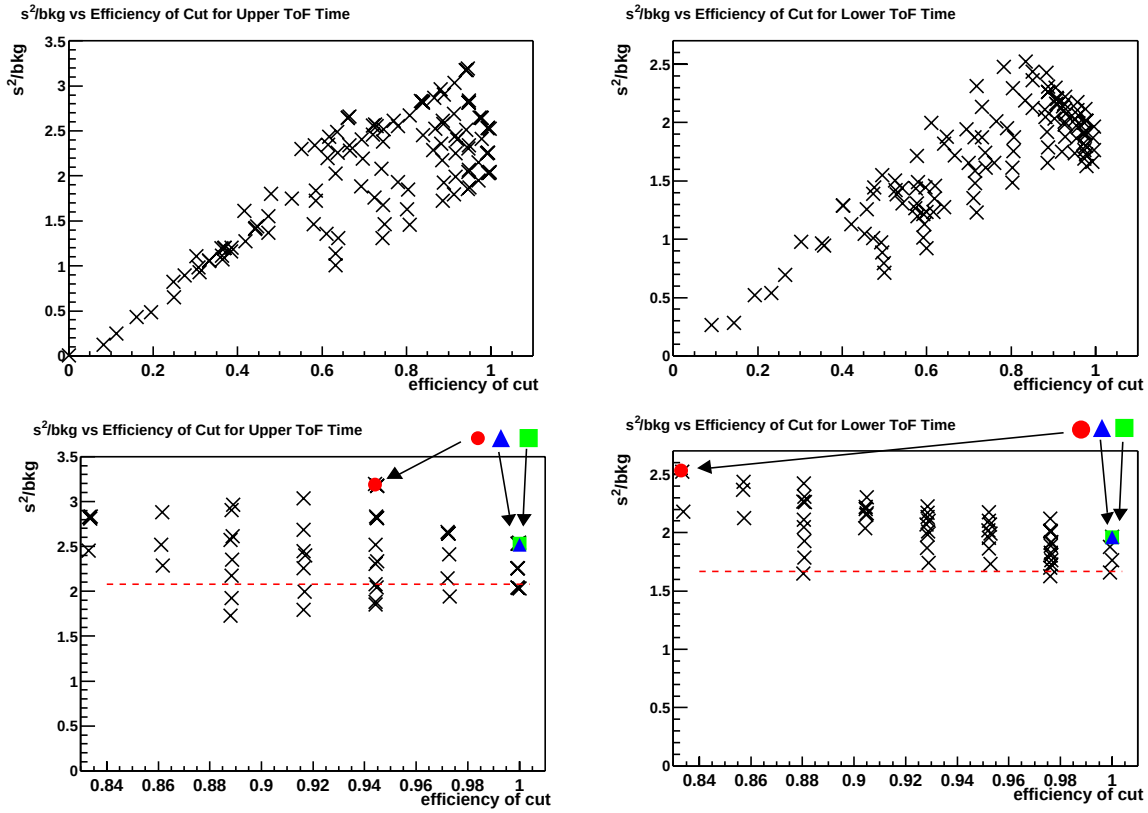

Figure 6.7: Signal^2/background vs efficiency for various Time-of-Flight (ToF) timing cuts for upper ToF timing (left) and lower ToF timing (right). The signal was from the Zee dielectron data sample (10.4 pb^{-1}) and background from a cosmic ray data sample. The upper plots show all the cuts and lower plots show cuts which are greater than 83 % efficient. The position of the highlighted markers for the upper and lower muon time cuts are displayed in Table 6.1 and Table 6.2 respectively.

The upper two plots in Figure 6.7 show s^2/b against efficiency for each cut, for the upper ToF time (left) and the lower ToF time (right). The lower plots are for the cuts which were greater than 83 % efficient. Table 6.1 and Table 6.2 summarise the results for both the electron and muon signal samples and respectively show the ToF upper and lower time cuts which had the maximum s^2/b ratio, maximum s^2/b ratio which were 100 % efficient and the chosen cuts which had the maximum s^2/b ratio which were 100 % efficient and were 9 ns wide. These cuts are highlighted in Figure 6.7 by the circle, square and triangle markers respectively. Also, the lower bound of the statistical error of the maximum s^2/b ratio cut is indicated in this figure by the horizontal dashed line.

Sample	Cut (ns)	s^2/b	Efficiency (%)	Cut width (ns)
Maximum s^2/b cut *(circle)*				
Zee	$2.5 \leq ToF_{Upper} \leq 9.5$	3.19 ± 1.11	94	7.0
Zmm	$3.5 \leq ToF_{Upper} \leq 8.5$	0.40 ± 0.13	88	5.0
Maximum s^2/b 100 % efficient cut *(square)*				
Zee	$1.0 \leq ToF_{Upper} \leq 9.5$	2.53 ± 0.85	100	8.5
Zmm	$1.0 \leq ToF_{Upper} \leq 8.5$	0.38 ± 0.12	100	7.5
Maximum s^2/b 100 % efficient cut with width 9.0 ns *(triangle)*				
Zee	$1.0 \leq ToF_{Upper} \leq 10.0$	2.52 ± 0.85	100	9.0
Zmm	$1.0 \leq ToF_{Upper} \leq 10.0$	0.35 ± 0.11	100	9.0

Table 6.1: Time-of-Flight (ToF) upper time cuts which had the maximum signal^2/background ratio (s^2/b), maximum s^2/b ratio which were 100 % efficient and maximum s^2/b ratio which were 100 % efficient and 9 ns wide. The signal was from the Zee dielectron data sample (10.4 pb^{-1}) and Zmm dimuon data sample (16.5 pb^{-1}) and background from a cosmic ray data sample. The *italics* refer to the Zee sample cuts indicated in the lower left plot of Figure 6.7.

Sample	Cut (ns)	s^2/b	Efficiency (%)	Cut width (ns)
Maximum s^2/b cut *(circle)*				
Zee	$2.5 \leq ToF_{Lower} \leq 7$	2.53 ± 0.86	83	4.5
Zmm	$2.5 \leq ToF_{Lower} \leq 8.5$	0.54 ± 0.16	98	6.0
Maximum s^2/b 100 % efficient cut *(square)*				
Zee	$0.0 \leq ToF_{Lower} \leq 9.0$	1.96 ± 0.61	100	9.0
Zmm	$1.5 \leq ToF_{Lower} \leq 8.5$	0.50 ± 0.50	100	7.0
Maximum s^2/b 100 % efficient cut with width 9.0 ns *(triangle)*				
Zee	$0.0 \leq ToF_{Lower} \leq 9.0$	1.96 ± 0.61	100	9.0
Zmm	$0.0 \leq ToF_{Lower} \leq 9.0$	0.40 ± 0.12	100	9.0

Table 6.2: Time-of-Flight (ToF) lower time cuts which had the maximum signal^2/background ratio (s^2/b), maximum s^2/b ratio which were 100 % efficient and maximum s^2/b ratio which were 100 % efficient and 9 ns wide. The signal was from the Zee dielectron data sample (10.4 pb^{-1}) and Zmm dimuon data sample (16.5 pb^{-1}) and background from a cosmic ray data sample. The *italics* refer to the Zee sample cuts indicated in the lower right plot of Figure 6.7.

For the dielectron sample, the cuts with the highest s^2/b ratio (s^2/b) which were 100 % for both the upper and the lower muon timing cut lay within the lower statistical error of the respective cuts which had the maximum s^2/b (as is illustrated in Figure 6.7 by the square markers, lying above the dashed lines). The maximum s^2/b ratio cuts only had an efficiency of 94 % and 83 % respectively. The maximum s^2/b ratio cuts which were 100 % efficient were 1.0 $\leq ToF_{Upper} \leq$ 9.5 ns for the upper muon timing and 0.0 $\leq ToF_{Lower} \leq$ 9.0 ns for the lower. This upper cut was 8.5 ns wide, whereas the lower was 9 ns wide. For consistency, the upper cut was widened to be 9.0 ns also. This wider cut, 1.0 $\leq ToF_{Upper} \leq$ 10.0 ns, had a s^2/b ratio, which,

to one decimal place, was identical to the narrower 8.5 ns cut (2.52 $\pm$ 0.85 compared to 2.53 $\pm$ 0.85, shown in Table 6.1). The two 9.0 ns cuts were selected, as high-lighted by triangles in Figure 6.7. The cuts were asymmetric because the background distributions were asymmetric, as illustrated in Figure 6.3.

Since the Zee sample was small, the same procedure was repeated with an independent Zmm sample (there were no common events). The results found with the two samples were consistent with each other and both samples gave the same final cuts; $1 \leq ToF_{Upper} \leq 10$ ns and $0 \leq ToF_{Lower} \leq 9$ ns, as displayed in Table 6.1 and Table 6.2.

Selection of the ToF time difference cut

Figure 6.4 and Figure 6.6 respectively show the Zee signal and cosmic ray background ToF time difference distributions. In this case, there was a very clear distinction between the signal and background distributions. The cosmic ray background peaked around -9.5 ns in contrast to the signal, which peaked around 0 and had no events below -2 ns. Therefore, a ratio of signal to background method was not needed to select the ToF time difference cut. The cosmic ray ToF difference plot shows some impurity in the sample, since there were some entries around 0, which indicated that the cosmic ray selection criteria identified some non-cosmic ray dimuons as cosmic rays. A cut could have been placed anywhere between -2 ns and -8 ns to remove all of the cosmic ray background, except the few mis-tagged events near 0, shown in Figure 6.6, and keep all of the signal events. The position of the cut was chosen to be in the centre of this range at $\Delta ToF_{Upper-Lower} \geq$ -5 ns. This cut had a signal efficiency of 100 %. This cut was also 100 % efficient for the Zmm signal sample, as can be seen from the Zmm signal ToF time difference distribution displayed in Figure 6.5.

Summary of the selected ToF timing cuts

The ToF timing cuts selected were 100 % efficient for the Zee and the Zmm signal samples studied and are summarised in Table 6.3.

ToF timing selection criteria
$\Delta ToF_{Upper-Lower} \geq$ -5 ns
$1 \leq ToF_{Upper} \leq 10$ ns
$0 \leq ToF_{Lower} \leq 9$ ns

Table 6.3: Summary of the Time-of-Flight (ToF) time selection criteria applied in the analysis.

6.2.2 Selection of the position of the TDC timing cuts

The hadron TDC cuts were chosen in a similar way to the ToF cuts, by finding the maximum s^2/b ratio and then considering the efficiency of the cut and the statistical error on this ratio, as described on page 107. In this case the signal data sample used was a Zmm dimuon data sample and a cosmic ray sample was used for the background sample.

The signal Zmm dimuon data sample was selected from the dimuon data set described in Section 4.1. Both muons were required to pass the muon identification selection criteria in Table 4.3 and the cosmic ray track cuts explained in Section 6.1.

In addition, the following ToF cuts were applied:

- if both muons had ToF timing then $\Delta ToF_{Upper-Lower} \geq$ -5 ns.
- if only the upper muon had ToF timing information $1 \leq ToF_{Upper} \leq 10$ ns.
- if only the lower muon had ToF timing information $0 \leq ToF_{Lower} \leq 9$ ns.

Also the dimuon events were selected to have charges of the opposite sign and be in the invariant mass range from 80 to 100 GeV/c^2, shown in Figure 6.8. This sample contained 69 events.

The cosmic ray background sample was also selected from the stripped dimuon data set. Both muons were required to pass the muon identification cuts in Table 4.3 and the event was identified as a cosmic ray by the cosmic ray track cuts (described in Section 6.1). In addition,

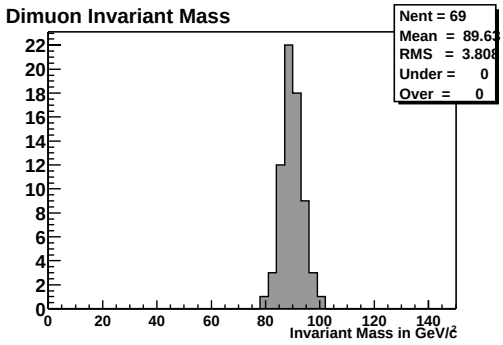

Figure 6.8: Zmm dimuon 'signal' data sample invariant mass distribution (16.5 pb^{-1}) used to select the hadron TDC timing cuts. This sample was selected to have an invariant mass between 80 to 100 GeV/c^2.

the event had to fail the applicable ToF timing cut (for upper, lower or both muons with information).

The TDC upper, lower and time difference timing cuts selected are summarised in Table 6.7. More details of the selection of the upper, lower and difference hadron TDC time cuts are given in the following sections.

Selection of upper and lower hadron TDC timing cuts

For the hadron TDC upper and lower timing cuts the minimum range of the cut was set to be from -11 to 0 ns, incremented in ns steps and the maximum cut range was from 0 to 10 ns in ns increments. The results are tabled in Appendix C.4. The hadron TDC upper and lower distributions for the Zmm dimuon signal and cosmic ray background sample are shown in Figure 6.9 and Figure 6.10 respectively.

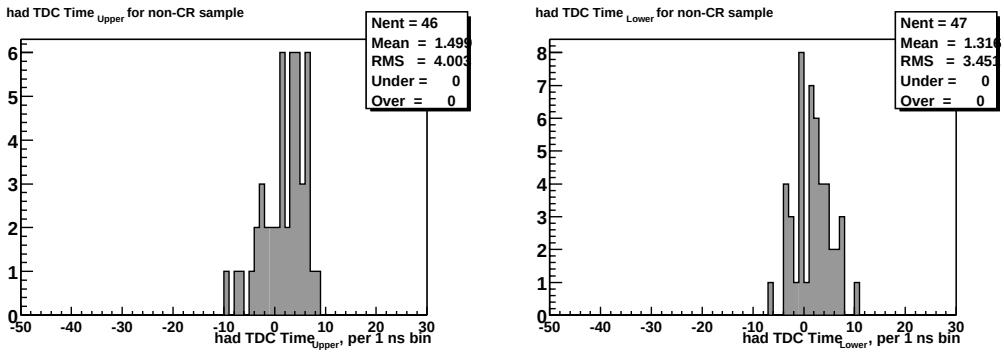

Figure 6.9: Hadron TDC time distribution for upper (left) and lower (right) muon for Zmm dimuon data sample (16.5 pb^{-1}). The times for both the upper and lower muon lie within the range from -10 to 11 ns.

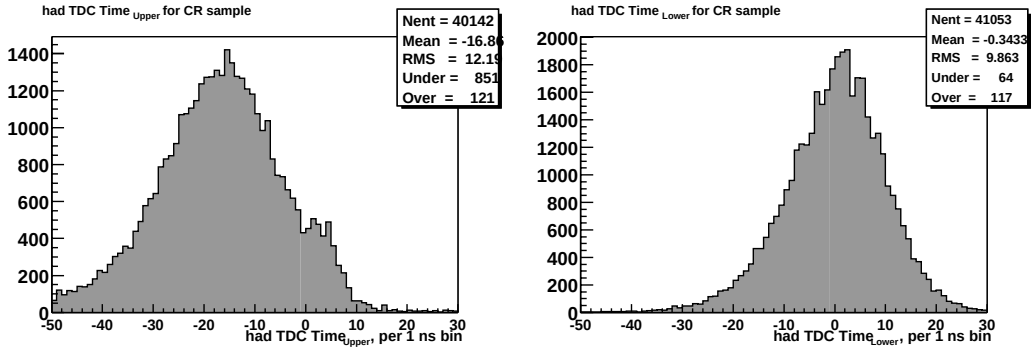

Figure 6.10: Hadron TDC time distribution for upper (left) and lower (right) muon for cosmic ray data sample (16.5 pb^{-1}). The cosmic ray upper and lower time distributions are asymmetric. The distributions have a large range, and many muons lie outside the range (-10 to 11 ns) of the Zmm dimuon data sample.

The s^2/b ratio vs efficiency plots for the upper and lower cuts are shown in the Figure 6.11 and Figure 6.12 respectively. Table 6.4 and Table 6.5 show the hadron TDC upper and lower cuts respectively, which had the maximum s^2/b ratio, maximum s^2/b ratio which were 100 % efficient and the chosen cut.

Selection of the hadron TDC upper timing cut

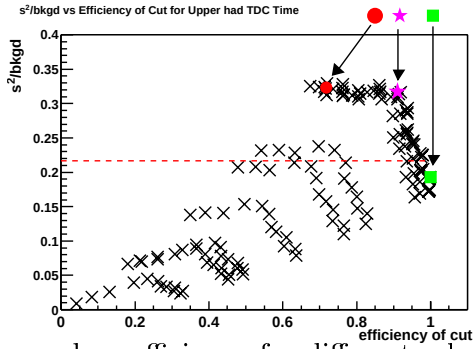

Figure 6.11: Signal^2/background vs efficiency for different selected cuts for the upper hadron TDC time. The signal was from the Zmm dimuon data sample (16.5 pb^{-1}) and background was a cosmic ray data sample. The position of the highlighted markers are displayed in Table 6.4.

Sample	Cut (ns)	s^2/b	Efficiency (%)
Maximum s^2/b cut *(circle)*			
Zmm	$0 \leq hadTDCTime_{Upper} \leq 9$	0.33 ± 0.11	72
Maximum s^2/b 100 % efficient cut *(square)*			
Zmm	-10 $\leq hadTDCTime_{Upper} \leq 9$	0.19 ± 0.06	100
Chosen cut, within statistical error of maximum s^2/b cut *(star)*			
Zmm	-4 $\leq hadTDCTime_{Upper} \leq 9$	0.32 ± 0.10	91

Table 6.4: Hadron TDC upper time cuts which had the maximum signal^2/background ratio (s^2/b), maximum s^2/b ratio which were 100 % efficient and the chosen cut. The signal was from a Zmm data sample (16.5 pb^{-1}) and the background from a cosmic ray data sample. The *italics* refer to Figure 6.11.

The upper muon hadron TDC time (hadTDCTime$_{Upper}$ cut, which was 100 % efficient and had the maximum s^2/b ratio, had a ratio (0.19 ± 0.06), which was less than the lower error on the maximum s^2/b ratio cut (0.32 ± 0.10). This is indicated in Figure 6.11 by the square marker lying below the dashed horizontal line. Unfortunately, the maximum s^2/b ratio cut had an efficiency of only 72 ± 7 %. However, the s^2/b vs efficiency distribution had a knee shape; with cuts rising in both s^2/b and efficiency up to a turn over point and then falling away again, as illustrated in Figure 6.11. The turn over of the curve occured for the cut -4 $\leq$ hadTDCTime$_{Upper}$ $\leq$ 9 ns, which had an efficiency of 91 ± 4 % (indicated by a star in Figure 6.11), and the s^2/b ratio of this cut lay within the lower error of the cut which had the maximum s^2/b ratio. (To one decimal place the s^2/b ratio was identical to that which had the maximum s^2/b; 0.33 compared to 0.32). Therefore, this cut, which optimised both the s^2/b ratio and the efficiency, was chosen.

Selection of the hadron TDC lower timing cut

The s^2/b vs efficiency curve for the lower muon TDC time (hadTDCTime$_{Lower}$) is shown in Figure 6.12. In this case, the cut with the maximum s^2/b ratio which was 100 % efficient lay within the error of the cut with the maximum s^2/b ratio. Therefore this cut of -7 $\leq$ hadTDCTime$_{Lower}$ $\leq$ 11 ns was chosen. (It was noted that the maximum s^2/b ratio cut was also the one at "knee" of the curve which optimised s^2/b and efficiency simultaneously.)

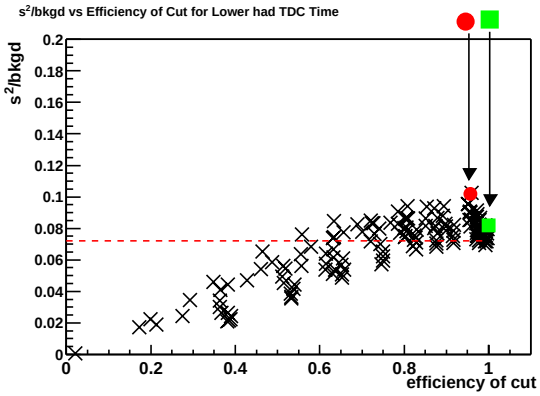

Figure 6.12: Signal^2/background vs efficiency for different selected cuts for the lower hadron TDC time. The signal was from the Zmm dimuon data sample (16.5 pb^{-1}) and background was a cosmic ray data sample. The position of the highlighted markers are displayed in Table 6.5.

Sample	Cut (ns)	s^2/b	Efficiency (%)
Maximum s^2/b cut *(circle)*			
Zmm	-4 $\leq$ $hadTDCTime_{Lower}$ $\leq$ 8	1.00 $\pm$ 0.03	96
Maximum s^2/b 100 % efficient cut / Chosen cut *(square)*			
Zmm	-7 $\leq$ $hadTDCTime_{Lower}$ $\leq$ 11	0.08 $\pm$ 0.02	100

Table 6.5: Hadron TDC lower time cuts which had the maximum signal^2/background ratio (s^2/b) and the maximum s^2/b ratio which was 100 % efficient, which was the chosen cut. The signal was from a Zmm data sample (16.5 pb^{-1}) and the background from a cosmic ray data sample. The *italics* refer to the right plot in Figure 6.12.

Selection of the hadron TDC time difference cut

Figure 6.13 and Figure 6.14 respectively show the Zmm dimuon signal and cosmic ray background hadron TDC time difference distributions. The hadron TDC time difference one-sided cut was selected from the s^2/b ratio and efficiency information for cuts from -11 to 0 ns incremented in 1 ns steps. Table 6.6 shows the hadron TDC time difference cut which had the maximum s^2/b ratio, maximum s^2/b ratio which were 100 % efficient and the cut at the turn over of the s^2/b vs efficiency distribution. These cuts are also high-lighted in Figure 6.15 by the circle, square and star marker respectively.

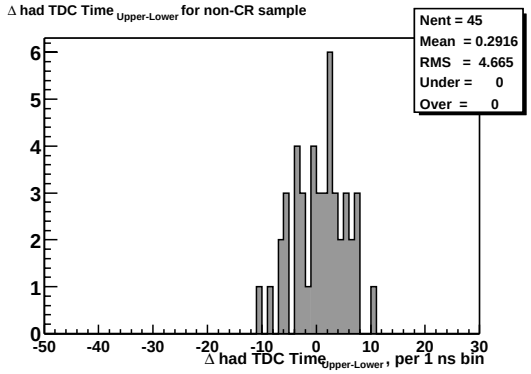

Figure 6.13: Hadron TDC time difference (upper-lower) distribution for the Zmm dimuon sample (16.5 pb^{-1}). The distribution peaks around zero and all the events lie above -11 ns.

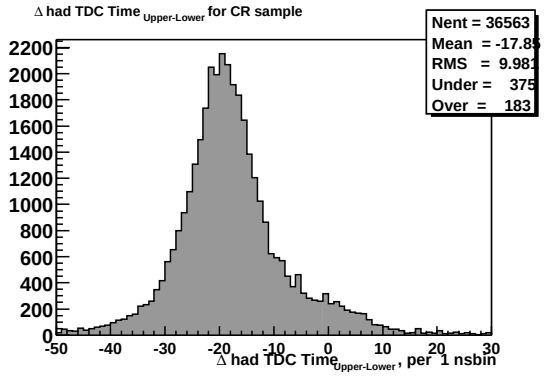

Figure 6.14: Hadron TDC time difference (upper-lower) distribution for the cosmic ray data sample (16.5 pb^{-1}). The distribution peaks around -21 ns and many events lie below -11 ns. The spread of the distribution is much larger than that from Zmm dimuons.

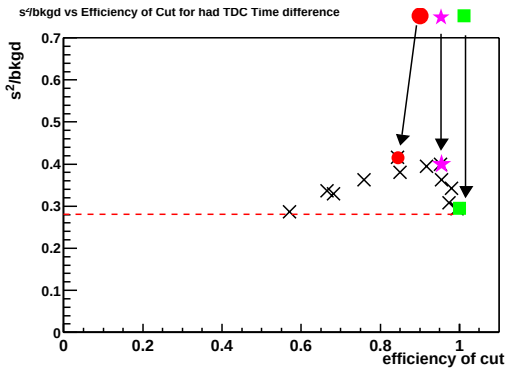

Figure 6.15: Signal^2/background vs efficiency for different selected cuts for the hadron TDC time difference cut, with a one-sided cut. The signal was from a Zmm data sample (16.5 pb^{-1}) and the background from a cosmic ray data sample. The cuts highlighted are summarised in Table 6.6.

Sample	Cut (ns)	s^2/b	Efficiency (%)
Maximum s^2/b cut *(circle)*			
Zmm	-4 $\leq hadTDCTime_{Upper-Lower}$	0.4 $\pm$ 0.1	84 $\pm$ 5
Maximum s^2/b 100 % efficient cut (Chosen cut) *(square)*			
Zmm	-11 $\leq hadTDCTime_{Upper-Lower}$	0.3 $\pm$ 0.1	100
Cut at distribution "knee" *(star)*			
Zmm	-7 $\leq hadTDCTime_{Upper-Lower}$	0.4 $\pm$ 0.1	96 $\pm$ 3

Table 6.6: Summary of the hadron TDC time difference cuts which had the maximum signal^2/background (s^2/b) ratio, maximum s^2/b ratio which was 100 % efficient and the cut position at the "knee" in the s^2/b vs efficiency distribution. The signal was from a Zmm data sample (16.5 pb^{-1}) and the background from a cosmic ray data sample. The *italics* refer to Figure 6.15.

The 100 % efficient cut with the highest s^2/b ratio lay within this statistical error of the maximum s^2/b ratio cut. This cut was therefore chosen and was -11 ns $\geq \Delta hadTDC_{Upper-Lower}$. For interest, the cut where the curve in Figure 6.15 seems to turn-over was -7 ns $\geq \Delta hadTDC_{Upper-Lower}$ and had an efficiency of 96 $\pm$ 3 % (high-lighted by the star in Figure 6.15). The chosen hadron TDC cuts are summarised in Table 6.7.

Summary of selected hadron TDC timing cuts

Hadron TDC timing selection criteria
$\Delta hadTDC_{Upper-Lower}$ $\geq$ -11 ns
-4 $\leq \Delta hadTDC_{Upper}$ $\leq$ 9 ns
-7 $\leq \Delta hadTDC_{Lower}$ $\leq$ 11 ns

Table 6.7: Summary of the chosen hadron TDC timing cuts.

6.2.3 Application of the timing cuts

The ToF time difference cut was found to be a very effective discriminator between signal and background events, because there was no overlap between the signal and pure background distributions. Therefore if a dimuon pair had ToF time information for both muons and the event passed the $\Delta ToF_{Upper-Lower} \geq$ -5 cut, then the dimuon event passed all the timing cuts (both ToF and hadron timing cuts). If both muons had timing information and the event failed the $\Delta ToF_{Upper-Lower} \geq$ -5 cut, then the event was rejected. If, however, only one of the muons had ToF timing information then the event was required to pass the individual ToF cut (upper or lower, which ever had timing information) and the relevant hadron TDC cut (upper, lower, both or pass if neither had hadron TDC timing information). If neither muon had ToF time, then the muons were only required to pass the applicable hadron TDC timing cuts. If both muons had neither ToF nor hadron TDC timing, then the event was not rejected.

Ideally, a more sophisticated optimisation of the timing cuts would have been performed, in which a combination of all the cosmic ray cuts, both tracking and timing, would have been optimised simultaneously. However, the limited statistics available made this unfeasible and made such a complex optimisation process futile.

Chapter 7: Dimuon data sample after analysis cuts

7.1 Effect of the selection criteria

The number of dimuons in the dimuon data sample after the cumulative application of the initial selection criteria (trigger, kinematic and fiducial), defined in Table 4.3, to the dimuon data sample, which is described in Section 4.1.2, are displayed in Table 7.1. 4466 dimuons remained in the sample after these initial cuts. Following the application of all the selection criteria, the final dimuon analysis sample consisted of 77 dimuons. The dimuon invariant mass distribution of these events is displayed in Figure 7.1 (a log plot is shown on the right). The highest dimuon invariant mass observed was 116 GeV/c^2. Of these events, 59 were in the Z peak region with an invariant mass between 80 and 100 GeV/c^2, as shown in Figure 7.2. The dimuon data was compared to the expected background from Standard Model processes, and this is illustrated in Figure 11.4 in Chapter 11.

Selection criteria applied to dimuon data sample	Number of dimuons remaining in sample
Event passes Level-1,2,3 CMUP trigger	42451
and both CMUP muons	23893
and both muons have $p_t{}^{\mu}$ (bc) > 20 GeV	9657
and both have $\lvert z_0{}^{\mu}\rvert < 60$ cm	4466

Table 7.1: Summary of number of dimuons in sample after the application of the specified initial selection criteria to the dimuon data sample described in Section 4.1.2. Note that this sample had initial selection criteria applied, which are stated in Table 4.1 and Table 4.2.

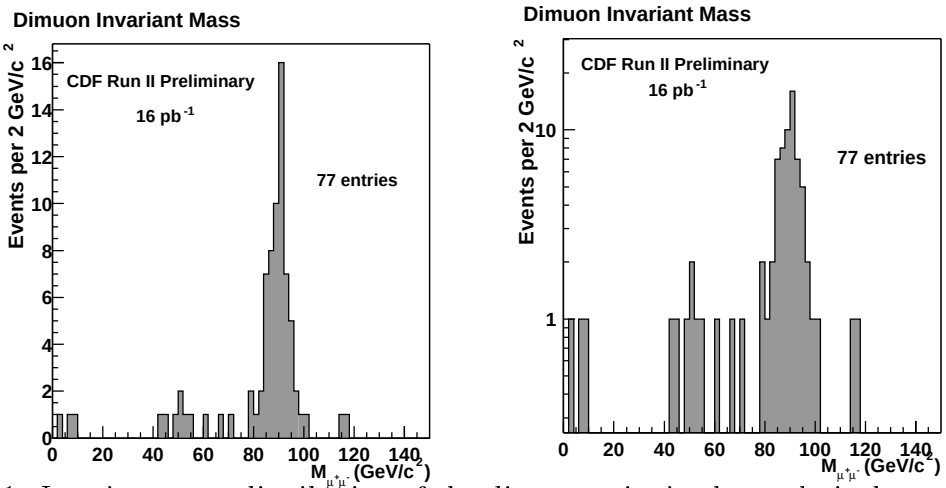

Figure 7.1: Invariant mass distribution of the dimuon pairs in the analysis data sample (16.5 pb^{-1}), after all cuts had been applied (the log of the distribution is shown on the right).

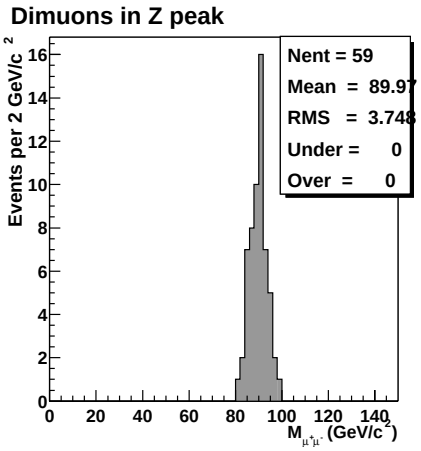

Figure 7.2: Invariant mass distribution of the dimuon pairs in the Z peak region (from 80 to 100 GeV/c^2) in the analysis data sample (16.5 pb^{-1}).

To investigate the effect of applying each muon identification and the cosmic ray rejection selection criterion, all the selection criteria were applied to the dimuon data sample and then one of the selection criteria was removed from both muons. The number of dimuons remaining in the sample and the number of events removed only by this cut were determined. The results are summarised in the Table 7.2.

Selection criteria removed	Number of dimuons remaining in sample	Number of dimuons removed only by this cut
None	77	-
${N_{ax}}^{COT} > 24$	77	0
${N_{st}}^{COT} > 24$	77	0
$\lvert\Delta X_{CMU}\rvert < 3$ cm	89	12
$\lvert\Delta X_{CMP}\rvert < 6$ cm	82	5
Sliding E_{EM}	81	4
Sliding E_{HAD}	78	1
Sliding $I_{0.4}$	80	3
$z_{vtx'}$ found and $\lvert {z_0}^{\mu\mu}$ - $z_{vtx'}\rvert < 3$ cm	88	11
$\lvert {z_0}^{\mu\mu}$ - $z_{vtx'}\rvert < 3$ cm	80	3
$\lvert z_0^{\mu 1} - z_0^{\mu 2}\rvert < 4$ cm	77	0
Cosmic ray cuts	1829	1752
Timing cuts	80	3

Table 7.2: All the selection criteria were applied to the sample and then the one of the muon identification or cosmic ray rejection selection criterion was removed from both muons. The number of dimuons remaining in the sample is summarised in the table and also the number of dimuons that were removed only by the specific selection criteria. The calorimeter isolation ($I_{0.4}$) and impact parameter (${d_0}^{corr}$) cuts are described in Table 4.3 and the sliding energy cuts in Table 5.1.

It was found that very few events, out of the 4466 after the initial cuts, were removed by exclusively one cut, *i.e.* most of the rejected events were removed by more than one selection criterion. The cut which removed the most events (12), when it was applied after the application of the other cuts, was the track-stub matching cut for the CMU muons ($|\Delta X_{CMU}| < 3$ cm). The cosmic ray cut which required the z co-ordinate of the event vertex to be near the dimuon intersection with the beamline also removed a similar number of events (11).

The large decrease in the number of dimuon events after the cosmic ray cuts were applied (from 1829 to 77) implied that the sample was dominated by cosmic rays. The dimuon invariant mass distribution after the application of only muon identification cuts and before cosmic ray cuts is displayed in Figure 7.3. After the cosmic ray track cuts had been applied, but no timing cuts, 80 dimuons remained, for which the invariant mass distribution is shown in Figure 7.4. The three events removed only by the timing cuts were investigated and the results are presented in Section 7.2. There was one event which had no timing information for either muon, this event was not rejected and it is described in Section 7.3.

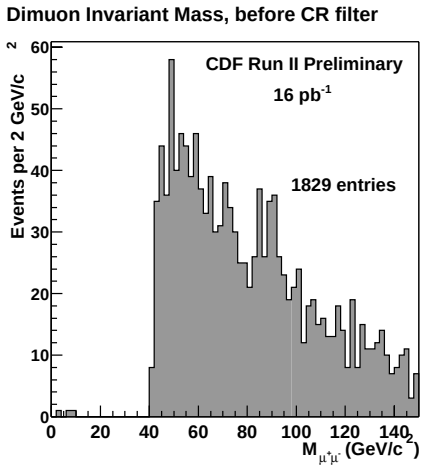

Figure 7.3: Invariant mass distribution of the dimuon pairs in the analysis data set (16.5 pb^{-1}) after only muon identification cuts had been applied.

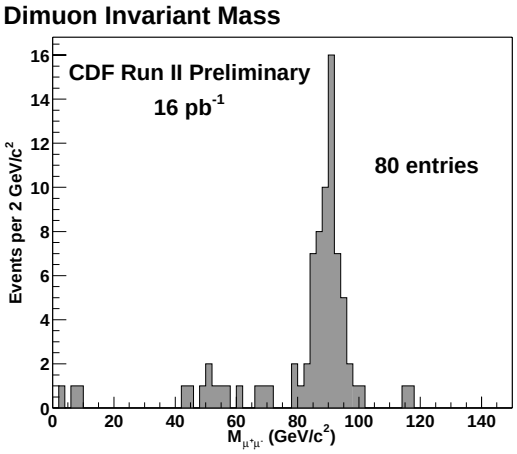

Figure 7.4: Invariant mass distribution of the dimuon pairs in the analysis data sample (16.5 pb^{-1}) after only muon identification cuts and cosmic ray track cuts, but with no timing cuts had been applied.

7.2 Events removed by timing cuts only

The three events removed only by the cosmic ray timing cuts were all excluded by the hadron TDC time difference cut, which required the muon time difference recorded by the upper and lower hadron TDCs to be greater than -11 ns. Two of the events also failed the lower ToF time cut ($0 \leq ToF_{Lower} \leq 9$ ns). The timing information and the invariant mass for these events, nominally labelled events (a), (b) and (c), is displayed in Table 7.3. The silicon event displays, which indicate r-ϕ view of the tracks in the silicon detector are shown in Figure 7.5, Figure 7.7 and Figure 7.9 corresponding to the events a, b and c respectively. The tracks in the central tracking chamber and the stub positions in the muon chambers for these events are shown in Figure 7.6, Figure 7.8 and Figure 7.10. Table 7.4 summarises the track parameters (z_0, d_0 and ϕ) for the two muons in these events as well as the difference in ϕ and sum of the ηs. Each of these events is discussed in turn.

Event	Time-of-Flight Time (ns)			Hadron TDC Time (ns)			Invariant Mass
Label	Upper	Lower	Upper-Lower	Upper	Lower	Upper-Lower	(GeV/c^2)
a	-	-	-	-2	10	-12	69
b	-	15.8	-	-7	12	-19	182
c	-	13.3	-	-11	9	-20	58

Table 7.3: Timing information for the three events which were removed only by the cosmic ray timing cuts imposed in the analysis.

Event	$d_0^{\mu 1}$ cm	$d_0^{\mu 2}$ cm	$z_0^{\mu 1}$ cm	$z_0^{\mu 2}$ cm	$\phi^{\mu 1}$ radians	$\phi^{\mu 2}$ radians	$\phi^{\mu 1}$ - $\phi^{\mu 2}$ radians	$\eta^{\mu 1} + \eta^{\mu 2}$ radians
a	0.124	0.048	28.7	30.6	1.24	4.38	-3.13	-0.007
b	0.036	0.015	-9.5	-9.0	5.35	2.21	3.14	-0.009
c	0.011	0.012	10.2	10.1	5.08	1.94	3.14	0.001

Table 7.4: Track information for the three events which were removed from the dimuon analysis data sample only by the cosmic ray timing cuts imposed in the analysis.

Event (a) had no ToF timing information for either muon, but both the upper and the lower muon had hadron TDC timing information which were within the individual hadron TDC timing cuts (Table 6.7). However, the difference in hadron TDC time was -12 ns; hence this event was rejected as a cosmic ray. The dimuons were back-to-back in η and ϕ, where the definition of back-to-back used was $|\eta_{\mu 1} + \eta_{\mu 2}| < 0.2$ radians and 3.15 $(180.5^\circ) > |\phi_{\mu 1} - \phi_{\mu 2}| \geq 3.13$ radians (179.5°). Also, the two muon tracks did not intersect the beamline at the same position in z and one muon had a much larger two-dimensional impact parameter (d_0) than the other (0.124 cm compared to 0.048 cm), shown in Table 7.4. The difference in d_0 is illustrated in Figure 7.5 which shows the r-ϕ view of the tracks in the silicon detector. The large d_0 for the muon labelled 1 indicated that this may have been one leg of a cosmic ray.

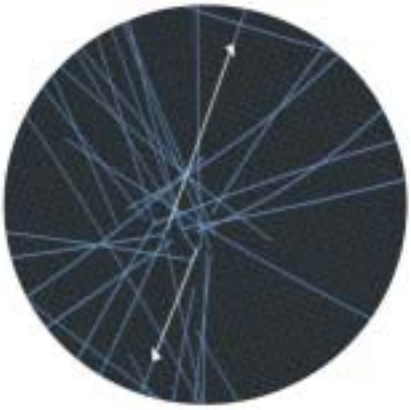

Figure 7.5: Silicon tracking event display view for event (a) rejected as a cosmic ray by timing cuts. The arrows indicate the position of the muon tracks.

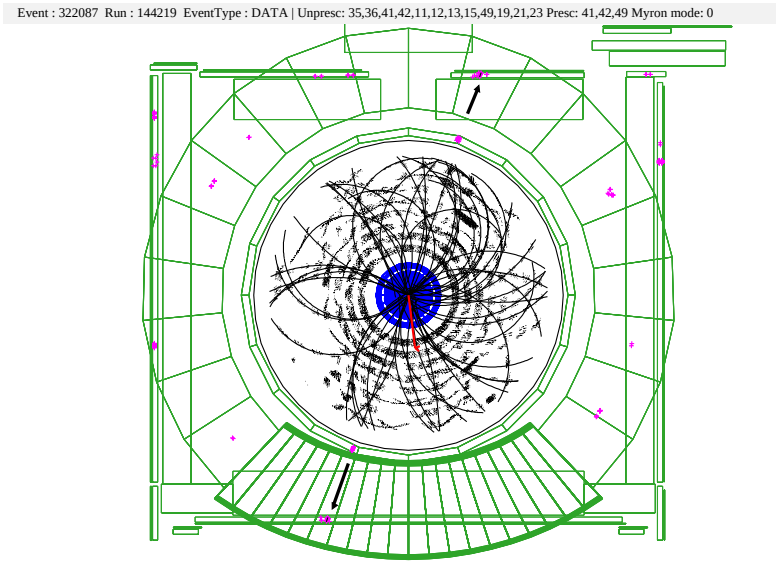

Figure 7.6: Central tracking chamber event display view for event (a) rejected as a cosmic ray from the dimuon analysis data sample by timing cuts. The arrows indicate the position of the muon tracks.

Event (b) had ToF timing information only for the lower muon, which was 15.8 ns. This lay outside the individual upper time of flight time window used in the analysis (summarised in Table 6.3). Both the upper and the lower muon had hadron TDC timing information, of which the lower time lay outside the individual hadron TDC timing cut (shown in Table 6.7) and in addition, the hadron TDC time difference was outside the time difference window. The two muons were also back-to-back in η and ϕ, which is shown clearly in Figure 7.7. It was surmised that the two muons in this event were the two legs of a cosmic ray.

Figure 7.7: Silicon tracking event display view for event (b) rejected as a cosmic ray by timing cuts. The arrows indicate the position of the muon tracks.

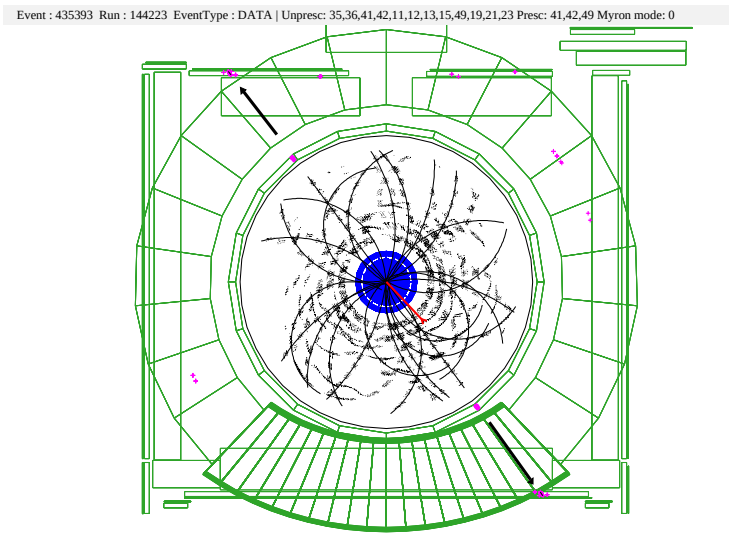

Figure 7.8: Central tracking chamber event display view for event (b) rejected as a cosmic ray from the dimuon analysis data sample by timing cuts. The arrows indicate the position of the muon tracks.

Event (c) had ToF timing information only for the lower muon, which was 13.3 ns. This was outside the individual upper ToF time window used in the analysis. Both the upper and lower muon had hadron TDC timing information, of which the upper time was outside the individual hadron TDC timing cuts (shown in Table 6.7), and the hadron TDC time difference was outside the time difference window for non cosmic ray muons. In addition, the two muons were back-to-back, shown in Table 7.4. This event can clearly be identified as a cosmic ray event from the event display diagrams. Figures 7.9 and 7.10 both show that the tracks were back-to-back and that there were very few tracks in the event, which is typical for a cosmic ray event. This can be compared to Figure 7.12 which shows an interaction event. In addition, Figure 7.9 demonstrates that the dimuon tracks were displaced from the vertex position of the other tracks in the event, which is characteristic for a cosmic ray event.

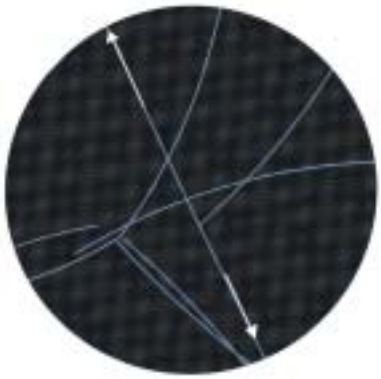

Figure 7.9: Silicon tracking event display view for event (c) rejected as a cosmic ray from the dimuon analysis data sample by timing cuts.

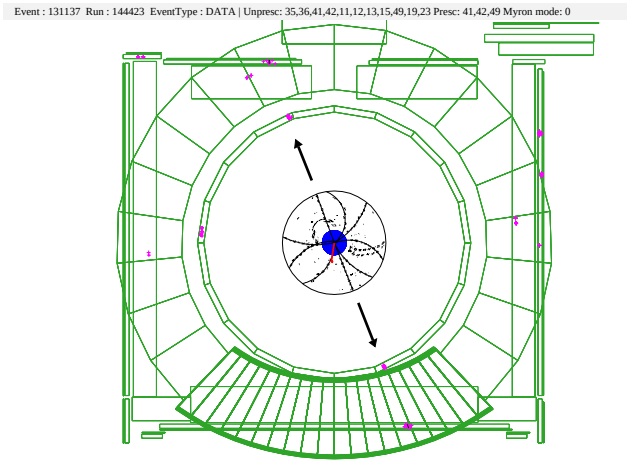

Figure 7.10: Central tracking chamber event display view for event (c) rejected as a cosmic ray from the dimuon analysis data sample by timing cuts. The arrows indicate the position of the muon tracks.

7.3 Event with no timing information

There was one event in the analysis sample which had no timing information. This event, labelled (d), was not rejected. Selected track parameters for the two muons in the event are shown in Table 7.5. The difference in ϕ was 3.31 radians, hence $|\pi$ - $(|\phi^{\mu 1}$ - $\phi^{\mu 2}|)| = 0.167$ radians, or 9.6°. The back-to-back cut rejected events if this angular separation was less than 0.009 radians or 0.5°, if the tracks were also back-to-back in η ($|\eta + \eta| < 0.2$). Therefore the tracks were not back-to-back, as illustrated in Figure 7.11 and Figure 7.12. Figure 7.11 also demonstrates that both of the muon tracks originated from the event interaction vertex.

Event	$d_0^{\mu 1}$ cm	$d_0^{\mu 2}$ cm	$z_0^{\mu 1}$ cm	$z_0^{\mu 2}$ cm	$\phi^{\mu 1}$ radians	$\phi^{\mu 2}$ radians	$\phi^{\mu 1}$ - $\phi^{\mu 2}$ radians	$\eta^{\mu 1}$ $+\eta^{\mu 2}$ radians
d	0.006	0.079	6.6	7.3	6.07	2.76	3.31	-0.058

Table 7.5: Track information for the event in the dimuon analysis data sample which had no timing information for either muon.

Figure 7.11: Silicon vertex detector event display view for event in the dimuon analysis data sample with no Time-of-Flight or hadron TDC timing information. The arrows indicate the position of the muon tracks.

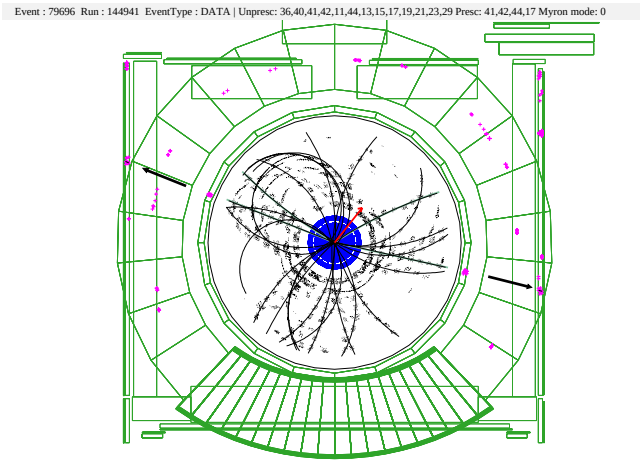

Figure 7.12: Central tracking chamber event display view for event in the dimuon analysis data sample with no Time-of-Flight or hadron TDC timing information. The arrows indicate the position of the muon tracks.

Chapter 8: Efficiencies

The efficiency for a dimuon event ($\epsilon_{\mu\mu}$) is the product of several efficiencies: the trigger efficiency for the event (ϵ_{trig}), the efficiency for cosmic ray rejection ($\epsilon_{CR}^{\mu\mu}$), the efficiency for each muon to be within the fiducial detector region (ϵ_{z_0}), the efficiency of the cut on difference of the z_0 for the two muons, the track efficiency (ϵ_{track}), the muon reconstruction efficiency (ϵ_{rec}) and the muon identification efficiency (ϵ_{ID}). These are related by Equation 8.1. The efficiency of each component was found using various data samples, as outlined in Table 8.1, and where possible the results were confirmed using a second sample. When a second sample was studied, for consistency, the efficiency from the larger of the two samples was used.

The following sections in this chapter describe the determination of each component of the total dimuon event efficiency. A summary of the efficiencies and their uncertainties is displayed in Table 8.18, Section 8.7.

$$\epsilon_{\mu\mu} = \epsilon_{trig}{}^{\mu\mu}\epsilon_{CRtiming}^{\mu\mu}\epsilon_{CRtrack}^{\mu\mu}\epsilon_{z_0}(\epsilon_{track}\epsilon_{rec}\epsilon_{ID})^2 \tag{8.1}$$

Efficiency type	Efficiency (%)	Sample
ϵ_{trig}	$99.7^{+0.1}_{-0.2}$	Zee and jet-20
$\epsilon_{CRtrack}^{\mu\mu}$	90.6 ± 4.2	Zee
$\epsilon_{CRtiming}^{\mu\mu}$	$99.9\ ^{+0.1}_{-1.5}$	Zee and Zmm
ϵ_{z_0}	94 ± 2	Minimum-bias
ϵ_{track}	$99.7\ ^{+0.3}_{-0.8}$	W-No-Track
ϵ_{rec}	92.5 ± 3.0	J/Ψ
ϵ_{ID}	82.9 ± 3.9	Zmm
$\epsilon_{\mu\mu}$	50 ± 6	Combined result

Table 8.1: Summary of the efficiencies, their uncertainties and the type of sample used to determine these efficiencies.

8.1 Muon identification efficiency

The muon identification efficiency (ϵ_{ID}) of the cuts was determined using a CMUP-CMUP Zmm data sample and was confirmed using a Zmm CMX-CMUP sample. Selection criteria

were applied to one of the muons in the CMUP-CMUP sample and to the CMX muon in the CMX-CMUP sample. The efficiency for each of the muon identification cuts was determined by applying each cut to the remaining CMUP muon.

Both data samples originated from the dimuon dataset, described in Section 4.1.2. The events in the CMUP-CMUP sample were required to pass the CMUP18 trigger and those in the CMX CMUP sample were required to pass either the CMX12 or the CMX18 trigger (described in Section 4.1.1). The two muon tracks were required to have beam constrained transverse momenta (p_T(bc)) greater than 20 GeV/c. In addition, in the CMUP-CMUP sample both muons had to have CMUP stubs so that they were within the fiducial region of the CMU and CMP detectors, and for the CMX-CMUP sample one muon was required to have a CMX stub with $|\Delta X_{CMX}| < 10$ cm and the other a CMUP stub. In every event, one of the muons in the CMUP-CMUP sample and the CMX muon was required to pass the selection criteria in Table 4.3. In order to obtain a pure Z sample, the dimuons were required to be of opposite charge and in the invariant mass range $66 < M_{\mu^+\mu^-} < 116$ GeV/c^2. The events also had to pass the cosmic ray track cuts. Table 8.2 summarises the cuts applied to create the two samples.

Variable	Cut placed on	
	First muon	Second muon
$p_T(bc)$	> 20 GeV/c	> 20 GeV/c
$\|z_0\|$	< 60 cm	60 cm
Sliding E_{EM}	< 2 GeV	-
Sliding E_{HAD}	< 6 GeV	-
N_{ax}	> 24	-
N_{st}	> 24	-
$I_{iso}(0.4)$ for $M_{\mu\mu} < 110$ GeV/c^2	< 4 GeV	-
$I_{iso}(0.4)/p_T(bc)$ for $M_{\mu\mu} > 110$ GeV/c	< 0.1	-
For CMUP-CMUP sample $\|\Delta X_{CMU}\|$	< 3 cm	CMU stub required
$\|\Delta X_{CMP}\|$	< 6 cm	CMP stub required
Event must pass Level-1, 2 and 3 MUON18 CMUP trigger		
For CMX-CMUP sample $\|\Delta X_{CMX}\|$	< 10 cm	CMUP stub required
Event must pass Level-1, 2 and 3 CMX12 or CMX18 trigger		
Cosmic ray track cuts		
Cosmic ray timing cuts		
Opposite sign charge		
$66 < M_{\mu\mu} < 116$ GeV/c^2		

Table 8.2: Selection criteria applied to the Zmm sample to select the CMUP-CMUP and CMX-CMUP Z dimuon data samples used to measure the efficiency of muon-identification cuts (ϵ_{ID}).

The efficiency of each individual cut was calculated using Equation 8.2 for the CMUP-CMUP sample. The derivation of this equation is given in Appendix D, in which the following definitions were made:

- T represents the tight cuts, which was the application of all of the muon identification selection criteria.
- N_{T*} was the number of dimuon events in which one muon satisfied the tight cut (T) requirements and no requirements were placed on the second muon.
- N_{Ti} was the number of dimuon events in which one muon satisfied the tight cut (T) requirements and the other muon satisfied the individual cut (i). (N_{Ti} was a subset of N_{T*}.)
- N_{TT} was the number of dimuon events in which both muons satisfied the tight cut requirements. (N_{TT} was a subset of N_{Ti}.)

The errors were calculated using the binomial expression in Equation 8.3. The results are shown in Table 8.3.

$$\varepsilon_{Ti} = \frac{N_{Ti} + N_{TT}}{N_{TT} + N_{T*}} \tag{8.2}$$

$$\sigma = \frac{\sqrt{\varepsilon_i(1-\varepsilon_i)N_{T*}}}{N_{T*}} \tag{8.3}$$

For the CMX-CMUP sample the efficiency for cut i (ε_i) was calculated by dividing the number which passed the cut (N_i^{CMX}) by the total number of CMX-CMUP dimuon events which passed the initial requirements N^{CMX}, as shown by Equation 8.4. The results are shown in Table 8.4 for the CMX-CMUP sample. Since there were correlations between the cuts, the efficiency calculated to pass all the cuts (ε_T) was not simply a product of the individual efficiencies. All the cuts were applied simultaneously to obtain the total efficiency. Calculation of the efficiencies assumed that there was no background in the data sample. This assumption was validated by the fact that before the application of the opposite charge requirement there were no same sign dimuon events in either of the samples.

$$\varepsilon_i^{CMX} = \frac{N_i^{CMX}}{N^{CMX}} \tag{8.4}$$

Identification cut	Number pass	Efficiency (%)
No cuts	92	
N_{Ax}^{COT}	92	100 ± 0.0
N_{St}^{COT}	92	100 ± 0.0
ΔX_{CMU}	79	91.7 ± 2.9
ΔX_{CMP}	85	95.5 ± 2.2
Sliding E_{EM}	87	96.8 ± 1.8
Sliding E_{HAD}	87	96.8 ± 1.8
Sliding $I_{0.4}$	90	98.7 ± 1.2
Pass all cuts	65	82.8 ± 3.9

Table 8.3: Efficiency of muon-identification cuts (ϵ_{ID}) using CMUP-CMUP Zmm data sample, with binomial errors.

Identification cut	Number pass	Efficiency (%)
No cuts	51	
N_{Ax}^{COT}	51	100.0 ± 0.0
N_{St}^{COT}	50	98.0 ± 1.9
ΔX_{CMU}	49	96.1 ± 2.7
ΔX_{CMP}	51	100.0 ± 0.0
Sliding E_{EM}	50	98.0 ± 1.9
Sliding E_{HAD}	51	100.0 ± 0.0
Sliding $I_{0.4}$	49	96.1 ± 2.7
Pass all cuts	46	90.2 ± 4.2

Table 8.4: Efficiency of muon-identification cuts (ϵ_{ID}) using CMX-CMUP Zmm data sample, with binomial errors.

In both samples the most inefficient selection criteria was the CMU detector track-stub matching[1]. The efficiency was 91.7 ± 2.9 % for the CMUP-CMUP sample and 96.1 ± 2.7 % for the CMX-CMUP sample. The efficiencies were higher for the CMX-CMUP sample than the CMUP-CMUP sample, with the exception of the calorimeter isolation cut. However, both samples were small and the results were consistent with each other within the large statistical errors. The overall efficiency measured from the larger sample, the CMUP-CMUP sample, was 82.8 ± 3.9 %, which was consistent within the statistical errors with the result from the

[1]The efficiency for the track-stub match in the CMU detector was calculated using the number of muons with a CMU stub with $|\Delta X| < 3$ cm out of the number of muons with a CMU stub, and similarly for the CMP track-stub match efficiency. By requiring that the muon had a CMU (or CMP) stub then the efficiency of only the track-stub matching was determined, and not the efficiency of forming the muon stub. Inefficiencies of the chambers, linking and tracking were accounted for in the reconstruction efficiencies.

CMUP-CMX sample of 90.2 ± 4.2 %. It was assumed that the efficiencies were independent of momentum of the muon. An attempt was made to investigate the momentum dependence of the efficiency, using both a $W \to \mu\nu$ and a $Z \to \mu\mu$ sample, however, the small samples available, and the associated large statistical uncertainties, made the study unviable. This assumption was supported by a study performed in Run I to investigate the transverse momentum dependence of similar identifiation cuts, in which it was concluded that there was no significant dependence of the efficiency on the transverse momentum [79].

8.2 Efficiency of the cosmic ray selection criteria

The efficiency of the cosmic ray selection criteria ($\epsilon_{CR}^{\mu\mu}$) was divided into four components, three cosmic ray track cuts and one cosmic ray timing;

- efficiency to find a "seeded primary vertex" ($z_{vtx'}$) within 10 cm of the dimuon seed z ($z_0^{\mu\mu}$), as described in Section 6.1, combined the efficiency for the vertex, if a vertex was found, to be separated in z by less than 3 cm from the seed z ($\epsilon^{\mu\mu}_{CR(z_0^{\mu\mu} - z_{vtx'})}$) (Section 8.2.1),
- efficiency for the d_0^{corr} cut ($\epsilon_{CR(d_0^{corr})}$) (Section 8.2.2),
- efficiency for the Δz_0 ($z_0^{\mu 1}$ - $z_0^{\mu 2}$) cut ($\epsilon_{\Delta z_0}$) (Section 8.2.3) and
- efficiency of timing cuts ($\epsilon_{CR(timing)}$) (Section 8.2.5).

The efficiency of the cosmic ray track and some of the timing cuts were determined using the Zee data sample. Lepton universality for electrons and muons from Z decays was assumed, so the results determined using the dielectron data set were assumed to be applicable to the dimuon data sample. The combined cosmic ray track cut efficiency is summarised in Section 8.2.4 and a summary of the efficiency of the timing cuts and of their combination is described in Section 8.2.6.

8.2.1 Efficiency of the cosmic ray vertex cut: $z_0{}^{\mu\mu}$ - $z_{vtx'}$

The Zee dielectron data sample, whose selection is described in Section 4.2, was used to determine the efficiency of the cosmic ray track "seed z - seeded vertex position" ($z_0{}^{\mu\mu}$ - $z_{vtx'}$) cut. In addition, the two electrons were required to pass the d_0^{corr} cosmic ray track cut. The sample consisted of 76 dielectron pairs. In all 76 events, tracks were found within a 10 cm window of the seed z of the two dielectrons ($z_0{}^{ee}$) and so a vertex was constructed ($z_{vtx'}$). Therefore, the efficiency for this component of the cosmic ray cuts was found to be 100 %. In 72 of the 76 events in which a vertex was constructed the seed z was separated by less than 3 cm from the mean vertex position ($z_{vtx'}$). The distribution of $z_0{}^{ee}$ - $z_{vtx'}$ is shown in Figure 8.1. Consequently the efficiency of the $z_0{}^{ee}$ - $z_{vtx'}$ cut, and assuming lepton universality also the efficiency of the $z_0{}^{\mu\mu}$ - $z_{vtx'}$ cut, was 94.7 $\pm$ 2.6 %. This information is summarised in Table 8.5.

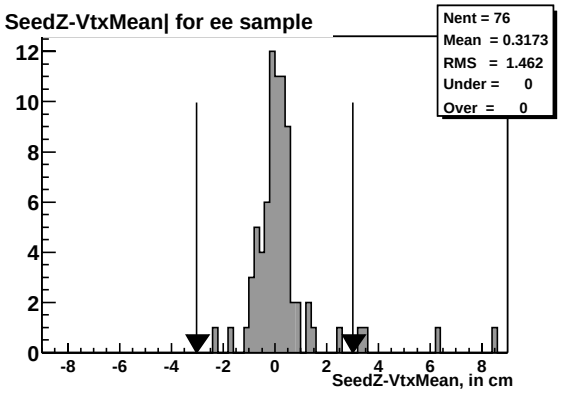

Figure 8.1: $z_0{}^{ee} - z_{vtx'}$ distribution for the Zee dielectron data sample.

Data sample	Cut	Pass cut	Total	Efficiency (%)
Zee	$z_{vtx'}$ found	76	76	100.0
Zee	$\lvert z_0{}^{ee} - z_{vtx'}\rvert < 3$	72	76	94.7 $\pm$ 2.6

Table 8.5: Efficiency of $z_0{}^{ee}$ - $z_{vtx'}$ cut found using the Zee data dielectron sample (10.4 pb^{-1}).

8.2.2 Efficiency of the cosmic ray impact parameter cut

The efficiency of the cosmic ray track impact parameter (d_0^{corr}) cut was also determined by using the Zee dielectron data sample (described in Section 4.2). The two electrons were required to

pass the $|{z_0}^{ee} - z_{vtx'}|$ cut. In 22 events, one or both of the tracks had silicon information available, of which 21 passed the cut requiring the impact parameter ($|d_0^{corr}(SVX)|$) to be less than 0.02 cm. This implied a cut efficiency of 95.5 ± 4.4 %. In the case where only COT track information was considered, 72 out of 75 events passed the COT impact parameter ($d_0^{corr}(COT)$) cut, which required $|d_0^{corr}(COT)|$ to be less than 0.15 cm. The efficiency of this cut was therefore 96.0 ± 2.3 %. This information is summarised in Table 8.6.

Data sample	Cut	Pass cut	Total	Efficiency (%)
Zee	$\|d_0^{corr}(SVX)\| < 0.02$ cm	21	22	95.5 ± 4.4
Zee	$\|d_0^{corr}(COT)\| < 0.15$ cm	72	75	96.0 ± 2.3

Table 8.6: Efficiency of the two-dimensional impact parameter cut for tracks with silicon hits (SVX) and without (COT), determined using a Zee dielectron data sample.

The total efficiency of the d_0^{corr} cut ($\epsilon_{d_0^{corr}}$) was calculated by combining the component $|d_0^{corr}(SVX)|$ and $|d_0^{corr}(COT)|$ efficiencies, as shown in Equation 8.5.

$$\epsilon_{d_0^{corr}} = \epsilon_{d_0^{corr}(SVX)} \times f_{SVX} + \epsilon_{d_0^{corr}(COT)} \times f_{COT} \tag{8.5}$$

f_{SVX} was the fraction of events in the final dimuon sample, with the impact parameter cuts removed, which had silicon tracking information. This was 36 of the 79 dimuon events (54.4 %). The fraction of events in the final dimuon sample which had no silicon tracking information and only COT information (f_{COT}) was 43 out of the 79 dimuon events (45.6 %). The total efficiency of the d_0^{corr} cut was determined, by substitution into Equation 8.5, to be 95.7 ± 3.4 %.

The combined efficiency of the impact parameter (d_0^{corr}) and nearby vertex (${z_0}^{\mu\mu}$ - $z_{vtx'}$) was 90.6 ± 4.2 % (where the errors were combined in quadrature). This was consistent, within errors, with the result obtained using a W → eν sample [65], which was 92.3 ± 0.3 ± 2.7 %, where the errors are the statistical and systematic respectively.

8.2.3 Efficiency of the Δz_0 cut

The efficiency for the Δz_0 ($z_0^{\mu 1}$ - $z_0^{\mu 2}$) cut ($\epsilon_{\Delta z_0}$) was determined using the Zee dielectron data sample, described in Section 4.2, with the impact parameter and nearby vertex cut applied. In the Zee dielectron sample, all of the 72 events passed the $|z_0^1 - z_0^2| < 4$ cm cut. Therefore the efficiency ($\epsilon_{\Delta z_0}$) was $100.0\ ^{+0.0}_{-1.0}$ %, where asymmetric errors were calculated [80]. This was confirmed by the result reported in the R ratio measurement analysis ($\sigma(\mathrm{W}\to\mu\nu)/\sigma(\mathrm{Z}\to\mu\mu)$), in which the efficiency of the Δz_0 cut was determined using a Monte Carlo $\mathrm{Z}\to\mu^+\mu^-$ sample. It was found that only 1/3994 of these events failed the cut, which implied an efficiency of 99.97 % [81]. An efficiency ($\epsilon_{\Delta z_0}$) of 99.9 $\pm$ 0.1 % was assigned to be the efficiency for a data sample, because the tracking resolution was known to be better in the simulation than in the data, since tracks had fewer hits in the data than in the simulation, confirmed by Figure 4.1 in Section 4.1.4.

8.2.4 Summary of efficiency of cosmic ray tracking cuts

The combined efficiency ($\epsilon_{CRtrack}$) was calculated as the product of the efficiency of the impact parameter (d_0^{corr}), nearby vertex ($z_0{}^{\mu\mu}$ - $z_{vtx'}$) and dimuon z_0 separation ($z_0^{\mu 1} - z_0^{\mu 2}$) cuts, as shown in Equation 8.6. After substitution this was determined to be 90.6 $\pm$ 4.3 %, where the errors were combined in quadrature.

$$\epsilon_{CRtrack} = \epsilon_{CR(d_0^{corr})} \times \epsilon_{CR(z_0{}^{\mu\mu} - z_{vtx'})} \times (\epsilon_{\Delta z_0}) \tag{8.6}$$

8.2.5 Efficiency of cosmic ray timing selection criteria

The cosmic ray (CR) timing cuts had two components, the ToF cuts and the hadron TDC cuts. To find the efficiency of the timing selection criteria, the efficiency of the individual ToF and hadron TDC cuts were calculated and then combined in the relevant fractions. In both cases two independent samples were used for confirmation, because the statistical errors were large due to the small data sample sizes. For the hadron TDC timing a CMUP-CMUP Zmm dimuon and

a CMX-CMUP Zmm dimuon data sample were used and for the ToF timing a Zee dielectron and CMUP-CMUP Zmm dimuon data sample were studied. Errors were calculated using the symmetrical binomial error formula $\sqrt{p(1-p)/N}$, where p was the number which passed the cut divided by the number (N) in the sample, except in the cases in which either the cuts were 100 % efficient or $p + \sqrt{p(1-p)/N}$ exceeded 100 %. In this case, asymmetric binomial errors were calculated [80].

Efficiency of hadron TDC timing cuts

The Zmm CMUP-CMUP dimuon data sample was obtained as described in Section 4.1.3, with the exception that the hadron TDC timing cuts were not applied and the dimuons were required to pass the ToF difference cut (*i.e.* both muons had to have ToF information and satisfy $\Delta ToF_{Upper-Lower} >$ -5 ns). Also, the muons were required to have the charge of the opposite sign and an invariant mass in the range from 66 to 116 GeV/c^2.

This sample consisted of 30 dimuons, 27 of which had hadron TDC time information for both muons, 29 had time information for the muon in the upper half of the detector (upper) and 29 had time information for the muon in the lower half of the detector (lower). The efficiency was defined to be the number of events which passed the specific timing cut (upper, lower or both) divided by the total number which had that timing information (upper, lower or both). The efficiencies found are summarised in Table 8.7. The hadron TDC time difference cut and the lower time cut were determined to be 100 % efficient and the upper hadron TDC time cut was 93.1 % efficient.

Timing cut	Number with timing (events)	Number pass (events)	Efficiency (%)
No TDC time cuts	30		
TDC time difference	27	27	100.0
Upper TDC time	29	27	93.10 ± 4.7
Lower TDC time	29	29	100.0

Table 8.7: Efficiency of hadron TDC timing cuts from a CMUP-CMUP Zmm sample.

The second Zmm dimuon data sample used was the Zmm CMUP-CMX dimuon data sample, whose selection criteria are explained in Section 4.1.5 with the exception that the timing criteria applied were more stringent. All the dimuon events were required to pass the ToF time difference cut. The upper and lower efficiencies were found using the CMUP muon in the event and the time difference used the CMX and CMUP muon timing[2]. The results are shown in Table 8.8. The hadron TDC timing cuts were all 100 % efficient for this sample.

Timing cut	Number with timing (events)	Number pass (events)	Efficiency (%)
No hadron time cuts	8		
TDC time difference	5	5	100.0
TDC time upper	3	3	100.0
TDC time lower	4	4	100.0

Table 8.8: Efficiency of hadron TDC timing cuts from the CMX-CMUP Zmm dimuon data sample.

The CMX-CMUP dimuon sample only consisted of 8 events, so, for interest only, a larger sample was studied. The sample was enlarged by loosening the initial ToF selection criteria. Events were included if just one muon had ToF timing which passed the respective individual ToF time cut in addition to events for which both muons had timing information and passed either the ToF time difference cut. Although loosening the selection criteria enlarged the sample, it also introduced impurities into the sample. In contrast to the ToF time difference cut, which does not pass cosmic rays (because cosmic rays do not have a time difference of greater than -5 ns, since they pass through the detector), the individual time cuts do pass cosmic ray events. This can be seen by considering Figure 6.2 and Figure 6.3, in which cosmic ray events lie within the cut range from 0 to 10 ns.

The results are shown in Table 8.9. This larger sample had a slight cosmic ray contamination, as can be seen from the decrease in efficiency of the TDC time difference cut. The hadron TDC

[2]Hence it was possible to find that there were fewer events with upper or lower CMUP time, than events with upper and lower timing; as was found (see Table 8.8). Of the 5 events which had both upper and lower timing, in 4 events the CMUP muon was the lower muon and in the other event, the CMUP muon was the upper muon. The remaining upper and lower CMUP time events originated from events in which only one muon had timing information.

upper and lower time cuts were still found to be 100 % efficient. (This sample was not used to determine the efficiency.)

Timing cut	Number with timing (events)	Number pass (events)	Efficiency (%)
No hadron time cuts	38		
TDC time difference	29	28	96.6 ± 3.4
TDC time upper	15	15	100.0
TDC time lower	21	21	100.0

Table 8.9: Efficiency of hadron TDC timing cuts from the looser CMX-CMUP Zmm dimuon data sample.

The efficiency was determined from the larger sample, *i.e.* the CMUP-CMUP rather than the CMX-CMUP sample, for which the results are shown in Table 8.7. The efficiency of the hadron TDC time difference and TDC lower cut were 100.0 % and the efficiency of the hadron upper TDC time cut was 93.1 ± 4.7 %. These results were confirmed by the results from the CMX-CMUP sample, for which identical efficiencies were obtained for the hadron TDC time difference and TDC lower cut, and the efficiency for the hadron upper TDC time cut was 100.0 %, which was higher than the efficiency found with the CMUP-CMUP sample.

Efficiency of the ToF cuts

To determine the efficiency of the ToF timing cuts, the Zee sample, described in Section 4.2, and a Zmm CMUP-CMUP dimuon data sample were used. The latter sample was selected using the criteria described in Section 4.1.3 with the exception that no ToF timing cuts were applied; instead, the events were required to pass the hadron TDC timing cuts (upper, lower or both). In addition, an invariant mass cut was placed on the dimuons requiring the mass to be in the range from 66 to 116 GeV/c^2 and the two muons were selected to have charge of the opposite in order to obtain a pure Z sample. The ToF time cut efficiencies for the samples are shown in Table 8.10 and Table 8.11.

Timing cut	Number with timing (events)	Number pass (events)	efficiency (%)
No ToF time cuts	63		
ToF time difference	30	30	100.0
Upper ToF time	38	38	100.0
Lower ToF time	48	48	100.0

Table 8.10: Efficiency of ToF timing cuts from a CMUP-CMUP Zmm dimuon data sample.

Timing cut	Number with timing (events)	Number pass (events)	Efficiency (%)
No ToF time cuts	79		
ToF time difference	18	18	100.0
Upper ToF time	38	38	100.0
Lower ToF time	42	42	100.0

Table 8.11: Efficiency of ToF timing cuts from a Zee data sample.

The efficiency of the all of the ToF cuts was 100.0 % for both samples, as shown in Table 8.10 and Table 8.11.

8.2.6 Summary and combination of timing cut efficiencies

The timing cuts were applied in the order described in Section 6.2.3 and summarised here. If both muons had ToF timing information, then the event either passed or failed depending on whether it satisfied the ToF time difference selection criteria, because this variable had the clearest discrimination between the signal and the cosmic ray background. If, however, one of the muons did not have any ToF timing information, then the event had to pass the individual ToF time cut (upper or lower, whichever had timing information) and also the relevant hadron TDC timing cut (upper, lower, both or pass if neither had any hadron TDC timing information). If neither muon had ToF timing information then the event had to pass just the relevant TDC timing cuts. If both muons had neither ToF nor hadron TDC timing then the event was not rejected.

To determine the efficiency of the cosmic ray timing cut, the efficiencies of the individual timing cuts were combined using Equation 8.7, in which the efficiency of the hadron component was determined using Equation 8.8. Equation 8.7 and 8.8 were also used to calculate the upper

and lower limit of the errors. To find the upper error, the maximum efficiencies were substituted, *i.e.* for the 100 % efficient cuts then 100 % was used, and to find the lower error, the lower limit of the efficiencies for all of the cuts were substituted simultaneously. 99 % was used for the 100 % efficient cuts, as calculated using asymmetric binomial errors [80]. The efficiencies of the individual timing cuts are summarised in Table 8.12.

Timing cut	Efficiency(%)
Hadron TDC time difference	100.0
Upper hadron TDC time	93.1 ± 4.7
Lower hadron TDC time	100.0
ToF Time difference	100.0
Upper ToF time	100.0
Lower ToF time	100.0
Combined timing cut	$99.9\ ^{+0.1}_{-1.5}$

Table 8.12: Summary of the efficiency of timing cuts.

$$\epsilon^{\mu\mu}_{CRTiming} = \epsilon_{ToFdiff} \times f^{ToF}_{both} + (\epsilon_{ToFUpper} \times f^{ToF}_{U} + \epsilon_{ToFLower} \times f^{ToF}_{L} + f^{ToF}_{neither}) \times \epsilon_{hadTDC} \quad (8.7)$$

$$\epsilon_{hadTDC} = \epsilon^{TDC}_{both} \times f^{TDC}_{both} + \epsilon^{TDC}_{U} \times f^{TDC}_{U} + \epsilon^{TDC}_{L} \times f^{TDC}_{L} + f^{TDC}_{neither} \quad (8.8)$$

In Equation 8.7 and 8.8, f represents a fraction, which was determined from the final dimuon analysis sample. The subscript "U" signifies upper only timing information; "L", lower only; "both", upper and lower timing information and "neither", neither muon having any timing information. The superscript "TDC" represents hadron TDC time information for the subscripted particles (upper only, lower only, both or neither). By analogy the superscript "ToF" indicates ToF time information for the subscripted particles (upper only, lower only, both or neither). The fractions of the events with particular timing information from the dimuon analysis sample, before the application of timing cuts, are displayed in Table 8.13 and the combinations of ToF and hadron TDC timing are listed in Table 8.14. 35 of the 80 dimuon events in the analysis sample had ToF and TDC timing information for both muons, and one event had no timing information (ToF or TDC) for either muon. The efficiency ascertained for the cosmic ray timing cuts ($\epsilon^{\mu\mu}_{CRTiming}$) was $99.9\ ^{+0.1}_{-1.5}$ %.

Timing	Number of dimuons
f_U^{ToF}	11
f_L^{ToF}	24
f_{both}^{ToF}	35
$f_{neither}^{ToF}$	10
f_U^{TDC}	2
f_L^{TDC}	4
f_{both}^{TDC}	72
$f_{neither}^{TDC}$	2
Total	80

Table 8.13: Number of dimuon events with timing information in the dimuon analysis sample. "U" represents the upper muon; "L", the lower muon; "both", both muons and "neither", neither muons having timing information. The superscript "ToF" indicates Time-of-Flight and "TDC" hadron TDC timing.

Timing combination	Number of dimuons
$f_L^{ToF} * f_{both}^{TDC}$	21
$f_L^{ToF} * f_U^{TDC}$	0
$f_L^{ToF} * f_L^{TDC}$	2
$f_L^{ToF} * f_{neither}^{TDC}$	1
$f_U^{ToF} * f_{both}^{TDC}$	11
$f_U^{ToF} * f_U^{TDC}$	0
$f_U^{ToF} * f_L^{TDC}$	0
$f_U^{ToF} * f_{neither}^{TDC}$	0
$f_{both}^{ToF} * f_{both}^{TDC}$	35
$f_{Neither}^{ToF} * f_{both}^{TDC}$	8
$f_{Neither}^{ToF} * f_U^{TDC}$	0
$f_{Neither}^{ToF} * f_L^{TDC}$	1
$f_{Neither}^{ToF} * f_{Neither}^{TDC}$	1
Total	80

Table 8.14: Number of dimuon events with various combinations of Time-of-Flight and hadron timing information in the dimuon analysis sample. "U" represents the upper muon; "L", the lower muon; "both", both muons and "neither", neither muons having timing information. The superscript "ToF" indicates Time-of-Flight and "TDC" hadron TDC timing.

8.3 Trigger efficiency

The trigger efficiency was measured using two independent samples, a jet and electron, and the results combined (Section 8.3.1). A second value for the trigger efficiency was obtained using a Zmm CMX-CMUP dimuon data sample, as described in Section 8.3.2.

8.3.1 Trigger efficiency measurement from a jet and electron sample

The muon trigger efficiency was measured using the high-p_T electron sample described in Section 4.2 and a JET20 sample [65]. Muon good runs (as previously defined in Section 4.1.1) were included from run number 139253 to 144674. The events in these data samples were collected by the electron or jet trigger respectively. The efficiency of the muon trigger was determined by whether the muon trigger bits were also set in events in which a reconstructed muon was found. Quality cuts were applied to the reconstructed muons, these are shown in Table 8.15. The muon trigger efficiency was obtained by dividing the number of events which contained a muon with the muon trigger bits by the total number of events which contained a muon. The events which contained a muon, but in which no muon trigger bit was set, indicated an inefficiency of the muon trigger. The trigger efficiency was recorded as a function of the muon transverse momentum (p_T), in bins of 0-4, 4-8, 8-12, 12-18 and above 18 GeV/c. These were chosen because of the coarse momentum resolution of the extremely fast tracker (XFT) which extrapolates the muon tracks from the central tracking chamber out to the muon chambers.

Variable	Cut
E_{EM}	< 2 GeV
E_{HAD}	< 6 GeV
$E_{EM} + E_{HAD}$	> 0 GeV
$\|d_0^{corr}\|$	$<$0.2 cm
N_{Ax}	> 24 hits
$\|\Delta X_{CMU}\|$	< 5 cm
$\|z_0^{\mu}\|$	< 60 cm
$\|z_0^{\mu} - z_{vtx}\|$	< 5 cm

Table 8.15: Quality cuts applied to muons in the electron triggered data sample to study the CMUP trigger efficiency.

A summary of the jet, electron and the combined results is given in Table 8.16 and illustrated in Figure 8.2 [65]. The two highest bins were combined to give a trigger efficiency (ϵ_T) of $94.5^{+1.5}_{-1.6}$ $\pm$ 1.0 % (statistical and systematic errors) for $p_T > 12$ GeV [65]. The systematic error was calculated from an estimate of the effect of that cosmic ray contamination would have on the

p_T range (GeV/c)	Electron sample		Jet sample		Combined
	Pass/Total	Efficiency (%)	Pass/Total	Efficiency (%)	Efficiency (%)
$p_T < 4$	160 / 687	23.0 ± 1.6	383 / 2062	18.6 ± 0.9	19.8 ± 0.8
$4 < p_T < 8$	415 / 467	88.9 ± 1.4	1308 / 1454	90.0 ± 0.8	89.7 ± 0.7
$8 < p_T < 12$	119 / 126	94.4 ± 2.0	242 / 277	87.4 ± 2.0	89.6 ± 1.5
$12 < p_T < 18$	59 / 61	96.7 ± 2.3	91 / 98	92.9 ± 2.6	$94.3\ ^{+1.8}_{-1.9}$
$p_T > 18$	33 / 34	97.1 ± 2.9	23 / 25	92.0 ± 5.4	$94.9\ ^{+2.8}_{-3.2}$

Table 8.16: Measurements of the muon trigger efficiency obtained using an electron triggered data sample, jet triggered data sample and the combined data sample.

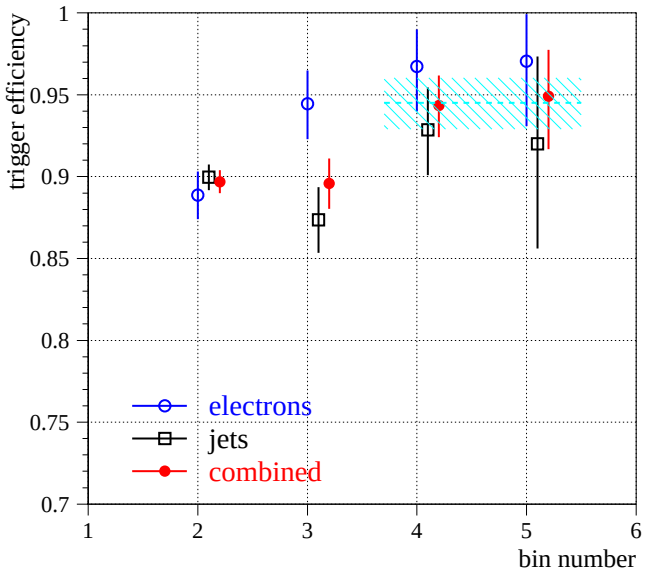

Figure 8.2: CMUP trigger efficiency, determined using a jet and an electron sample [65].

efficiency measurement. This was studied by reversing the impact parameter cut (*i.e* muons were required to have $|d_0^{corr}| > 0.2$ cm) and the $|z_0^{\mu} - z_{vtx}|$ cut, which required that the intersection of the muon track with the beam-line was within a certain separation in the z direction from the reconstructed vertex of the tracks in the event, was removed. It was expected that cosmic rays would have a lower trigger efficiency than for prompt muons and this was observed. Table 8.17 displays the trigger efficiencies found with the electron sample with the cosmic ray cuts. For $p_T > 4$ GeV/c, these efficiencies were lower than the corresponding efficiencies found with the original cuts applied, shown in Table 8.16. The efficiency for the combined jet and electron sample with the cosmic ray cuts applied ($\epsilon_{trig,CR}$) was found to be 83 ± 8 % for a $p_T > 12$ GeV/c [65].

An estimation of the cosmic ray contamination was made by assuming a contamination fraction p in the jet and electron sample [65]. The efficiency (ϵ_T) as a function of p was computed using ϵ_T = (1-p)$\epsilon_{trig,\mu}$ + p$\epsilon_{trig,CR}$, where $\epsilon_{trig,\mu}$ was the trigger efficiency for interaction muons, and $\epsilon_{trig,CR}$ the trigger efficiency for cosmic rays. This was rearranged to give $\epsilon_{trig,\mu}$(p) = (ϵ_T - p$\epsilon_{trig,CR}$)/(1-p). The contamination was assumed to be much less than 10 %, so p was varied from 0 to 0.1. The equation was solved for $\epsilon_{trig,\mu}$ as a function of p. The difference $\epsilon_{trig,\mu}(0.1)$ - $\epsilon_{trig,\mu}(0)$ = 0.010 was taken as the systematic uncertainty.

p_T Range (GeV/c)	Electron "cosmic ray" sample	
	Pass/Total	Efficiency (%)
$p_T < 4$	468 / 1800	26.0 ± 1.0
$4 < p_T < 8$	1201 / 1363	88.1 ± 0.9
$8 < p_T < 12$	329 / 353	93.2 ± 1.3
$12 < p_T < 18$	135 / 142	95.1 ± 1.8
$p_T > 18$	90 / 96	93.8 ± 2.5

Table 8.17: Estimation of the cosmic ray CMUP trigger efficiency measured using an electron triggered data sample.

8.3.2 Trigger efficiency from a CMX-CMUP Zmm dimuon data sample

The CMUP trigger efficiency was confirmed using a Zmm CMX-CMUP dimuon data sample. This data sample was a similar to that of the CMX-CMUP Z data sample described in Section 4.1.5. The same quality cuts were applied to both muons and the dimuons were required to have an invariant mass in the range from 66 to 116 GeV/c^2. The only timing cut applied was a hadron time difference cut, which required that, if both muons had timing, the difference (upper-lower) was greater than -12 ns. The events were also required to have passed the CMX trigger path (described in Section 4.1.5), so that the events could have been triggered by the CMX rather than the CMUP muon in the event. In each event it was then determined whether the CMUP Level-1, 2 and 3 trigger bits had been set. The trigger efficiency ($\epsilon_{CMUPtrig}$) was calculated from the fraction of events in which the Level-1, 2 and 3 trigger bits were set ($N_{CMX,CMUPtrig}$) out of the total number of CMX-CMUP events ($N_{CMX,*}$), as shown in Equation 8.9.

$$\epsilon_{CMUPtrig} = \frac{N_{CMX,CMUPtrig}}{N_{CMX,*}} \tag{8.9}$$

The data sample consisted of 40 dimuon events. 39 of these had the CMUP Level-1 (L1_CMUP6_PT4 CMUP) trigger bit set as well as the CMX Level-1, Level-2 and Level-3 trigger bits set. The Level-2 (L2_AUTO_L1_CMUP6_PT4) trigger was programmed to auto accept and the efficiency found was 100 % as expected. The 39 events also had the Level-3 (MUON_CMUP18) trigger bits set. Therefore, the trigger efficiency, which was obtained by suitable substitution into Equation 8.9, was 97.5 ± 2.5 %. This was consistent with the trigger efficiency of 97.1 ± 2.9 % for $p_T > 18$ GeV/c from the electron sample alone and combined electron and jet efficiency of $94.5^{+1.5}_{-1.6}$ ± 1.0 % for $p_T > 12$ GeV/c.

8.3.3 Trigger efficiency for a dimuon event

In a dimuon event, either of the muons in the event could have been the trigger muon. Given that the efficiency for a single muon to pass the trigger is ϵ^{μ}_{trig} then the trigger efficiency per dimuon event ($\epsilon^{\mu\mu}_{trig}$) is given by Equation 8.10, which is derived in Appendix E.

$$\epsilon^{\mu\mu}_{trig} = \epsilon^{\mu}_{trig} \times (2 - \epsilon^{\mu}_{trig}) \tag{8.10}$$

Equation 8.10 was used to determine the dimuon event trigger efficiency using the single muon trigger efficiency of $94.5^{+1.5}_{-1.6}$ ± 1.0 % from the electron and jet sample. The trigger efficiency per event was calculated to be 99.7 %. The upper/lower statistical/systematic error for the dimuon case was determined by substituting the upper/lower statistical/systematic error for the one muon case into Equation 8.10. This resulted in a dimuon trigger efficiency of $99.7\ ^{+0.1}_{-0.2}$ ± 0.1 % for the electron and jet sample, which was consistent, within errors, with the efficiency calculated using the CMX-CMUP sample of 99.9 ± 0.1 %. The statistical and systematic uncertainties were combined in quadrature. The trigger efficiency ($\epsilon^{\mu\mu}_{trig}$) was found to be $99.7\ ^{+0.1}_{-0.2}$ %.

8.4 Efficiency of fiducial volume cut

The efficiency of the fiducial z_0^μ cut (ϵ_{z_0}) was determined to be 94 ± 2 % using a minimum-bias sample[3] [82]. The error quoted is statistical; no systematic uncertainty was reported. This result was confirmed using the Zee dielectron data sample, described in Section 4.2, with the cosmic ray track impact parameter and dimuon vertex cuts applied. The Zee dielectron data sample had no cuts initially applied to the z_0 of the tracks. Two events out of 72 had $z_0 > 60$ cm for at least one of the electrons (in both cases both electrons had $z_0 > 60$ cm and satisfied the cut $|z_0^1 - z_0^2| < 4$ cm). Therefore, the efficiency was determined to be 97 ± 2 %, which was higher than obtained using the minimum bias sample, but consistent within the statistical errors of the two results.

8.5 Tracking efficiency

The tracking efficiency (ϵ_{track}) was determined, by the tracking group, using the W-No-Track sample to be $\epsilon_{track} = 99.7^{+0.3}_{-0.8}$ % [83]. No systematic uncertainty was reported. The W-candidates were identified using information from the calorimeter and matched to stand-alone tracks (a track which was formed using silicon tracking information only). The track reconstruction efficiency result was confirmed using a sample of W-candidates identified using calorimeter information with a matched hit in the ToF detector [83]. The efficiency found with the latter sample was 97.7 ± 0.4 %, where the uncertainty was the binomial statistical error.

8.6 Muon reconstruction efficiency

The CMUP muon reconstruction efficiency (ϵ_{rec}) was estimated, using a J/Ψ sample, to be $92.5 \pm 1.5 \pm 2.6$ %, where the errors are the statistical and systematic respectively [84]. The individual chamber efficiencies were $\epsilon_{CMU} = 97.0 \pm 1.0 \pm 2$ % and $\epsilon_{CMP} = 94.6 \pm 1.3 \pm 1.8$ %.

[3] A minimum-bias sample is one which is collected every pre-determined number of clock counts, rather than being accepted because the event satisfies specific trigger selection criteria. It therefore represents an unbiased sample, because the event selection is not determined by any particular properties of the event.

The systematic and statistical errors were combined in quadrature to give an uncertainty on the efficiency of 3 %. The reconstruction efficiency included inefficiencies of the muon chambers and stub-track linking. Track-stub matching efficiency was accounted for in the muon identifcation efficiency.

8.7 Total dimuon event efficiency

Table 8.18 summarises the efficiency of the dimuon event and its various components. The constituent efficiencies were combined according to Equation 8.1. The event efficiency was determined to be 50 ± 6 %. The most inefficient component was the muon identification selection criteria, which were applied to both muons and so its efficiency contributed twice to the dimuon event efficiency. Similarly, the muon reconstruction efficiency contributed for both muons and this was the second most inefficient component. The dimuon event efficiency determined was lower than that obtained in the Run I the $Z' \rightarrow \mu\ \mu$ search [75] and the Z^0 cross section measurement (using 110 pb^{-1}) [76], for which the efficiency was of the order of 85 %. However, the samples used in this analysis were in general very small and consequently the statistical errors large. For consistency throughout, the efficiency from the larger sample was used to calculate the event efficiency when more than one sample was studied. Had the highest component efficiencies from the samples used been combined, then the event efficiency would have been of the order of 60 % rather than 50 %.

Efficiency type	Efficiency (%)
ϵ_{trig}	$99.7^{+0.1}_{-0.2}$
$\epsilon^{\mu\mu}_{CRtrack}$	90.6 ± 4.2
$\epsilon^{\mu\mu}_{CRtiming}$	$99.9\ ^{+0.1}_{-1.5}$
ϵ_{z_0}	94 ± 2
ϵ_{track}	$99.7\ ^{+0.3}_{-0.8}$
ϵ_{rec}	92.5 ± 3.0
ϵ_{ID}	82.9 ± 3.9
$\epsilon_{\mu\mu}$	50 ± 6

Table 8.18: Summary of the efficiencies and their uncertainties for the analysis dimuon events.

Chapter 9: Acceptance

9.1 Acceptance for Z' boson

Monte Carlo was used to estimate the acceptance of Z' bosons as a function of their mass. 5000 $Z' \to \mu^+\mu^-$ events, with Z' masses from 200 to 800 GeV/c^2, in 50 GeV/c^2 steps, were generated, simulated and reconstructed as described in Section 4.3.

Acceptance was defined to include both the fiducial and the kinematic cuts. Therefore, the total acceptance was the fraction of $p\bar{p} \to Z' \to \mu^+\mu^-$ events which had two CMUP muons with beam constrained transverse momentum (p_T(bc)) greater than 20 GeV. Here a "CMUP muon" meant a muon which had at least three hits in CMU and CMP reconstructable as stubs, and was linked to a track. Inefficiencies of the chambers, linking and tracking were accounted for in the reconstruction efficiencies. Although the chamber efficiencies were 100 %, in some cases it was found that a muon passed through the active region of the chambers and did not result in a reconstructed CMUP muon. These discrepancies were investigated [65] and the loss in the CMU was found to be caused by the spaces between the three modules inside the wedge. This loss was 1.6 %. In the CMP the losses occured at the "corners" where it was difficult to define the exact fiducial region; this amounted to 3.4 % [65]. The combined "efficiency" was 95.5 %. Because these losses were taken into account in the estimation of the reconstruction efficiency [84], the net acceptance was corrected by a factor of $(1/0.995)^2$ (the square factor accounts for there being two muons) in order to avoid double-counting these losses. The acceptance was found to be a function of the Z' mass and is displayed in Table 9.1 and Figure 9.1. The dimuon acceptance ranged from 4.8 $\pm$ 0.3 % for a Z' mass of 200 GeV/c^2 up to 11.7 $\pm$ 0.4 % for a Z' mass of 800 GeV/c^2, where the uncertainties given here are statistical, the systematic uncertainties were estimated as summarised in Section 12.3. The CMUP-CMUP acceptance increased with generated Z' mass. This is because more massive Z' are closer to being at rest in the detector

reference frame and therefore the decay particles, which are produced back-to-back in the Z' rest frame, are boosted less in the z direction (as viewed in the detector frame) and so more are detected in the central region, with $|\eta| < 0.6$.

$M_{Z'}$ (GeV/c^2)	Acceptance (%) without/with correction factor	
200	4.7 ± 0.3	4.8 ± 0.3
250	5.2 ± 0.3	5.3 ± 0.3
300	6.1 ± 0.3	6.1 ± 0.3
350	7.2 ± 0.4	7.3 ± 0.4
400	8.0 ± 0.4	8.1 ± 0.4
450	7.7 ± 0.4	7.7 ± 0.4
500	8.6 ± 0.4	8.7 ± 0.4
550	9.1 ± 0.4	9.2 ± 0.4
600	10.0 ± 0.4	10.1 ± 0.4
650	10.2 ± 0.4	10.4 ± 0.4
700	11.2 ± 0.4	11.3 ± 0.4
750	10.9 ± 0.4	11.0 ± 0.4
800	11.6 ± 0.5	11.7 ± 0.5

Table 9.1: Summary of dimuon acceptance for CMUP-CMUP as a function of Z' mass from Monte Carlo, where binomial statistical errors are shown.

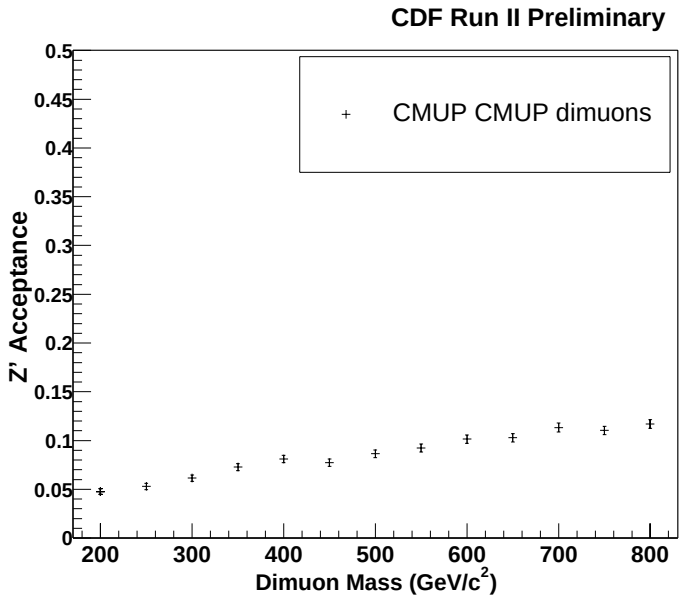

Figure 9.1: Acceptance as a function of Z' mass for Monte Carlo CMUP CMUP dimuon combinations of $Z' \to \mu\mu$.

9.2 Acceptance for Randall-Sundrum graviton resonances

The acceptance for the Randall-Sundrum graviton (RS) model was determined in a similar way to that for the Z'. However, the dependency of the acceptance on the width of graviton was first studied. Monte Carlo graviton samples were generated with a mass of 400 GeV/c^2 and with a range of width parameters ($k/\bar{M}_{Pl}$) from 0.002 to 0.1. The width parameter was chosen to be less than 0.1 for theoretical reasons, as described in Section 1.3.3.

For the range of width parameters studied, the width of the invariant mass distribution of the Randall-Sundrum graviton decay to dimuons was found to be dominated by the intrinsic detector resolution width, rather than the theoretical width, which is proportional to the square of the width parameter ($(k/\bar{M}_{Pl})^2$), as explained in Section 1.3.3. This is illustrated in Figure 9.2, which shows the invariant mass distribution for several different width parameters.

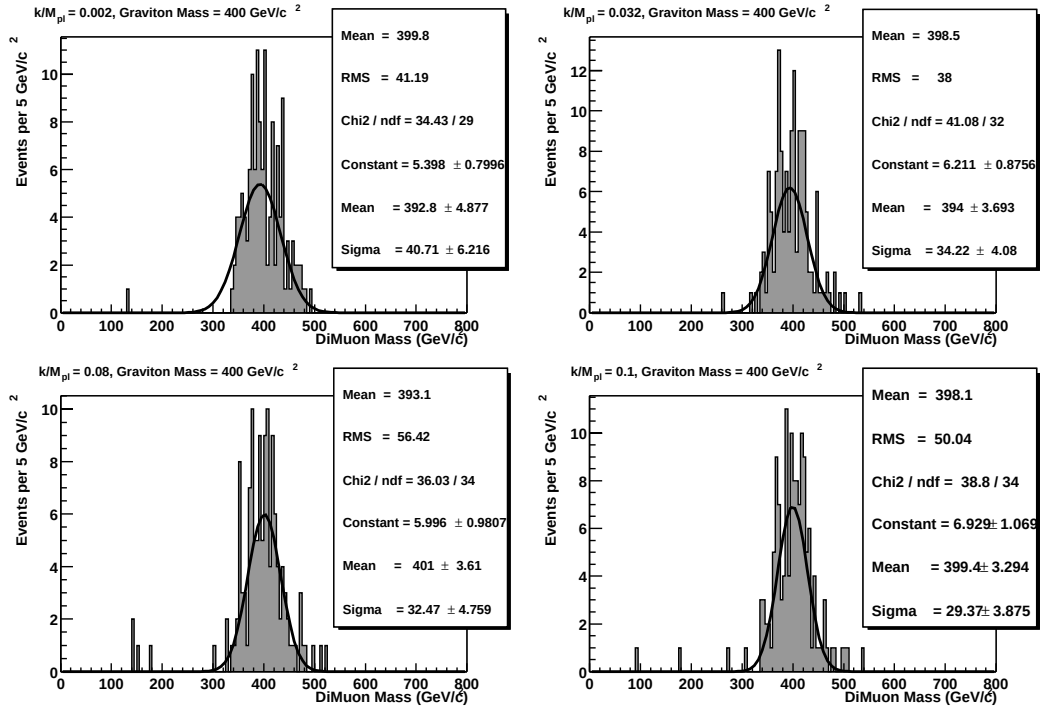

Figure 9.2: Width of a Monte Carlo generated Randall-Sundrum model graviton resonance of mass 400 GeV/c^2 for values of width parameter (k/$\bar{M}_{Pl}$) 0.002, 0.032, 0.08 and 0.1.

The acceptance for the 400 GeV/c^2 graviton samples are shown in Figure 9.3 and numerically in Table 9.2. The acceptance was found to be independent of the width parameter (k/$\bar{M}_{Pl}$) within statistical uncertainties. The acceptance used to determine the 95 % confidence level

upper production cross section limit times branching fraction of G $\rightarrow \mu^+ \mu^-$ was that calculated using gravitons with a width parameter ($k/\bar{M}_{Pl}$) of 0.1.

$k/\bar{M}_{Pl}$	Acceptance
0.002	0.105 ± 0.007
0.01	0.102 ± 0.007
0.032	0.101 ± 0.007
0.05	0.106 ± 0.007
0.06	0.109 ± 0.007
0.08	0.100 ± 0.007
0.1	0.099 ± 0.007

Table 9.2: Acceptance as a function of Randall-Sundrum model graviton width parameter ($k/\bar{M}_{Pl}$) for a fixed graviton mass of 400 GeV/c^2.

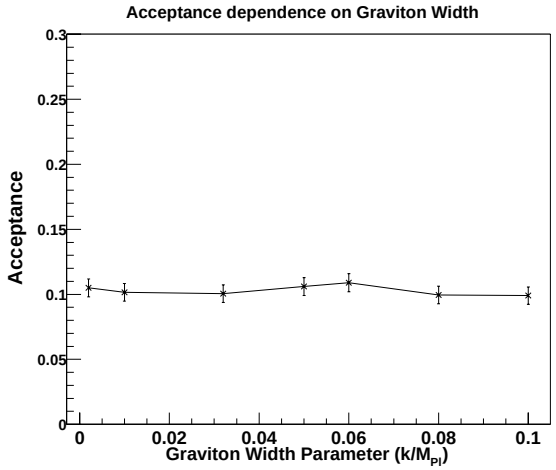

Figure 9.3: Dependence of the graviton acceptance on the Randall-Sundrum model graviton width parameter ($k/\bar{M}_{Pl}$) for a fixed graviton mass of 400 GeV/c^2, determined using Monte Carlo.

Monte Carlo was used to estimate the geometrical acceptance of gravitons as a function of their mass. 10000 G $\rightarrow \mu^+\mu^-$ events, with graviton masses from 200 to 600 GeV/c^2 in 50 GeV/c^2 steps with a width ($k/\bar{M}_{Pl}$) of 0.1, were generated, simulated and reconstructed as described in Section 4.3. As previously defined, the acceptance included both fiducial (CMUP) and kinematic cuts (p_T(bc) $>$ 20 GeV/c). The acceptance correction factor to avoid double counting errors, described on page 152, was also applied. The acceptance varied with the graviton mass and the results are displayed in Table 9.3 and illustrated in Figure 9.4. Figure 9.4 compares the acceptance of the Z' boson to the RS graviton as a function of dimuon invariant mass. The acceptance at 450 GeV/c^2 appeared to be slightly high (11.3 ± 0.3 % as opposed to 11.1 ±

0.3 % at 500 GeV/c^2), however, this was a statistical fluctuation and was within the statistical errors. When another sample of 500 events was generated with a graviton mass of 450 GeV/c^2 the acceptance found was 11.1 ± 0.3 %.

M_G (GeV/c^2)	Acceptance (%) without/with correction factor	
200	7.7 ± 0.3	7.8 ± 0.3
250	8.2 ± 0.3	8.3 ± 0.3
300	8.6 ± 0.3	8.7 ± 0.3
350	9.6 ± 0.3	9.7 ± 0.3
400	10.3 ± 0.3	10.5 ± 0.3
450	11.3 ± 0.3	11.5 ± 0.3
500	11.1 ± 0.3	11.2 ± 0.3
550	12.0 ± 0.3	12.1 ± 0.3
600	13.1 ± 0.3	13.3 ± 0.3
650	13.0 ± 0.3	13.2 ± 0.3
700	14.6 ± 0.4	14.7 ± 0.4
750	14.3 ± 0.4	14.4 ± 0.4
800	13.8 ± 0.3	13.9 ± 0.3

Table 9.3: Acceptance for RS graviton masses ranging from 200 to 600 GeV/c^2 and Width k/$\bar{M}_{Pl}$= 0.1. Binomial statistical errors were used for the acceptance errors.

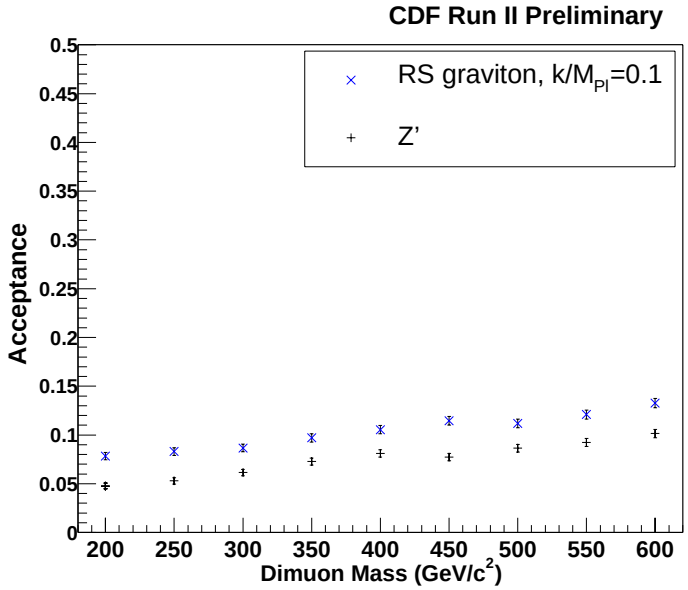

Figure 9.4: Acceptance of the Randall-Sundrum graviton (×) as a function of dimuon mass, compared to the Z' acceptance (+), for Monte Carlo CMUP-CMUP dimuons.

9.3 Comparison of Z' to graviton acceptance

From the Z' and Randall-Sundrum graviton Monte Carlo dimuon acceptance studies performed, it was found that there was a higher dimuon acceptance for Randall-Sundrum graviton decays than Z' decays, as illustrated in Figure 9.4. This is caused by the different spin of the Z' boson (spin 1) and the graviton (spin 2), consequently, their decay products have different angular distributions, as discussed on page 40 and illustrated in Figure 1.8.

9.4 Cross-check of the efficiency and acceptance

As a cross-check of the efficiency ($\epsilon_{\mu\mu}$) and the acceptance (A_{M_Z}), the Z cross section ($\sigma(Z^0)$) was estimated using Equation 9.1. The parameters used are summarised in Table 9.4 and their origin explained below.

$$\sigma(Z^0) = \frac{N_Z - N_{bkgd}}{\epsilon_{\mu\mu} \times A_{M_Z} \times \mathcal{L}} \tag{9.1}$$

Acceptance ($A_{(M_Z)}$)	2.9 ± 0.2 %
Efficiency ($\epsilon_{\mu\mu}$)	50 ± 6 %
Observed events (N_Z)	59 ± 7.7
Estimated background events	0.06 ± 0.01
Integrated luminosity ($\mathcal{L}$)	16.5 ± 1.0 pb^{-1}
Z boson cross section ($\sigma(Z^0)$.B)	
Run II at $\sqrt{s}$ = 1.96 TeV (16 pb^{-1})	247 ± 64 pb
Pythia at $\sqrt{s}$ = 1.96 TeV	237 pb
Run I at $\sqrt{s}$ = 1.8 TeV (110 pb^{-1})	233 ± 18 pb

Table 9.4: Z boson cross section and parameters used for the cross section calculation using the analysis dimuon data sample (16.5 pb^{-1}).

The dimuon event efficiency ($\epsilon_{\mu\mu}$) was 50 ± 6 %, obtained as outlined in Chapter 8. The acceptance (A) at the Z mass was determined to be 2.9 ± 0.2 %, where the uncertainty stated is statistical. This was measured using a sample of 5000 $Z^0 \rightarrow \mu\mu$ events generated, simulated and reconstructed as described in Section 4.3, and using the acceptance correction factor (explained

on page 152, Section 9.1). The number of events observed (N_Z) in the Z mass region (from 80 to 100 GeV/c^2) was 59 and the statistical error is the square root of this number. The number of background events (N_{bkgd}) expected in this region from *WW, WZ,* $Z/\gamma \rightarrow \tau\tau$ and $t\bar{t}$ is shown in Figure 11.4 in Section 11, and was 0.06 $\pm$ 0.01 (the error of 0.01, was determined by 0.06 $\times$ 0.15, where 0.15 was the uncertainty on the background calculated for a Z' of 200 GeV/c^2 as explained in Section 12.4 and includes the uncertainty in the efficiency and acceptance for the expected background). The cosmic ray background was assumed to be zero. The integrated luminosity ($\mathcal{L}$) was 16.5 $\pm$ 1.0 pb^{-1} (6 % systematic uncertainty).

The resulting estimation of the cross section ($\sigma(Z^0)$.B($Z^0 \rightarrow \mu\mu$)) was 247 $\pm$ 64 pb, where the errors were combined in quadrature. This can be compared to 233 $\pm$ 18 pb found in Run I at a centre of mass energy ($\sqrt{s}$) of 1.8 TeV [76]. The result obtained lies within the errors of the Run I result. The leading order cross section from Pythia at the Run II centre of mass energy ($\sqrt{s}$) of 1.96 TeV was found to be 182 pb. This was multiplied by a K factor[1] (K_f) of 1.3 to give $\sigma(Z^0)$.B($Z^0 \rightarrow \mu\mu$) 237 pb, where the K-factor is used to account for higher order effects, such as higher order QCD corrections. The cross section times branching ratio to dimuons obtained was also consistent with the cross section from Pythia. Table 9.4 summarises the cross sections obtained in Run I, from theory and this Run II estimate. Consistency of the Z^0 cross section obtained with the theoretical and Run I result implied that the measurement of both the efficiency and acceptance used in the analysis were of the correct order.

[1]The K-factor accounts for higher QCD corrections to the mass distribution, and is multiplied to the leading-order cross section. $K(M^2) = 1 + \frac{4}{3}(1 + \frac{4}{3}\pi^2)\ \alpha_s(M^2)/2\pi$, where α_s is the two loop QCD coupling. This K-factor is used as an event weight and was used in Run I analyses to calculate the Z^0 cross section [76].

Chapter 10: Signal Region

In order to set a cross section limit, an invariant mass window, called signal region, for each signal (Z' or Randall-Sundrum graviton) mass was selected. If a signal had been present, an excess of events over that expected from the Standard Model in this region would have been observed. Several factors were considered when the signal regions were chosen. These included the shape of the signal invariant mass distribution, the background contribution in the specified region and how well the signal region could be defined. To study the latter, the muon track resolution and its dependence on momentum was investigated; this is discussed in Section 10.1. The determination of the Z' boson signal region is explained in Section 10.2 and for Randall-Sundrum graviton in Section 10.3.

10.1 Momentum resolution

The muon momentum resolution (σ_{p_t}) has three components; from detector resolution, radiation and multiple scattering. These are related by Equation 10.1.

$$\left(\frac{\sigma_{p_t}}{p_t}\right)^2 = \left(\frac{\sigma_{p_t}}{p_t}\right)^2_{resolution} + \left(\frac{\sigma_{p_t}}{p_t}\right)^2_{radiation} + \left(\frac{\sigma_{p_t}}{p_t}\right)^2_{scattering} \tag{10.1}$$

For high p_t tracks the contribution from multiple scattering can be neglected and the fractional contribution from the radiation is a constant [52]. At very high p_t, the resolution of the transverse momentum is therefore dominated by the COT intrinsic resolution and by systematic effects, such as alignments. By comparing the reconstructed J/ψ mass against various COT track parameters, it was found that the misalignment biases in the COT were found to be negligible and therefore there were no residual misalignments in the COT that would affect the intrinsic resolution of the detector [52]. Consequently the high p_t muon resolution was predominantly limited by the intrinsic COT detector resolution, which depends on the transverse momentum,

as shown in Equation 10.2.

$$\left(\frac{\sigma_{p_T}}{p_T}\right)_{resolution} = c \times p_T \tag{10.2}$$

From Equation 10.2 it can be deduced that the error on the transverse momentum increases as the transverse momentum increases and hence, the resolution decreases. This can be qualitatively understood from comparing the resolution of two tracks. The transverse momentum of a particle is inversely proportional to the curvature of the track which it produces in COT detector (Equation 2.3). The higher the momentum of a muon, then the larger the radius of curvature of its track and therefore the straighter the track. Very high momentum muon tracks appear to be essentially straight lines within the resolution of the detector. The difference in momentum of two tracks is determined by the difference in the curvature of the two tracks. Consequently, the momentum of two very high energy muons can not be distinguished if their transverse momenta are sufficiently large, since they both appear as straight lines.

The momentum dependence of the momentum resolution was qualitatively verified using Monte Carlo. Samples were generated to have a specific transverse momentum (p_T) of 50, 100, 200, 300, 400 and 500 GeV/c. In order to study central muons, $|\eta|$ was restricted to be less than 0.6. The samples were generated with FakeEvent, simulated with cdfSim and reconstructed with version 3.13.0int4 of the offline code. Figure 10.1 shows the momentum distributions[1] after detector simulation and reconstruction for the Monte Carlo muons.

[1]Note that the distributions shown here are for the momentum (p_T), not $1/p_T$. Distributions in $1/p_T$ would be expected to be gaussian shaped.

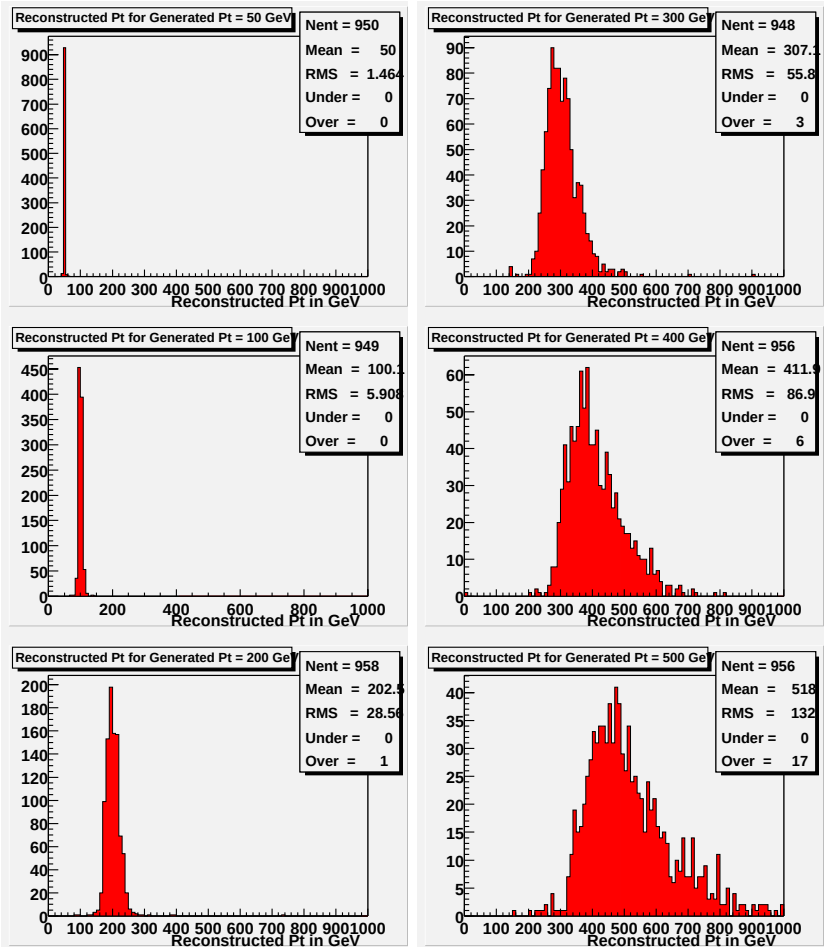

Figure 10.1: Transverse momentum distributions for Monte Carlo muons after detector reconstruction compared to the generated transverse momentum.

The reconstructed momentum was well-defined for the generated transverse momentum (p_T) of 50 GeV/c, which is shown in Figure 10.1. As the generated transverse momentum increased the reconstructed transverse momentum distribution became wider. From comparing the plots in Figure 10.1 the degradation of the momentum resolution as a function of muon transverse momentum can be observed. For example, a 400 GeV/c muon could be mistaken for a 350 GeV/c muon, as could a 500 GeV/c muon, however, it is much less likely that a 100 GeV/c muon would be reconstructed and therefore misidentified as a 50 GeV/c muon.

The invariant mass for high energy dimuons is calculated from the two muons' track information. Its calculation depends on three track parameters; the direction in the transverse plane (ϕ), the direction in the r-z view ($s = \cot(\theta)$) and the curvature (C), which is inversely proportional to the transverse momentum of the track (p_t) (shown in Equation 2.3). The error on the invariant mass (σ_M) is related to the error on these quantities, by Equation 10.3, and therefore depends on the single track transverse momentum resolution. Note that the fractional error on the transverse momentum is equal to the fractional error on the curvature; $\frac{\sigma_{P_{t1}}}{P_{t1}} = \frac{\sigma_C}{C}$, which can be derived from Equation 2.3.

$$\left(\frac{\sigma_M}{M}\right)^2 = \left(\frac{\sigma_{P_{t1}}}{P_{t1}}\right)^2 + \left(\frac{\sigma_{P_{t2}}}{P_{t2}}\right)^2 + \left[sin^2\Delta\phi\left(\sigma^2_{\phi_{0_1}} + \sigma^2_{\phi_{0_1}}\right) + (s_1 - s_2)^2\left(\sigma^2_{\phi_{0_1}} + \sigma^2_{\phi_{0_1}}\right)\right]\frac{2P_{t1}P_{t2}}{M^2}. \tag{10.3}$$

For back-to-back tracks with large opening angles, which are expected from the signal event, $\Delta\phi \sim 180^\circ$ and $s_1 \sim s_2$, Equation 10.3 reduces to Equation 10.4 if $P_{t1} \sim P_{t2} \sim P_t$.

$$\left(\frac{\sigma_M}{M}\right)^2 \sim 2\left(\frac{\sigma_{P_t}}{P_t}\right)^2 \tag{10.4}$$

Therefore the resolution of the invariant mass is dependent on the resolution of the transverse momentum. The transverse momenta of particles from a decay depend on the mass of the particle which decays. The higher the mass of the original particle, the larger the momenta of the particles produced in its decay[2]. Because the transverse momentum resolution of the decay particles decreases with increasing transverse momentum, it is expected that the invariant mass resolution will decrease the higher the mass of the particle which decays. The resolution of the dimuon invariant mass distribution as a function of generated mass for the Z' boson and the graviton was studied using Monte Carlo and the results are presented in Section 10.2 and 10.3 respectively.

[2]The mean momenta of dimuons from Z' boson decay ($p^{\bar{\mu}}$) was found to be related to the mass of the Z' boson ($M_{Z'}$) by: $p^{\bar{\mu}} = \frac{1.1M_{Z'}}{2}$ [75]. The transverse momentum of a muon (p_T^{μ}) is related to its momentum by $p^{\mu} \times \sin\theta$, where θ is measured by the COT track associated with the muon.

10.2 Z' boson signal region

To select an invariant mass signal region for the Z' search, the invariant mass distribution for the Z' signal was determined as a function of the Z' boson mass.

5000 Z' events were generated using Pythia and simulated with cdfSim, then reconstructed as described in Section 4.3. The invariant mass distribution for each Z' mass, after the application of muon identification cuts, are shown in Figure 10.2 and Figure 10.3. Gaussian fits were made to the distributions in order to appreciate quantitatively the increasing width of the distributions. For masses from 200 up to 550 GeV/c^2 solid arrows either side of the peak indicate the region $\pm$ 3 standard deviations (σ) from the mean. The mean and standard deviation for each Z' mass are displayed in Table 10.1. The width of the gaussian fit increases with the Z' invariant mass. This was attributed to the resolution dependency. In all cases the signal was found to lie predominantly above 150 GeV/c^2, the position of which is indicated by the dotted arrows in Figure 10.2 and Figure 10.3. Also, below 150 GeV/c^2 there is significantly more background from Standard Model processes, shown in Table 11.2 in Section 11, so 150 GeV/c^2 was taken as the lower bound. Because the momentum resolution degrades for very high momentum muons, rather than taking a two sided region around the signal distribution, a one sided region was defined and no upper limit was imposed. Not defining an upper limit did not significantly increase the expected background, since very few Standard Model processes predict very high momentum dimuons (see Chapter 11).

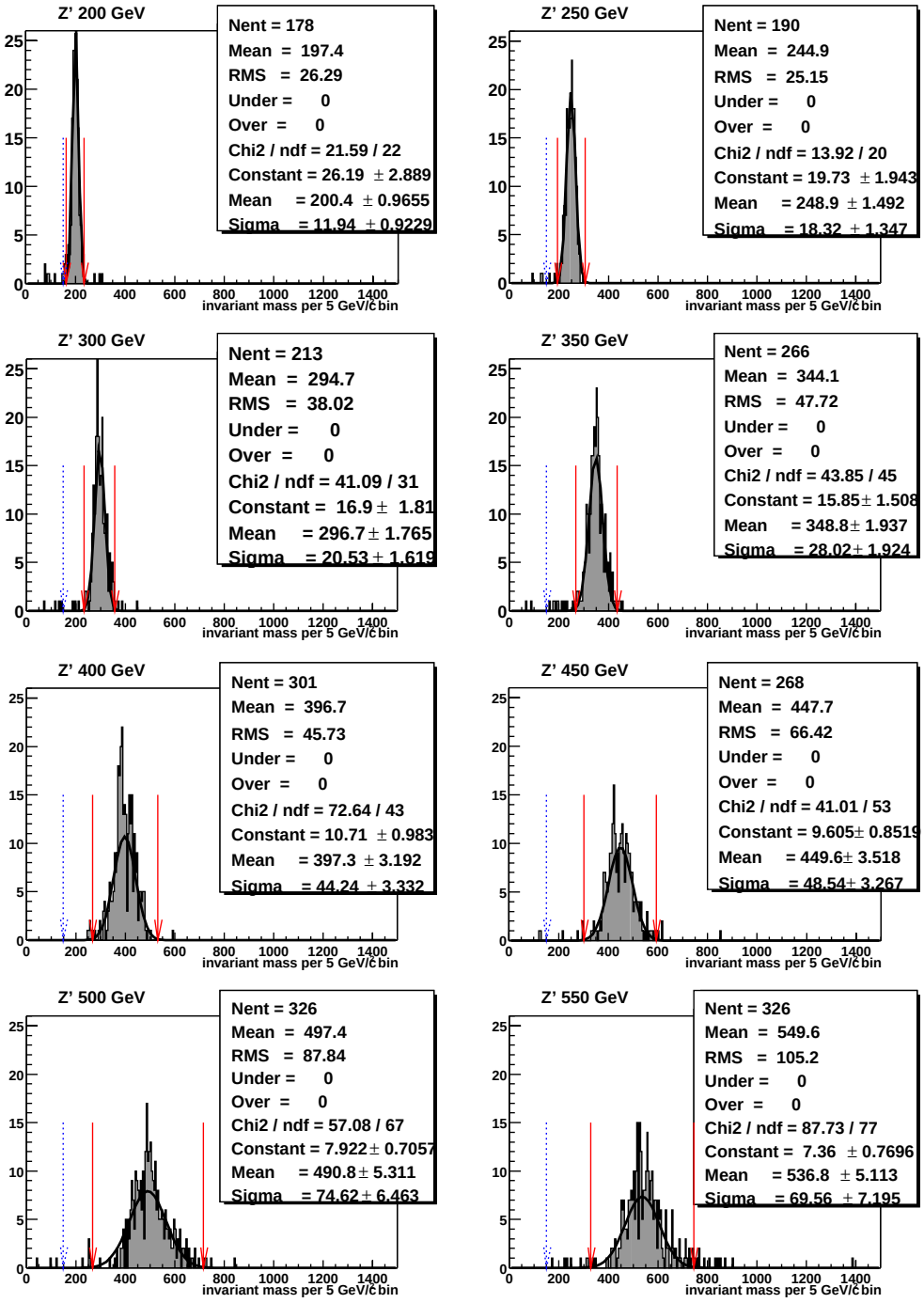

Figure 10.2: Invariant mass distribution of $Z' \to \mu\mu$ Monte Carlo. For each Z' mass a gaussian was fitted to the Z' signal sample. The two arrows either side of the peaks indicate the region $\pm$ 3 standard deviations from the mean and the dotted arrows at 150 GeV/c^2 indicate the lower bound of the signal region.

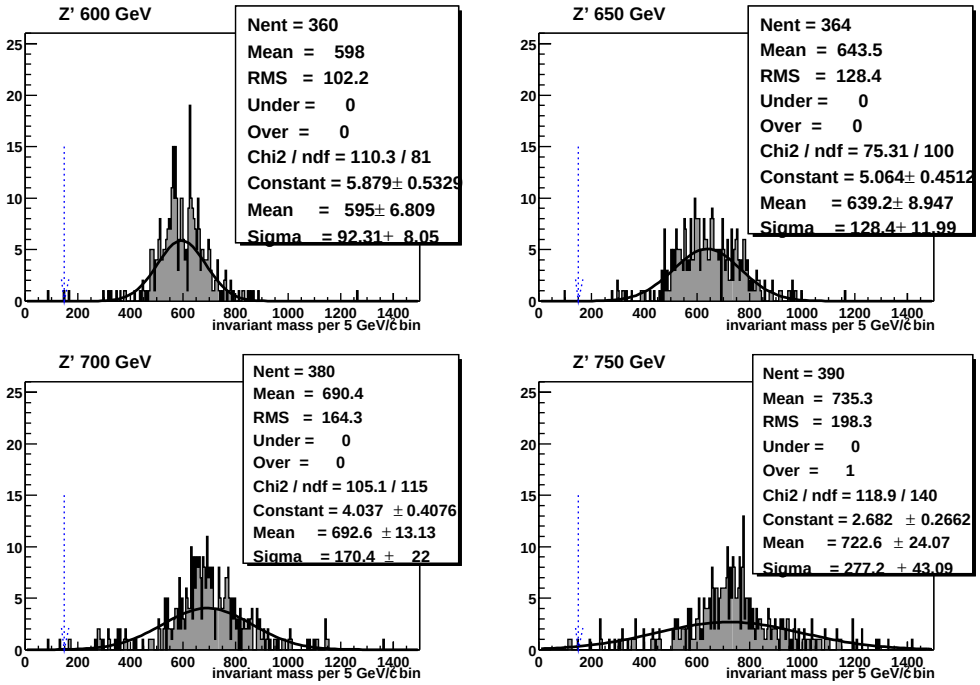

Figure 10.3: Invariant mass distribution of $Z' \to \mu\mu$ Monte Carlo. For each Z' mass a gaussian was fitted to the Z' signal sample. The arrows indicate the lower bound of the signal region, at 150 GeV/c^2.

$M_{Z'}$ GeV/c^2	mean GeV/c^2	$\sigma_{M_{Z'}}$ GeV/c^2
200	200	12
250	249	18
350	349	28
400	397	44
450	450	48
500	491	75
550	537	70
600	595	92
650	639	128
700	693	170
750	723	277
800	789	313

Table 10.1: Comparison of the reconstructed Monte Carlo Z' mean and standard deviation ($\sigma_{M_{Z'}}$) of the gaussian distribution fit to the invariant mass distribution as a function of mass ($M_{Z'}$) generated.

10.3 Randall-Sundrum graviton signal region

By analogy to the Z' search, a one sided signal region with a lower limit of 150 GeV/c^2 was used for for all graviton masses. This was because, similarly to the Z' signal, the dimuon invariant mass distributions were found to become wider the higher the graviton mass, due to the worsening muon transverse momentum resolution at high momentum. This is shown in Figure 10.4, which displays the dimuon invariant mass distributions after detector reconstruction for gravitons of mass from 100 to 800 GeV/c^2, generated using Pythia with width parameter $k/\bar{M}_{Pl} = 0.002$. The gaussian width of the resonance reconstructed after detector simulation (σ_{M_G}) is displayed in Table 10.2. For graviton masses above 200 GeV/c^2 the signal was found to lie predominantly above 150 GeV/c^2. So the signal region was, as for the Z' search, set to be above 150 GeV/c^2.

M_G (GeV/c^2)	σ_{M_G} (GeV/c^2)
100	2.74
150	5.71
200	8.01
250	14.5
300	19.6
350	23.9
400	33.8
450	41.1
500	49.4
550	58.2
600	72.0
650	95.2
700	98.4
750	152
800	139

Table 10.2: Graviton mass (M_G) generated using Monte Carlo and the gaussian width observed (σ_{M_G}) after detector effects for graviton resonances with $k/\bar{M}_{Pl} = 0.002$, shown to three significant figures.

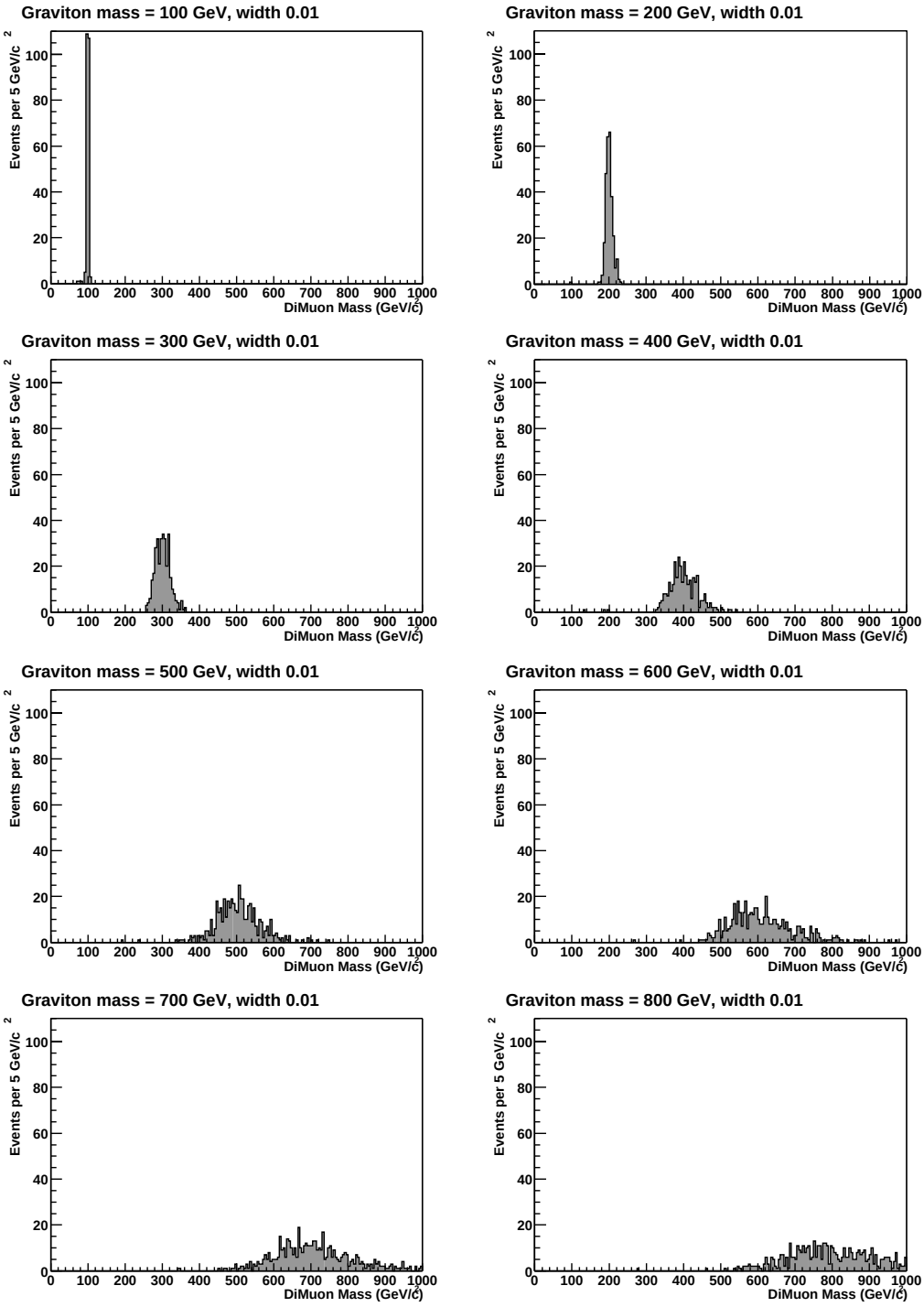

Figure 10.4: Dimuon invariant mass distribution of G $\rightarrow \mu^+ \mu^-$ with $k/\bar{M}_{Pl} = 0.002$ (where width in the figure heading refers to $k/\bar{M}_{Pl}/0.54 = 0.01$) for graviton masses from 100 up to 800 GeV^2.

Chapter 11: Expected Background

In order to set a limit, the expected number of background dimuons in the signal region was determined. The background was classified to be from four main sources;

- Drell-Yan,
- $b\bar{b}$, $t\bar{t}$, $c\bar{c}$, diboson productions (WW, WZ and ZZ) and $Z \to \tau^+\tau^-$,
- charge symmetric background and
- cosmic rays.

11.1 Drell-Yan

After cosmic ray removal, Drell-Yan ($q\bar{q} \to \mathrm{Z}/\gamma \to l^+l^-$) is the major background in high transverse momentum dimuon searches. To estimate this background, 29907 Drell-Yan events were generated with $p_T > 18$ GeV/c^2 and $|\eta| < 3$. They were generated using Pythia, then simulated and reconstructed as described in Section 4.3. The Drell-Yan distribution was normalised, by scaling it such that the number of dimuon events in the Z peak region, taken to be 80 to 100 GeV/c^2, was equal to the number in the data sample for the same Z peak region. The normalised Drell-Yan distribution and the contributions from other backgrounds in 50 GeV/c^2 invariant mass bins are shown, at the end of this chapter, in Figure 11.3 and also with finer binning in Figure 11.4. The expected background contribution per 50 GeV/c^2 mass bin is displayed in Table 11.2. After scaling there were 0.44 Drell-Yan events expected in the data sample above an invariant mass of 150 GeV/c^2.

11.2 $b\bar{b}$, $t\bar{t}$, $c\bar{c}$, $Z/\gamma \to \tau^+\tau^-$ and diboson productions

Backgrounds processes other than from Drell-Yan which produce dimuons are $b\bar{b}$, $t\bar{t}$, $c\bar{c}$, diboson productions (WW, WZ and ZZ) and $Z/\gamma \to \tau^+\tau^-$. This background can be estimated either by finding the number of electron-muon events in the data sample and assuming that half of these events gives an estimate of the background in the $\mu^+\mu^-$ channel, or alternatively by using Monte Carlo. The latter method was used here, because there was a very limited amount of $e\mu$ data available.

WW, WZ, $Z/\gamma \to \tau^+\tau^-$ and $t\bar{t}$ events were generated using Pythia, simulated using cdfSim and reconstructed using version 4.5.3 of the offline code as described in Section 4.3. These events were relatively normalised to the DY cross section (σ_{DY}) and to the normalised number of Drell-Yan events (N_{DYgen}), using Equation 11.1, which is derived in Appendix F.

$$s_X = \frac{s_{DY} \times N_{DYgen} \times \sigma_X}{N_{Xgen} \times \sigma_{DY}} \tag{11.1}$$

In Equation 11.1 s_X is the relative scaling factor for the background process (X) with known cross section (σ_X), N_{Xgen} the number of events generated, N_{DYgen} the number of Drell-Yan events generated and s_{DY} the Drell-Yan scaling factor. Table 11.1 summarises the background process cross sections (from Pythia), the number of events generated and the scaling factors used to determine the background contribution for each process. The number of expected background events per 50 GeV/c^2 mass bin are shown in Table 11.2. The expected background contribution from these and from the Drell-Yan process, together with the data, are plotted in Figure 11.3 and Figure 11.4. The background from these processes was small (0.02 above 150 GeV/c^2), which was consistent with the statement made in the Run I Z' boson search, that the background contribution, other than from Drell-Yan, which produced dilepton final states was negligible [20].

Process (X)	σ_X (pb)	N_{gen}	s_X
DY $\rightarrow \mu\mu$	167	29907	0.867
$W^+W^- \rightarrow \mu^+\mu^-\ \nu_\mu\ \bar{\nu_\mu}$	0.945	1445	0.0104
WZ where $Z \rightarrow \mu\mu$	0.0294	2861	0.000163
$Z/\gamma \rightarrow \tau\ \tau\ \mu^+\mu^-\ \nu_\mu\ \bar{\nu_\mu}\nu_\tau\ \bar{\nu_\tau}$	25.2	20100	0.0198
$\bar{t}\ t \rightarrow \mu^+\mu^-\ \nu_\mu\ \bar{\nu_\mu}\bar{b}\ b$	0.671	5000	0.00212

Table 11.1: Background process (X) cross sections (σ_X), the number of Monte Carlo events generated (N_{gen}) and the scaling factors (s_X) used to determine the background contribution for each process. σ_X and s_X are shown to three significant figures.

Invariant Mass	Background Process					Total in bin	Total above bin minimum
	DY	W^+W^-	WZ	$Z/\gamma \rightarrow \tau\ \tau$	$t\,\bar{t}$		
	Number of dimuon events						
(GeV/c^2)							
50 - 100	64.7	0.0207	0.0153	1.76	0.0255	66.6	70.0
100 - 150	2.91	0	0.00163	0.0198	0.0255	2.96	3.42
150 - 200	0.265	0.0104	0.000326	0	0.0085	0.284	0.463
200 - 250	0.0883	0	0	0	0	0.0883	0.179
250 - 300	0	0	0.000163	0	0.0021	0.0023	0.0906
300 - 350	0.0883	0	0	0	0	0.0883	0.0883
350 - 400	0	0	0	0	0	0	0
Above 400	0	0	0	0	0	0	0

Table 11.2: Number of expected background events (to three significant figures) in 16.5 pb^{-1} data, in 50 GeV invariant mass bins from Drell-Yan (DY), W^+W^-, WZ, $Z/\gamma \rightarrow \tau\ \tau$ and $t\bar{t}$ processes. The last column shows the total number of background events expected above the minimum mass of the mass range.

11.3 Charge symmetric

11.3.1 Same-sign method

Charge symmetric background typically originates from jets, hadronic punch-through and decays in flight of pions and kaons. This background can be estimated by assuming that the number of opposite charge dimuons is equal to the number of same charge dimuons, and hence can be removed by subtracting the number of same sign charge pairs from the number of opposite charge pairs[1]. In the signal sample none of the 77 dimuons events contained two muons with the same sign. From this it was inferred that the background from jets, punch-throughs or decays

[1]Distinguishing the sign of curvature of the track, and therefore the charge, becomes difficult for very high momenta muons, which have very straight tracks. The highest transverse momentum track in the dimuon analysis sample had a beam constrained transverse momentum of 87.5 GeV/c. Therefore this was not a problem for the muons in the analysis.

in flight was negligible.

11.3.2 Isolation vs isolation background estimation

An estimate of the jet-jet and hadronic background (QCD background) was also made from the non-isolated muons in the dimuon analysis sample. It was assumed that the isolation variables of the two muons, $Iso_{\mu 1}$ and $Iso_{\mu 2}$, (defined in Section 4.1.3) were uncorrelated. Thus it was supposed that the ratio of the number of background events at small calorimeter isolation for one muon ($Iso_{\mu 1}$) to the number at large $Iso_{\mu 1}$ was the same when the calorimeter isolation for the other muon ($Iso_{\mu 2}$) was small as when it was large, so that Equation 11.2 could be applied.

$$N_{QCD}^{S,S} = \frac{N^{l,s} \times N^{s,l}}{N^{l,l}} \tag{11.2}$$

Here, "small" was defined as $Iso_{\mu 1} < 4$ GeV and "large" as $Iso_{\mu 1} > 6$ GeV. The selection criteria applied to the dimuon sample were the same as those used for the dimuon analysis sample, except the calorimeter isolation cut was not applied to either muon. The sample consisted of 80 dimuon pairs. An invariant mass distribution for these events is shown in Figure 11.1 and the distribution of the isolation variables is shown in Figure 11.2.

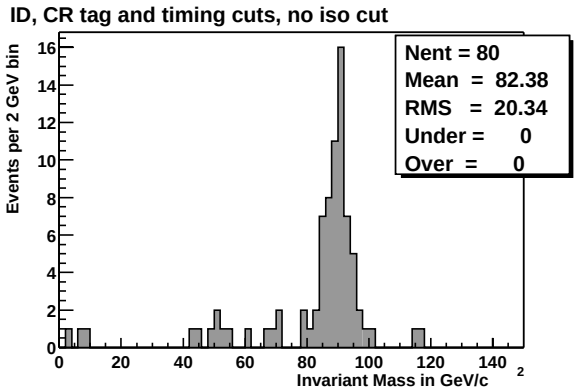

Figure 11.1: Invariant mass distribution for the analysis dimuon data sample (16.5 pb^{-1}), with all cuts applied except the isolation cut.

There was one event in the large-large isolation region, no events in the small-large isolation region and one in the large-small isolation region ($N^{l,s}$=1 $N^{s,l}$=0 $N^{l,l}$= 1). After substitution

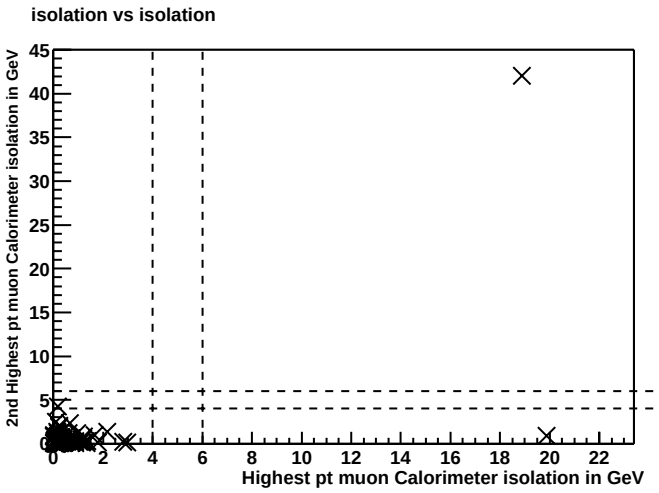

Figure 11.2: Isolation vs isolation for the analysis dimuon data sample (16.5 pb^{-1}).

into Equation 11.2 ($N_{QCD}^{S,S} = 1 \times 0 \ /1 = 0$), it was estimated that there was no non-isolated background in the sample. This result was consistent with the background estimated using the same-sign method. The QCD background was therefore assumed to be negligible, which was consistent with the assumption made in Run I that the backgrounds other than from the Drell-Yan process were negligible[2].

11.4 Cosmic ray background

The cosmic ray background was estimated by using a cosmic ray sample to determine the percentage of cosmic ray events which the cosmic ray track and timing cuts allowed to pass. The number of cosmic rays in the signal region of the sample was then approximated, and an estimate of the number of cosmic rays remaining after the application of the cosmic ray cuts

[2]The lack of observed jet-jet or hadronic background could have been interpreted as being less than one event in 77, and an upper limit on the number of expected background events at a particular confidence level could have been estimated rather than assuming no background contribution from these processes. The effect of increasing the number of background events observed, given no events had been observed was investigated. The results showed that the 95 % confidence level upper limit on the number calculated by Poilim ($N_{95\%}$) (as described in Section 13.1.3) did not change signficantly if the number of background events was increased, in both the case with zero uncertainty and for a relative uncertainty on the signal acceptance of 0.14 and an uncertainty on the background of 0.06 events. For the former case, with zero uncertainties, changing the background from 0.1 to 7 events resulted in $N_{95\%}$ increasing slightly from 2.995 $\pm$ 0.004 to 3.001 $\pm$ 0.004 events and including uncertainties, $N_{95\%}$ changed from 3.089 $\pm$ 0.001 to 3.090 $\pm$ 0.001 events. Therefore it was concluded that neglecting this background contribution would not significantly affect the values calculated for $N_{95\%}$.

was made.

To find the fraction of cosmic ray events which the cosmic ray timing cuts allowed to pass, a cosmic ray sample was selected using the cosmic ray track cuts. The analysis dimuon CMUP CMUP sample was used, as described in Section 4.1.3, without the inclusion of the cosmic ray cuts. Instead, in order to create a cosmic ray sample, a "reverse" impact parameter cut was imposed, which required both muons to have an impact parameter of greater than 0.2 cm. This sample consisted of 1409 dimuons, of which 68 passed the cosmic ray timing cuts. Therefore the it was determined that the cosmic ray timing cuts passed 4.8 % of the cosmic ray events.

By analogy, the percentage of cosmic ray events which the cosmic ray track cuts allowed to pass, was ascertained using a cosmic ray sample selected by the cosmic ray timing cuts. In this case, the dimuon data sample was selected from the dimuon data sample described in Section 4.1.2 and consisted of CMU, CMP and CMX muon combinations with the track-stub matching requirements $|\Delta X_{CMU}| < 3$ cm, $|\Delta X_{CMU}| < 6$ cm and $|\Delta X_{CMU}| < 10$ cm respectively. The muon identification cuts displayed in Table 4.3 were applied, with the exception that no cosmic ray cuts were applied. The events were then required to fail one of the time difference cuts; $\Delta ToF_{Upper-Lower} <$ -5 ns or $\Delta hadTDC_{Upper-Lower} <$ -20 ns. 5242 dimuons passed these requirements, of which 3 passed the cosmic ray track cuts. Therefore the cosmic ray track cuts were deemed to pass 0.06 % of the cosmic ray events.

The cosmic ray contamination in the signal region was estimated from the number of dimuon events in this region (above 150 GeV/c^2) in the dimuon analysis data sample, which passed all the selection criteria except the cosmic ray cuts. It was assumed that this sample of 288 events were potential cosmic rays and the number of cosmic rays expected to pass both the cosmic ray track and timing cuts was calculated (288 $\times$ 0.06 % $\times$ 4.8 %) to be 0.008 events. Therefore it was concluded that the cosmic ray contamination in the signal region above 150 GeV/c^2 was expected to be 0.01 events.

11.5 Total expected background

The total expected background and the data is shown in Figure 11.3 in 50 GeV/c^2 mass bins and also in finer bins in Figure 11.4 (with the exception that the cosmic ray contribution is not included in the figures). The background processes producing dimuons were the Drell-Yan process, $Z/\gamma \rightarrow \tau\ \tau$, WZ, W^+W^-, $\bar{t}\ t$. No significant deviations from the expected background were observed and therefore the results were not inconsistent with the Standard Model. This data was used to set limits on new physics processes. Upper limits on the cross section times branching ratio of both Z' and Randall-Sundrum model gravitons decaying to dimuons were obtained, as described in Chapter 13.

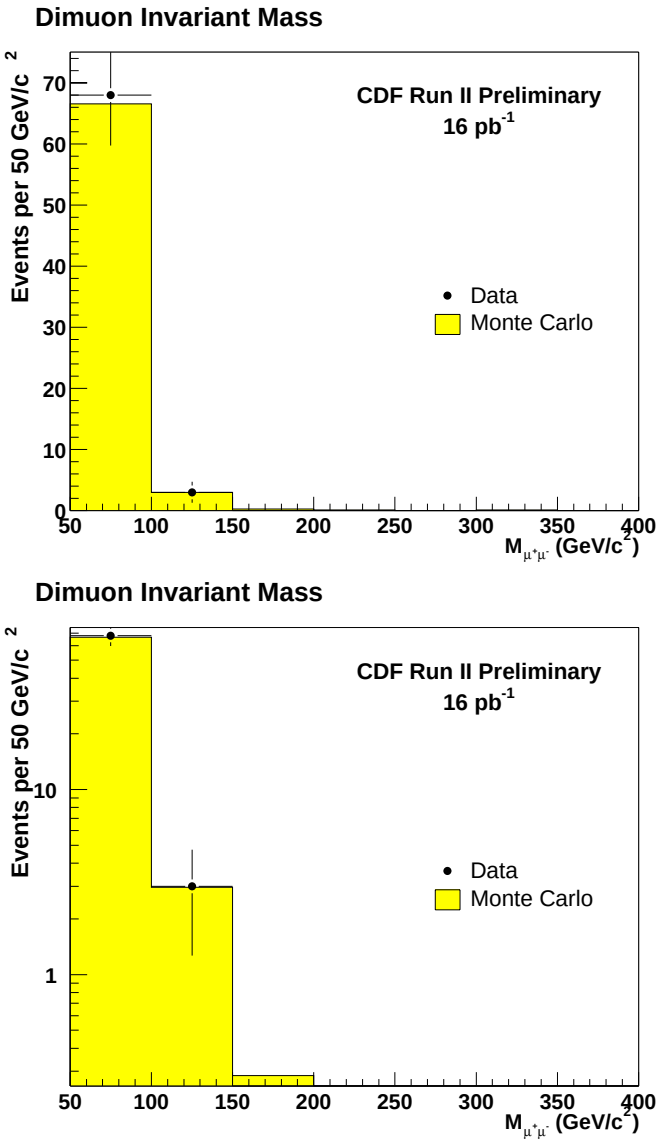

Figure 11.3: Expected background (estimated from Monte Carlo and normalised to data) (shaded yellow) and data (points) with 16 pb^{-1} data as a function of dimuon invariant mass per 50 GeV/c^2 mass bin. The lower plot shows the expected background on a log scale.

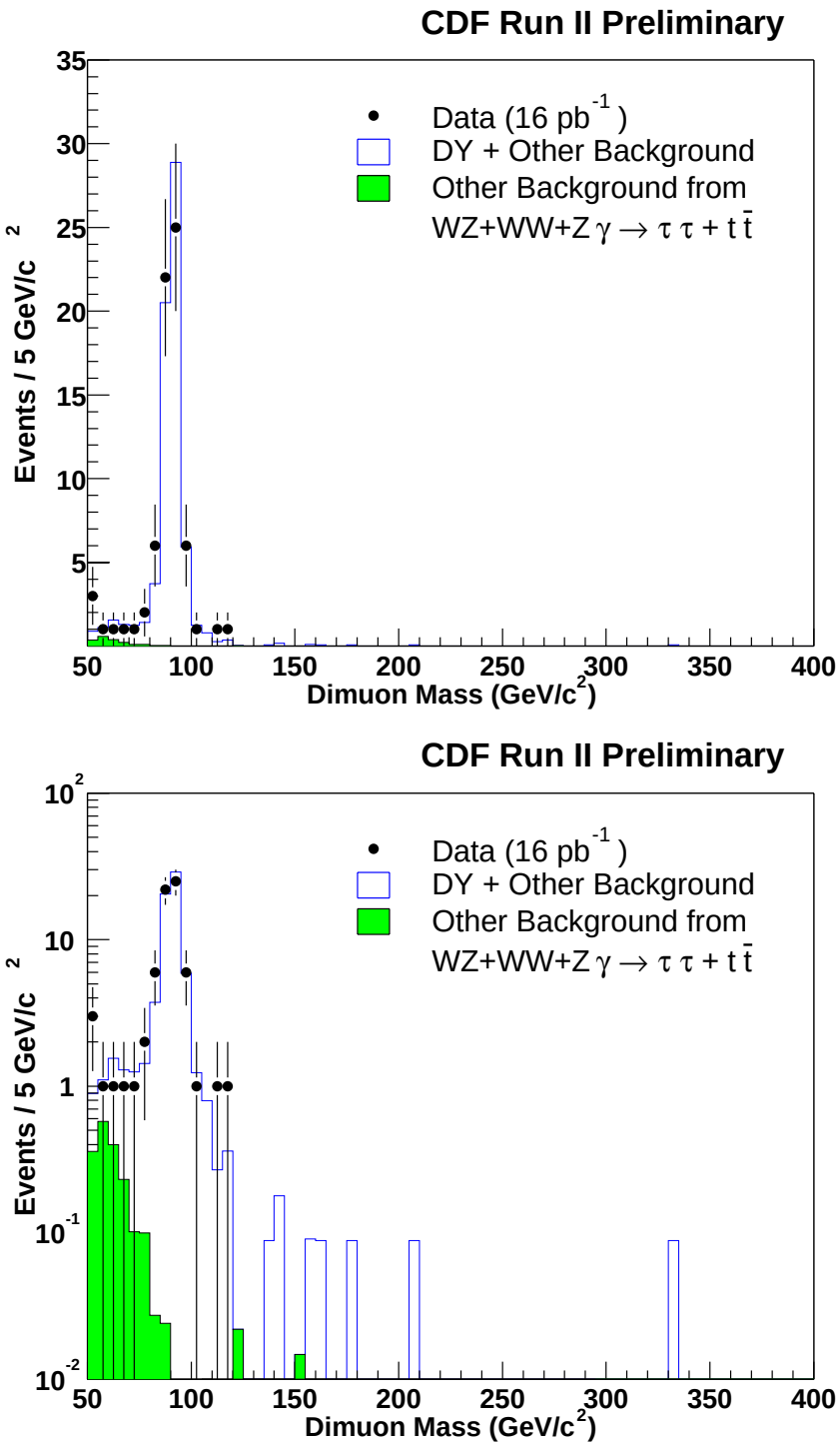

Figure 11.4: Expected background (estimated from Monte Carlo and normalised to data) (line) and data (points) with 16 pb^{-1} data as a function of dimuon invariant mass. The lower plot shows the expected background on a log scale.

Chapter 12: Uncertainties

In order to determine an upper limit on the number of signal events present in the sample, given the number of observed events and assuming an expected number of background events, the uncertainty on both the number of expected background events and on the signal acceptance was calculated. The following sources of uncertainties were considered:

- uncertainty on the efficiency (Section 12.1),
- uncertainty on the luminosity (Section 12.2) and
- uncertainty on the acceptance (Section 12.3).

12.1 Uncertainty on the efficiency

The uncertainty of the measured efficiency ($\epsilon_{\mu\mu}$) was composed of the statistical and systematic uncertainties of the efficiency for the muon identification cuts, the cosmic ray timing cuts, the cosmic ray track cuts, the fiducial (z_0) cut, trigger, track reconstruction and muon reconstruction. These uncertainties were combined in quadrature. The uncertainty on each measured efficiency was described in Chapter 8 and is summarised in Table 8.18. The total relative uncertainty on the efficiency was calculated to be 12 %. This was dominated by the statistial uncertainty, due to the small data samples, on the muon identification efficiency and the cosmic ray track cut efficiency.

12.2 Uncertainty on the luminosity

The systematic uncertainty on luminosity was of order 6 %, as reported by the CDF luminosity group [62]. The luminosity was measured using two cherenkov luminosity counters (CLC), positioned either side of the interaction region, located at a small angle from the beam pipe

inside the plugs of the CDF (within a cone angle of 3° from the centre of the detector). The CLCs were used to detect $p\bar{p}$ inelastic processes caused by beam interactions, from which the luminosity was calculated. Several sources contributed to the uncertainty in the luminosity measurement. The dominant source was from the CLC acceptance to the $p\bar{p}$ inelastic processes (4.0 %), which had contributions from the geometry of the detector, beam offset and generators used to calculate the acceptance to inelastic processes. Other factors which also contributed were the total inelastic cross-section, from CDF Run I, scaled to Run II energy (2.5 %), and the detector stability (2.0 %) [62].

12.3 Uncertainty on the acceptance

The statistical uncertainty on the acceptance was determined by the number of Monte Carlo events used to calculate the acceptance. The statistical uncertainties as a function of mass are displayed in Table 9.1 and 9.3 for the Z' and graviton respectively.

The systematic uncertainty on the acceptance was dependent on the verity of the simulation and Monte Carlo used to calculate the acceptance, compared to the real detector and signal events. The acceptance consisted of two components; it required both muons to have a beam constrained transverse momentum (p_T(bc)) greater than 20 GeV and have stubs in the CMUP chambers. Three sources of systematic uncertainty were considered:

- momentum resolution,
- fiducial acceptance and
- parton distribution functions (pdfs).

The kinematic requirement, of $p_T(\text{bc}) > 20$ GeV/c for both muons, was sensitive to the resolution and the momentum scale of the simulation compared to the detector. The relative systematic uncertainty for this component of the acceptance was estimated by comparing the position of the Z peak in a $Z \to \mu\mu$ Monte Carlo sample to the position in a data sample, and

also by comparing the lepton p_T distribution of a W $\rightarrow \mu\nu$ Monte Carlo sample to that of a W $\rightarrow \mu\nu$ data sample. The relative uncertainty was determined to be 1.8 % [65].

The acceptance CMUP stub requirement restricted $|\eta| < 0.6$. The acceptance therefore relied on a realistic and correct detector geometry in the simulation. The systematic uncertainty due to misalignment or inaccurate modelling of the detector was estimated by comparing the differences in the distributions of the (CMU and CMP) stub ϕ and z position of a $W \rightarrow \mu\nu$ data sample to Monte Carlo. A relative systematic uncertainty of 1.5 % was determined [65].

The acceptance was calculated using Monte Carlo samples and the results were therefore dependent on the beam energy, vertex distribution and the parton distribution functions (pdfs) used to generate the signal samples. The latter was considered to be the dominant source of systematic uncertainty [65] and the uncertainty due to this was calculated by comparing the acceptance of samples generated with different pdfs; CTEQ5L and CTEQ3M [71]. 5000 Z' events were generated at the Z' mass of 250, 300 and 600 GeV/c^2 with each pdf. The difference in the acceptance for the two pdfs at each mass was taken as the systematic uncertainty. The results are shown in Table 12.1. Similarly, for the RS model, 5000 RS model graviton events were generated with a width (k/$\bar{M}_{Pl}$) of 0.1 and masses 200, 250 and 300 GeV/c^2 using Pythia with CTEQ5L and CTEQ3M. The difference in the acceptance was studied and the results are displayed in Table 12.2. The uncertainties were assumed to be independent of mass and the average relative uncertainty in the acceptance was 5.7 % for the Z' boson and 10.1 % for the graviton. The uncertainty was larger for the graviton than for the Z' boson due to the uncertainty in the gluon distribution which contributes in graviton production.

$M_{Z'}$	Acceptance (A_{pdf})		Systematic ($\sigma_{A_{pdf}}$)	Relative ($\sigma_{A_{pdf}}/A_{pdf}$)
(GeV/c^2)	CTEQ5L	CTEQ3M	uncertainty (%)	uncertainty (%)
250	262/5000 = 0.0524	274/5000 = 0.055	0.26	5.0
300	304/5000 = 0.0608	280/5000 = 0.056	0.48	7.9
600	502/5000 = 0.1004	481/5000 = 0.0962	0.42	4.2

Table 12.1: Systematic uncertainty in the acceptance caused by a change in Monte Carlo parton distribution function (CTEQ5L to CTEQ3M) for Z' masses (M_Z) 250, 300 and 600 GeV/c^2.

M_G (GeV/c^2)	Acceptance (A_{pdf}) CTEQ5L	CTEQ3M	Systematic ($\sigma_{A_{pdf}}$) uncertainty (%)	Relative ($\sigma_{A_{pdf}}/A_{pdf}$) uncertainty (%)
200	387/5000 = 0.077	419/5000 = 0.0838	0.64	10.1
250	411/5000 = 0.082	450/5000 = 0.09	0.78	9.5
300	429/5000 = 0.086	475/5000 = 0.095	0.92	10.7

Table 12.2: Systematic uncertainty in the acceptance caused by a change in Monte Carlo parton distribution function (CTEQ5L to CTEQ3M) for RS model graviton masses (M_G) 200, 250 and 300 GeV/c^2.

The relative statistical and systematic uncertainties on the acceptance were combined in quadrature. Although the systematic uncertainties were assumed to be independent of mass, the resulting uncertainty on the acceptance was dependent on the mass of the Z'/graviton due to the statistical uncertainty. The statistical, systematic and the total uncertainty on the acceptance (A) are shown in left-hand columns of Table 12.3 and 12.4 for the Z' and graviton respectively.

$M_{Z'}$ (GeV/c^2)	Relative uncertainty (%) A			ϵ	$\mathcal{L}$	ϵ A	ϵ A $\mathcal{L}$
	Statistical	Systematic	Combined			σ_B/B	σ_S/S
200	6.3	6.2	8.8	12	6	14.9	16.0
250	5.7	6.2	8.4	12	6	14.6	15.8
300	4.9	6.2	7.9	12	6	14.4	15.6
350	5.5	6.2	8.3	12	6	14.6	15.8
400	4.9	6.2	7.9	12	6	14.4	15.6
450	5.2	6.2	8.1	12	6	14.5	15.7
500	4.6	6.2	7.7	12	6	14.3	15.5
550	4.3	6.2	7.6	12	6	14.2	15.4
600	4.0	6.2	7.4	12	6	14.1	15.3
650	3.9	6.2	7.3	12	6	14.1	15.3
700	3.5	6.2	7.1	12	6	14.0	15.2
750	3.6	6.2	7.2	12	6	14.0	15.2
800	3.4	6.2	7.1	12	6	14.0	15.2

Table 12.3: The uncertainty on the acceptance (A) as a function of the Z' mass is displayed. The second, third and forth columns show the systematic, statistical and the total (systematic, statistical combined in quadrature) relative uncertainty on the acceptance. The relative uncertainty on the number of background events (σ_B/B) is also shown, which is the combination of the uncertainty of the efficiency (ϵ) and A. The right-hand column displays the uncertainty on the signal acceptance (σ_S/S) as a function of Z' mass, which is the combination of the uncertainties on ϵ, A and the luminosity ($\mathcal{L}$).

M_G (GeV/c^2)	Relative uncertainty (%)						
	A			ϵ	$\mathcal{L}$	ϵ A	ϵ A $\mathcal{L}$
	Statistical	Systematic	Combined			σ_B/B	σ_S/S
200	3.8	10.4	11.1	12	6	16.3	17.4
250	3.6	10.4	11.0	12	6	16.3	17.4
300	3.4	10.4	11.0	12	6	16.2	17.3
350	3.1	10.4	10.9	12	6	16.2	17.3
400	2.9	10.4	10.8	12	6	16.1	17.2
450	2.6	10.4	10.7	12	6	16.1	17.2
500	2.7	10.4	10.7	12	6	16.1	17.2
550	2.5	10.4	10.7	12	6	16.1	17.2
600	2.3	10.4	10.6	12	6	16.1	17.1

Table 12.4: The uncertainty on the acceptance (A) as a function of the Randall-Sundrum graviton mass is displayed. The second, third and forth columns show the systematic, statistical and the total (systematic, statistical combined in quadrature) relative uncertainty on the acceptance. The relative uncertainty on the number of background events (σ_B/B) is also shown, which is the combination of the uncertainty of the efficiency (ϵ) and A. The right-hand column displays the uncertainty on the signal acceptance (σ_S/S) as a function of graviton mass, which is the combination of the uncertainties on ϵ, A and the luminosity ($\mathcal{L}$).

12.4 Uncertainty summary

In order to calculate an upper limit on the number of signal events present in the sample at a desired confidence level, the uncertainty on the number of background events and the signal acceptance (σ_S/S) was required. The relative uncertainty on the number of background events (σ_B/B) was determined from the combination, in quadrature, of the relative uncertainty of the efficiency (σ_ϵ/ϵ) and the acceptance (σ_A/A). The relative uncertainty on the signal acceptance was obtained from the combination of this uncertainty with the uncertainty in the luminosity ($\sigma_\mathcal{L}/\mathcal{L}$). The uncertainty on the number of background events did not include the luminosity systematic uncertainty, because the background was normalised to the data (via the number of Drell-Yan events in the Z peak region which was normalised to the data). The uncertainties are shown in Table 12.3 for the Z' and in Table 12.4 for the Randall-Sundrum graviton search. For the Z' boson, the relative uncertainty in the number of background events was approximately 14.5 % and the uncertainty in the signal acceptance ranged from 16.0 % for a Z' mass of 200 GeV/c^2 to 15.2 % for a mass of 800 GeV/c^2, where the mass dependence originated from the

statistical uncertainty in the acceptance. The uncertainties for the graviton were approximately 16 % and 17 % respectively. The latter uncertainties were greater than those for the Z', because of the larger relative uncertainty on the RS model pdfs.

Chapter 13: Run II Z' and RS graviton dimuon limits

Using the dimuon data collected, limits were set on the cross section times branching ratio of both Z' and Randall-Sundrum model gravitons decaying to dimuons. From these, lower mass limits on the Z' and the graviton were obtained, as explained in Section 13.3. The general method of setting limits, first without and then with uncertainties, is introduced in Section 13.1.1 and Section 13.1.2 respectively. The latter can be implemented using the Poilim program, as advocated by the CDF Collaboration, which is outlined in Section 13.1.3 [85].

13.1 Statistical determination of upper limits

In many new physics searches, given the number of observed events (n_0), it is desired to determine an upper limit on the number of signal events present in the sample at some desired confidence level, assuming an expected number of background events. Typically the selection requirements are such that the number of events in the data sample is small, therefore Poisson statistics are used.

13.1.1 Upper limits without uncertainties

If there are no uncertainties on either the number of background events or the overall acceptance, then in the case of no background events, the probability of observing n_0 (P) events depends on the mean number of events expected (μ) according to the Poisson distribution:

$$P(n_0;\mu) = \frac{\mu^{n_0} e^{-\mu}}{n_0!}. \tag{13.1}$$

From this distribution it is possible to calculate the upper limit ($N_{C.L.}$) on the number of expected events[1] at a specified confidence level. $N_{C.L.}$ is defined to be the value of μ for which the probability to observe n_0 or fewer events is ϵ. The C.L. of the upper limit is 1 - ϵ. The probability (ϵ) can be calculated by summing over the Poisson probabilities [86]:

$$\epsilon = \sum_{n=0}^{n_0} P(n;\mu). \tag{13.2}$$

To find $N_{C.L.}$, μ is varied until the value of ϵ corresponding to the desired C.L. is found and $N_{C.L.}$ is the resulting value of μ.

If an average of μ_B background events is expected among the n_0 observed events, then the Poisson upper limit $N_{C.L.}$ on the number of signal events present in the observation can be calculated using Equation 13.3. In this case, $N_{C.L.}$ represents the value of the mean number of signal events expected (μ_S), for which the probability is 1 - ϵ that in a random experiment, in which more than n_0 events are observed and the number of background events present in the sample (n_B) is less than the number of observed events (*i.e* $n_B \leq n_0$). In analogy with the case of no background events, $N_{C.L.}$ can be determined by adjusting $N_{C.L.}$ until the relation shown in Equation 13.3 is obtained [86].

$$\epsilon = \frac{\sum_{n=0}^{n_0} P(n;\mu_B + N_{C.L.})}{\sum_{n=0}^{n_0} P(n;\mu_B)} \tag{13.3}$$

13.1.2 Incorporation of uncertainties

In the presence of uncertainties (both statistical and systematic) in the signal acceptance (σ_S) and the background (σ_B), the upper limits on Poisson processes can be determined using Equation 13.4 [85]. As previously defined, the Poisson upper limit ($N_{C.L.}$) on μ_S is the value of the true μ_S, for which more than n_0 events are observed and $n_B \leq n_0$. $N_{C.L.}$ is determined at the

[1] $N_{C.L.}$ is a real number, not an integer.

required C.L. (1 - ϵ) from Equation 13.4, in which $\sigma_N = N_{C.L.}\sigma_S/S$.

$$\epsilon = \frac{\sum_{n=0}^{n_0} \frac{1}{\sqrt{2\pi\sigma^2_{N_{C.L.}}}} \int_0^\infty \int_0^\infty P(n;\mu'_B+\mu'_S) e^{-\frac{(\mu_B+\mu'_B)^2}{2\sigma^2_B}} e^{-\frac{(N_{C.L.}+\mu'_S)^2}{2\sigma^2_{N_{C.L.}}}} d\mu'_B d\mu'_S}{\sum_{n=0}^{n_0} \int_0^\infty P(n;\mu_B) e^{-\frac{(\mu_B+\mu'_B)^2}{2\sigma^2_B}} d\mu'_B} \tag{13.4}$$

This method assumes an *a priori* gaussian distribution of the true values of μ_S and μ_B about the values obtained in subsidiary studies, with width given by the uncertainties in those studies (μ'_S and μ'_B). The effect of including the uncertainties is to make the Poisson upper limits larger than if there were zero uncertainty.

13.1.3 Poilim limit program

The Poilim program, which is used by the CDF Collaboration, was written to solve Equation 13.4 using numerical techniques [85]. In order to solve this equation, rather than performing the integral directly, for each test value of $N_{C.L.}$ the Poilim program generates a large ensemble of pseudo-experiments, varying the expected number of signal and background events about their nominal values according to a gaussian distribution. In each experiment, the expected number of signal and background events are chosen from gaussian distributions, and Poisson-distributed numbers of signal (n_S) and background (n_B) events are generated. For the trials in which $n_B \leq n_0$, the fraction (f) in which $n_B + n_S > n_0$ is recorded. The C.L., 1 - ϵ, for a given $N_{C.L.}$ is equal to f, therefore, to obtain the required C.L., $N_{C.L.}$ is varied. The details of how this method is implemented in the Poilim fortran code are described by Conway *et. al.* [85]. The Poilim program calculates the Poisson upper limit $N_{C.L.}$ on the number of signal events present ($N_{95\%}$), from the inputs;

- the required confidence level (C.L.),
- the number of observed events (N_{data}),
- the number of expected background events ($N_{background}$),

- the total relative uncertainty on the signal acceptance (σ_S/S), which includes contributions from the acceptance (A), the efficiency (ϵ) and the luminosity ($\mathcal{L}$)
- the uncertainty on the number of expected background events ($N_{background} \times \frac{\sigma_B}{B}$).

13.2 Run II cross section upper limits

A 95 % C.L. upper limit on the number of expected events above the background ($N_{95\%}$) was calculated using the Poilim poisson limit program [85]. The values input into Poilim were: 95 % for the desired confidence level, zero for the number of events observed in the signal region (above 150 GeV/c^2), 0.47 for the number of expected background events in the signal region (shown in Table 11.2, plus 0.01 cosmic ray background events), the relative uncertainty on the signal acceptance (σ_S/S) used is shown in Table 12.3/12.4 as a function of Z'/graviton mass respectively, and the input for the uncertainty on the number of expected background events was obtained from the product of the expected number of background events (0.47) and the relative uncertainty on the number of background events (σ_B/B), which is also shown in Table 12.3/12.4 as a function of Z'/graviton mass respectively. $N_{95\%}$ calculated by Poilim, was 3.1 for all Z'/graviton masses. Without uncertainties $N_{95\%}$ changed by less than 5 % to 3.0.

$N_{95\%}$ was converted to a 95 % C.L. upper limit on the cross section times branching fraction of Z'/G decaying to dimuons ($\sigma_{95\%}$·B(Z'/G $\rightarrow \mu^+ \mu^-$)) using Equation 13.5.

$$\sigma_{95\%} \cdot B(Z'/G \rightarrow \mu^+\mu^-) = \frac{N_{95\%}}{\mathcal{L} \times \epsilon \times A(M)} \tag{13.5}$$

The values of $N_{95\%}$, $\mathcal{L}$ and $\epsilon \times A$ which were substituted into Equation 13.5 and the resulting $\sigma_{95\%}$ as a function of mass are shown in Table 13.1 and 13.2 for the Z' excluding and including uncertainties. Similarly, the values for the graviton are displayed in Table 13.3 and 13.4 as a function of mass excluding and including uncertainties respectively. For the Z', $\sigma_{95\%}$ decreased from 7.8 pb at 200 GeV/c^2 to 3.2 pb at 800 GeV/c^2 and for the RS model $\sigma_{95\%}$ decreased from 4.8 pb at 200 GeV/c^2 to 2.8 pb at 600 GeV/c^2.

Z' mass	N_{signal}	$N_{background}$	N_{data}	$N_{95\%}$	$\epsilon \times A(Z')$	$\sigma_{95\%} \cdot B(Z' \to \mu^+ \mu^-)$
(GeV/c^2)	(dimuons)	above 150 GeV/c^2		(dimuons)	(%)	pb
200	7.8	0.47	0	3.0	2.4	7.6
250	3.9	0.47	0	3.0	2.6	7.0
300	2.3	0.47	0	3.0	3.0	6.1
350	1.5	0.47	0	3.0	3.6	5.1
400	1.0	0.47	0	3.0	4.0	4.5
450	0.54	0.47	0	3.0	3.8	4.8
500	0.36	0.47	0	3.0	4.3	4.2
550	0.23	0.47	0	3.0	4.6	4.0
600	0.16	0.47	0	3.0	5.0	3.6
650	0.10	0.47	0	3.0	5.1	3.6
700	0.07	0.47	0	3.0	5.6	3.2
750	0.040	0.47	0	3.0	5.5	3.3
800	0.026	0.47	0	3.0	5.8	3.1
Luminosity = 16.5 ± 1.0 pb^{-1}						

Table 13.1: The number of signal (N_{signal}) events expected, for a Z' of the specified mass, and number of background ($N_{background}$) events expected in the search region are shown for a data sample with an integrated luminosity of 16.5 pb^{-1}. This can be compared to the number of observed dimuon (N_{data}) events. The upper limit on the number of expected events ($N_{95\%}$) calculated without uncertainties is shown. The 95 % confidence level limit on the production cross section times branching fraction of Z' decaying to dimuons ($\sigma_{95\%} \cdot B(Z' \to \mu^+ \mu^-)$) was calculated using $N_{95\%}$, the efficiency (ϵ) and the acceptance $A(Z')$, which is dependent on the Z' mass.

Z' mass	N_{signal}	$N_{background}$	N_{data}	$N_{95\%}$	$\epsilon \times A(Z')$	$\sigma_{95\%} \cdot B(Z' \to \mu^+ \mu^-)$
(GeV/c^2)	(dimuons)	above 150 GeV/c^2		(dimuons)	(%)	pb
200	7.8 ± 1.2	0.47 ± 0.06	0	3.1	2.4	7.8
250	3.9 ± 0.6	0.47 ± 0.06	0	3.1	2.6	7.2
300	2.3 ± 0.4	0.47 ± 0.06	0	3.1	3.0	6.3
350	1.5 ± 0.2	0.47 ± 0.06	0	3.1	3.6	5.2
400	1.0 ± 0.2	0.47 ± 0.06	0	3.1	4.0	4.7
450	0.54 ± 0.08	0.47 ± 0.06	0	3.1	3.8	4.9
500	0.36 ± 0.06	0.47 ± 0.06	0	3.1	4.3	4.4
550	0.23 ± 0.03	0.47 ± 0.06	0	3.1	4.6	4.1
600	0.16 ± 0.02	0.47 ± 0.06	0	3.1	5.0	3.8
650	0.10 ± 0.02	0.47 ± 0.06	0	3.1	5.1	3.7
700	0.07 ± 0.01	0.47 ± 0.06	0	3.1	5.6	3.5
750	0.040 ± 0.006	0.47 ± 0.06	0	3.1	5.5	3.4
800	0.026 ± 0.004	0.47 ± 0.06	0	3.1	5.8	3.2
Luminosity = 16.5 ± 1.0 pb^{-1}						

Table 13.2: The number of signal (N_{signal}) events expected, for a Z' of the specified mass, and number of background ($N_{background}$) events expected in the search region are shown for a data sample with an integrated luminosity of 16.5 pb^{-1}. This can be compared to the number of observed dimuon (N_{data}) events. The upper limit on the number of expected events ($N_{95\%}$) shown was calculated including the uncertainties displayed in Table 12.3. The 95 % confidence level limit on the production cross section times branching fraction of Z' decaying to dimuons ($\sigma_{95\%} \cdot B(Z' \to \mu^+ \mu^-)$) was calculated using $N_{95\%}$, the efficiency (ϵ) and the acceptance $A(Z')$, which is dependent on the Z' mass.

M_G	N_{signal}	$N_{background}$	N_{data}	$N_{95\%}$	$\epsilon \times$A(G)	$\sigma_{95\%}$·B(G $\rightarrow \mu^+ \mu^-$)
(GeV/c^2)	k/$\bar{M}_{pl} = 0.1$	above 150 GeV/c^2		(dimuons)	(%)	pb
200	9.0	0.47	0	3.0	3.9	4.7
250	3.1	0.47	0	3.0	4.1	4.4
300	1.4	0.47	0	3.0	4.3	4.2
350	0.80	0.47	0	3.0	4.8	3.8
400	0.47	0.47	0	3.0	5.2	3.5
450	0.28	0.47	0	3.0	5.7	3.2
500	0.15	0.47	0	3.0	5.5	3.3
550	0.11	0.47	0	3.0	6.0	3.0
600	0.072	0.47	0	3.0	6.6	2.8
Luminosity = 16.5 ± 1.0 pb^{-1}						

Table 13.3: The number of signal (N_{signal}) events expected, for a RS model graviton of the specified mass (M_G), and number of background ($N_{background}$) events expected in the search region are shown for a data sample with an integrated luminosity of 16.5 pb^{-1}. This can be compared to the number of observed dimuon (N_{data}) events. The upper limit on the number of expected events ($N_{95\%}$) which was calculated without uncertainties is shown. The 95 % confidence level limit on the production cross section times branching fraction of RS model graviton decaying to dimuons ($\sigma_{95\%}$·B(G $\rightarrow \mu^+ \mu^-$)) was calculated using $N_{95\%}$, the efficiency (ϵ) and the acceptance A(G), which is dependent on the graviton mass.

M_G	N_{signal}	$N_{background}$	N_{data}	$N_{95\%}$	$\epsilon \times$A(G)	$\sigma_{95\%}$·B(G $\rightarrow \mu^+ \mu^-$)
(GeV/c^2)	k/$\bar{M}_{pl} = 0.1$	above 150 GeV/c^2		(dimuons)	(%)	pb
200	9.0 ± 1.6	0.47 ± 0.08	0	3.1	3.9	4.8
250	3.1 ± 0.5	0.47 ± 0.08	0	3.1	4.1	4.6
300	1.4 ± 0.2	0.47 ± 0.08	0	3.1	4.3	4.4
350	0.80 ± 0.14	0.47 ± 0.08	0	3.1	4.8	3.9
400	0.47 ± 0.08	0.47 ± 0.08	0	3.1	5.2	3.6
450	0.28 ± 0.05	0.47 ± 0.08	0	3.1	5.7	3.3
500	0.15 ± 0.03	0.47 ± 0.08	0	3.1	5.5	3.4
550	0.11 ± 0.02	0.47 ± 0.08	0	3.1	6.0	3.1
600	0.072 ± 0.01	0.47 ± 0.08	0	3.1	6.6	2.8
Luminosity = 16.5 ± 1.0 pb^{-1}						

Table 13.4: The number of signal (N_{signal}) events expected, for a RS model graviton of the specified mass (M_G), and number of background ($N_{background}$) events expected in the search region are shown for a data sample with an integrated luminosity of 16.5 pb^{-1}. This can be compared to the number of observed dimuon (N_{data}) events. The upper limit on the number of expected events ($N_{95\%}$) shown was calculated including the uncertainties displayed in Table 12.4. The 95 % confidence level limit on the production cross section times branching fraction of RS model graviton decaying to dimuons ($\sigma_{95\%}$·B(G $\rightarrow \mu^+ \mu^-$)) was calculated using $N_{95\%}$, the efficiency (ϵ) and the acceptance A(G), which is dependent on the graviton mass.

Tables 13.1, 13.2 13.3 and 13.4 also show the number of expected signal events (N_{signal}), one would expect to observe in the signal region if a Z'/graviton of the specified mass existed. N_{signal} was calculated from the product: $\epsilon \times \mathrm{A} \times 16.5 \times \sigma_{signal}$, where σ_{signal} was the production cross section times branching ratio to dimuons given by Pythia multiplied by the K factor (of 1.3). For example, if a Z' boson of 250 GeV/c^2 existed then 3.9 $\pm$ 0.6 events would be expected to be observed for an integrated luminosity of 16.5 pb^{-1}. This can be compared to the number of background, number of observed and the upper limit on the number of expected events, which are also displayed in these tables.

13.3 Run II Z'/graviton lower mass limits

The 95 % C.L. lower limits on the mass of the Z' boson and the RS graviton were determined by the position of the intersection of the theoretical cross sections, for their respective production, and the 95 % C.L. upper cross section limits ($\sigma_{95\%}$) on cross section vs mass plots. Predicted theoretical limits for Z' and RS graviton production were obtained by generating events for a range of masses using PYTHIA 6.203 and multiplying the cross sections by the correction K factor (of 1.3). The theoretical cross section times branching ratio for Z' decay to dimuons ($\sigma \cdot$B) as a function of mass is shown (by the smooth more steeply decreasing red curve) in both Figure 13.1 and Figure 13.2 for the Z' boson. In Figure 13.1, $\sigma_{95\%} \cdot \mathrm{B}(Z' \rightarrow \mu^+ \mu^-)$ calculated excluding uncertainties is also displayed (indicated by the black curve with data points), and Figure 13.2 contains $\sigma_{95\%} \cdot \mathrm{B}(Z' \rightarrow \mu^+ \mu^-)$ obtained including uncertainties. For the RS graviton, theoretical cross sections times branching ratios to dimuons were determined for four different width parameters (k/$\bar{M}_{Pl}$): 0.01, 0.07, 0.085 and 0.1. These cross sections are shown, as a function of the graviton mass, in Figure 13.3 and Figure 13.4. The former figure also shows $\sigma_{95\%} \cdot \mathrm{B}(\mathrm{G} \rightarrow \mu^+ \mu^-)$ calculated excluding uncertainties, and the latter shows $\sigma_{95\%} \cdot \mathrm{B}(\mathrm{G} \rightarrow \mu^+ \mu^-)$ determined including uncertainties.

Without uncertainties, the 95 % C.L. lower mass limit obtained was 280 GeV/c^2 for the

Z' boson, and for the graviton, the limits obtained were 225, 240 and 255 GeV/c^2 for width parameters 0.07, 0.085 and 0.1 respectively. When uncertainties were included, the 95 % C.L. lower mass limit obtained was 275 GeV/c^2 for the Z' boson and for the graviton, the limits obtained were 220, 240 and 250 GeV/c^2 for width parameters 0.07, 0.085 and 0.1. From these RS limits, a 95 % C.L. exclusion region on the graviton mass vs k/$\bar{M}_{Pl}$ plane was produced, and is shown in Figure 13.5.

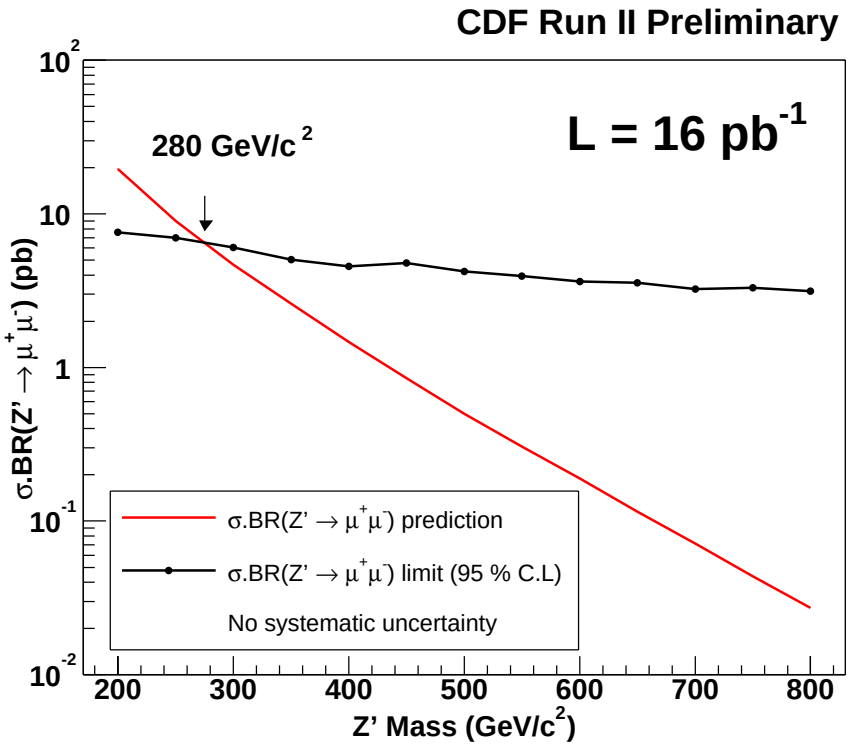

Figure 13.1: 95 % confidence level limit on the production cross section times branching fraction of $Z' \to \mu\mu$ ($\sigma \cdot$ BR($Z' \to \mu^+ \mu^-$)) for an integrated luminosity of 16 pb^{-1} as a function of Z' mass, without uncertainties and using CMUP-CMUP dimuon combinations. Also shown is the predicted production cross section times branching fraction of $Z' \to \mu\mu$. The intersection of these curves indicates the 95 % C.L. lower Z' mass limit.

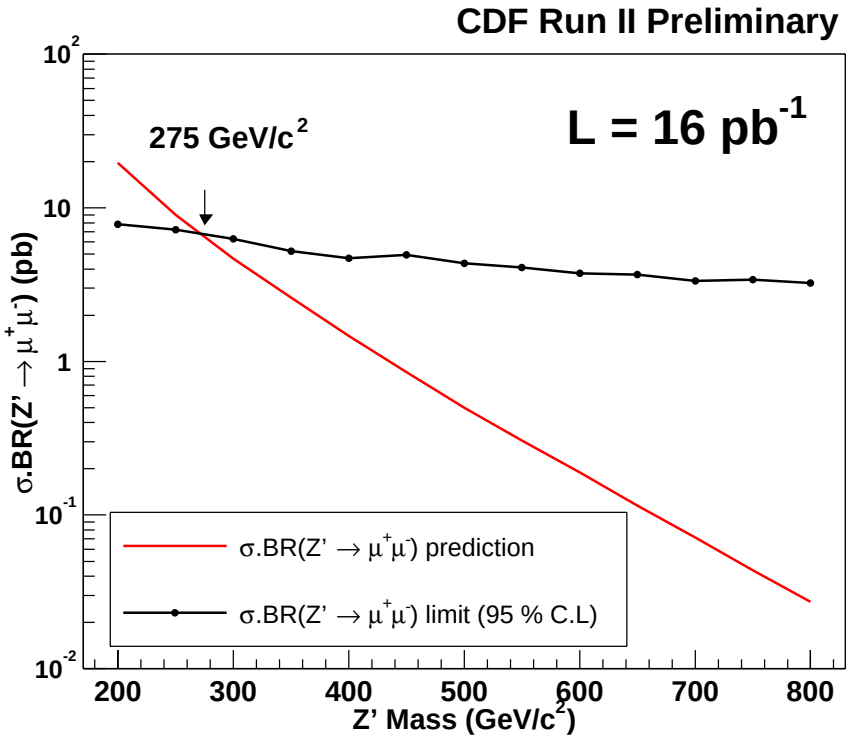

Figure 13.2: 95 % confidence level (C.L.) limit on the production cross section times branching fraction of $Z' \to \mu\mu$ ($\sigma \cdot$ BR($Z' \to \mu^+ \mu^-$)) for an integrated luminosity of 16 pb^{-1} as a function of Z' mass, with uncertainties included and using CMUP-CMUP dimuon combinations. Also shown is the predicted production cross section times branching fraction of $Z' \to \mu\mu$. The intersection of these curves indicates the 95 % C.L. lower Z' mass limit.

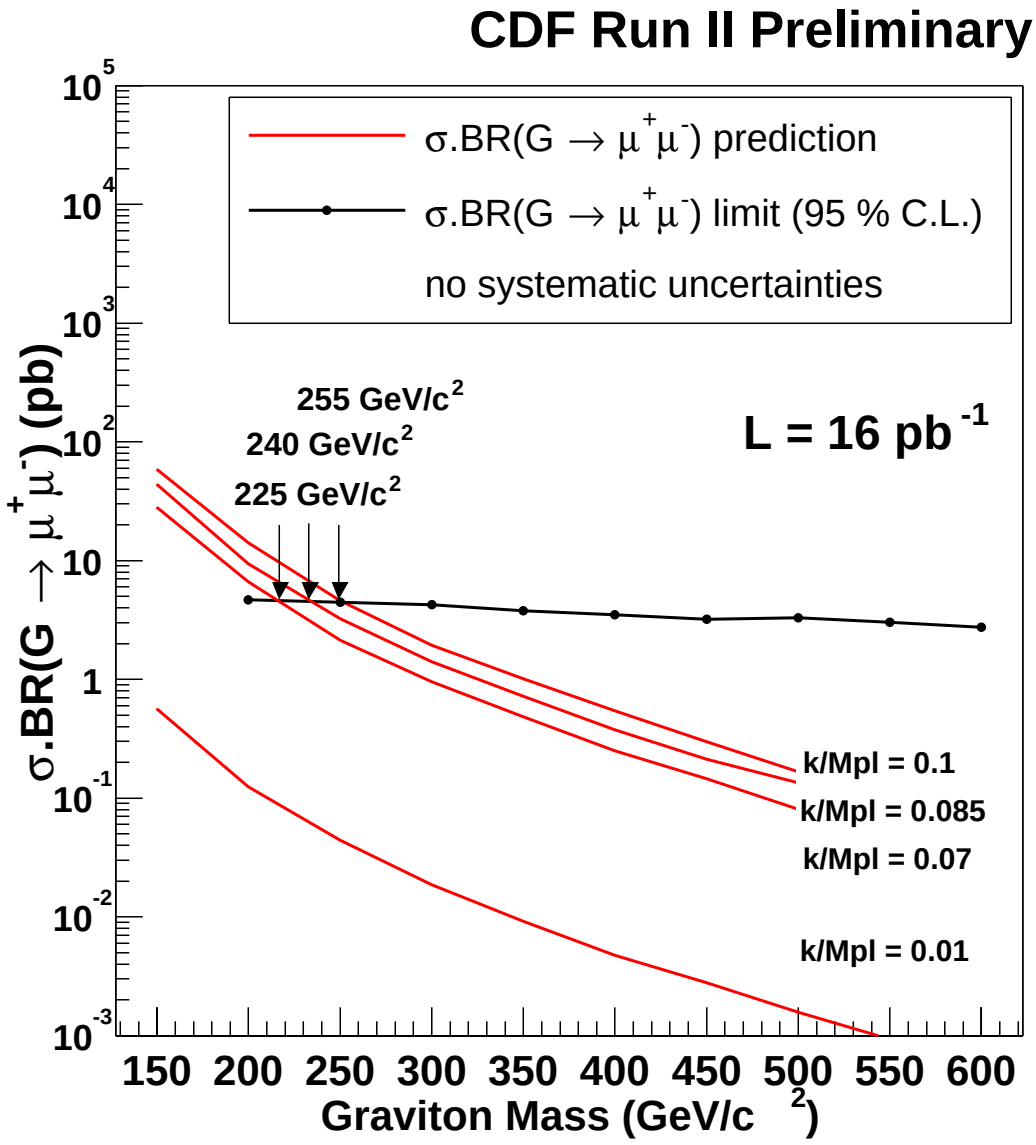

Figure 13.3: 95 % confidence level upper limit on the production cross section times branching fraction of an RS model graviton decaying to dimuons ($\sigma \cdot$ BR(G $\rightarrow \mu^+ \mu^-$)) as a function of graviton mass, for an integrated luminosity of 16 pb^{-1}, with no uncertainties included and using CMUP-CMUP dimuon combinations. Also shown are the predicted $\sigma \cdot$ Br(G $\rightarrow \mu^+ \mu^-$) curves for k/$\bar{M}_{Pl}$ = 0.01, 0.07, 0.085 and 0.1.

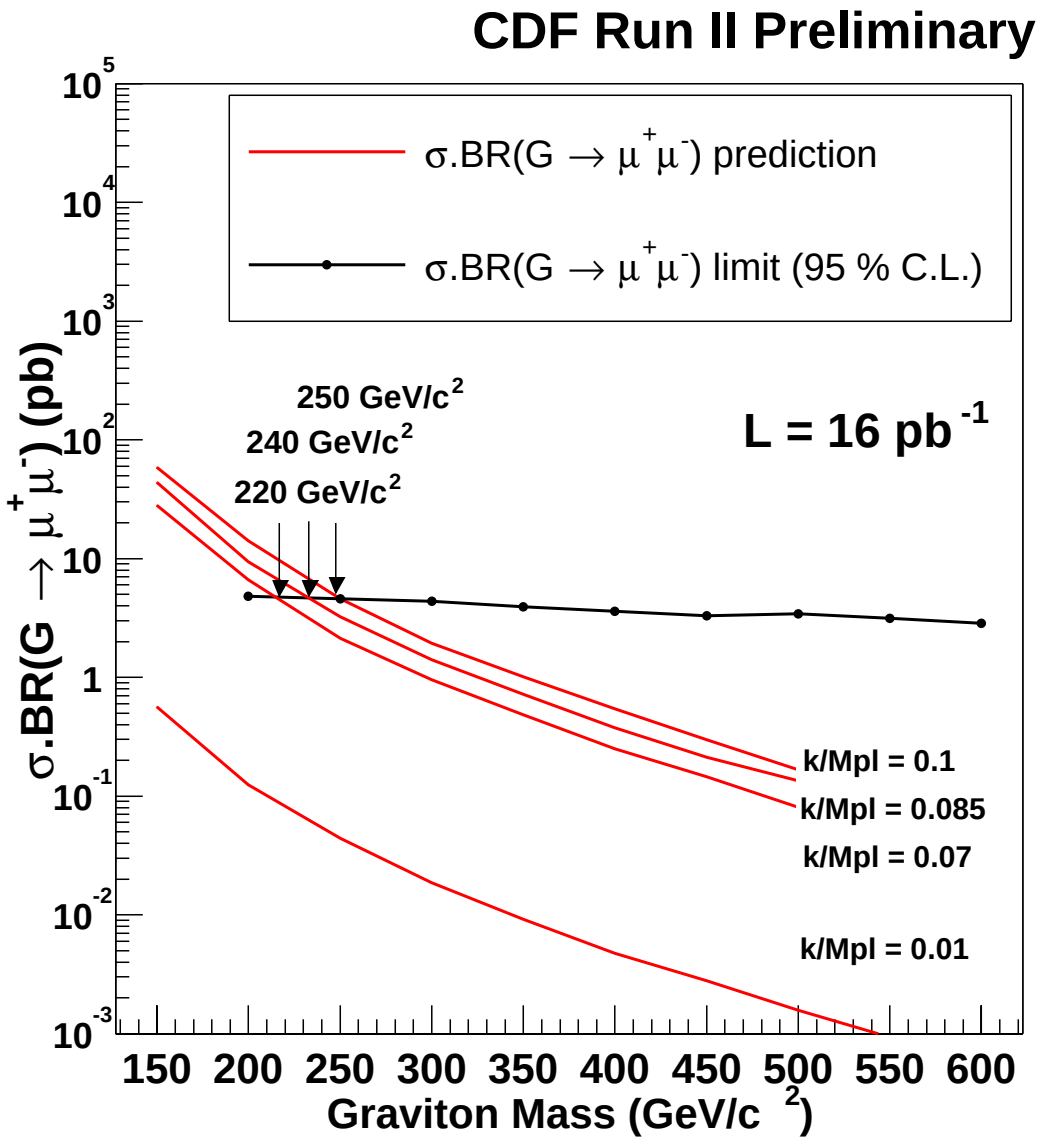

Figure 13.4: 95 % confidence level upper limit on the production cross section times branching fraction of an RS model graviton decaying to dimuons ($\sigma \cdot$ BR(G $\rightarrow \mu^+ \mu^-$)) as a function of graviton mass, for an integrated luminosity of 16 pb^{-1}, with uncertainties included and using CMUP-CMUP dimuon combinations. Also shown are the predicted $\sigma \cdot$ Br(G $\rightarrow \mu^+ \mu^-$) curves for k/$\bar{M}_{Pl}$ = 0.01, 0.07, 0.085 and 0.1.

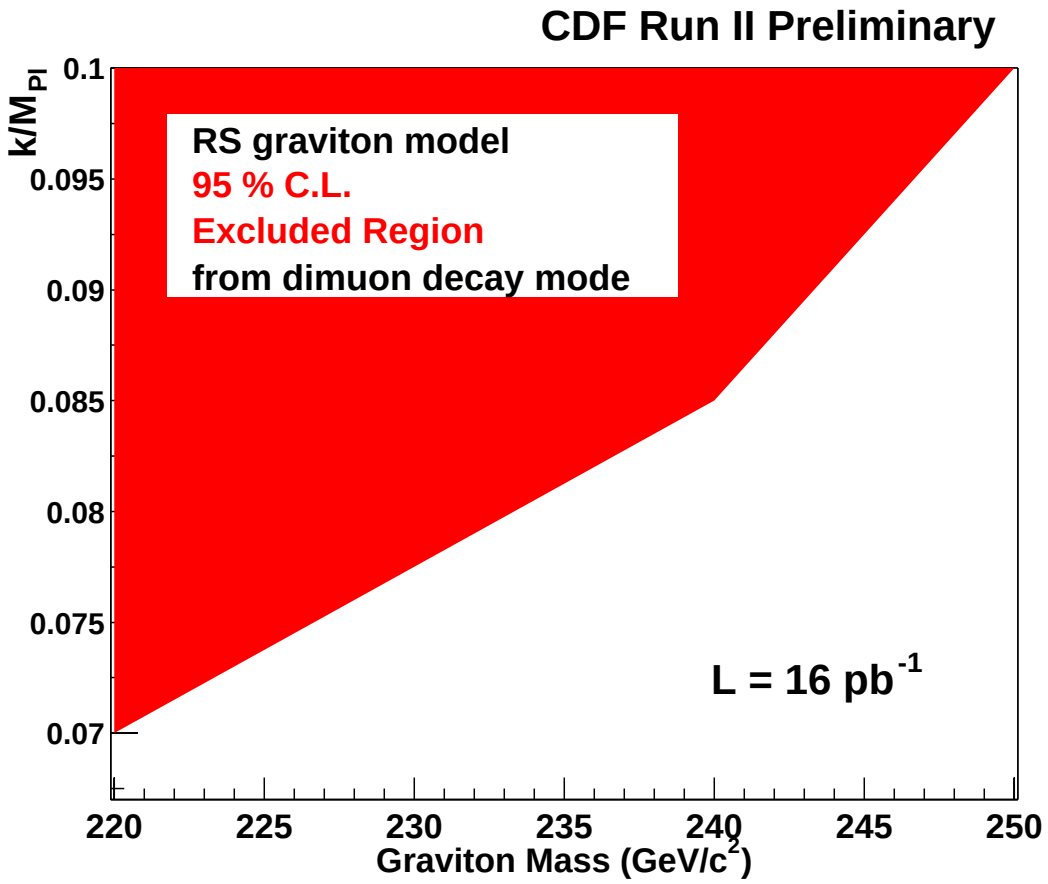

Figure 13.5: 95 % confidence level excluded region on the plane for graviton mass vs $k/\bar{M}_{Pl}$ for an integrated luminosity of 16 pb^{-1}.

Chapter 14: Run I Randall-Sundrum graviton dilepton limits

Randall-Sundrum graviton lower mass limits, at the 95 % C.L., were obtained using the published Run I 95 % C.L. upper limit on the production cross section times branching ratio of a Z' boson decaying to dileptons[1] ($\sigma_{95\%}\cdot$ B($Z'\rightarrow l^+ l^-$)) [20]. ($\sigma_{95\%}\cdot$ B($Z'\rightarrow l^+ l^-$)) can be used as a conservative limit for ($\sigma_{95\%}\cdot$ B(G$\rightarrow l^+ l^-$)), because the acceptance for graviton decay to dileptons is higher than the acceptance for Z' decay to dileptons, as shown in Section 14.1. The larger acceptance results in a smaller $\sigma_{95\%}$, as explained in Section 14.2 and demonstrated with Run II data. The Randall-Sundrum graviton mass limits obtained using the Run I dimuon and dielectron samples, which consisted of an integrated luminosity of 107 pb^{-1} and 110 pb^{-1} respectively, are presented in Section 14.3.

14.1 Comparison of the Z' to graviton dilepton acceptance

The acceptance for Randall-Sundrum gravitons decaying to dimuons was found to be higher than that for Z' decays. This is illustrated in Figure 9.4, which shows the acceptance of the Randall-Sundrum graviton and the Z' decaying to dimuons as a function of mass. This was obtained using Monte Carlo samples which were generated as described in Chapter 9. The difference in the acceptance is caused by the different spins of the particles, as was explained in Section 9.3. Similarly for decays to dielectrons, the acceptance for Randall-Sundrum gravitons was determined to be higher than that for Z' decays [87], which can be seen by comparing the two acceptance plots in Figure 14.1. In this figure, C represents electrons which were detected in the central electromagnetic calorimeter and P represents electrons which were detected in the

[1] Throughout this chapter the term dileptons is used to refer to dimuons and dielectrons only, and does not include taus.

plug electromagnetic calorimeter[2].

Because the acceptance for the Z' boson was found to be less than that of the Randall-Sundrum graviton for decays to both the dimuons and dielectrons, the Z' boson acceptance determined in Run I was used as conservative estimate of the Run I Randall-Sundrum graviton acceptance. This was consequently used to obtain a conservative 95 % C.L. upper limit on the production cross section for Randall-Sundrum graviton decays to dileptons, as explained in the following section.

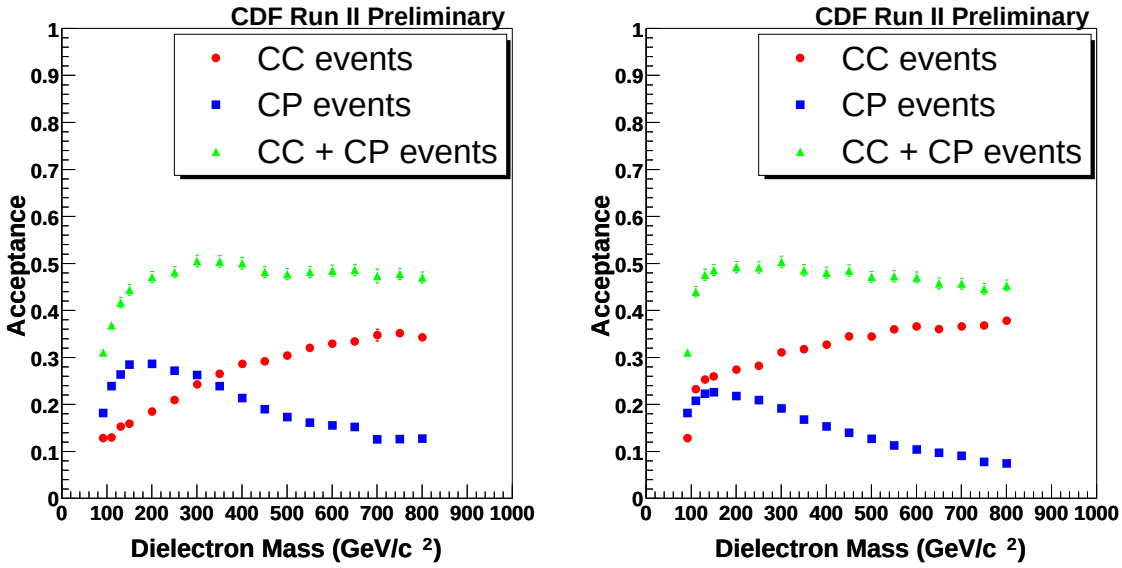

Figure 14.1: Acceptance of the Z' boson (left) and of the Randall-Sundrum graviton (right) as a function of Monte Carlo dielectron mass [87]. Electrons detected in the plug electromagnetic calorimeter are labelled P and those detected in the central electromagnetic calorimeter are labelled C.

[2]The acceptance in the CDF detector is much larger for electrons than for dimuons, because of the plug electromagnetic calorimeter, which extends the pseudorapidity range of the central electromagnetic calorimeter coverage of 0 to 1.1 up to 3.6, compared to the central muon chambers which cover a pseudorapidity range from 0 to 0.6 only.

14.2 Cross section limit dependence on acceptance

A 95 % C.L. upper cross section limit can be obtained ($\sigma_{95\%}$) from the 95 % C.L. upper limit on the number of expected events above the background ($N_{95\%}$), the efficiency (ϵ) and the acceptance (A(M)), which is a function of invariant mass. These are related by Equation 14.1.

$$\sigma_{95\%} \cdot B(Z'/G \rightarrow l^+l^-) = \frac{N_{95\%}}{\mathcal{L} \times \epsilon \times A(M)} \tag{14.1}$$

$N_{95\%}$ depends on the number of events observed in the signal region, the number of expected background events and the uncertainties on the signal acceptance and on the number of expected background events. Therefore, if Z' and Randall-Sundrum graviton searches were made using the same data sample, uncertainties and signal region (and hence also have the same expected background), then $N_{95\%}$ would be identical for both searches. If it were also assumed that the same integrated luminosity was used for both searches and the efficiency was the same, then the difference in $\sigma_{95\%}$ in the two searches would only arise from difference in the acceptance (as shown by Equation 14.1). In this scenario, the larger acceptance for the Randall-Sundrum graviton than that for the Z' boson for both dielectrons and dimuons would translate, via Equation 14.1, into a lower $\sigma_{95\%}$ for the Randall-Sundrum graviton than the Z' boson. This was demonstrated using Run II data, as is illustrated in Figure 14.2 for dimuons, which shows $\sigma_{95\%}\cdot$ B($Z'\rightarrow \mu^+ \mu^-$) and $\sigma_{95\%}\cdot$ B(G$\rightarrow \mu^+ \mu^-$) as a function of dimuon invariant mass, obtained using 16.5 pb^{-1} Run II data (from Chapter 13). Figure 14.3 shows these limits for dielectrons, which were determined using an integrated luminosity of 10.4 pb^{-1} Run II data [87]. These figures confirmed that $\sigma_{95\%}\cdot$B was smaller for the Randall-Sundrum graviton than the Z' boson for decays to both dimuons and dielectrons. It was therefore concluded that the 95 % C.L. upper limit on the cross section times branching ratio of the Z' boson to dileptons ($\sigma_{95\%}\cdot$ Br($Z'\rightarrow l^+ l^-$)) could be used as a conservative estimate of the 95 % C.L. upper cross section times branching ratio of the Randall-Sundrum graviton to dileptons ($\sigma_{95\%}\cdot$ Br(G$\rightarrow l^+ l^-$)). This method was used to set Run I limits.

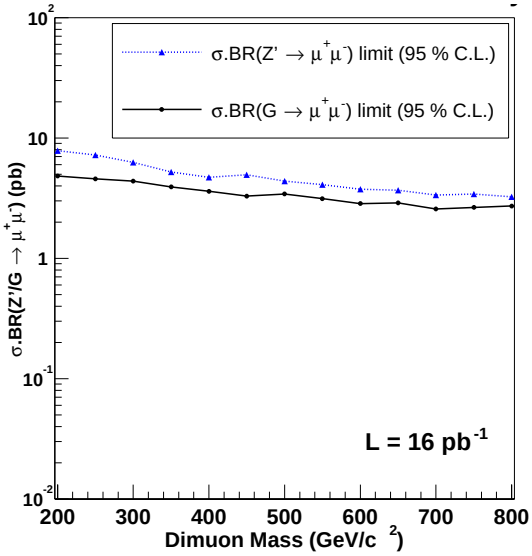

Figure 14.2: Comparison of the 95 % confidence level upper limit on the production cross section times branching fraction of Randall Sundrum graviton decaying to dimuons ($\sigma \cdot \mathrm{BR}(\mathrm{G} \rightarrow \mu^+ \mu^-)$) to that of Z' boson decaying to dimuons ($\sigma \cdot \mathrm{BR}(Z' \rightarrow \mu^+ \mu^-)$) as a function of dimuon invariant mass, for an integrated luminosity of 16 pb^{-1} of Run II data.

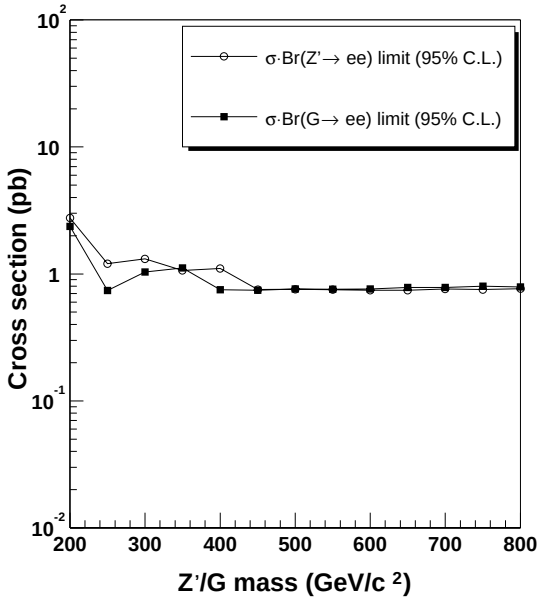

Figure 14.3: Comparison of the 95 % confidence level upper limit on the production cross section times branching fraction of Randall Sundrum graviton decaying to dielectrons ($\sigma \cdot \mathrm{BR}(\mathrm{G} \rightarrow e^+ e^-)$) to that of Z' boson decaying to dielectrons ($\sigma \cdot \mathrm{BR}(Z' \rightarrow e^+ e^-)$) as a function of dielectron invariant mass, for an integrated luminosity of 10 pb^{-1} of Run II data [87].

14.3 Run I Randall Sundrum graviton lower mass limits

In order to obtain Run I mass limits for the Randall Sundrum graviton, the Run I result for $\sigma_{95\%}\cdot$ B($Z'\rightarrow l^+ l^-$) was used as a conservative estimate of $\sigma_{95\%}\cdot$ B(G$\rightarrow l^+ l^-$). The same search region, dataset, backgrounds, efficiencies and uncertainties were used as for the determination of $\sigma_{95\%}\cdot$ B($Z'\rightarrow l^+ l^-$) in Run I [20]. As in the Run II search, mass limits were obtained from the position of the intersection of the $\sigma_{95\%}\cdot$ B curve and the theoretically predicted $\sigma\cdot$ B(G$\rightarrow l^+ l^-$) curve. Predicted theoretical $\sigma\cdot$ B curves were obtained by generating events with graviton masses in the range from 100 to 800 GeV/c^2, using PYTHIA 6.203 and using a correction K factor (of 1.3), for a range of width parameters from 0.01 to 0.1. Four of these $\sigma\cdot$ B curves are shown in Figure 14.4 (by the four approximately parallel decreasing red curves). Also illustrated in this figure is the $\sigma_{95\%}\cdot$ B($Z'\rightarrow l^+ l^-$) curve which was obtained in Run I. The "bumps" in this curve appear where events were observed in the signal region. In dielectron searches signal regions can have an upper and a lower bound (because the invariant mass resolution at high invariant masses is much better than for dimuons, as discussed in Section 15.8). Hence, if an event is observed in the data sample, this causes a "bump" in $\sigma_{95\%}\cdot$ B curve, rather than an upwards shift of the whole curve. The 95 % C.L. lower mass limits obtained for the graviton were 280, 490 and 680 GeV/c^2 for width parameters 0.02, 0.05 and 0.1 respectively. From these limits, a 95 % C.L. exclusion region on the graviton mass vs k/$\bar{M}_{Pl}$ plane was produced, and is presented in Figure 14.5.

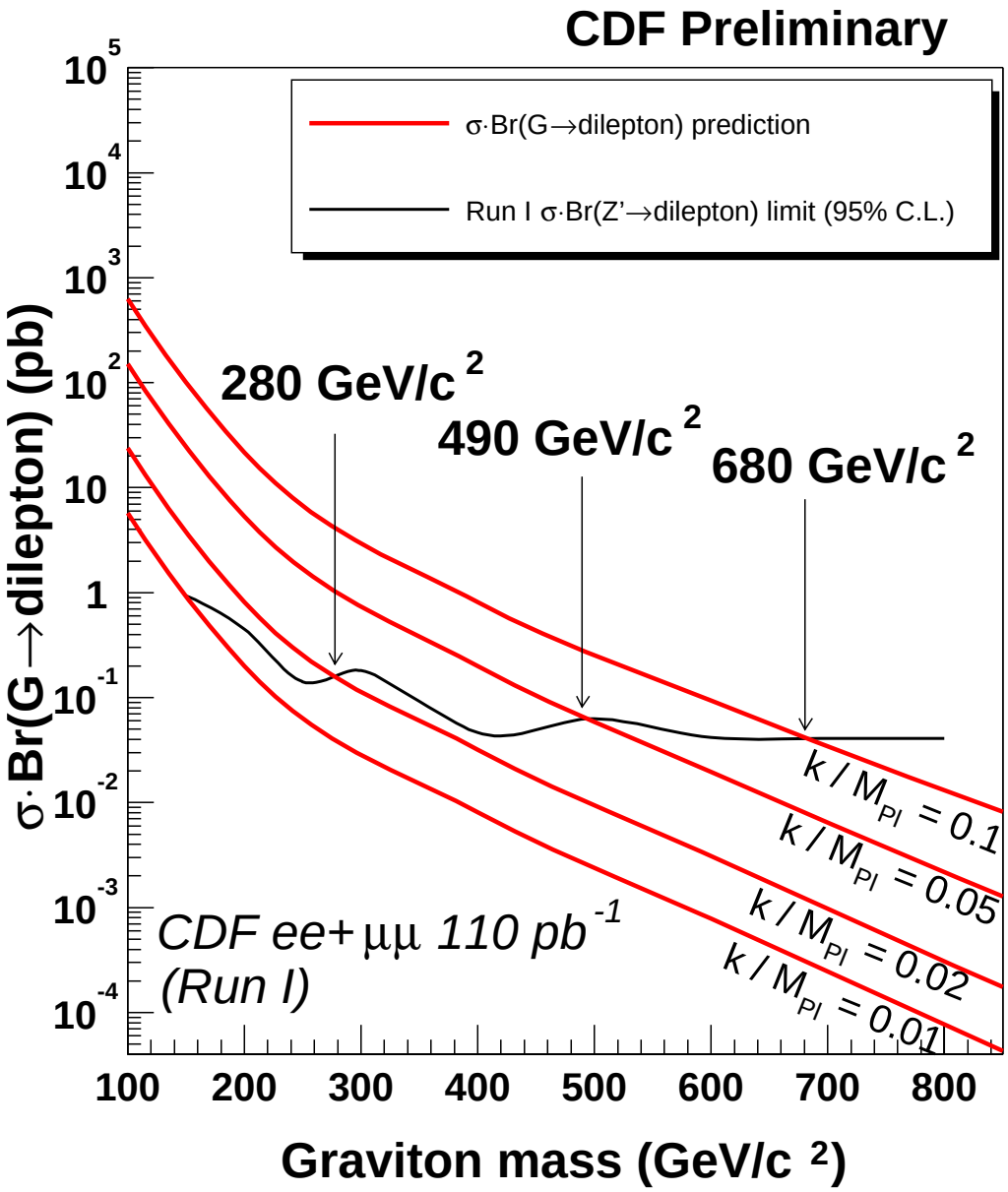

Figure 14.4: 95 % confidence level upper limit on the production cross section times branching fraction of Randall Sundrum graviton decaying to dileptons ($\sigma \cdot \mathrm{Br}(\mathrm{G} \rightarrow \mathrm{dileptons})$) as a function of dimuon invariant mass, for an integrated luminosity of 110 pb^{-1} Run I dilepton data.

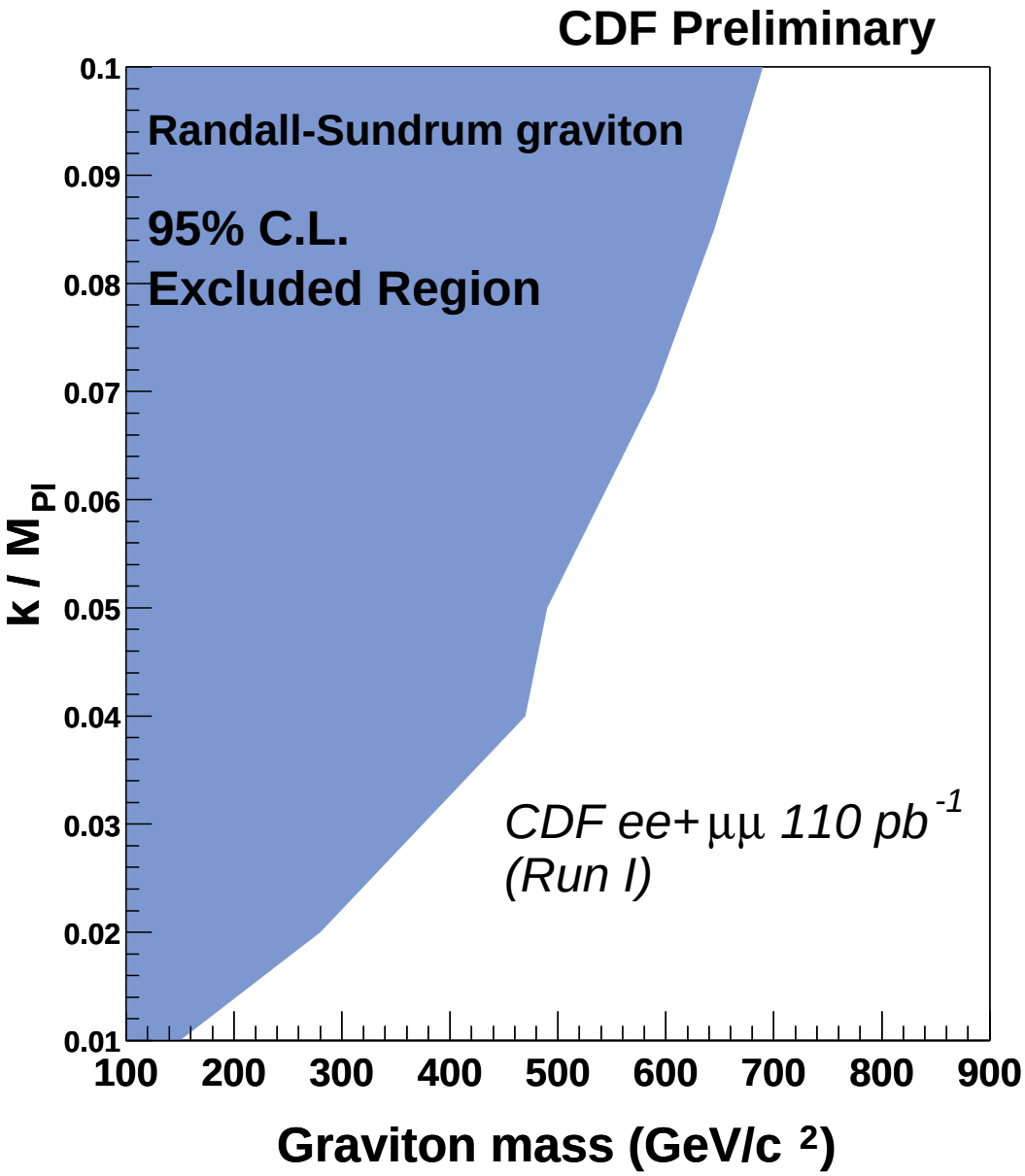

Figure 14.5: 95 % confidence level excluded region on the plane for Randall-Sundrum model graviton mass vs $k/\bar{M}_{Pl}$ for an integrated luminosity of 110 pb^{-1} Run I dilepton data.

Chapter 15: Analysis developments

15.1 Summary of results

A search was performed in the dimuon channel at high invariant mass using an integrated luminosity of 16 pb^{-1}. No events were observed in the signal region greater than 150 GeV/c^2 and no significant deviations from the expected background were observed. From these results, the first cross section and mass limits, using Run II data, were obtained for both the Z' boson and the Randall-Sundrum model graviton decaying dimuons. The 95 % confidence level upper cross section limits on the production cross section times branching ratio for the Z' boson and the Randall-Sundrum model graviton decaying dimuons are displayed in Figure 13.2 and Figure 13.4 respectively. The cross section limit decreased from 7.8 pb at 200 GeV/c^2 to 3.2 pb at 800 GeV/c^2 for the Z', including the uncertainties and ranged from 4.8 pb at 200 GeV/c^2 to 2.8 pb at 600 GeV/c^2 for the RS model graviton. From these limits, the 95 % C.L. lower mass limit obtained for the Z' was 275 GeV/c^2 (including uncertainties) and the mass limits for the graviton were 220, 240 and 250 GeV/c^2 for width parameters 0.07, 0.085 and 0.1 respectively (including uncertainties). The resulting graviton mass vs width parameter exlusion region is displayed in Figure 13.5.

In addition, mass limits on the Randall-Sundrum model graviton were obtained using the previously published Run I CDF upper limit on the cross section times branching ratio for Z' decays to dileptons (110 pb^{-1}). The graviton lower mass limits determined were 280, 490 and 680 GeV/c^2 for width parameters (k/$\bar{M}_{Pl}$) 0.02, 0.05 and 0.1 respectively, as illustrated in the exclusion plot of graviton mass vs k/$\bar{M}_{Pl}$ plane, Figure 14.5.

The Run II lower mass limit obtained for the Z' decaying to dimuons was lower than that obtained in Run I (summarised in Table 15.2) using an integrated luminosity of 18.8 pb^{-1}, which was 440 GeV/c^2 [88] and also lower than the final Run I result of 550 GeV/c^2 determined using

107 pb^{-1} of data [89]. This can be attributed to several factors; the Run I analyses included more data, had higher efficiency per dimuon event and included a larger acceptance (because CMU, CMP and CMX stub combinations were used, not only CMUP).

There are a number of ways that this analysis could be developed in order to improve the achievable upper cross section and lower mass limits obtainable. Possible extensions are discussed in the following sections of this chapter and the expected Run II reaches with an integrated luminosity of 2 fb^{-1} are summarised in Section 15.11.

15.2 Other limits

Limits were obtained on the Sequential Standard Model Z' and the Randall-Sundrum model graviton. The same dimuon data could also be used to set limits on other Z' models, such as the E_6 models, discussed in Section 1.2.2, and on alternative extra dimensional models, for example those which predict Z' like gauge bosons, mentioned in Section 1.3.3. In this analysis, limits were not set on these other models because the data samples were so small that any results would not have exceeded existing limits.

15.3 Include more CMUP-CMUP data

One possible extension to the analysis is simply to add more CMUP-CMUP dimuon data. In order to appreciate the effect of increasing the sample size, limits for an increased luminosity were estimated by extrapolating the results determined using the 16 pb^{-1} sample. It was assumed that there were no events in the signal region and that the efficiency, acceptance, background[1] and uncertainties were identical to those used to obtain the cross section limit with 16 pb^{-1}, as calculated in Chapter 8, 9, 11 and 12 respectively. $\sigma_{95\%}$ was then calculated using

[1]It should be noted that the increase in expected background was not comprehensively accounted for here. The same background estimation of 0.47 events was used, even though with more data one would expect more background events, *i.e.* scaled by the luminosity. However, to compensate for this, a higher signal region could have been selected, which would effectively decrease the expected background in the signal region. For example, if the signal region was raised to 250 GeV/c^2 and the luminosity studied was 100 pb^{-1}, from Table 11.2, one would expect 0.55 background events (neglecting cosmic ray background), which is comparable to that used in the estimation and results in the same value for $N_{95\%}$. This study was used only to appreciate improvements attainable by increasing the luminosity and not to obtain Run II reaches.

Equation 15.1. The values of $\epsilon \times A$ and $N_{95\%}$ substituted into this formula are displayed in Table 13.2 and 13.4 as a function of Z' and graviton mass respectively. From this $\sigma_{95\%}$.B was determined as a function of mass for a luminosity ($\mathcal{L}$) of 100, 200 pb^{-1} and 2 fb^{-1}. $\sigma_{95\%}$·B(Z' $\rightarrow \mu^+\mu^-$) for an integrated luminosity of 100 and 200 pb^{-1} as a function of mass is shown in Figure 15.1, and Figure 15.2 shows a similar limit plot for 100, 200 pb^{-1} and 2 fb^{-1} for RS model graviton production. (These cross section limits are for CMUP-CMUP dimuon combinations.) Mass limits were obtained from the intersection of these $\sigma_{95\%}$· B curves with the theoretically predicted σ· B curves, which were determined using Pythia, as in Section 13.3. In the specific case of Z' decaying to dimuons; for an integrated luminosity of 100 pb^{-1}, the Z' lower mass limit increased from 275 GeV/c^2 for 16 pb^{-1} up to 455 GeV/c^2, and doubling this amount of data was found to extend the obtainable lower mass limit up to 540 GeV/c^2.

Considering a more general case; increasing the luminosity ($\mathcal{L}$) decreases $\sigma_{95\%}$ · B(Z'/G $\rightarrow \mu^+$ μ^-). This can be appreciated quantitatively from Equation 15.1 and qualitatively from Figure 15.1.

$$\sigma_{95\%} \cdot B(Z'/G \rightarrow \mu^+\mu^-) = \frac{N_{95\%}}{\mathcal{L} \times \epsilon \times A} \tag{15.1}$$

Schematically the effect of an increase in the luminosity is to move the upper limit cross section curve down the plot to a parallel position. The lower mass limit achievable is therefore higher, because the intersection of the upper cross section limit ($\sigma_{95\%}$·B) curve with the theoretical cross section curve occurs at a higher invariant mass. There is an approximately logarithmic dependence of the lower mass limit on the integrated luminosity. (The dependence would be logarithmic if the upper cross section curves were horizontal lines and the theoretical curves were straight lines on these plots.) If this was exactly true then doubling the integrated luminosity would effectively increase the lower mass limit by (ln 2/(gradient of the theory curve)). Increasing the luminosity consequently increases the achievable lower mass limit (as is illustrated in both Figure 15.1 and Figure 15.2).

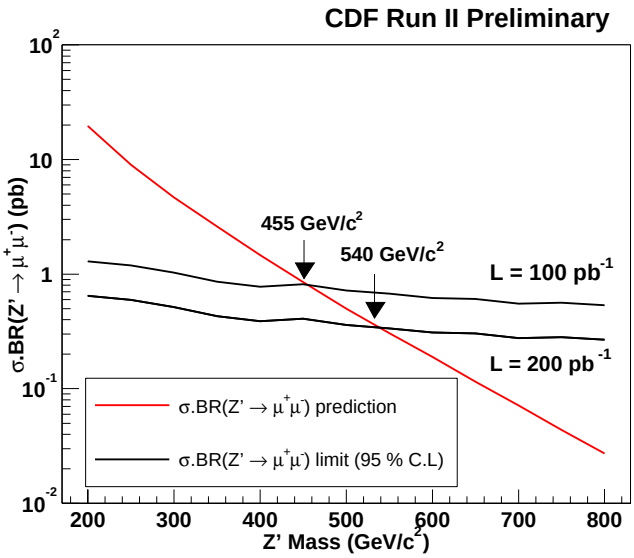

Figure 15.1: Projected 95 % confidence level upper limit on the production cross section times branching fraction of Z' decaying to dimuons ($\sigma \cdot \mathrm{BR}(\mathrm{G} \rightarrow \mu^+ \mu^-)$) as a function of Z' mass for an integrated luminosity of 100 and 200 pb^{-1}. Uncertainties were included and only CMUP-CMUP dimuon combinations were used. It was assumed that no events were observed in the signal region.

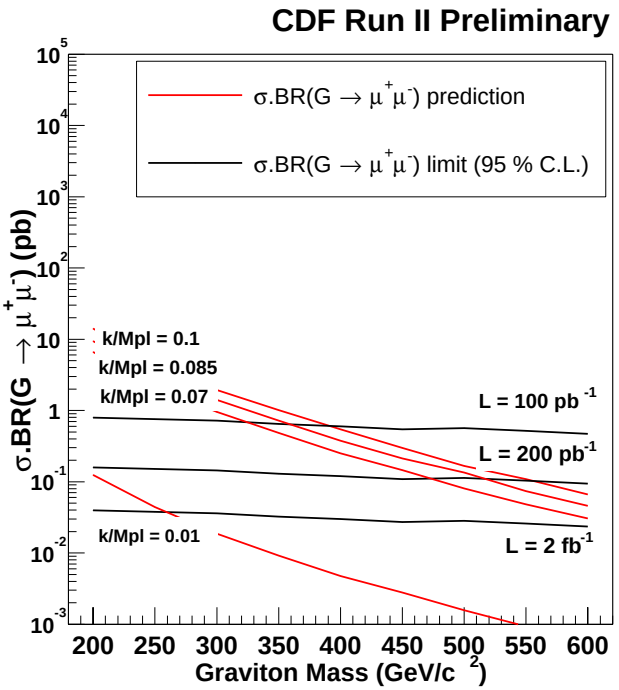

Figure 15.2: Projected 95 % confidence level upper limit on the production cross section times branching fraction of G decaying to dimuons ($\sigma \cdot \mathrm{BR}(\mathrm{G} \rightarrow \mu^+ \mu^-)$) as a function of graviton mass for an integrated luminosity of 100, 200 and 2000 pb^{-1}. Uncertainties were included and only CMUP-CMUP dimuon combinations were used. It was assumed that no events were observed in the signal region.

15.4 Increase the efficiency

An increase in the dimuon event efficiency (ϵ) would have a similar effect as an increase in the integrated luminosity, as can be appreciated from Equation 15.1. If it were assumed that the efficiency were independent of mass, then an increase in the efficiency would also move the $\sigma_{95\%}$·B curve downwards to a parallel position.

In the analysis, the dimuon event efficiency was determined to be 50 ± 6 %, which was lower than the ∼ 85 % obtained in both the Run 1 $Z' \to \mu\ \mu$ search [75] and the Z^0 cross section measurement [76] using 110 pb^{-1}. This discrepancy was discussed in Chapter 8 and the low value found was caused by the low muon reconstruction and muon identification efficiencies. The latter efficiency was determined to be only 82.8 ± 3.9 % for the CMUP-CMUP muon sample studied, compared to 90.2 ± 4.2 % using a CMUP-CMX sample. The low result for the CMUP-CMUP sample could have been a statistical fluctuation. If larger samples were used the statistical uncertainties would be smaller therefore the efficiency could be determined more accurately and this may result in an increased efficiency. The reconstruction efficiencies are expected to improve as the reconstruction code develops. For example more efficient stub-track linking, improved extrapolation techniques, better stub finding algorithms, more precise alignment of the muon geometry in the code to the physical detector system would all increase the reconstruction efficiency.

15.5 Increase in the search acceptance

15.5.1 Include forward muon detector data

Rather than increasing the achievable upper cross section limit by increasing either the efficiency or the integrated luminosity, the acceptance could be increased. This can also be appreciated from Equation 15.1.

The CDF detector has muon coverage beyond the CMUP detector used in the analysis. The

CMX detector extends the CMUP pseudorapidity coverage from 0.6 up to 1.0, and the BMU covers a pseudorapidity region from 1.0 to 1.5. In the analysis performed, only CMUP-CMUP muon combinations were included, because there were sporadic noise problems in the CMX chambers and the forward BMU muon chambers were in the process of being commissioned. When the CDF muon detectors are fully operational the increased in acceptance from these detectors could be exploited.

The increase in the acceptance of the Z' boson caused by including CMUP-CMX dimuon combinations was investigated using Monte Carlo Z' samples. The samples studied were those used to determine the CMUP-CMUP acceptance, as described in Section 9.1. The acceptance[2] for the CMUP-CMX dimuon combination as a function of Z' boson mass is shown in Table 15.1 and illustrated by the square marker in Figure 15.3. For example, including just CMUP-CMX combinations was found to increase the acceptance, relative to the CMUP-CMUP acceptance, by ~ 100 % for a Z' boson of mass 200 GeV/c^2 and this increase reduced to ~ 60 % for a Z' boson of mass 800 GeV/c^2. Extending the pseudorapidity range of the chamber coverage by including the CMX chamber was found to give a smaller percentage increase for higher mass Z' bosons or gravitons. This was expected, because the higher the mass Z' bosons/gravitons decay to more central muons.

15.5.2 Loosen the muon stub criteria

An alternative method to enhance the muon data sample size, rather than including other muon detectors, would be to increase the acceptance in the central region. This could be achieved by loosening the muon stub matching criteria. Rather than requiring that the two muons both have CMU and CMP stubs, one muon (or even both) could be required to have only one stub, either a CMU or a CMP, so that CMUP-CMU and CMUP-CMP dimuon combinations would also be included. This would increase the acceptance, because there are regions of the CMU

[2]The acceptances shown in Table 15.1 were not corrected for the chamber inefficiencies, as described on page 152, because the inefficiencies of the CMX chambers had not been determined.

detector which are not covered by the CMP detector and vice-versa, as shown in the η vs ϕ plot for the central muon detectors in Figure 2.12, Section 2.2.6. Demanding the presence of a CMU and a CMP stub reduces the attainable acceptance of the detector.

	Acceptance (%)			
Z′ (GeV/c^2)	CMUP-CMUP	CMUP CMU only	CMUP CMP only	CMUP-CMX
200	4.7 ± 0.3	2.4 ± 0.2 (51)	2.6 ± 0.2 (55)	4.9 ± 0.3 (104)
250	5.2 ± 0.3	2.9 ± 0.2 (56)	2.9 ± 0.2 (56)	6.3 ± 0.3 (121)
300	6.1 ± 0.3	3.1 ± 0.2 (51)	3.3 ± 0.3 (54)	5.8 ± 0.3 (95)
350	7.2 ± 0.4	3.0 ± 0.2 (42)	3.1 ± 0.2 (43)	6.9 ± 0.4 (96)
400	8.0 ± 0.4	3.1 ± 0.2 (39)	4.1 ± 0.3 (51)	7.0 ± 0.4 (88)
450	7.7 ± 0.4	3.2 ± 0.2 (42)	4.5 ± 0.3 (58)	7.1 ± 0.4 (92)
500	8.6 ± 0.4	3.8 ± 0.3 (44)	4.6 ± 0.3 (53)	7.8 ± 0.4 (91)
550	9.1 ± 0.4	3.7 ± 0.3 (41)	4.3 ± 0.3 (47)	7.7 ± 0.4 (85)
600	10.0 ± 0.4	3.5 ± 0.3 (35)	5.6 ± 0.3 (56)	7.7 ± 0.4 (77)
650	10.2 ± 0.4	4.0 ± 0.3 (39)	5.3 ± 0.3 (52)	8.0 ± 0.4 (78)
700	11.2 ± 0.4	4.2 ± 0.3 (37)	4.6 ± 0.3 (41)	7.8 ± 0.4 (70)
750	10.9 ± 0.4	4.7 ± 0.3 (43)	5.4 ± 0.3 (50)	7.0 ± 0.4 (64)
800	11.6 ± 0.5	5.0 ± 0.4 (43)	5.5 ± 0.3 (47)	7.2 ± 0.4 (62)

Table 15.1: Summary of acceptance for CMUP-CMUP, CMUP-CMU, CMUP-CMP, CMUP-CMX dimuon combinations as a function of Z' mass from Monte Carlo. Binomial statistical errors are included for the acceptance. In brackets are the percentage increase in acceptance relative to the CMUP-CMUP acceptance.

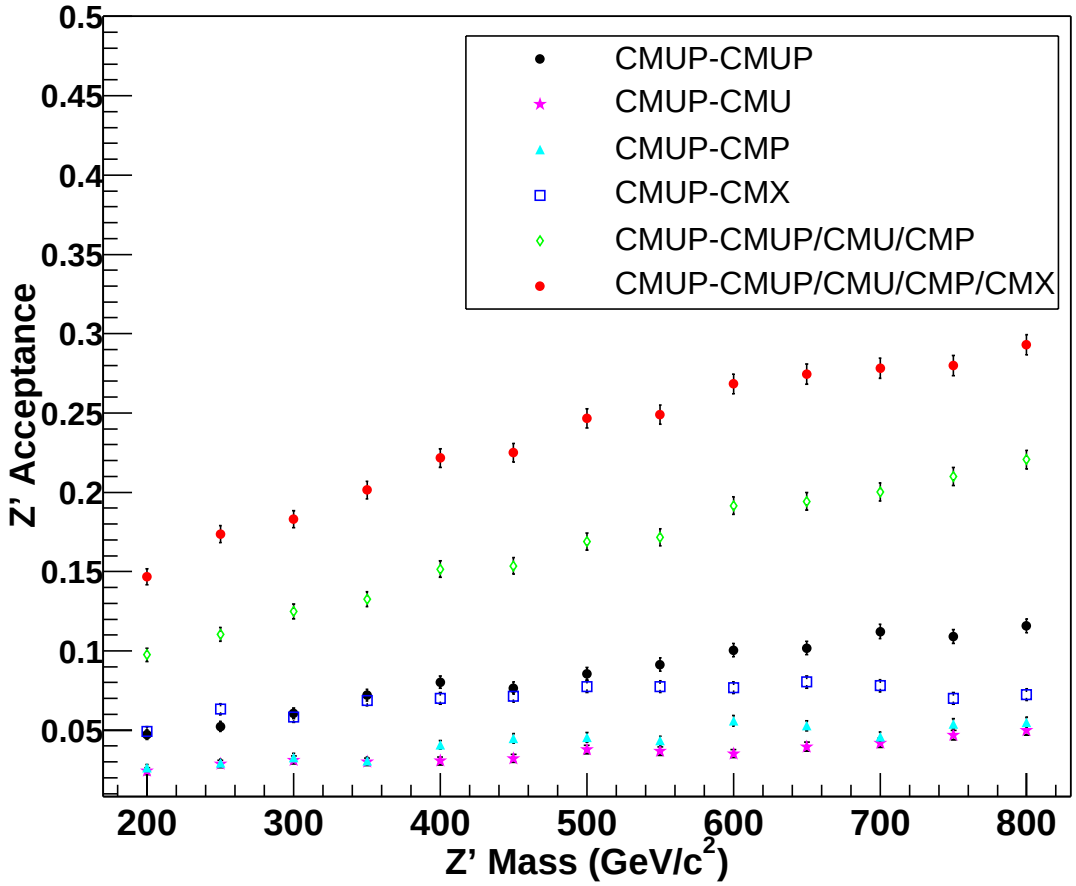

Figure 15.3: Acceptance as a function of Z' mass for various Monte Carlo dimuon combinations (CMUP-CMUP/CMU/CMP/CMX) for $Z' \to \mu\mu$.

The increased acceptance of permitting other muon stub combinations was investigated and the results are shown in Table 15.1 and illustrated in Figure 15.3. Allowing CMUP-CMU combinations (indicated by star markers) increased the acceptance by approximately 40 % relative to the CMUP-CMUP combinations (shown by the darker (black) circle markers). The increase ranged from at 56 % at 250 GeV/c^2 to 35 % at 600 GeV/c^2. The CMUP-CMP combinations produced a similar increase (illustrated by triangles markers in Figure 15.3).

In the analysis, CMUP muons were required in order to reduce the background from punch-throughs. In punch-through events it is typical for a hadron, such as a pion, to produce a CMU stub, but then be stopped by the steel between the CMU and CMP detectors and so a CMP stub is not formed. Therefore including the CMU only and the CMP only stubs, and particularly the CMU only, potentially adds more background as well as more noise events in addition to more signal events. Consequently, the relative gain would need to be investigated. The background could be estimated by comparing regions covered by both the CMU and CMP detectors to regions with only CMU or CMP coverage. An alternative would be to require both CMU and CMP stubs in regions covered by both detectors, but also to allow one stub muons in the regions not covered by both detectors. Such an analysis would require a tool which extrapolated the muon track to the radius of the relevant muon chamber and determined whether there was chamber coverage there or not. Such an "isFiducial" tool was in the process of being developed during the analysis, but was not complete enough to be used.

15.6 Reduce uncertainties

An alternative method to decrease the upper cross section limit would be to decrease $N_{95\%}$, as can be deduced from Equation 15.1. This could be achieved by reducing the uncertainties. The uncertainty is composed of statistical and systematic uncertainties. The former could be reduced by using larger data samples (if they are available). As the detector is more fully understood, the sources of systematic uncertainty could be identified more precisely, and improved estimations of

each component of the uncertainties could be made. Also the detector models used to simulate Monte Carlo events could be improved, in order to reduce the observed discrepancies between Monte Carlo and data.

15.7 Reduce the number of expected background events

Other potential improvements of the analysis include the reduction of the number of background events. Because the Z' mass lower limit has already (in Run I) been determined to be above 690 GeV/c^2 [89], one method to reduce the backgrounds would be to alter the signal region. As discussed in Chapter 10, two-sided signal regions are impractical for high energy dimuon searches, because of the poor invariant mass resolution caused by the degradation of the transverse momentum resolution with increasing transverse momentum. However, the one-sided signal region could be raised from 150 GeV/c^2 used in the analysis. For example, the invariant mass distribution for a Z' boson mass of 700 GeV/c^2, shown in Figure 10.3, lies predominantly above 250 GeV/c^2. Above this invariant mass there are very few dimuon events expected from the SM background (see Table 11.2). Consequently, the signal region could be raised for searches for higher mass Z' bosons, and similarly for graviton searches.

The main background contribution to high mass dimuons is from cosmic rays. In order to minimise the backgrounds, the cosmic ray rejection techniques employed could be improved. It was found that the most effective discriminator between cosmic rays and interaction dimuon events was the ToF time difference between the muon in the upper and the lower half of the detector. However, only approximately 45 % of the events in the final dimuon sample had ToF timing information for both muons. The low percentage was found to be caused predominantly by inefficient track to ToF hit linking. Increasing the number of dimuon events with ToF information for both muons would mean that the ToF time difference could be used in more events, which would consequently improve cosmic ray rejection. Also alternative methods could be used to identify cosmic rays, for example the COT timing. The pattern and timing of the

hits that a cosmic ray track leaves in the tracking chamber could be used to identify it as a cosmic ray, because of the characteristic way in which a muon passes through the chamber; the upper leg of the cosmic ray leaves hits in the outer layers of the COT chamber before the inner layers, which is in contrast to a muon which originates from the centre of the detector.

15.8 Other decay channels

Searching in other decay channels and combining the results with dimuon data would enhance the chance of discovering a new particle and, if no excess of events above the number expected in the SM is observed, could enable more stringent limits to be obtained. The improvement gained by including other channels is model-dependent.

In Run I the $\sigma_{95\%} \cdot \mathrm{B}(Z' \rightarrow \mu^+ \mu^-)$ obtained with an integrated luminosity of 110 pb^{-1} data was 550 GeV/c^2 and $\sigma_{95\%} \cdot \mathrm{B}(Z' \rightarrow e^+ e^-)$ was 650 GeV/c^2. Combining the dielectron and dimuon data sample increased the limit to 690 GeV/c^2. The Run I Z' mass limits for searches conducted in the dimuon, dielectron and their combined results, as a function of the luminosity of the data analysed, are summarised in Table 15.2.

Run and data set	Luminosity (pb^{-1})	Mass limit (GeV/c^2)
Run 1A $\mu\mu$	18.8	440
Run 1B $\mu\mu$	88.6	575
Run 1A+1B $\mu\mu$	18.8 + 88.6	550
Run 1A ee	19.7	505
Run 1A +1B ee	19.7 + 71.3	650
Run 1A ee + Run 1A $\mu\mu$	19.7 + 18.8	540
Run 1A ee + Run 1A+1B $\mu\mu$	19.7 + 71.3	590
Run 1A+1B ee + Run 1A+1B $\mu\mu$	110.1 + 107.4	690

Table 15.2: 95 % confidence level lower limits on the Z' mass obtained using dimuon ($\mu\mu$) and dielectron (ee) Run I data [88] [89] [90].

For high mass searches, electrons have several advantages over muons in the CDF detector. One advantage is that electrons have a larger acceptance, because the plug calorimeter extends

the electron pseudorapidity coverage up to 3.6 (compared coverage up to 1.5 for muons). Another advantage, which is particularly relevant for very high mass searches, is that the energy of electrons can be determined using calorimeter information, rather than tracking information, because electrons, unlike muons, deposit most of their energy in the electromagnetic calorimeter. The calorimeter energy resolution (ΔE α $\sqrt{E}$) decreases more slowly with increasing energy than the transverse momentum resolution from the tracking detector (Δp_T α p_T^2). Consequently, more sensitive electron energy and therefore invariant mass measurements can be made in the dielectron channel at high mass.

Dilepton data could also be combined with other search channels to optimise the potential of discovery or to set more stringent limits. Diphoton production is one of the best probes of TeV scale gravity at hadron colliders. In the Standard Model, photon-photon scattering only takes place via box diagrams of W bosons and quarks so that it is loop suppressed. However, in graviton models, photons can scatter via exchanges of gravitons. Combining diphoton and dilepton data is an excellent way to improve the dilepton limits achievable in the ADD model. In Run I at CDF, 5 events with $M_{\gamma\gamma} > 150$ GeV/c^2 were found, when 4.5 ± 0.6 were expected (100 pb^{-1}), which set the ADD model effective Planck scale lower limit (M_s) > 0.9 TeV for four extra dimensions [31].

15.9 Study different distributions

In addition to studying only the invariant mass distribution, with more data it would also be possible to study the angular distribution of the dileptons, rather than just the invariant mass distribution. This is advantageous for several reasons.

The sensitivity of extra dimensional searches can be improved by studying the double differential cross section in invariant mass and scattering angle. The improvement in limit on the ADD model effective Planck scale lower limit (M_s) is equivalent to a 30 % decrease in the integrated luminosity needed to obtain a certain sensitivity in M_s [33].

In addition, if an excess of events above the number predicted by the SM is observed, it could indicate the presence of any one of a plethora of new physics scenarios; for example, the existence of new bosons, quark-lepton compositeness, technicolor or extra dimensions. The new physics different processes could be distinguished by the nature of the deviation from the SM in the angular distribution as well as the invariant mass distribution of the dileptons/diphotons. For example, graviton exchange has a particularly identifiable signature, because it distinctively alters the dilepton/diphoton angular distribution, as illustrated in Figure 1.8, because the graviton is a spin two particle. Extra dimensional models could be distinguished from each other by the nature of the excess observed in the invariant mass spectrum: a narrow excess in cross section or a series of resonances (RS model, illustrated in Figure 1.7, Section 1.3.3) in contrast to a broad increase in cross section (ADD model, shown in Figure 1.5, Section 1.3.2).

Angular information can also be a useful probe of new physics. For example, if a Z' boson existed then the relative strengths of the Z' gauge couplings could be tested using the forward-backward asymmetry (A_{FB}) of the dimuons or dielectrons [91]. This is one of the cleanest ways to investigate a particular combination of quark and lepton couplings. Another useful distribution which could be studied is the ratio of cross sections in different pseudorapidity bins. This was recognised as a valuable complementary probe to the A_{FB} which enables separation of the Z' couplings to the u and d quarks, due to the harder u-valence quark contribution in the proton relative to the d quark [92]. However, the ability to measure these quantities depends on the statistics of the data sample under consideration.

15.10 Increase the centre of mass energy

The increase in the mass limit caused by increasing the luminosity of the search (or the equivalent increase in efficiency or acceptance as considered in previous sections in this chapter) can be contrasted to the gain resulting from an increase in the centre of mass energy. The latter was investigated by determining the cross section for Z' production and decay to dimuons as a

function of Z' mass, by generating Z' events with a range of masses from 200 to 800 GeV/c^2 using Pythia, at the centre of mass energy of 1.8, 1.96 and 3.92 TeV. After multiplication by the K-factor (1.3), the σ.B results were plotted as a function of mass together with the $\sigma_{95\%} \cdot$ B(Z' $\rightarrow \mu^+ \mu^-$) limits determined in Section 15.3, using CMUP-CMUP dimuon combinations for an integrated luminosity of 100, 200 pb^{-1} and 2 fb^{-1}. The effects of increasing the centre of mass energy and the luminosity were compared, and are described below, first for a general case and then with reference to Figure 15.4.

If the luminosity were increased then the upper cross section limit would equivalently move down the plane, which would result in an increase in lower mass limit, since the position of the intersection of the upper cross section limit and the theoretical cross section would occur at a higher mass. The luminosity increase would result in only a logarithmic increase in the lower mass limit. In contrast, an increase in the centre of mass energy would equivalently leave the position of the upper cross section curve unchanged, but would alter the position of the theoretical cross section curve. In Figure 15.4, this curve would move to the right, which would also make the intersection of the two cross section curves occur at a higher invariant mass, however, this would increase the mass limit faster than the logarithmic increase caused by an increase in the luminosity. Consequently, raising the centre of mass energy would significantly enhance the mass reach obtainable and decrease the amount of luminosity required to set a specific lower mass limit. A small increase in the centre of mass energy would be equivalent to a large increase in integrated luminosity. For example, if the integrated luminosity were doubled from 100 pb^{-1} to 200 pb^{-1}, then the Z' upper mass limit would increase by about 85 GeV/c^2, from 455 GeV/c^2 to 540 GeV/c^2, as shown in Figure 15.4, whereas, doubling the centre of mass energy would increase the Z' upper mass limit by approximately 255 GeV/c^2, from 455 GeV/c^2 to 710 GeV/c^2 for 100 pb^{-1} of data. In addition, for a specific increase in luminosity, the higher the centre of mass energy, the larger the resulting increase in the upper mass limit would be. This is demonstrated in Figure 15.4; doubling the integrated luminosity from 100 pb^{-1} to 200

pb^{-1} would increase the upper mass limit by 130 GeV/c^2 for a centre of mass energy of 3.92 GeV, compared to an increase of 85 GeV/c^2 for a centre of mass energy of 1.96 GeV.

The results found by extrapolating 16 pb^{-1} of Run II dimuon data were confirmed by similar extrapolations from 110 pb^{-1} of Run I dilepton data, shown in Figure 15.5 [51]. This figure shows the expected mass reach vs integrated luminosity at the Tevatron for Z' decaying to dileptons, at a centre of mass energy ($\sqrt{s}$) of 1.8 TeV (indicated by the square marker) and 2.0 TeV (triangle marker). It demonstrates (as does Figure 15.4) that the possible reach can be increased both by using more data and by increasing the centre of mass energy. The position of the labels, IA, IB and II, indicate the position of the limits obtained in Run IA ($\sim$ 20 pb^{-1}), Run IB ($\sim$ 90 pb^{-1}) and those predicted for Run II with an integrated luminosity of 2 fb^{-1} respectively. The predicted Z' mass limit, using dilepton data, can be extended to 900 GeV/c^2 assuming Standard Model couplings and a centre of mass energy ($\sqrt{s}$) of 1.8 TeV for an integrated luminosity of 2 fb^{-1}, and the limits are approximately 100 GeV/c^2 higher if the centre of mass energy is assumed to be 2.0 TeV.

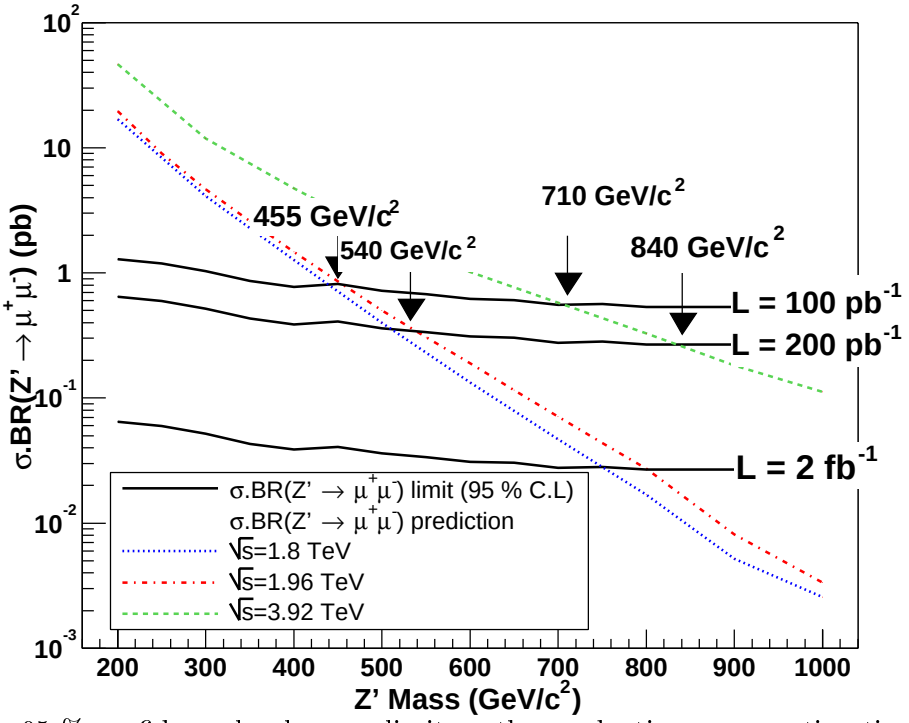

Figure 15.4: 95 % confidence level upper limit on the production cross section times branching fraction of $Z' \to \mu^+ \mu^-$ ($\sigma \cdot \mathrm{BR}(\mathrm{Z'} \to \mu^+ \mu^-)$) as a function of Z' mass for increasing the integrated luminosity of 100 and 200 pb^{-1}. The uncertainties calculated for the 16 pb^{-1} sample were included and only CMUP-CMUP dimuon combinations were considered. It was assumed that no events were observed in the signal region. Three predicted $\sigma \cdot \mathrm{BR}(\mathrm{Z'} \to \mu^+ \mu^-)$ curves are shown, corresponding to different centre of mass energies.

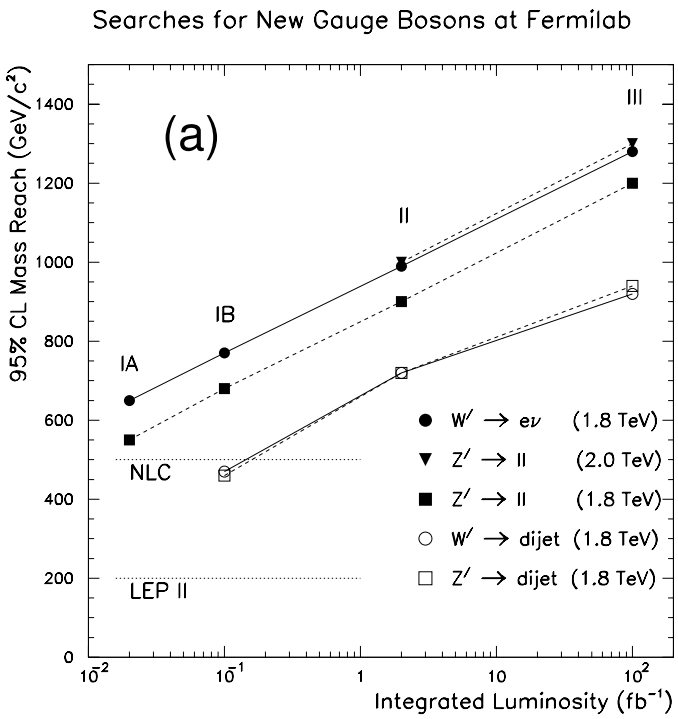

Figure 15.5: The expected mass reach, defined as the 95% C.L. lower limit on the mass vs. integrated luminosity at the Tevatron for searches for new gauge bosons [51].

15.11 Future Limits

At present the Tevatron is the highest energy collider in the world, so it is one of the best place to be searching for new physics. The higher statistics anticipated to be available in future in Run II will permit the study of angular distributions in addition to invariant mass distributions. With more data it is expected that the limits on new physics set in Run I will be exceeded in Run II. The predicted limits expected in Run II with an integrated luminosity of 2 fb^{-1} are presented below.

If the Run I Z' results, obtained using an integrated luminosity of 110 pb^{-1} of dilepton data, are extrapolated to Run II energies with 2 fb^{-1}, the predicted Z' mass limit is 1000 GeV/c^2 with $\sqrt{s}$ = 2.0 TeV. This can be compared to Run I result of 690 GeV/c^2. The extrapolated mass reaches are illustrated in Figure 15.5, in which it is assumed that no candidate events in the high mass region are found and that the Z' has Standard Model couplings [51].

It is expected that with an integrated luminosity of 2 fb^{-1} the RS model graviton exclusion region, in the k/$\bar{M}_{Pl}$ and m_1^{grav} plane, could be extended. The expected exclusion reach from dilepton and dijet data collected at the Tevatron detectors is illustrated in Figure 15.6. The lower mass limit predicted from dilepton data for k/$\bar{M}_{Pl}$=0.01 is $\sim$ 500 GeV/c^2 and that for k/$\bar{M}_{Pl}$=0.1 is $\sim$ 900 GeV/c^2. The resulting sensitivities to the RS model parameter Λ_π achievable in the contact interaction regime[3] at the Tevatron for an integrated luminosity of 2 fb^{-1} are compared to those anticipated from the combined LEP II experiments for 2.5 fb^{-1} and LHC for 100 fb^{-1} of data in Table 15.3 [24].

	Luminosity (fb^{-1})	k/$\bar{M}_{Pl}$	
		0.01	0.1
Tevatron Run II	2	5.0	1.5
LEP II	2.5	4.0	1.5
LHC	100	20.0	7.0
LC $\sqrt{s}$	500	20.0	5.0
LC $\sqrt{s}$	500	40.0	10.0

Table 15.3: 95 % confidence level search reach for Λ_π in the contact interaction regime at LEP II, the Tevatron, LHC, and a linear collider (LC) [24].

[3]The contact interaction regime is one in which the mass of the first resonance is so large that a resonance is not observed, but instead the effects of the graviton's existence can be detected via virtual graviton exchange.

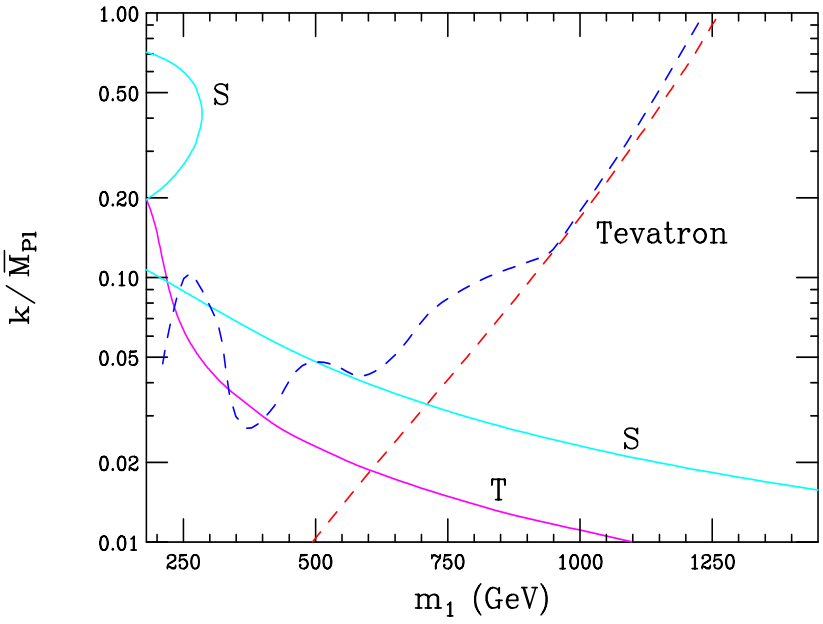

Figure 15.6: Excluded region in the k/$\bar{M}_{Pl}$ and m_1^{grav} plane for RS model gravitons, in which the SM particles are confined to the TeV-brane. The purple (T) and light blue (S) solid curves arise from oblique correction constraints and the excluded regions are below and to the left of these curves. The dark blue bumpy dashed and red straight dashed curved are the predicted bounds from Run II (2 fb^{-1}) Tevatron from dijet and dilepton searches respectively and will exclude regions above and to the left [43].

It is interesting to note that in the case where the SM field content resides on the TeV-brane, the LHC should be able to probe the entire region of parameter space of the RS model with 100 fb^{-1} of integrated luminosity, provided that the scale of electroweak physics (Λ_π) on the 3-brane is less than 10 TeV (which is required to solve the hierarchy problem). This is illustrated by the solid diagonal line on the right of Figure 15.7. Hence, in this scenario, the LHC should be able to either discover or exclude the existence of the RS graviton [43].

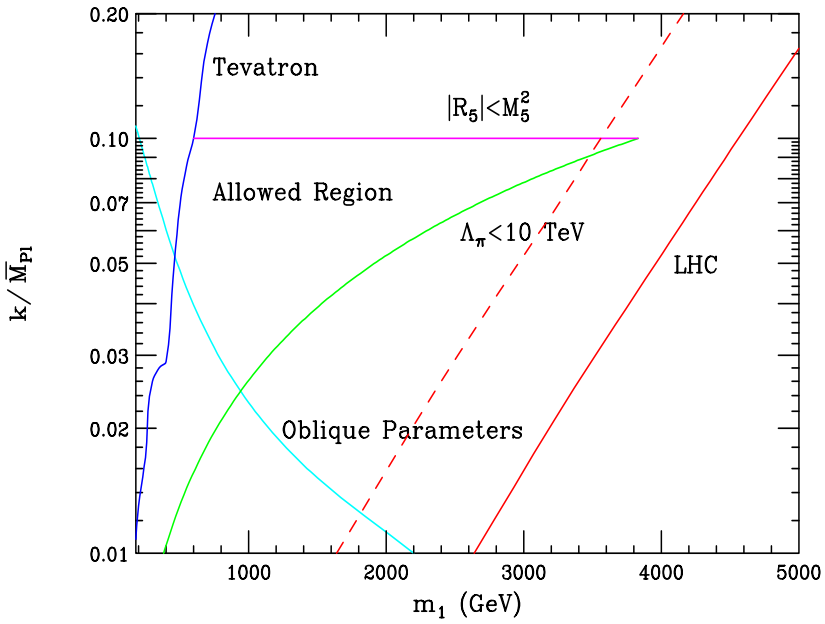

Figure 15.7: Summary of present experimental, theoretical and the predicted LHC constraints on the RS model, in the $k/\bar{M}_{Pl}$ and m_1^{grav} plane. The allowed region lies in the centre, as indicated. The limits obtained from the Tevatron for the data collected between 1992 and 1996 is shown by the solid curve on the left. The theoretical constraints limiting $k/\bar{M}_{Pl} < 0.1$ and $\Lambda_\pi < 10$ TeV arise from the bound on the curvature of the 5-dimensional space and the desire to solve the hierarchy problem. The LHC sensitivity to graviton resonances in the dilepton channel is represented by the diagonal dashed and solid curves, corresponding to 10 and 100 fb^{-1} of integrated luminosity, respectively [43].

It is a very exciting time to be working at CDF and it is hoped that, in Run II, CDF data will either enable new physics to be discovered or stringent new limits to be obtained, before the turn on of the LHC.

References

[1] D. Perkins, *"Introduction to High Energy Physics"*, Addison-Wesley (1982); P. Renton, *"Electroweak Interactions"*, Cambridge University Press (1990).

[2] K. Hagiwara *et. al.* (Particle Data Group). Phys. Rev. D **66**, 010001 (2002) (URL:http://pdg.lbl.gov).

[3] R. Robinett and J. Rosner, Phys. Rev. D**25**, 3036 (1982); R. Robinett and J. Rosner, Phys. Rev. D**25**, 3036 (1982); R. Robinett and J. Rosner, Phys. Rev., D**26**, 2396 (1982); P. Langacker, R. Robinett, and J. Rosner, Phys. Rev. D**30**, 1470 (1984).

[4] E. Faraggi and M. Thormeier, Nucl. Phys. B**624**, 163 (2002); E. Faraggi, Phys.Lett. B**499**, 147 (2001).

[5] U. Baur *et.al.*, Phys. Rev. D**35**, 297 (1987).

[6] Particle Data Group, *"Standard Model Review"*, 21 (2001) (http://pdg.lbl.gov/2002/stanmodelrpp.pdf).

[7] A. Leike, Fortsch. Phys. **50**, 538 (2002) [arXiv:hep-ph/0111300].

[8] K. Hagiwara *et al.*, Phys. Rev. D**66**, 010001 (2002) (http://pdg.lbl.gov/2002/gutsrpp.pdf).

[9] F. del. Aguila, Acta Phys. Polon. B**25**, 1317 (1994) [arXiv:hep-ph/hep-ph9404323].

[10] K. Hagiwara *et al.*, Phys. Rev. D**66**, 010001 (2002) (http://pdg.ge.infn.it/2002/zprime_s056215.pdf).

[11] G. Cho, Mod. Phys. Lett. A**15**, 311 (2000).

[12] K. Babu, C. Kolda and J. March-Russell, Phys. Rev. D**57**, 6788 (1998); A. Leike, S. Riemann and T. Riemann, Phys. Lett. B**291**, 187 (1992).

[13] DELPHI Collaboration, CERN-PPE/94-121 (1994).

[14] C. Geweniger, C. Goy, M-N Minard, M. Elsing, J. Holt, W. Liebig, P. Renton, D. Bourilkov, S. Riemann and S. Wynhoff, 2002-096 PHYS 926, (2002).

[15] Bob Holdom, Phys. Lett. B**259**, 329 (1991).

[16] M. Cvetič and P. Langacker, Phys. Rev. D**46**, 4943 (1992).

[17] M. Cvetič and P. Langacker, Phys. Rev. D**46**, R14 (1992); J. Hewett and T. Rizzo, Phys. Rev. D**47**, 4981 (1993); F. del Aguila, B.Allés, Ll. Ametller and A. Grau, Phys. Rev. D**48**, 425 (1993).

[18] T. Rizzo, Phys. Rev. D**47**, 956 (1993).

[19] S. Chapstick and S. Godfrey, Phys. Rev. D**37**, 2466 (1988).

[20] CDF Collaboration (F. Abe *et al.*), Phys. Rev. Lett. **79**, 2192 (1997).

[21] D0 Collaboration (B. Abbott *et al.*), FERMILAB-CONF-97-367-E (1997).

[22] N. Arkani-Hamed, S. Dimopoulos, G.Dvali, Phys. Lett. B**429**, 263 (1998).

[23] L. Randall and R. Sundrum, Phys. Rev. Lett **83**, 3370 (1999) [arXiv:hep-ph/9905221].

[24] J. Hewett and M. Spiropulu, arXiv:hep-ph/0205106.

[25] I. Antoniadis, N. Arkani-Hamed, S. Dimopoulos and G. Dvali, Phys. Lett. B**436**, 257 (1998) [arXiv:hep-ph/9804398].

[26] I. Antoniadis, K. Benakli, Int. J. Mod. Phys. A**15**, 4237 (2000) [arXiv:hep-ph/0007226].

[27] T.Han, J. Lykken, and R. Zhang, Phys. Rev. D**59**, 105006 (1999) [arXiv:hep-ph/9811350].

[28] G. Guidice, R. Ratazzi, and J. Wells, Nucl. Phys. B**595**, 250 (2001) [arXiv:hep-ph/0002178].

[29] N. Arkani-Hamed, S. Dimopoulos, and G. Dvali, Phys. Rev. D**59**, 086004 (1999).

[30] G. Guidice, R. Ratazzi, and J. Wells, Nucl. Phys. B**544**, 3 (1999) [arXiv:hep-ph/9811291].

[31] K. Cheung and G. Landsberg, Phys. Rev. D**62**, 076003 (2000) [arXiv:hep-ph/9909218].

[32] R. Hamberg, W. van Neerven and T. Matsuura, Nucl. Phys. B**359**, 343 (1991).

[33] K. Cheung and G. Landsberg, arXiv:hep-ph/hep-ph 9909218.

[34] A. Gupta, N. Mondal and S. Raychaudhuri, arXiv:hep-ph/9904234.

[35] Y. Uehara, Mod. Phys. Lett. A**17**, 1551 (2002) [arXiv:hep-ph/0203244].

[36] S. Cullen and M. Perelstein, Phys. Rev. Lett. **83**, 268 (1999) [arXiv:hep-ph/9903422].

[37] E. Mirabelli, M. Peskin, and M. Perelstein, Phys. Rev. Lett. **82**, 2236 (1999) [arXiv:hep-ph/9811337].

[38] J. Hewett, Phys. Rev. Lett. D**82**, 4765 (1999) [arXiv:hep-ph/9811356].

[39] D0 Collaboration (B. Abbott *et al.*), Phys. Rev. Lett. **86**, 1156 (2001).

[40] K. Cheung and G. Landsberg, Phys. Rev. D**62**, 076003 (2000) [arXiv:hep-ph/9909218].

[41] H. Davoudiasl, J. Hewett and T. Rizzo, arXiv:hep-ph/9909255.

[42] W. Goldberger and M. Wise, Phys. Rev. Lett. **83**, 4922 (1999).

[43] H. Davoudiasl, J. Hewett and T. Rizzo, Phys. Rev. D**63**, 075004 (2001) [arXiv:hep-ph/0006041].

[44] H. Davoudiasl, J. Hewett and T. Rizzo, Phys. Lett. D**473**, 43 (2000); A. Pomarol, Phys. Lett. B**486**, 153, (2000) [arXiv:hep-ph/9911294].

[45] L. Randall and R. Sundrum, Phys. Rev. Lett. **83**, 4690 (1999) [arXiv:hep-th/9906064].

[46] K. Dienes, E. Dudas and T. Gherghetta, Phys. Lett. B**436**, 55 (1998).

[47] A. Pomarol and M. Quiros, Phys. Lett. B**438**, 255 (1998).

[48] M. Masip and A. Pomeral, Phys. Rev. D**60**, 096005 (1999).

[49] N. Arkani-Hamed and M. Schmaltz, Phys. Rev. D**61**, 033005 (2000) [arXiv:hep-ph/9806263].

[50] http://www.fnal.gov/pub/inquiring/physics/accelerators/chainaccel.html

[51] CDF II Collaboration (F. Abe *et al.*), FERMILAB-Pub-96/390-E (1996).

[52] M. Bishai, P Lukens, R. Madrak, T. Miao, R. Tesarek, S. Tkaczyk and W. Wester, CDF/DOC/TRACKING/CDFR/5931 (2002).

[53] M. Jones, CDF/DOC/TOF/CDFR/5930 (2002).

[54] M. Cordelli, S. Dell'Agnello, F. Happacher, M. J. Kim, N. Luthzesky, S. Miscetti, F. Ptohos, J. Russ, A. Sansoni and I. Sfiligoi, CDF/DOC/CALORIMETRY/GROUP/5856 (2002).

[55] CDF Collaboration (F. Abe *et. al.*), Phys. Rev. D**50**, 2966 (1994); CDF Collaboration (F. Abe *et. al.*), Phys. Rev. Lett. **73**, 225 (1994); CDF Collaboration (F. Abe *et. al.*), Phys. Rev. Lett. **74**, 2646 (1995).

[56] CDF Collaboration (F. Abe *et. al.*), Phys. Rev. Lett. **75**, 11 (1995).

[57] CDF Collaboration (F. Abe *et. al.*), Phys. Rev. Lett. **74**, 4988 (1995).

[58] CDF Collaboration (F. Abe *et. al.*), Phys. Rev. Lett. **74**, 3538 (1995).

[59] CDF Collaboration (F. Abe *et. al.*), Phys. Rev. D., Rapid Communications **51**, 949 (1995).

[60] http://www.fnal.gov/pub/now/lumrecord-9-24.html

[61] http://lotus.phys.nwu.edu/ schmittm/cdfmuon/

[62] Jaco Konigsberg *et al.*, http://www-cdf.fnal.gov/internal/people/links/JacoboKonigsberg/lum_official_page.html, "The Uncertainty in the CLC Luminosity", Presentation at CDF joint physics meet (12-Jul-2002).

[63] D. Saltzberg and M. Shochet *et. al.*, CDF/PHYS/TRIGGER/CDFR/4718 (1998).

[64] Young-Kee Kim *et al.*, http://www-cdf.fnal.gov/internal/people/links/Young-KeeKim/COT_Validation.html

[65] K. Bloom, E. James, J. Kang, V. Martin, T. Pratt, M. Schmitt, A. Taffard, A. Varganov, CDF/PHYS/ELECTROWEAK/PUBLIC/6017 (2002).

[66] Jaco Konigsberg *et al.*, http://www-cdf.fnal.gov/internal/people/links/JacoboKonigsberg/lum_official_page.html

[67] http://cdfcodebrowser.fnal.gov/CdfCode/source/StripMods/src/StripHighPtMuon.cc

[68] Criteria used for skimming inclusive muon data into Z and W datasamples http://fcdfhome.fnal.gov/usr/varganov/RunIIAnalysis/stripping.html, skimmed by Alexei Vargonav, University of Michigan.

[69] http://www-cdf.fnal.gov/cdfsim/cdfsim_main.html

[70] http://www.thep.lu.se/tf2/staff/torbjorn/Pythia.html

[71] http://www.phys.psu.edu/ cteq/

[72] http://www-cdf.fnal.gov/cdfsim/cdfsim_main.html

[73] http://cdfcodebrowser.fnal.gov/CdfCode/source/Production/

[74] http://cdfcodebrowser.fnal.gov/CdfCode/source/?v=4.5.3

[75] P. de Barbaro, A. Bodek, E. Hayashi, K. Maeshima, C. Grosso-Pilcher and M. Pillai, CDF/ANAL/EXOTIC/CDFR/2910 (1995).

[76] CDF Collaboration (F. Abe *et. al.*), Phys. Rev. D**59**, 052002 (1999) [CDF/PUB/ELECTROWEAK/PUBLIC/4092 (1997)].

[77] Private communication from Willis Sakumoto, University of Rochester (September 2002).

[78] http://cdfcodebrowser.fnal.gov/CdfCode/source/CosmicMods/

[79] M. Pillai, CDF/ANAL/EXOTIC/CDFR/3776 (1996).

[80] Binomial upper and lower limits were calculated using Formulas 31.50a and 31.50b from Section 31.4.2.4 on page 21, with $F_{F^{-1}} = 1$, from the Particle Data Group's webpage; http://pdg.lbl.gov/2002/contents_sports.html#mathtoolsetc, link "Statistics (Rev.)". The program used was coded by Michael Schmitt at Northwestern University, USA.

[81] K. Bloom, J. Kang, V. Martin, T.Pratt, M. Schmitt, A. Taffard and A. Varganov, CDF/PHYS/ELECTROWEAK/CDFR/6025 (2002).

[82] A. Hocker and W. Sakumoto, Private communication for W cross section analysis [65].

[83] D. Glenzinksi, M. Herndon, C. Lin, T. Liu, J. Thom, P. Wilson, Wittich and A. Yagil, CDF/PHYS/ELECTROWEAK/CDFR/5973 (2002).

[84] K. Bloom and W. Dagenhart, CDF/ANAL/COMP_UPG/CDFR/6029 (2002).

[85] J. Conway and K. Maeshima, CDF/PUB/EXOTIC/PUBLIC/4476 (1998).

[86] Particle Data Group, http://pdg.lbl.gov/2002/statrpp.pdf (2002).

[87] T.Huffman, K. Ikado, K. Maeshima and T. Pratt, CDF/ANAL/EXOTIC/CDFR/6080 (2002).

[88] M. Pillai, P. de Barbaro, B. Kim, A. Bodek, W. Sakumoto, K. Maeshima, E. Hayashi, C. Grosso-Pilcher, CDF/ANAL/EXOTIC/GROUP/3598 (1996).

[89] M. Pillai, P. de Barbaro, A. Bodek, K. Maeshima, E. Hayashi and C. Grosso-Pilcher, CDF/ANAL/EXOTIC/CDFR/4120 (1997).

[90] M. Pillai, P. de Barbaro, A. Bodek, K. Maeshima, E. Hayashi and C. Grosso-Pilcher, CDF/ANAL/EXOTIC/CDFR/3020 (1995).

[91] P. Langacker, R. Robinett and J. Rosner, Phys. Rev. D**30**, 1470 (1984).

[92] F. del Aguila, M. Cvetič and P. Langacker, Phys. Rev. D**48**, R969 (1993).

Appendix A: Appendix

A.1 The Higgs mechanism

The Higgs mechanism generates masses in the SM and is based on spontaneous symmetry breaking of the electroweak $\mathrm{SU}(2)_L \times \mathrm{U}(1)_Y$ symmetry [1]. The Higgs mechanism is an extension of the Goldstone Theorem which states that if a Lagrangian has a global symmetry, which is not a symmetry of the vacuum (*i.e.* the ground state), then there must exist one massless boson, scalar or pseudoscalar, associated to each generator which does not annihilate the vacuum. These modes are known as Goldstone Bosons. The Goldstone Theorem is not gauge invariant.

A weak isospin doublet of complex scalar fields (ϕ) is introduced which belongs to the $SU(2)_L \times U(1)_Y$ multiplets:

$$\phi = \begin{pmatrix} \phi^+ \\ \\ \phi^0 \end{pmatrix}, \tag{A.1}$$

along with the scalar potential $V(\phi)$:

$$V(\phi) = \mu^2 \phi^\dagger \phi + \lambda (\phi^\dagger \phi)^2. \tag{A.2}$$

This gives an additional contribution to the electroweak Lagrangian:

$$\mathcal{L}_{Higgs} = (D_\mu \phi)^\dagger (D^\mu \phi) - V(\phi) \tag{A.3}$$

where the covariant derivative D_μ is defined as:

$$D_\mu = \delta_\mu + ig\frac{\sigma}{2} \cdot W_\mu + ig' B_\mu. \tag{A.4}$$

For the choice $\mu^2 < 0$ and $\lambda > 0$, then the minimum potential occurs at:

$$|\phi^2| = \left(\frac{-\mu^2}{2\lambda}\right) = \frac{v^2}{2} \tag{A.5}$$

where v is the vacuum expectation value. Using gauge invariance the ground state can be chosen to be:

$$| < 0|\phi|0 > | = \begin{pmatrix} 0 \\ \\ \frac{v}{\sqrt{2}} \end{pmatrix}. \tag{A.6}$$

These solutions are degenerate and allow the introduction of four real fields all with zero vacuum expectation values, such that:

$$\phi(x) = \frac{1}{\sqrt{2}} \begin{pmatrix} \sigma_1(x) + i\sigma_2(x) \\ \\ v + \eta_1(x) + i\eta_2(x) \end{pmatrix}. \tag{A.7}$$

On substitution of this into the electroweak Lagrangian with the addition of the Higgs term (Equation A.3), it can be shown that there will be three massless Goldstone bosons ($\sigma_1(x)$, $\sigma_2(x)$, η_2) and a massive scalar particle, $\eta_1(x)$, with mass $M_H = \sqrt{2\lambda v^2}$, known as the Higgs boson.

These three Goldstone bosons are 'gauged' away, by requiring that ϕ satisfies the unitary transformation:

$$\phi'(x) = \frac{1}{\sqrt{2}} \begin{pmatrix} 0 \\ \\ v + H \end{pmatrix} = U\phi(x) \tag{A.8}$$

Thus by applying the Higgs mechanism to the original massless electroweak Lagrangian, local gauge invariance is ensured and massless Goldstone bosons become the longitudinal polarisation states of the massive vector boson W and Z. The W and Z have acquired the masses:

$$M_W = g\frac{v}{2}; \qquad M_Z = g\frac{v}{2}cos\theta_W. \tag{A.9}$$

The Higgs mechanism also generates fermions masses, by the inclusion of a term representing an interaction of the fermions with the Higgs field. The fermions couple to the Higgs proportionally to their mass.

A.2 Newtonian gravity

Following is a derivation of Gauss's Law in 4+n dimensions. Two test masses, m_1 and m_2 positioned a distance r apart in n extra spatial dimensions of radius R_c such that r << R_c, will experience a gravitational potential from Gauss's Law in (4+n) dimensions [22]:

$$V(r) \approx \frac{m_1 m_2}{M_{Pl(4+n)}^{n+2}} \frac{1}{r^{n+1}} \quad for \;\; r << R_c. \tag{A.10}$$

where $M_{Pl(4+n)}$ is the fundamental 4+n-dimensional Planck scale in the bulk. Alternatively, if the masses are placed at distances such that r >> R_c, then their gravitational flux lines cannot continue to penetrate into the extra dimensions and the usual 1/r potential is obtained:

$$V(r) \approx \frac{m_1 m_2}{M_{Pl(4+n)}^{n+2} R_c^n} \frac{1}{r} \quad for \;\; r >> R_c. \tag{A.11}$$

From comparing Equation A.10 to Equation A.11, it can be deduced that the effective 4-dimensional M_{Pl} satisfies the relationship:

$$M_{Pl}{}^2 \approx M_{Pl(4+n)}{}^{n+2} R_c^n. \tag{A.12}$$

Consequently, in the scenario of large extra dimensions, deviations from the usual inverse-square gravitational force (where the force is the derivation of the potential with respect to r) law can occur. For n=2 transitions in the force from $1/r^2$ to $1/r^4$ are searched for.

A.3 Suppression of graviton emission

For any physical process involving the emission of a graviton, the amplitude of this process is proportional to $1/M_{Pl}$ and therefore the rate to $1/M_{Pl}^2$. In the ADD scenario, there are $(ER_c)^n$ massive Kaluza-Klein modes that are kinematically accessible in a collider process with energy scale E. In the case for n=2 and E=1 TeV, there are therefore 10^{30} graviton KK states which may individually contribute to a process. The total combined rate (r) for emitting any one of the available gravitons is

$$r \sim \frac{1}{M_{Pl}^2}(ER_c)^n. \tag{A.13}$$

Substituting $M_{Pl}^2 = V_n M_S^{2+n}$ and $V_n \sim R_c^n$ into Equation A.13 it can be seen that the phase space summation for the Kaluza-Klein modes cancels out the dependence on M_{Pl} (because of the high density of massive KK graviton states after compactification) and thus reduces the suppression. The rate becomes

$$\sim \frac{E^n}{M_S^{2+n}}. \tag{A.14}$$

Thereby, after summation, the suppression of $1/M_{Pl}$ is reduced to $1/M_S$, which is the order of $\sim TeV^{-1}$ (M_{EW}^{-1}). Consequently, the effective gravitational interaction is of comparable strength to that of the electroweak interaction.

Appendix B: Derivation of first order beam offset correction to d_0

The two-dimensional impact parameter (d_0) is defined as the minimum perpendicular distance from the origin to the track, this is illustrated in Figure B.1. However, usually the beam interaction point does not occur at the centre of the detector, therefore d_0 needs to be corrected for the displacement of the beam. A first order correction to the impact parameter is derived here.

The impact parameter with respect to the beam position ($d_0^{corrected}$) can be calculated by rotating the beam axis (originally X,Y to X$'$,Y$'$) about the detector origin, such that the track is parallel to the rotated X$'$-axis. In the rotated frame the corrected impact parameter ($d_0^{corrected}$) is the difference between the track's d_0 in the original frame and the rotated y-coordinate of the beam position in the X$'$Y$'$ frame (beamy$'$), as shown in the Figure B.1 and in Equation B.1. This calculation is exact for straight tracks, and is a very good approximation for any momentum that can be reconstructed.

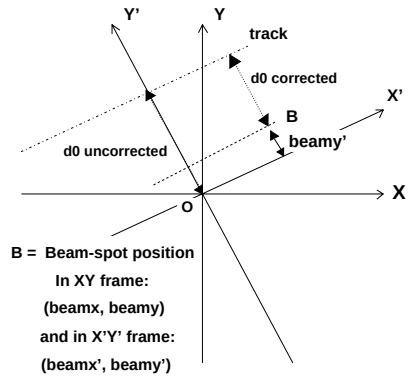

Figure B.1: Figure to show first order d_0 correction.

$$d_0^{corrected} = d_0^{uncorrected} - beamy'. \tag{B.1}$$

The following algebra derives the formula for beamy$'$ (Equation B.3) in terms of the beam position in the unrotated detector frame (beamx,beamy) and the angle of rotation of the axis (ϕ).

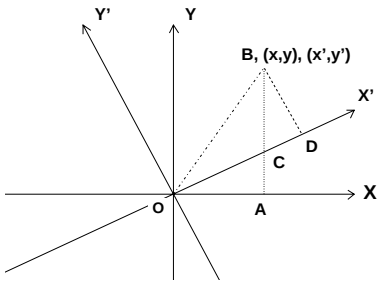

Figure B.2: Figure to show relationship between co-ordinates in a rotated reference frame.

The relationship between the position of a point (x,y) in one frame measured in a frame rotated about the origin by phi, (x$'$,y$'$) is derived here: (see Figure B.2)

x$'$ = OC + CD = $\frac{x}{cos\phi}$ + BC $\times sin\phi$

but BC = AB - AC = y - x $\times tan\phi$

so by substitution for BC, x$'$ becomes:

x$'$ = $\frac{x}{cos\phi}$ + $(y - x \times tan\phi) \times sin\phi$

x$'$ = $\frac{x}{cos\phi}$ + ysinϕ - $\frac{x \times sin^2\phi}{cos\phi}$

x$'$ = $\frac{x \times (1 - sin^2\phi)}{cos\phi}$ + y $\times sin\phi$

x$'$ = $\frac{x \times cos^2\phi}{cos\phi}$ + y $\times sin\phi$

x$'$ = x $\times cos\phi$ + y $\times sin\phi$

and

y$'$= BD = BC $\times cos\phi$

and by substitution for BC, y$'$ becomes:

y$'$ = (y - x $\times tan\phi$)$\times cos\phi$

$$y' = -x \times sin\phi + y \times cos\phi \tag{B.2}$$

Therefore, from Equation B.2, a y co-ordinate of the beam position in the rotated frame (beamx′, beamy′) is related to the beam position in the detector frame (beamx,beamy) and the rotation angle (ϕ) by Equation B.3, where ϕ is defined to be the azimuthal direction of the track at minimum approach.

$$beamy' = -beamx \times sin\phi + beamy \times cos\phi \tag{B.3}$$

The corrected impact parameter for the beam position, d_0^{corr}, is given by Equation B.4, from substitution for beamy′ from Equation B.3 into Equation B.1.

$$d_0^{corr} = d_0^{track} + beamx \times sin\phi - beamy \times cos\phi. \tag{B.4}$$

The explicit beam position in Equation B.4 can be absorbed into a sine function and its parameters, A and B. Equation can therefore be rewritten as Equation B.5.

$$d_0^{corr} = d_0^{track} - A \times sin(\phi + B) \tag{B.5}$$

In the offline code the beam position and slope used for each event is the average of the beam position calculated for the previous run. This position is determined using both SVX tracks and COT tracks. The derivation shown above is for the two dimensional impact parameter correction. The two dimensional beam position per track is calculated by extrapolating the beam position to the same position as the intersection of the track with the beam line (z_0) in the Z direction using the beam slope.

Appendix C: Cosmic ray rejection

C.1 Inefficiency of a back-to-back cut

The efficiency of the back-to-back cut used in the Run I Z' dimuon search [75] was investigated using 2000 $Z' \rightarrow \mu\mu$ Monte Carlo events generated with Z' masses from 100 to 800 GeV/c^2. These events were generated, simulated and reconstructed as described in Section 4.3. The dimuons were required to both have $p_T > 20$ GeV/c and have stubs in the CMU and CMP chambers. A back-to-back cut of $|\eta_{\mu 1} + \eta_{\mu 2}| < 0.2$ radians (11.5°) and $|\pi$ - $|\phi_{\mu 1} - \phi_{\mu 2}|| < 0.0087$ radians (or 0.5^0) was placed on the dimuons and the efficiency as a function of the Z' boson mass was calculated; this is shown in Figure C.1. For Z' bosons with a mass of 100 GeV/c^2 the back-to-back cut was found to be 96 % efficient; however, for a Z' mass of 800 GeV/c^2 the efficiency fell to 83 %. A similar effect was observed for dimuons from graviton decays. The decrease in efficiency for more massive Z' bosons/gravitons occured because they were closer to being at rest in the detector reference frame. If a particle at rest decays to two particles, the two decay particles are produced back-to-back in the same frame. Consequently, a back-to-back cut becomes increasingly inefficient for Z' and graviton signals the higher the Z' boson/graviton mass. For this reason a back-to-back cut was not applied in the analysis, instead, track cuts and timing selection criteria, which were more efficient and did not have a mass dependency, were applied to remove cosmic rays from the data sample.

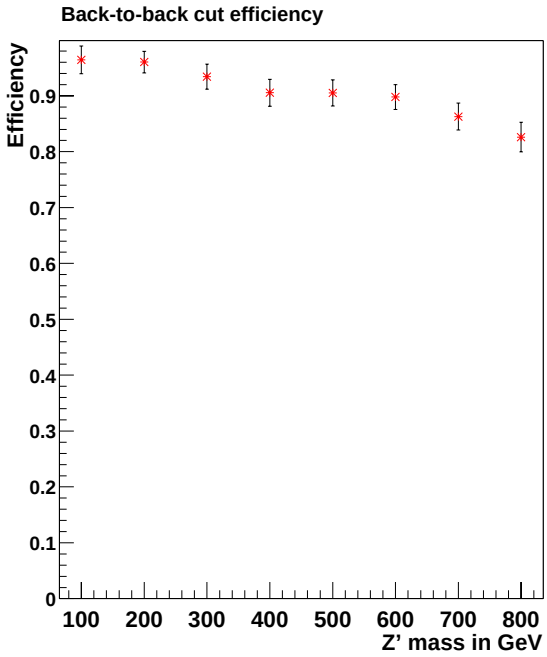

Figure C.1: Efficiency of a back-to-back cut on a Z' signal sample as a function of Z' mass, for Monte Carlo Z and Z' samples.

C.2 Derivation of statistical error on signal^2/background ratio

The error on the quantity is signal^2/background (Δ ($\frac{s^2}{b}$)) depends on the error on both the signal (Δs) and background samples (Δb), and is derived from Equation C.2.

$$\Delta(\frac{s^2}{b}) = \frac{d}{ds}\frac{s^2}{b}\Delta s + \frac{d}{db}\frac{s^2}{b}\Delta b \quad \text{(C.1)}$$

$$= 2\frac{s}{b}\Delta s - \frac{s^2}{b^2}\Delta b \quad \text{(C.2)}$$

The errors are added in quadrature, It is assumed that the signal and background samples are statistically independent and therefore the errors are added in quadrature, as shown in Equation C.3. The resulting error on the variable (s^2/b) is given by Equation C.4, where Δs is the square root of the number of signal events in the signal sample ($\sqrt{N_s}$) and Δb is square root of the number of background events in the signal sample $\sqrt{N_{bkgd}}$.

$$(\Delta(\frac{s^2}{b}))^2 = 4\frac{s^2}{b^2}\Delta s^2 + (\frac{s^2}{b^2})^2\Delta b^2 \quad \text{(C.3)}$$

$$\Delta(\frac{s^2}{b}) = \sqrt{4\frac{s^2}{b^2}\Delta s^2 + (\frac{s^2}{b^2})^2\Delta b^2} \quad \text{(C.4)}$$

C.3 Data used to select Time-of-Flight selection criteria

C.3.1 Time-of-Flight upper muon time

ToF muon upper time							
Cut min.	Cut max.	Signal (s)	Background (b)	s^2/b	Error on s^2/b	Efficiency	Error on efficiency
(ns)	(ns)	(dimuons)					
0.0	5.5	23	528	1.00	0.420	0.639	0.0801
0.0	6.0	27	557	1.31	0.507	0.750	0.0722
0.0	6.5	29	578	1.46	0.544	0.806	0.0660
0.0	7.0	32	592	1.73	0.616	0.889	0.0524
0.0	7.5	33	606	1.80	0.630	0.917	0.0461
0.0	8.0	34	617	1.87	0.647	0.944	0.0382
0.0	8.5	34	624	1.85	0.640	0.944	0.0382
0.0	9.0	35	631	1.94	0.661	0.972	0.0274
0.0	9.5	36	634	2.04	0.686	1.000	0.0000
0.0	10.0	36	636	2.04	0.684	1.000	0.0000
0.0	10.0	36	636	2.04	0.684	1.000	0.0000
0.5	5.5	23	468	1.13	0.474	0.639	0.0801
0.5	6.0	27	497	1.47	0.568	0.750	0.0722
0.5	6.5	29	518	1.62	0.607	0.806	0.0660
0.5	7.0	32	532	1.92	0.686	0.889	0.0524
0.5	7.5	33	546	1.99	0.700	0.917	0.0461
0.5	8.0	34	557	2.08	0.717	0.944	0.0382
0.5	8.5	34	564	2.05	0.708	0.944	0.0382
0.5	9.0	35	571	2.15	0.731	0.972	0.0274
0.5	9.5	36	574	2.26	0.758	1.000	0.0000
0.5	10.0	36	576	2.25	0.756	1.000	0.0000
0.5	10.0	36	576	2.25	0.756	1.000	0.0000
1.0	5.5	23	406	1.30	0.547	0.639	0.0801
1.0	6.0	27	435	1.68	0.650	0.750	0.0722
1.0	6.5	29	456	1.84	0.690	0.806	0.0660
1.0	7.0	32	470	2.18	0.777	0.889	0.0524
1.0	7.5	33	484	2.25	0.790	0.917	0.0461
1.0	8.0	34	495	2.34	0.808	0.944	0.0382
1.0	8.5	34	502	2.30	0.797	0.944	0.0382
1.0	9.0	35	509	2.41	0.821	0.972	0.0274
1.0	9.5	36	512	2.53	0.851	1.000	0.0000
1.0	10.0	36	514	2.52	0.848	1.000	0.0000
1.0	10.0	36	514	2.52	0.848	1.000	0.0000

Table C.1: Ratio of signal^2/background to determine the choice of the ToF upper cut.

ToF muon upper time							
Cut min.	Cut max.	Signal (s)	Background (b)	s^2/b	Error on s^2/b	Efficiency	Error on efficiency
(ns)	(ns)	(dimuons)					
1.5	5.5	22	356	1.36	0.584	0.611	0.0812
1.5	6.0	26	385	1.76	0.694	0.722	0.0747
1.5	6.5	28	406	1.93	0.736	0.778	0.0693
1.5	7.0	31	420	2.29	0.829	0.861	0.0576
1.5	7.5	32	434	2.36	0.842	0.889	0.0524
1.5	8.0	33	445	2.45	0.860	0.917	0.0461
1.5	8.5	33	452	2.41	0.846	0.917	0.0461
1.5	9.0	34	459	2.52	0.872	0.944	0.0382
1.5	9.5	35	462	2.65	0.905	0.972	0.0274
1.5	10.0	35	464	2.64	0.901	0.972	0.0274
1.5	10.0	35	464	2.64	0.901	0.972	0.0274
2.0	5.5	21	302	1.46	0.643	0.583	0.0822
2.0	6.0	25	331	1.89	0.762	0.694	0.0768
2.0	6.5	27	352	2.07	0.805	0.750	0.0722
2.0	7.0	30	366	2.46	0.907	0.833	0.0621
2.0	7.5	31	380	2.53	0.918	0.861	0.0576
2.0	8.0	32	391	2.62	0.935	0.889	0.0524
2.0	8.5	32	398	2.57	0.919	0.889	0.0524
2.0	9.0	33	405	2.69	0.946	0.917	0.0461
2.0	9.5	34	408	2.83	0.982	0.944	0.0382
2.0	10.0	34	410	2.82	0.977	0.944	0.0382
2.0	10.0	34	410	2.82	0.977	0.944	0.0382
2.5	5.5	21	256	1.72	0.759	0.583	0.0822
2.5	6.0	25	285	2.19	0.887	0.694	0.0768
2.5	6.5	27	306	2.38	0.927	0.750	0.0722
2.5	7.0	30	320	2.81	1.04	0.833	0.0621
2.5	7.5	31	334	2.88	1.05	0.861	0.0576
2.5	8.0	32	345	2.97	1.06	0.889	0.0524
2.5	8.5	32	352	2.91	1.04	0.889	0.0524
2.5	9.0	33	359	3.03	1.07	0.917	0.0461
2.5	9.5	34	362	3.19	1.11	0.944	0.0382
2.5	10.0	34	364	3.18	1.10	0.944	0.0382
2.5	10.0	34	364	3.18	1.10	0.944	0.0382
3.0	5.5	17	211	1.37	0.671	0.472	0.0832
3.0	6.0	21	240	1.84	0.811	0.583	0.0822
3.0	6.5	23	261	2.03	0.855	0.639	0.0801
3.0	7.0	26	275	2.46	0.976	0.722	0.0747
3.0	7.5	27	289	2.52	0.982	0.750	0.0722
3.0	8.0	28	300	2.61	0.999	0.778	0.0693
3.0	8.5	28	307	2.55	0.976	0.778	0.0693
3.0	9.0	29	314	2.68	1.01	0.806	0.0660
3.0	9.5	30	317	2.84	1.05	0.833	0.0621
3.0	10.0	30	319	2.82	1.04	0.833	0.0621
3.0	10.0	30	319	2.82	1.04	0.833	0.0621

Table C.2: Ratio of signal^2/background to determine the choice of the ToF upper cut.

ToF muon upper time							
Cut min.	Cut max.	Signal (s)	Background (b)	s^2/b	Error on s^2/b	Efficiency	Error on efficiency
(ns)	(ns)	(dimuons)					
3.5	5.5	13	157	1.08	0.603	0.361	0.0801
3.5	6.0	17	186	1.55	0.762	0.472	0.0832
3.5	6.5	19	207	1.74	0.809	0.528	0.0832
3.5	7.0	22	221	2.19	0.945	0.611	0.0812
3.5	7.5	23	235	2.25	0.95	0.639	0.0801
3.5	8.0	24	246	2.34	0.967	0.667	0.0786
3.5	8.5	24	253	2.28	0.94	0.667	0.0786
3.5	9.0	25	260	2.40	0.973	0.694	0.0768
3.5	9.5	26	263	2.57	1.02	0.722	0.0747
3.5	10.0	26	265	2.55	1.01	0.722	0.0747
3.5	10.0	26	265	2.55	1.01	0.722	0.0747
4.0	5.5	11	110	1.10	0.672	0.306	0.0768
4.0	6.0	15	139	1.62	0.847	0.417	0.0822
4.0	6.5	17	160	1.81	0.888	0.472	0.0832
4.0	7.0	20	174	2.30	1.04	0.556	0.0828
4.0	7.5	21	188	2.35	1.04	0.583	0.0822
4.0	8.0	22	199	2.43	1.05	0.611	0.0812
4.0	8.5	22	206	2.35	1.02	0.611	0.0812
4.0	9.0	23	213	2.48	1.05	0.639	0.0801
4.0	9.5	24	216	2.67	1.10	0.667	0.0786
4.0	10.0	24	218	2.64	1.09	0.667	0.0786
4.0	10.0	24	218	2.64	1.09	0.667	0.0786
4.5	5.5	3	73	0.123	0.143	0.0833	0.0461
4.5	6.0	7	102	0.480	0.366	0.194	0.0660
4.5	6.5	9	123	0.659	0.443	0.250	0.0722
4.5	7.0	12	137	1.05	0.613	0.333	0.0786
4.5	7.5	13	151	1.12	0.627	0.361	0.0801
4.5	8.0	14	162	1.21	0.654	0.389	0.0812
4.5	8.5	14	169	1.16	0.626	0.389	0.0812
4.5	9.0	15	176	1.28	0.667	0.417	0.0822
4.5	9.5	16	179	1.43	0.723	0.444	0.0828
4.5	10.0	16	181	1.41	0.715	0.444	0.0828
4.5	10.0	16	181	1.41	0.715	0.444	0.0828
5.0	5.5	0	34	0.00	0.000	0.000	0.0000
5.0	6.0	4	63	0.254	0.256	0.111	0.0524
5.0	6.5	6	84	0.429	0.353	0.167	0.0621
5.0	7.0	9	98	0.827	0.557	0.250	0.0722
5.0	7.5	10	112	0.893	0.571	0.278	0.0747
5.0	8.0	11	123	0.984	0.600	0.306	0.0768
5.0	8.5	11	130	0.931	0.567	0.306	0.0768
5.0	9.0	12	137	1.05	0.613	0.333	0.0786
5.0	9.5	13	140	1.21	0.677	0.361	0.0801
5.0	10.0	13	142	1.19	0.668	0.361	0.0801
5.0	10.0	13	142	1.19	0.668	0.361	0.0801

Table C.3: Ratio of signal^2/background to determine the choice of the ToF upper cut.

C.3.2 Time-of-Flight lower muon time

ToF muon lower time							
Cut min.	Cut max.	Signal (s)	Background (b)	s^2/b	Error on s^2/b	Efficiency	Error on efficiency
(ns)	(ns)	(dimuons)					
0.0	5.5	25	506	1.24	0.497	0.595	0.0757
0.0	6.0	27	570	1.28	0.495	0.643	0.0739
0.0	6.5	32	618	1.66	0.590	0.762	0.0657
0.0	7.0	38	670	2.16	0.704	0.905	0.0453
0.0	7.5	39	733	2.08	0.669	0.929	0.0397
0.0	8.0	40	790	2.03	0.645	0.952	0.0329
0.0	8.5	41	840	2.00	0.629	0.976	0.0235
0.0	9.0	42	899	1.96	0.609	1.000	0.0000
0.0	9.5	42	942	1.87	0.581	1.000	0.0000
0.0	10.0	42	997	1.77	0.549	1.000	0.0000
0.0	10.0	42	1058	1.67	0.517	1.000	0.0000
0.5	5.5	24	483	1.19	0.490	0.571	0.0764
0.5	6.0	26	547	1.24	0.488	0.619	0.0749
0.5	6.5	31	595	1.62	0.584	0.738	0.0678
0.5	7.0	37	647	2.12	0.701	0.881	0.0500
0.5	7.5	38	710	2.03	0.664	0.905	0.0453
0.5	8.0	39	767	1.98	0.639	0.929	0.0397
0.5	8.5	40	817	1.96	0.623	0.952	0.0329
0.5	9.0	41	876	1.92	0.603	0.976	0.0235
0.5	9.5	41	919	1.83	0.575	0.976	0.0235
0.5	10.0	41	974	1.73	0.542	0.976	0.0235
0.5	10.0	41	1035	1.62	0.510	0.976	0.0235
1.0	5.5	24	440	1.31	0.538	0.571	0.0764
1.0	6.0	26	504	1.34	0.529	0.619	0.0749
1.0	6.5	31	552	1.74	0.630	0.738	0.0678
1.0	7.0	37	604	2.27	0.751	0.881	0.0500
1.0	7.5	38	667	2.16	0.707	0.905	0.0453
1.0	8.0	39	724	2.10	0.677	0.929	0.0397
1.0	8.5	40	774	2.07	0.658	0.952	0.0329
1.0	9.0	41	833	2.02	0.634	0.976	0.0235
1.0	9.5	41	876	1.92	0.603	0.976	0.0235
1.0	10.0	41	931	1.81	0.567	0.976	0.0235
1.0	10.0	41	992	1.69	0.532	0.976	0.0235

Table C.4: Ratio of signal^2/background to determine the choice of the ToF lower cut.

ToF muon lower time							
Cut min.	Cut max.	Signal (s)	Background (b)	s^2/b	Error on s^2/b	Efficiency	Error on efficiency
(ns)	(ns)	(dimuons)					
1.5	5.5	24	400	1.44	0.592	0.571	0.0764
1.5	6.0	26	464	1.46	0.575	0.619	0.0749
1.5	6.5	31	512	1.88	0.679	0.738	0.0678
1.5	7.0	37	564	2.43	0.805	0.881	0.0500
1.5	7.5	38	627	2.30	0.753	0.905	0.0453
1.5	8.0	39	684	2.22	0.717	0.929	0.0397
1.5	8.5	40	734	2.18	0.694	0.952	0.0329
1.5	9.0	41	793	2.12	0.666	0.976	0.0235
1.5	9.5	41	836	2.01	0.632	0.976	0.0235
1.5	10.0	41	891	1.89	0.593	0.976	0.0235
1.5	10.0	41	952	1.77	0.554	0.976	0.0235
2.0	5.5	23	368	1.44	0.604	0.548	0.0768
2.0	6.0	25	432	1.45	0.583	0.595	0.0757
2.0	6.5	30	480	1.88	0.690	0.714	0.0697
2.0	7.0	36	532	2.44	0.819	0.857	0.0540
2.0	7.5	37	595	2.3	0.762	0.881	0.0500
2.0	8.0	38	652	2.21	0.724	0.905	0.0453
2.0	8.5	39	702	2.17	0.699	0.929	0.0397
2.0	9.0	40	761	2.10	0.669	0.952	0.0329
2.0	9.5	40	804	1.99	0.633	0.952	0.0329
2.0	10.0	40	859	1.86	0.592	0.952	0.0329
2.0	10.0	40	920	1.74	0.553	0.952	0.0329
2.5	5.5	22	321	1.51	0.648	0.524	0.0771
2.5	6.0	24	385	1.50	0.616	0.571	0.0764
2.5	6.5	29	433	1.94	0.727	0.690	0.0713
2.5	7.0	35	485	2.53	0.862	0.833	0.0575
2.5	7.5	36	548	2.36	0.795	0.857	0.0540
2.5	8.0	37	605	2.26	0.750	0.881	0.0500
2.5	8.5	38	655	2.20	0.720	0.905	0.0453
2.5	9.0	39	714	2.13	0.687	0.929	0.0397
2.5	9.5	39	757	2.01	0.648	0.929	0.0397
2.5	10.0	39	812	1.87	0.603	0.929	0.0397
2.5	10.0	39	873	1.74	0.561	0.929	0.0397
3.0	5.5	20	276	1.45	0.654	0.476	0.0771
3.0	6.0	22	340	1.42	0.612	0.524	0.0771
3.0	6.5	27	388	1.88	0.729	0.643	0.0739
3.0	7.0	33	440	2.48	0.870	0.786	0.0633
3.0	7.5	34	503	2.30	0.795	0.810	0.0606
3.0	8.0	35	560	2.19	0.745	0.833	0.0575
3.0	8.5	36	610	2.12	0.713	0.857	0.0540
3.0	9.0	37	669	2.05	0.677	0.881	0.0500
3.0	9.5	37	712	1.92	0.636	0.881	0.0500
3.0	10.0	37	767	1.78	0.590	0.881	0.0500
3.0	10.0	37	828	1.65	0.547	0.881	0.0500

Table C.5: Ratio of signal^2/background to determine the choice of the ToF lower cut.

ToF muon lower time							
Cut min.	Cut max.	Signal (s)	Background (b)	s^2/b	Error on s^2/b	Efficiency	Error on efficiency
(ns)	(ns)	(dimuons)					
3.5	5.5	17	224	1.29	0.632	0.405	0.0757
3.5	6.0	19	288	1.25	0.580	0.452	0.0768
3.5	6.5	24	336	1.71	0.706	0.571	0.0764
3.5	7.0	30	388	2.32	0.855	0.714	0.0697
3.5	7.5	31	451	2.13	0.772	0.738	0.0678
3.5	8.0	32	508	2.02	0.718	0.762	0.0657
3.5	8.5	33	558	1.95	0.684	0.786	0.0633
3.5	9.0	34	617	1.87	0.647	0.810	0.0606
3.5	9.5	34	660	1.75	0.605	0.810	0.0606
3.5	10.0	34	715	1.62	0.558	0.810	0.0606
3.5	10.0	34	776	1.49	0.514	0.810	0.0606
4.0	5.5	13	174	0.971	0.544	0.310	0.0713
4.0	6.0	15	238	0.945	0.492	0.357	0.0739
4.0	6.5	20	286	1.40	0.631	0.476	0.0771
4.0	7.0	26	338	2.00	0.792	0.619	0.0749
4.0	7.5	27	401	1.82	0.706	0.643	0.0739
4.0	8.0	28	458	1.71	0.652	0.667	0.0727
4.0	8.5	29	508	1.66	0.619	0.690	0.0713
4.0	9.0	30	567	1.59	0.583	0.714	0.0697
4.0	9.5	30	610	1.48	0.542	0.714	0.0697
4.0	10.0	30	665	1.35	0.497	0.714	0.0697
4.0	10.0	30	726	1.24	0.455	0.714	0.0697
4.5	5.5	8	122	0.525	0.374	0.190	0.0606
4.5	6.0	10	186	0.538	0.342	0.238	0.0657
4.5	6.5	15	234	0.962	0.500	0.357	0.0739
4.5	7.0	21	286	1.54	0.679	0.500	0.0772
4.5	7.5	22	349	1.39	0.596	0.524	0.0771
4.5	8.0	23	406	1.30	0.547	0.548	0.0768
4.5	8.5	24	456	1.26	0.519	0.571	0.0764
4.5	9.0	25	515	1.21	0.488	0.595	0.0757
4.5	9.5	25	558	1.12	0.451	0.595	0.0757
4.5	10.0	25	613	1.02	0.410	0.595	0.0757
4.5	10.0	25	674	0.927	0.373	0.595	0.0757
5.0	5.5	4	61	0.262	0.264	0.0952	0.0453
5.0	6.0	6	125	0.288	0.237	0.143	0.0540
5.0	6.5	11	173	0.699	0.425	0.262	0.0678
5.0	7.0	17	225	1.28	0.629	0.405	0.0757
5.0	7.5	18	288	1.12	0.534	0.429	0.0764
5.0	8.0	19	345	1.05	0.483	0.452	0.0768
5.0	8.5	20	395	1.01	0.456	0.476	0.0771
5.0	9.0	21	454	0.971	0.426	0.500	0.0772
5.0	9.5	21	497	0.887	0.389	0.500	0.0772
5.0	10.0	21	552	0.799	0.350	0.500	0.0772
5.0	10.0	21	613	0.719	0.315	0.500	0.0772

Table C.6: Ratio of signal^2/background to determine the choice of the ToF lower cut.

C.4 Data used to select hadron TDC time selection criteria

C.4.1 Hadron TDC upper muon time

Hadron TDC muon upper time							
Cut min.	Cut max.	Signal (s)	Background (b)	s^2/b	Error on s^2/b	Efficiency	Error on efficiency
(ns)	(ns)	(dimuons)					
-11	1	15	9306	0.0242	0.0125	0.326	0.0691
-11	2	21	9813	0.0449	0.0196	0.457	0.0734
-11	3	23	10290	0.0514	0.0214	0.500	0.0737
-11	4	29	10703	0.0786	0.0292	0.630	0.0712
-11	5	35	11192	0.109	0.0370	0.761	0.0629
-11	6	38	11552	0.125	0.0406	0.826	0.0559
-11	7	44	11806	0.164	0.0495	0.957	0.0301
-11	8	45	12020	0.168	0.0503	0.978	0.0215
-11	9	46	12153	0.174	0.0514	1.000	0.0000
-11	10	46	12216	0.173	0.0511	1.000	0.0000
-11	11	46	12280	0.172	0.0508	1.000	0.0000
-11	12	46	12332	0.172	0.0506	1.000	0.0000
-10	1	15	8124	0.0277	0.0143	0.326	0.0691
-10	2	21	8631	0.0511	0.0223	0.457	0.0734
-10	3	23	9108	0.0581	0.0242	0.500	0.0737
-10	4	29	9521	0.0883	0.0328	0.630	0.0712
-10	5	35	10010	0.122	0.0414	0.761	0.0629
-10	6	38	10370	0.139	0.0452	0.826	0.0559
-10	7	44	10624	0.182	0.0550	0.957	0.0301
-10	8	45	10838	0.187	0.0557	0.978	0.0215
-10	9	46	10971	0.193	0.0569	1.000	0.0000
-10	10	46	11034	0.192	0.0566	1.000	0.0000
-10	11	46	11098	0.191	0.0563	1.000	0.0000
-10	12	46	11150	0.190	0.0560	1.000	0.0000
-9	1	14	7050	0.0278	0.0149	0.304	0.0678
-9	2	20	7557	0.0529	0.0237	0.435	0.0731
-9	3	22	8034	0.0602	0.0257	0.478	0.0737
-9	4	28	8447	0.0928	0.0351	0.609	0.0720
-9	5	34	8936	0.129	0.0444	0.739	0.0647
-9	6	37	9296	0.147	0.0484	0.804	0.0585
-9	7	43	9550	0.194	0.0591	0.935	0.0364
-9	8	44	9764	0.198	0.0598	0.957	0.0301
-9	9	45	9897	0.205	0.0610	0.978	0.0215
-9	10	45	9960	0.203	0.0607	0.978	0.0215
-9	11	45	10024	0.202	0.0603	0.978	0.0215
-9	12	45	10076	0.201	0.0600	0.978	0.0215

Table C.7: Ratio of signal^2/background to determine the choice of the hadron TDC upper cut.

Hadron TDC muon upper time							
Cut min.	Cut max.	Signal (s)	Background (b)	s^2/b	Error on s^2/b	Efficiency	Error on efficiency
(ns)	(ns)	(dimuons)					
-8	1	14	6066	0.0323	0.0173	0.304	0.0678
-8	2	20	6573	0.0609	0.0272	0.435	0.0731
-8	3	22	7050	0.0687	0.0293	0.478	0.0737
-8	4	28	7463	0.105	0.0397	0.609	0.0720
-8	5	34	7952	0.145	0.0499	0.739	0.0647
-8	6	37	8312	0.165	0.0542	0.804	0.0585
-8	7	43	8566	0.216	0.0659	0.935	0.0364
-8	8	44	8780	0.221	0.0665	0.957	0.0301
-8	9	45	8913	0.227	0.0678	0.978	0.0215
-8	10	45	8976	0.226	0.0673	0.978	0.0215
-8	11	45	9040	0.224	0.0668	0.978	0.0215
-8	12	45	9092	0.223	0.0664	0.978	0.0215
-7	1	13	5029	0.0336	0.0186	0.283	0.0664
-7	2	19	5536	0.0652	0.0299	0.413	0.0726
-7	3	21	6013	0.0733	0.0320	0.457	0.0734
-7	4	27	6426	0.113	0.0437	0.587	0.0726
-7	5	33	6915	0.157	0.0549	0.717	0.0664
-7	6	36	7275	0.178	0.0594	0.783	0.0608
-7	7	42	7529	0.234	0.0724	0.913	0.0415
-7	8	43	7743	0.239	0.0729	0.935	0.0364
-7	9	44	7876	0.246	0.0742	0.957	0.0301
-7	10	44	7939	0.244	0.0736	0.957	0.0301
-7	11	44	8003	0.242	0.0730	0.957	0.0301
-7	12	44	8055	0.240	0.0725	0.957	0.0301
-6	1	12	4198	0.0343	0.0198	0.261	0.0647
-6	2	18	4705	0.0689	0.0325	0.391	0.0720
-6	3	20	5182	0.0772	0.0345	0.435	0.0731
-6	4	26	5595	0.121	0.0474	0.565	0.0731
-6	5	32	6084	0.168	0.0595	0.696	0.0678
-6	6	35	6444	0.190	0.0643	0.761	0.0629
-6	7	41	6698	0.251	0.0784	0.891	0.0459
-6	8	42	6912	0.255	0.0788	0.913	0.0415
-6	9	43	7045	0.262	0.0801	0.935	0.0364
-6	10	43	7108	0.260	0.0794	0.935	0.0364
-6	11	43	7172	0.258	0.0787	0.935	0.0364
-6	12	43	7224	0.256	0.0781	0.935	0.0364

Table C.8: Ratio of signal^2/background to determine the choice of the hadron TDC upper cut.

Hadron TDC muon upper time							
Cut min.	Cut max.	Signal (s)	Background (b)	s^2/b	Error on s^2/b	Efficiency	Error on efficiency
(ns)	(ns)	(dimuons)					
-5	1	12	3457	0.0417	0.0241	0.261	0.0647
-5	2	18	3964	0.0817	0.0386	0.391	0.0720
-5	3	20	4441	0.0901	0.0403	0.435	0.0731
-5	4	26	4854	0.139	0.0547	0.565	0.0731
-5	5	32	5343	0.192	0.0678	0.696	0.0678
-5	6	35	5703	0.215	0.0727	0.761	0.0629
-5	7	41	5957	0.282	0.0882	0.891	0.0459
-5	8	42	6171	0.286	0.0883	0.913	0.0415
-5	9	43	6304	0.293	0.0895	0.935	0.0364
-5	10	43	6367	0.290	0.0886	0.935	0.0364
-5	11	43	6431	0.288	0.0878	0.935	0.0364
-5	12	43	6483	0.285	0.0871	0.935	0.0364
-4	1	11	2723	0.0444	0.0268	0.239	0.0629
-4	2	17	3230	0.0895	0.0434	0.370	0.0712
-4	3	19	3707	0.0974	0.0447	0.413	0.0726
-4	4	25	4120	0.152	0.0607	0.543	0.0734
-4	5	31	4609	0.209	0.0750	0.674	0.0691
-4	6	34	4969	0.233	0.0799	0.739	0.0647
-4	7	40	5223	0.306	0.0970	0.870	0.0497
-4	8	41	5437	0.309	0.0967	0.891	0.0459
-4	9	42	5570	0.317	0.0978	0.913	0.0415
-4	10	42	5633	0.313	0.0967	0.913	0.0415
-4	11	42	5697	0.310	0.0956	0.913	0.0415
-4	12	42	5749	0.307	0.0948	0.913	0.0415
-3	1	9	2059	0.0393	0.0262	0.196	0.0585
-3	2	15	2566	0.0877	0.0453	0.326	0.0691
-3	3	17	3043	0.095	0.0461	0.370	0.0712
-3	4	23	3456	0.153	0.0639	0.500	0.0737
-3	5	29	3945	0.213	0.0792	0.630	0.0712
-3	6	32	4305	0.238	0.0842	0.696	0.0678
-3	7	38	4559	0.317	0.103	0.826	0.0559
-3	8	39	4773	0.319	0.102	0.848	0.0530
-3	9	40	4906	0.326	0.103	0.870	0.0497
-3	10	40	4969	0.322	0.102	0.870	0.0497
-3	11	40	5033	0.318	0.101	0.870	0.0497
-3	12	40	5085	0.315	0.0996	0.870	0.0497

Table C.9: Ratio of signal^2/background to determine the choice of the hadron TDC upper cut.

Hadron TDC muon upper time							
Cut min.	Cut max.	Signal (s)	Background (b)	s^2/b	Error on s^2/b	Efficiency	Error on efficiency
(ns)	(ns)	(dimuons)					
-2	1	6	1440	0.025	0.0204	0.130	0.0497
-2	2	12	1947	0.074	0.0427	0.261	0.0647
-2	3	14	2424	0.0809	0.0433	0.304	0.0678
-2	4	20	2837	0.141	0.0631	0.435	0.0731
-2	5	26	3326	0.203	0.0798	0.565	0.0731
-2	6	29	3686	0.228	0.0848	0.630	0.0712
-2	7	35	3940	0.311	0.105	0.761	0.0629
-2	8	36	4154	0.312	0.104	0.783	0.0608
-2	9	37	4287	0.319	0.105	0.804	0.0585
-2	10	37	4350	0.315	0.104	0.804	0.0585
-2	11	37	4414	0.310	0.102	0.804	0.0585
-2	12	37	4466	0.307	0.101	0.804	0.0585
-1	1	4	886	0.0181	0.0181	0.087	0.0415
-1	2	10	1393	0.0718	0.0454	0.217	0.0608
-1	3	12	1870	0.077	0.0445	0.261	0.0647
-1	4	18	2283	0.142	0.0670	0.391	0.072
-1	5	24	2772	0.208	0.0849	0.522	0.0737
-1	6	27	3132	0.233	0.0897	0.587	0.0726
-1	7	33	3386	0.322	0.112	0.717	0.0664
-1	8	34	3600	0.321	0.110	0.739	0.0647
-1	9	35	3733	0.328	0.111	0.761	0.0629
-1	10	35	3796	0.323	0.109	0.761	0.0629
-1	11	35	3860	0.317	0.107	0.761	0.0629
-1	12	35	3912	0.313	0.106	0.761	0.0629
0	1	2	455	0.00879	0.0124	0.0435	0.0301
0	2	8	962	0.0665	0.0471	0.174	0.0559
0	3	10	1439	0.0695	0.044	0.217	0.0608
0	4	16	1852	0.138	0.0692	0.348	0.0702
0	5	22	2341	0.207	0.0883	0.478	0.0737
0	6	25	2701	0.231	0.0927	0.543	0.0734
0	7	31	2955	0.325	0.117	0.674	0.0691
0	8	32	3169	0.323	0.114	0.696	0.0678
0	9	33	3302	0.330	0.115	0.717	0.0664
0	10	33	3365	0.324	0.113	0.717	0.0664
0	11	33	3429	0.318	0.111	0.717	0.0664
0	12	33	3481	0.313	0.109	0.717	0.0664

Table C.10: Ratio of signal^2/background to determine the choice of the hadron TDC upper cut.

C.4.2 Hadron TDC lower muon time

Hadron TDC muon lower time							
Cut min.	Cut max.	Signal (s)	Background (b)	s^2/b	Error on s^2/b	Efficiency	Error on efficiency
(ns)	(ns)	(dimuons)					
-11	1	18	15921	0.0204	0.00959	0.383	0.0709
-11	2	25	17814	0.0351	0.0140	0.532	0.0728
-11	3	31	19722	0.0487	0.0175	0.660	0.0691
-11	4	35	21294	0.0575	0.0195	0.745	0.0636
-11	5	39	23001	0.0661	0.0212	0.830	0.0548
-11	6	41	24704	0.0680	0.0213	0.872	0.0487
-11	7	43	26125	0.0708	0.0216	0.915	0.0407
-11	8	46	27395	0.0772	0.0228	0.979	0.0210
-11	9	46	28698	0.0737	0.0217	0.979	0.0210
-11	10	46	29850	0.0709	0.0209	0.979	0.0210
-11	11	47	30770	0.0718	0.0209	1.000	0.0000
-11	12	47	31620	0.0699	0.0204	1.000	0.0000
-10	1	18	15141	0.0214	0.0101	0.383	0.0709
-10	2	25	17034	0.0367	0.0147	0.532	0.0728
-10	3	31	18942	0.0507	0.0182	0.660	0.0691
-10	4	35	20514	0.0597	0.0202	0.745	0.0636
-10	5	39	22221	0.0684	0.0219	0.830	0.0548
-10	6	41	23924	0.0703	0.0220	0.872	0.0487
-10	7	43	25345	0.0730	0.0223	0.915	0.0407
-10	8	46	26615	0.0795	0.0234	0.979	0.0210
-10	9	46	27918	0.0758	0.0224	0.979	0.0210
-10	10	46	29070	0.0728	0.0215	0.979	0.0210
-10	11	47	29990	0.0737	0.0215	1.000	0.0000
-10	12	47	30840	0.0716	0.0209	1.000	0.0000
-9	1	18	14250	0.0227	0.0107	0.383	0.0709
-9	2	25	16143	0.0387	0.0155	0.532	0.0728
-9	3	31	18051	0.0532	0.0191	0.660	0.0691
-9	4	35	19623	0.0624	0.0211	0.745	0.0636
-9	5	39	21330	0.0713	0.0228	0.830	0.0548
-9	6	41	23033	0.073	0.0228	0.872	0.0487
-9	7	43	24454	0.0756	0.0231	0.915	0.0407
-9	8	46	25724	0.0823	0.0243	0.979	0.0210
-9	9	46	27027	0.0783	0.0231	0.979	0.0210
-9	10	46	28179	0.0751	0.0221	0.979	0.0210
-9	11	47	29099	0.0759	0.0222	1.000	0.0000
-9	12	47	29949	0.0738	0.0215	1.000	0.0000

Table C.11: Ratio of signal^2/background to determine the choice of the hadron TDC lower cut.

Hadron TDC muon lower time							
Cut min.	Cut max.	Signal (s)	Background (b)	s^2/b	Error on s^2/b	Efficiency	Error on efficiency
(ns)	(ns)	(dimuons)					
-8	1	18	13290	0.0244	0.0115	0.383	0.0709
-8	2	25	15183	0.0412	0.0165	0.532	0.0728
-8	3	31	17091	0.0562	0.0202	0.660	0.0691
-8	4	35	18663	0.0656	0.0222	0.745	0.0636
-8	5	39	20370	0.0747	0.0239	0.830	0.0548
-8	6	41	22073	0.0762	0.0238	0.872	0.0487
-8	7	43	23494	0.0787	0.0240	0.915	0.0407
-8	8	46	24764	0.0854	0.0252	0.979	0.0210
-8	9	46	26067	0.0812	0.0239	0.979	0.0210
-8	10	46	27219	0.0777	0.0229	0.979	0.021
-8	11	47	28139	0.0785	0.0229	1.000	0.0000
-8	12	47	28989	0.0762	0.0222	1.000	0.0000
-7	1	18	12111	0.0268	0.0126	0.383	0.0709
-7	2	25	14004	0.0446	0.0179	0.532	0.0728
-7	3	31	15912	0.0604	0.0217	0.660	0.0691
-7	4	35	17484	0.0701	0.0237	0.745	0.0636
-7	5	39	19191	0.0793	0.0254	0.830	0.0548
-7	6	41	20894	0.0805	0.0251	0.872	0.0487
-7	7	43	22315	0.0829	0.0253	0.915	0.0407
-7	8	46	23585	0.0897	0.0265	0.979	0.0210
-7	9	46	24888	0.0850	0.0251	0.979	0.0210
-7	10	46	26040	0.0813	0.0240	0.979	0.0210
-7	11	47	26960	0.0819	0.0239	1.000	0.0000
-7	12	47	27810	0.0794	0.0232	1.000	0.0000
-6	1	17	10887	0.0265	0.0129	0.362	0.0701
-6	2	24	12780	0.0451	0.0184	0.511	0.0729
-6	3	30	14688	0.0613	0.0224	0.638	0.0701
-6	4	34	16260	0.0711	0.0244	0.723	0.0652
-6	5	38	17967	0.0804	0.0261	0.809	0.0574
-6	6	40	19670	0.0813	0.0257	0.851	0.0519
-6	7	42	21091	0.0836	0.0258	0.894	0.0450
-6	8	45	22361	0.0906	0.0270	0.957	0.0294
-6	9	45	23664	0.0856	0.0255	0.957	0.0294
-6	10	45	24816	0.0816	0.0243	0.957	0.0294
-6	11	46	25736	0.0822	0.0243	0.979	0.0210
-6	12	46	26586	0.0796	0.0235	0.979	0.0210

Table C.12: Ratio of signal^2/background to determine the choice of the hadron TDC lower cut.

Hadron TDC muon lower time							
Cut min.	Cut max.	Signal (s)	Background (b)	s^2/b	Error on s^2/b	Efficiency	Error on efficiency
(ns)	(ns)	(dimuons)					
-5	1	17	9668	0.0299	0.0145	0.362	0.0701
-5	2	24	11561	0.0498	0.0203	0.511	0.0729
-5	3	30	13469	0.0668	0.0244	0.638	0.0701
-5	4	34	15041	0.0769	0.0264	0.723	0.0652
-5	5	38	16748	0.0862	0.0280	0.809	0.0574
-5	6	40	18451	0.0867	0.0274	0.851	0.0519
-5	7	42	19872	0.0888	0.0274	0.894	0.0450
-5	8	45	21142	0.0958	0.0286	0.957	0.0294
-5	9	45	22445	0.0902	0.0269	0.957	0.0294
-5	10	45	23597	0.0858	0.0256	0.957	0.0294
-5	11	46	24517	0.0863	0.0255	0.979	0.0210
-5	12	46	25367	0.0834	0.0246	0.979	0.0210
-4	1	17	8367	0.0345	0.0168	0.362	0.0701
-4	2	24	10260	0.0561	0.0229	0.511	0.0729
-4	3	30	12168	0.0740	0.0270	0.638	0.0701
-4	4	34	13740	0.0841	0.0289	0.723	0.0652
-4	5	38	15447	0.0935	0.0303	0.809	0.0574
-4	6	40	17150	0.0933	0.0295	0.851	0.0519
-4	7	42	18571	0.0950	0.0293	0.894	0.0450
-4	8	45	19841	0.1020	0.0304	0.957	0.0294
-4	9	45	21144	0.0958	0.0286	0.957	0.0294
-4	10	45	22296	0.0908	0.0271	0.957	0.0294
-4	11	46	23216	0.0911	0.0269	0.979	0.0210
-4	12	46	24066	0.0879	0.0259	0.979	0.0210
-3	1	13	6764	0.0250	0.0139	0.277	0.0652
-3	2	20	8657	0.0462	0.0207	0.426	0.0721
-3	3	26	10565	0.0640	0.0251	0.553	0.0725
-3	4	30	12137	0.0742	0.0271	0.638	0.0701
-3	5	34	13844	0.0835	0.0286	0.723	0.0652
-3	6	36	15547	0.0834	0.0278	0.766	0.0618
-3	7	38	16968	0.0851	0.0276	0.809	0.0574
-3	8	41	18238	0.0922	0.0288	0.872	0.0487
-3	9	41	19541	0.0860	0.0269	0.872	0.0487
-3	10	41	20693	0.0812	0.0254	0.872	0.0487
-3	11	42	21613	0.0816	0.0252	0.894	0.0450
-3	12	42	22463	0.0785	0.0242	0.894	0.0450

Table C.13: Ratio of signal^2/background to determine the choice of the hadron TDC lower cut.

Hadron TDC muon lower time							
Cut min.	Cut max.	Signal (s)	Background (b)	s^2/b	Error on s^2/b	Efficiency	Error on efficiency
(ns)	(ns)	(dimuons)					
-2	1	10	5250	0.0190	0.0120	0.213	0.0597
-2	2	17	7143	0.0405	0.0196	0.362	0.0701
-2	3	23	9051	0.0584	0.0244	0.489	0.0729
-2	4	27	10623	0.0686	0.0264	0.574	0.0721
-2	5	31	12330	0.0779	0.0280	0.660	0.0691
-2	6	33	14033	0.0776	0.0270	0.702	0.0667
-2	7	35	15454	0.0793	0.0268	0.745	0.0636
-2	8	38	16724	0.0863	0.0280	0.809	0.0574
-2	9	38	18027	0.0801	0.0260	0.809	0.0574
-2	10	38	19179	0.0753	0.0244	0.809	0.0574
-2	11	39	20099	0.0757	0.0242	0.830	0.0548
-2	12	39	20949	0.0726	0.0233	0.830	0.0548
-1	1	9	3631	0.0223	0.0149	0.191	0.0574
-1	2	16	5524	0.0463	0.0232	0.340	0.0691
-1	3	22	7432	0.0651	0.0278	0.468	0.0728
-1	4	26	9004	0.0751	0.0295	0.553	0.0725
-1	5	30	10711	0.0840	0.0307	0.638	0.0701
-1	6	32	12414	0.0825	0.0292	0.681	0.0680
-1	7	34	13835	0.0836	0.0287	0.723	0.0652
-1	8	37	15105	0.0906	0.0298	0.787	0.0597
-1	9	37	16408	0.0834	0.0274	0.787	0.0597
-1	10	37	17560	0.0780	0.0256	0.787	0.0597
-1	11	38	18480	0.0781	0.0254	0.809	0.0574
-1	12	38	19330	0.0747	0.0242	0.809	0.0574
0	1	1	1859	0.000538	0.00108	0.0213	0.0210
0	2	8	3752	0.0171	0.0121	0.170	0.0548
0	3	14	5660	0.0346	0.0185	0.298	0.0667
0	4	18	7232	0.0448	0.0211	0.383	0.0709
0	5	22	8939	0.0541	0.0231	0.468	0.0728
0	6	24	10642	0.0541	0.0221	0.511	0.0729
0	7	26	12063	0.0560	0.0220	0.553	0.0725
0	8	29	13333	0.0631	0.0234	0.617	0.0709
0	9	29	14636	0.0575	0.0213	0.617	0.0709
0	10	29	15788	0.0533	0.0198	0.617	0.0709
0	11	30	16708	0.0539	0.0197	0.638	0.0701
0	12	30	17558	0.0513	0.0187	0.638	0.0701

Table C.14: Ratio of signal^2/background to determine the choice of the hadron TDC lower cut.

C.4.3 Hadron TDC time difference

Hadron TDC time difference							
Cut min.	Cut max.	Signal (s)	Background (b)	s^2/b	Error on s^2/b	Efficiency	Error on efficiency
(ns)	(ns)	(dimuons)					
-11	31	45	6871	0.295	0.0879	1.000	0.0000
-10	31	44	6257	0.310	0.0935	0.978	0.0215
-9	31	44	5653	0.342	0.103	0.978	0.0215
-8	31	43	5082	0.364	0.111	0.956	0.0301
-7	31	43	4630	0.399	0.122	0.956	0.0301
-6	31	41	4259	0.395	0.123	0.911	0.0415
-5	31	38	3797	0.380	0.124	0.844	0.0529
-4	31	38	3475	0.416	0.135	0.844	0.0529
-3	31	34	3192	0.362	0.124	0.756	0.0627
-2	31	31	2926	0.328	0.118	0.689	0.0675
-1	31	30	2665	0.338	0.123	0.667	0.0688
0	31	26	2350	0.288	0.113	0.578	0.0720

Table C.15: Ratio of signal^2/background to determine the choice of the hadron TDC difference (upper-lower) cut.

Appendix D: Efficiency derivation for CMUP-CMUP dimuons

The efficiency of muon cuts can be determined using a Z dimuon data sample, in which one muon (leg) has selection criteria applied, this muon is called the tight muon. The second leg has only very loose initial requirements and is called the loose muon. The cuts are applied individually and simultaneously to the second leg in order to determine their efficiency. To create a pure Z sample an invariant mass cut is placed on the dimuon sample and also cosmic ray cuts are imposed.

The cut efficiency is not simply given by the number of dimuon muon events which have a tight muon and the other muon passes the particular cut (N_{Ti}) divided by the total number of dimuon events in the data sample. This is because to create the data sample there is already the requirement that one muon passes the tight cut. Instead, what can be determined is the the probability of there being a tight muon and another muon passing the individual cut, given that one muon already passed the tight cuts. From this the probability for an individual muon to pass the individual cut (ε_i) can be calculated, using Equation D.1. An explanation of the origin of this equation follows.

$$\varepsilon_i = \frac{N_{Ti} + N_{TT}}{N_{TT} + N_{T*}} \tag{D.1}$$

Let the probability for one muon to pass cut i be (ε_i) and the probability for one muon to pass the tight cuts be (ε_T).

The following definitions are made:

- N is the total number of dimuon events in the sample, with no requirement on either of the muons.

- N_{T*} is the total number of dimuon events in the sample in which one muon passes the tight cuts, and there is no requirement on the other. (N_{T*} is a subset of N.) The N_{T*} sample contains dimuons events in which both muons satisfy the tight cuts, or one muon is defined as tight and the other not tight:

  i) N_{T*} = N$\times\varepsilon_T\times\varepsilon_T$ + N$\times\varepsilon_T\times$(1-$\varepsilon_T$) + N$\times$(1-$\varepsilon_T$)$\times\varepsilon_T$ = N$\times\varepsilon_T\times$(2-$\times\varepsilon_T$).

- N_{Ti} is the number of dimuon events in which one muon satisfies the tight cut requirements and the other muon satisfies the individual cut. (N_{Ti} is a subset of N and N_{TT} is a subset of this group.) Therefore the N_{Ti} sample contains events in which there are either two tight muons, or one tight and the other muon passes the cut i but not the tight cut:

  ii) N_{Ti} = N$\times\varepsilon_T\times\varepsilon_T$ + N$\times\varepsilon_T\times$($\varepsilon_i$-$\varepsilon_T$) + N$\times$($\varepsilon_i$-$\varepsilon_T$)$\times\varepsilon_T$ = N$\times\varepsilon_T\times$(2$\varepsilon_i$-$\varepsilon_T$).

- N_{TT} is the number of dimuon events where both muons satisfy the tight cut requirements. (N_{TT} is a subset of N, N_{T*} and N_{Ti}.)

  iii) N_{TT} = N$\times\varepsilon_T\times\varepsilon_T$

From Equations (i), (ii) and (iii) the efficiencies for the individual cuts (ε_i) and all of the cuts ε_T can be obtained.

Dividing (iii) by (i) gives;

$$\frac{N_{TT}}{N_{T*}} = \frac{N \times \varepsilon_T \times \varepsilon_T}{N \times \varepsilon_T \times (2 - \varepsilon_T)} = \frac{\varepsilon_T}{(2 - \varepsilon_T)}. \tag{D.2}$$

After cross-multiplication Equation D.2 becomes 2$\times N_{TT}$ - $\varepsilon_T\times N_{TT}$ = $\varepsilon_T\times N_{T*}$, which can be rearranged to obtain ε_T:

$$\varepsilon_T = \frac{2N_{TT}}{N_{TT} + N_{T*}}. \tag{D.3}$$

The efficiency of an individual cut can be obtained by adding (ii) and (iii) and dividing this by the sum of (i) and (iii):

ii) + iii) : $N_{Ti} + N_{TT} = \mathrm{N}\times\varepsilon_T\times(2\varepsilon_i\text{-}\varepsilon_T) + \mathrm{N}\times\varepsilon_T\times\varepsilon_T = 2\mathrm{N}\times\varepsilon_T\varepsilon_i$

i) + iii) : $N_{TT} + N_{T*} = 2\times\mathrm{N}\times\varepsilon_T$.

On division these gives;

$$\varepsilon_i = \frac{N_{Ti} + N_{TT}}{N_{TT} + N_{T*}}. \tag{D.4}$$

Appendix E: Dimuon event trigger efficiency

In a dimuon event, either of the muons in the event could be the trigger muon. Given that the efficiency for a single muon to pass the trigger is ϵ^{μ}_{trig}, then the trigger efficiency per dimuon event is $\epsilon^{\mu}_{trig}\times$(2-$\epsilon^{\mu}_{trig}$), which can be derived as follows.

For trigger to fire, at least one muon must pass the trigger requirements, *i.e.* either only 1 muon passes and the other fails (which has probability $2 \times \epsilon^{\mu}_{trig}(1 - \epsilon^{\mu}_{trig})$) or both pass (with probability $\epsilon^{\mu}_{trig} * \epsilon^{\mu}_{trig}$). The probability for the trigger to fire is the sum of these:

$$2 \times \epsilon^{\mu}_{trig}(1 - \epsilon^{\mu}_{trig}) + \epsilon^{\mu}_{trig} \times \epsilon^{\mu}_{trig} = \epsilon^{\mu}_{trig}(2 - 2\epsilon^{\mu}_{trig} + \epsilon^{\mu}_{trig}) \quad \text{(E.1)}$$

$$= \epsilon^{\mu}_{trig} * (2 - \epsilon^{\mu}_{trig}). \quad \text{(E.2)}$$

Appendix F: Background normalisation to Drell-Yan

Backgrounds from physics sources with known cross sections can be normalised to the data by relatively normalising their cross sections to the DY cross section and the number of Drell-Yan events. Where the number of Drell-Yan events is normalised to the number of dimuons observed in the Z peak region of the data sample.

The number of Drell-Yan events generated (N_{DYgen}) is the product of the production cross section for the Drell-Yan process (σ_{DY}) and the generated luminosity ($\mathcal{L}_{gen}^{DY}$).

$$N_{DYgen} = \sigma_{DY} \times \mathcal{L}_{gen}^{DY} \tag{F.1}$$

This is normalised to the Z region, using a scale factor (s_{DY}), which is equivalent to normalising the generated integrated luminosity ($\mathcal{L}_{gen}^{DY}$) to the integrated luminosity of the data ($\mathcal{L}_{data}$).

$$s_{DY} \times N_{DYgen} = \sigma_{DY} \times \mathcal{L}_{data} \tag{F.2}$$

Similarly when another physics process (X) is generated the number of generated events (N_{Xgen}) is related to the production cross section (σ_X) and the integrated luminosity of the generated data ($\mathcal{L}_{gen}^{X}$) by Equation F.3.

$$N_{Xgen} = \sigma_X \times \mathcal{L}_{gen}^{X} \tag{F.3}$$

By analogy to the Drell-Yan case, the generated luminosity ($\mathcal{L}_{gen}^{X}$) can be scaled to the integrated luminosity of the data ($\mathcal{L}_{data}$).

$$s_X \times N_{Xgen} = \sigma_X \times \mathcal{L}_{data} \tag{F.4}$$

The scaling factor s_X can be related to the Drell-Yan scaling factor (s_{DY}) by equating $\mathcal{L}_{data}$ in Equation F.2 and Equation F.4.

$$\frac{s_X \times N_{Xgen}}{\sigma_X} = \frac{s_{DY} \times N_{DYgen}}{\sigma_{DY}} \tag{F.5}$$

This can be rearranged to give:

$$s_X = \frac{s_{DY} \times N_{DYgen} \times \sigma_X}{N_{Xgen} \times \sigma_{DY}}. \tag{F.6}$$

So the relative scaling factor (s_X) for another background process (X) with known cross-section (σ_X) is given by the product of the ratio of the number of events generated (N_{DYgen}/N_{Xgen}), the inverse ratio of their cross-sections (*i.e.* σ_X/σ_{DY}) and the Drell-Yan scaling factor (s_{DY}) to the data.